UNIVERSITÄT
DUISBURG
ESSEN

Open-Minded

Analysis of the Dynamics of Adsorbed Organic Molecules

von der

Fakultät für Physik

der

Universität Duisburg-Essen

genehmigte

Dissertation

zur Erlangung des akademischen Grades

Dr. rer. nat.

vorgelegt von

Johannes Schaffert

geboren am 27. August 1983 in Essen

eingereicht am:	23. August 2013
Tag der Disputation:	16. Dezember 2013
Prüfungsvorsitz:	Prof. Dr. Jürgen König
Gutachter und Prüfer:	Prof. Dr. Rolf Möller
Gutachter und Prüfer:	Dr. Nicolás Lorente
Gutachter und Prüfer:	Prof. Dr. Gerhard Wurm
Prüfer:	Prof. Dr. Heiko Wende

"Estudiad como si fuérais a
vivir siempre;
vivid como si fuérais a morir
mañana."

(San Isidoro de Sevilla)

Contents

Abstract

This thesis presents the analysis of the dynamics of an adsorbed organic molecular species on a metal surface. When individual copper phthalocyanine molecules (CuPc) on Cu(111) are imaged by low-temperature scanning tunneling microscopy (STM), fluctuations which can be identified as 'random telegraph noise' are observed. The noise manifests itself in jumps of the tunneling current and documents bi-stable dynamics on the nanometer scale.

A new method of detection is presented, which allows to analyze random telegraph noise during ongoing STM experiments in real-time. The strength of the 'scanning noise microscopy and spectroscopy' technique (SNM, SNS) relies on the fact that it provides a full characterization of the noise with the same lateral resolution as provided by the STM. The results for the studied system show in great detail where the switching events are localized and provide the corresponding rates. Furthermore, the amplitude of the current jumps, as well as the relative occupation of the two observed states, are being detected. From the new information, a model for the underlying molecular dynamics is deduced: The molecule performs a frustrated rotation, a so called libration, within its adsorption plane, excited by the injected tunneling electrons. Furthermore, the spectroscopy mode reveals a one-electron process for the rotational excitation and gives access to the contributing orbital structure: The LUMO, HOMO and HOMO-1 states are detected.

The geometry and electronic properties of the organic-metallic system are also addressed by density functional theory (DFT). As a result, the molecular rotor can be described by a potential energy surface exhibiting potential wells for a ground state and two rotated configurations of the molecule. In addition, the experimental orbital structure and the STM images are reproduced and finally, the simulation of the excitation mechanism yields a calculated excitation map, which corresponds well to the experimental observations.

Kurzfassung

Die vorliegende Arbeit analysiert die Dynamik einzelner organischer Moleküle auf einer Kupfer (111) Oberfläche. Wenn Kupfer-Phthalocyanin (CuPc) mit dem Tieftemperatur-Rastertunnelmikroskop (STM) abgebildet wird, erscheint das an ein vierblättriges Kleeblatt erinnernde Molekül verrauscht. Das Phänomen tritt selektiv auf zwei der vier Kleeblätter auf und äußert sich durch zufällige Sprünge im Messsignal, die sich als 'statistisches Telegraphen-Rauschen' identifizieren lassen. Dieses Rauschen entspricht einem Schalten zwischen zwei Zuständen verschiedener Leitfähigkeit und enthält somit wertvolle Informationen über dynamische Phänomene einzelner Moleküle.

Zur Analyse dieses Informationskanals fehlte bislang eine praktikable Methode, die in Echtzeit Schaltereignisse aus dem Messsignal herausfiltert und quantitativ auswertet, während die volle Ortsauflösung des verwendeten STM erhalten bleibt. Dies leistet die im Rahmen dieser Arbeit entwickelte Rauschmikroskopie und -Spektroskopie Methode. Die damit erzielten Ergebnisse zeigen im Detail, wo und mit welcher Frequenz die Fluktuationen auftreten und darüber hinaus, wie groß die Amplituden der Sprungereignisse sind und in welchem Besetzungsverhältnis die beiden Leitfähigkeitszustände zueinander stehen. Die Messergebnisse zeigen, dass das CuPc Molekül eine frustrierte Rotation (auch: Libration) innerhalb seiner Adsorptionsebene ausführt, stimuliert durch ins Molekül injizierte Tunnelelektronen. Die Rauschspektroskopie zeigt, dass die Anregung durch einen Ein-Elektronen-Prozess geschieht und detektiert die energetische Lage der Molekülorbitale LUMO, HOMO und HOMO-1.

Zur Unterstützung der Erklärung werden dichtefunktionaltheoretische Simulationen präsentiert. Diese reproduzieren die STM Daten und die gemessene Orbitalstruktur. Darüber hinaus beschreibt eine simulierte Potentialfläche den molekularen Rotor, der sich nach einer Anregung aus seinem Grundzustand in einem von zwei rotierten Zuständen befinden kann. Der Anregungsmechanismus durch inelastisch tunnelnde Elektronen wird schließlich verwendet, um eine Anregungskarte für das Molekül zu simulieren. Das Ergebnis entspricht den experimentellen Beobachtungen.

1. Motivation

One of many goals of nanotechnology is to realize nanometer-scaled organic electronic devices which can be produced on an industrial scale. However, the fundamental physical properties of the prospective systems in interaction with their environment on the nanoscale often remain unknown. To bridge this gap, intense studies are conducted in order to fundamentally research the properties of organic molecules in the so called bottom-up approach. This means to first characterize individual molecules in different environments and to subsequently study larger systems, like molecular clusters, nano-wires, or thin films, with the available techniques in nanoscience and surface science, for instance by means of scanning tunneling microscopy (STM). Once new concepts are derived from the scientific approach, these 'building blocks' can be considered candidates for future applications in integrated circuits [1].

In the future, functional molecules could accomplish a broad variety of tasks, providing a low-cost alternative that would slowly replace silicon wafer-based technology. Organic electronics already demonstrate their fascinating potential at present. An example is the field of flexible electronics, where devices can be attached to skin [2], or can even be implanted in vivo and will biodegrade and be resorbed by the body after use [3]. Organic displays [4] are already being used for mobile devices and are on the verge of entering the television market. Flexible and transparent displays are expected to be the next evolution steps that find the way into our everyday lives [5, 6, 7]. While single molecular data storage bits have recently been demonstrated in STM-based experiments [8, 9], organic lighting panels [10] and photovoltaic cells [11] are already market-ready and challenge the established techniques.

Key challenges on the pathway to organic devices remain and include the discovery, the understanding and the control of nanometer-scaled switches. Single organic molecules are promising candidates since they offer a variety of functional properties [12, 13] that may

be switched by external parameters like voltage, temperature, illumination, or by controlled manipulation, e.g. within the STM [14].

When switching processes are monitored by STM, the measurement signal is the tunneling current and the switching events are observed by means of jumps of the current signal. A molecule that acts as a two-level reversible switch under the tip of an STM will possess two distinct levels in the tunneling current. Any kind of atomic or molecular rearrangement (hopping, rotation, bending, folding, diffusion, reaction, ...) or in general any kind of dynamics, may lead to a bi-stable signal. When the two levels occur randomly, with constant probabilities for the transition from one state to the other, the resulting signal is called random telegraph noise. Exemplary references are given in chapter 2.5.

Random telegraph noise is a widespread phenomenon that occurs in many electronic devices, such as MOSFETs (metal-oxide-semiconductor field-effect transistors) [15, 16, 17], flash memories [18], resistance random access memories (RRAM) [19], CMOS-sensors (complementary metal oxide semiconductors) [20] and it can be used for the task of generating random numbers [21, 22].

We wanted to study the random telegraph noise that occurs when tunneling electrons interact with the orbitals of individually adsorbed CuPc molecules on the Cu(111) surface. Previous results obtained in the Möller group exhibited the noise in terms of a fuzzy appearance of the molecules in the STM data and the two-level jumps were monitored by current-vs-time traces at fixed position of the tunneling tip [23, 24]. However, the physics behind the phenomenon remained unknown so far and only speculations existed about the possibility of molecular dynamics happening under the STM tip.

The scientific access to the underlying processes causing telegraph noise on the nanoscale requires an efficient analysis. With the aim of exploring the physics of the dynamic system, the details of the lateral distribution of the noise in the current signal needed to be addressed. Based on this information, a computational approach within the framework of density functional theory should be pursued in order to provide theoretical understanding. Unfortunately, a tool that characterizes telegraph noise on-line in an automated way was missing until now. Hence, this experimental challenge defines the starting point of the presented work.

The open questions were

1. How can we detect the noise characteristics during an ongoing STM experiment using a simple design by capturing the full lateral information on the occuring switching events?

2. Which kind of information is hidden in the noise from individual CuPc molecules and can it be exploited to unravel the underlying dynamic process?

3. Does the new information channel give access to the electronic structure of CuPc on Cu(111)?

4. Is it possible to prove or exclude deductions made from the noise measurements in a theoretical approach?

The structure of this work is the following: We start with the general chapters 2 and 3 that introduce the experimental and theoretical background. Subsequently, chapter 4 outlines the setup of the low-temperature STM experiment, the studied system and the new electronics. Chapter 5 contains the development of the theoretical model of CuPc on Cu(111). The results are presented in chapter 6 (experimental) and chapter 7 (theoretical), and are discussed in chapter 8. The thesis is summarized in chapter 9, followed by future prospects (chapter 10). Finally, two appendices recapitulate the work on a porphyrin molecule on Cu(111) (app. A), as well as a heterogeneous system consisting of CuPc in combination with a perylene based molecule (app. B).

2. Introduction to Scanning Tunneling Microscopy (STM)

For many decades, physicists have intensely studied surfaces with a remarkable set of experimental methods but without the opportunity to 'see' the atomic configuration of their sample surfaces in real space. Optical microscopes provide a maximal resolution that is limited by roughly half the wavelength of the light source used. Considering the shortest wavelength of visible light to be approximately 400nm (violet), standard optical microscopes will not distinguish details smaller than 200nm.[1]

Instead, surface scientists could rely on valuable information about the periodic atomic structure of surfaces that were derived from diffraction experiments. Especially clean surfaces of single crystals can be analyzed in terms of their symmetries and lattice parameters with great precision. A rather strict selection rule for classical diffraction experiments is, that only periodic structures can be observed. For ordered, but non-periodic systems like quasicrystals it is still possible to study average distances. In contrast to standard low-energy electron diffraction (LEED), the more sophisticated spot profile analysis low-energy electron diffraction technique (SPA-LEED) is even capable of analyzing e.g. the surface roughness for non-ordered structures.

However, the local access to single surface imperfections cannot be achieved. Thus, the conformation of atomic vacancies or individual adsorbates like adatoms or single molecules remains unknown.

At the beginning of the 1980s when Binnig and Rohrer invented the scanning tunneling microscope, it became possible to image a surface atom by atom in real space. The concept of tunneling through a vacuum barrier first appeared in literature back to 1928 [26]. Since

[1] An exception is the scanning near-field optical microscope (SNOM) presented by IBM in 1986. This scanning probe method breaks the resolution limit of far-field optics by using a fiber probe in a sub-wavelength distance to the sample. Twenty nanometers of lateral resolution has been achieved [25]. Still, individual surface atoms could not be imaged.

then, it took more than half a century until this quantum mechanic effect was used to image a surface. The pioneering work by Binnig and Rohrer opened the door for researchers to access the nanoscale in an unforeseen way. Nowadays, the scanning tunneling microscope together with a growing number of methods derived from it have become settled techniques in surface science. Soon after their invention, Binnig and Rohrer were awarded with the *Nobel Price* in Physics in 1986 [27].[2]

2.1. Principle of Measurement

How could Binnig, Rohrer and coworkers combine the quantum mechanical tunneling effect with the idea of realizing a microscope with atomic resolution? The family of scanning probe microscopes, with the STM being the first and most famous representative, uses a special way of imaging. The samples are scanned by a probe that interacts with the surface in a very close distance of only a few Ångströms ($1\text{Å} = 0.1\text{nm}$). This distance is so small, that quantum-mechanical effects come into play. While the probe performs a raster scan line by line (orange dotted arrows in Fig. 2.1), this interaction is monitored as a function of position, resulting in topographic maps that represent the surface.

Due to this imaging procedure, scanning probe microscopes differ from conventional optical microscopes or cameras, where images are obtained 'at once'.

The Tunneling Effect

The STM takes advantage of the tunneling effect, which noticeable occurs when two electrodes are brought together very closely (less than 1nm). At such small distances, the wave functions of the two electrodes considerably overlap. The electrodes 'feel' each other, but the sample and probe surfaces are not mechanically damaged. This is why STM is considered a minimal invasive technique.

The electrons at each side are capable of hopping back and forth with some probability, although there is a vacuum barrier in between. Here, the quantum mechanical character of electrons becomes obvious, because in classical physics, a particle is not allowed to overcome a barrier higher than the energy the particle carries. In tunneling, the electron is able to 'leak through' such a barrier albeit its height.

[2] jointly with Ernst Ruska for the invention of the scanning electron microscope (SEM), another successful and versatile technique, which scans an electron beam across the metallic samples. The SEM offers a high depth of field and wide range of magnification, but does not deliver atomic resolution.

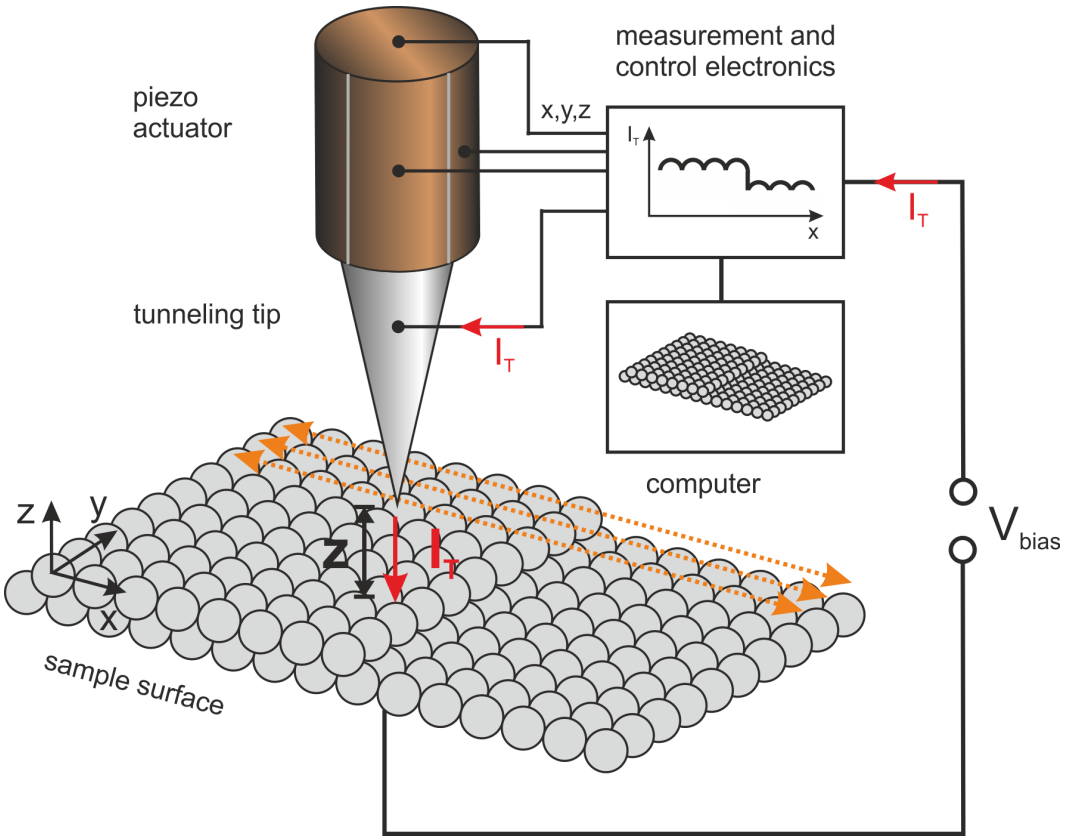

Figure 2.1.: Schematic view of a scanning tunneling microscope. A sharp metallic tip mounted to a piezo actuator scans the surface at a tunneling distance z ≈ 3...7Å). In between the tip and the surface a bias voltage V is applied and the resulting tunneling current I is measured. The raster motion is indicated for three line scans by orange dotted arrows. While the tip scans the surface (x, y), it witnesses a corrugation (z) of the surface like for example an atomic step. The tunneling current is kept constant by retracting and approaching the probe according to the topography or, more precisely, according to an interaction isosurface. Based on [28, 29].

The Tunneling Current

If the probe and the sample are conductive and a bias voltage, V_{bias}, is applied between both, the electrons will tunnel in a predominant direction. E.g., electrons from the occupied states of the tip tunnel into the unoccupied states of the sample resulting in a so called net tunneling current I_T. This current is the quantity monitored for STM operation. As the metallic probe scans the sample in a close distance, the tunneling current will change dramatically with every change in the topography of the sample. This results from the very sensitive dependency of the tunneling probability as a function of the probe-sample distance. It is given by an exponential behavior with a very small characteristic decay length in the order of 1Å. This guarantees the outstanding resolution in height differences, that the STM offers.

2.2. Theoretical Description of Tunneling Through a Vacuum Barrier

The theoretical treatment of the tunneling effect in the STM by J. Tersoff and D.R. Hamann is the most common three dimensional tunneling theory. It includes the tip and the sample and introduces reasonable approximations to explain in principle the lateral resolution of STM images [30, 31]. The work was published in 1985, three years after the presentation of the STM by Binnig and Rohrer.

The Tersoff-Hamann theory is based on the work by J. Bardeen, whose perturbation theory approach to the tunneling problem for planar junction geometries dates back to 1961 [32]. In Bardeen's theory the wavefunctions of tip and sample are assumed to not effect each another. Only the overlap of the two wavefunctions is used to describe the tunneling current I (eq. (2.1)).

$$I = \frac{2\pi e}{\hbar} \sum_{\mu,\nu} (f(E_\mu)\left[1 - f(E_\nu + e\,V)\right] |M_{\mu\nu}|^2\, \delta(E_\mu - E_\nu) \tag{2.1}$$

$$f(E) = \frac{1}{exp\left(\frac{E-E_F}{k_B T} + 1\right)} \tag{2.2}$$

The square of the absolute value of the matrix element $M_{\mu\nu}$ provides the tunneling

probability between a state at the tip Ψ_μ and a state of the sample Ψ_ν. The function f represents the Fermi distribution for the occupation of electronic states as a function of energy, V is the sample bias voltage, E is the energy of the indexed state and δ is the Dirac delta function. Finally, $\hbar$ is the reduced Planck's constant and k_B is the Boltzmann constant.

The formalism (esp. $M_{\mu\nu}$) is symmetric in μ and ν, reflecting the fact, that tunneling appears in both directions, from the tip to the sample and vice versa. The Fermi functions assure that tunneling occurs from occupied to unoccupied states only. The tunneling theory does not account for any energy loss processes during tunneling: It is an elastic tunneling theory.

Tersoff and Hamann approximate Bardeen's expression for the tunneling current by assuming low temperatures. This means, that thermally excited electron tunneling is neglected. This approximation as well as the assumption of small sample bias voltages are justified for experimental temperatures ranging from mK to room temperature in most cases and for tunneling bias voltages in the meV regime. Such small voltages are appropriate for metallic samples although STM experiments are not restricted to mV. Rather, voltages in the whole range between $\pm 3V$ are typical. The simplified expression reads:

$$I = \frac{2\pi e^2}{\hbar} V \sum_{\mu,\nu} |M_{\mu\nu}|^2 \ \delta(E_\nu - E_F) \ \delta(E_\mu - E_F). \tag{2.3}$$

At this stage, Tersoff and Hamann insert a parenthesis in their original work, as it is interesting to consider an imaginary ideal point probe (with a perfectly localized wave function). For this case, the matrix element is proportional to the amplitude of the wave function of the sample, Ψ_ν, at the position of the tip:

$$I_{ideal\ point\ probe} \propto \underbrace{\sum_{\nu} |\Psi_\nu(\vec{r_0})|^2 \ \delta(E_\nu - E_F)}_{LDOS\ \rho_\nu(\vec{r_0}, E_F).}. \tag{2.4}$$

The right side of eq. (2.4) equals the local density of states (LDOS) of the sample at Fermi energy, E_F, at the position of the virtual point probe, $\vec{r_0}$. Thus, the tunneling current can be regarded proportional to the integral over the sample's LDOS. A constant current STM image therefore represents a constant-LDOS map of the surface [31].

We will now continue with the evaluation of eq. (2.3). The main problem is to calculate the matrix element, since at this point the wave function of the tip, Ψ_μ, and the wave function of the sample, Ψ_ν, contribute explicitly:

$$M_{\mu\nu} = -\frac{\hbar^2}{2m} \int d\vec{S} \left[\Psi_\mu \, {}^*\nabla \Psi_\nu - \Psi_\nu \nabla \Psi_\mu^* \right]. \tag{2.5}$$

The term within the brackets is the so called current operator. The integration is over a surface which separates tip and sample and lies entirely in the vacuum gap as indicated in Fig. 2.2.

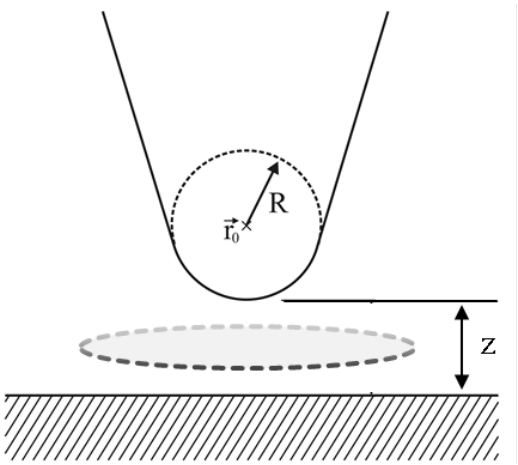

Figure 2.2.: The STM theory by Tersoff and Hamann approximates the tip apex by a (spherical) s-orbital with radius R. z is the tip-surface distance (the tunneling gap). An exemplary integration area (eq.(2.5)) which lies in between sample and tip is indicated by the gray-shaded ellipse.

To simplify the treatment of the tip, it is assumed to be representable by a spherical potential well, in other words, Tersoff and Hamann describe the wave function of the tip as a spherical s-orbital.

Other than the tip, the surface is treated 'exact' in the Tersoff-Hamann theory. For the wavefunction of the sample standing Bloch waves are used. The Bloch waves decay exponentially into the vacuum. Under the additional assumption of equal work functions of both, tip and sample, $\Phi_\mu = \Phi_\nu = \Phi$, the expression simplifies to

$$
\begin{aligned}
I &= \frac{32\pi^3 e^2 \Phi^2 R^2}{\hbar \kappa^4} \cdot \exp\left(2\kappa R\right) \cdot V \cdot \rho_\mu(E_F) \\
&\quad \cdot \sum_\nu \left|\Psi_\nu(\vec{r}_0)\right|^2 \cdot \delta(E_\nu - E_F) \qquad (2.6) \\
with\ \kappa &= \sqrt{\frac{2m\Phi}{\hbar^2}}, \qquad (2.7)
\end{aligned}
$$

where ρ_μ is the DOS of the tip. κ is the reciprocal decay length for the wave functions into the vacuum. It depends on the work function, Φ. For a typical metal work function of 4eV to 5eV (e.g. Ag, Cu, Au), we obtain a small value of about $\kappa \approx 1\text{Å}^{-1}$ which indicates the high sensitivity of the tunneling current to small changes in z with the tip-surface distance in the order of 1-10Å.

We can again identify the summation in eq. (2.6) with the DOS of the surface at the position of the tip at Fermi energy, $\rho_\nu\left(\vec{r_0}, E_F\right)$. That means we can write

$$
I \propto V \cdot \rho_\nu\left(\vec{r_0}, E_F\right). \qquad (2.8)
$$

For a small bias voltages V and metallic probe and sample the tunneling current depends linearly on the bias and the LDOS of the sample. The latter can be described by Bloch waves that decay exponentially into the vacuum and therefore we obtain for the simplest case:

$$
\begin{aligned}
I &\propto \exp\left(-2\kappa\, z\right), \qquad (2.9) \\
\kappa &\approx 1/\mathring{A}. \qquad (2.10)
\end{aligned}
$$

The latter expressions yield the following resumée:

The tunneling current scales exponentially as a function of the tip-surface distance, with a reciprocal decay constant κ in the regime of 1Å^{-1} that explains the high sensitivity of the scanning tunneling microscope for small tip-surface distances z in the order of 1...10Å.

The Tersoff-Hamann theory calculates the matrix element for the tunneling probability between tip and sample under the assumption of a spherical s-orbital. The resulting expression for the tunneling current mainly depends on the local density of states (LDOS) of the sample.

For the application of the Tersoff-Haman theory as a function of the bias voltage V, one can write the tunneling current in the following integral over energy:

$$I(V) \propto \int_0^{eV} \rho(x, y, E)\, T(E, eV)\, dE. \tag{2.11}$$

In contrast to the sample LDOS from eq. (2.4), which was introduced at Fermi energy only, here all electron density within the interval from E_F to $E_F + eV$ contributes to the tunneling current. An experimental tunneling current measured at the sample voltage V arises from the sum of all available tunneling channels (states) within that energy window. In eq. (2.11), the LDOS of the sample is explicitly written as a function of x and y to highlight the local information that will be observed when the STM scans the surface. The tunneling probability (or transmission coefficient) which includes all properties of the tip, is named T. The tip's density of states is assumed constant and therefore not mentioned here.

The Tersoff-Hamann theory has become a standard theory for STM experiments and albeit several approximations it can meet the experimental reality for simple systems. The s-orbital with its finite size accounts for some lateral averaging and sets a limit to the resolution of the STM. The choice of s-orbital tips deals with the general problem, that the exact state of the tip remains unknown in STM experiments. This experimental shortcoming did not change in the years that passed since Tersoff and Hamann decided to make this assumption, no matter how sophisticated the many STM-related experiments have become.[3]

[3] One interesting experimental approach that tries to characterize the tunneling tip is a field-ion microscope

Criticism may be expressed concerning several approximations made above:

The Bardeen theory breaks down as soon as the mutual interaction between the two electrodes is not negligible. Tersoff's and Hamann's low-voltage approximation does not fit the typical experimental customs, where STMs are operated between the 1mV and the 1V regime. The spherical (s-orbital) tip which was chosen for simplicity indeed does not explain the experimentally achieved sub-angström resolution of STM [33].

Advancements of STM theory

Since 1985, the theory of the scanning tunneling microscope was extended several times [34]:

Atomically resolved images were explained by C.J. Chen, who implemented p_z and d_{z^2} orbitals to represent the tunneling tip. He could show, that these spatially more located orbitals could reproduce the high resolution that was found in the experiments [33].

As soon as one considers adsorbates in between tip and sample, the theoretical description becomes more complicated. Already in the early days of STM surface scientists started to study organic molecules or biological specimens on surfaces [35, 36, 37]. Tunneling was found to be still possible provided that the few Å thin adsorbates were deposited on a metal substrate.

Chemical contrast in the STM was addressed by Lang. The tunneling junction was modeled by two planar electrodes described within the jellium model (homogeneous electron gas) with additional chemisorbed adsorbates. Using the Bardeen formalism, Lang could explain the chemical contrast resulting in depressions (for O and C adatoms) or protrusions (for Na and S adatoms) in STM images [38, 39] as well as spectroscopic features [40].

Tsukada *et al.* theoretically confirmed an assumption often made before: The tunneling current is concentrated almost exclusively on one tip atom (chapter 5.4 in reference [41]).

for the analysis of the tunneling tip inside the cooled (10K) LT-STM before and after tunneling. Such an experiment is currently under construction in the Möller group.

Scattering theory approaches went even further and incorporated tip-surface interactions [34]. The ESQC (elastic scattering quantum chemistry) theory by Sautet and Joachim [42] treats the tunneling junction in terms of a defect embedded within an otherwise periodic system (one-dimensional periodic chain). The defect system consists of the tunneling tip together with the vacuum gap, the adsorbate and the first surface layer. The scattering matrix and the transmission coefficients are calculated for the electrons passing the defect on their way from tip to sample or vice versa [43]. ESQC is able to quantitatively compare theory and experiment. For example, simulated STM images were presented for CuPc on Cu(100) in 1992 [44]. In another scattering approach, Doyen *et al.* could explain the contrast inversion sometimes observed in STM: Strong tip-surface interactions let the positions in between surface atoms appear as protrusions in the STM data.

2.3. Scanning Tunneling Spectroscopy

Scanning tunneling spectroscopy (STS) is the energy-selective analysis of the tunneling current. The energy dependence is obtained by varying the sample bias voltage while measuring the tunneling current at a fixed position of the tip. The opportunity to study both, the occupied and the unoccupied states is one key advantage of STS as compared to ultraviolet photoelectron spectroscopy methods which rely on occupied states only. Besides that, STS allows to analyze the electronic properties at specific positions of the surface like adsorbed molecules, adatoms and defects with ultimate spatial resolution [45], whereas photoelectron spectroscopy methods always measure a lateral average of a larger spot ($\geq \mu m^2$). Low-Temperature STMs offer the possibility to study e.g. single molecules in detail, as the cryogenic temperatures stabilize the tunneling conditions. For instance, the tunneling is protected from temperature induced drift of the tunneling tip versus the sample (see sec. 4.3). Thus, spectroscopic measurements can be performed slowly (several minutes) to enhance the signal-to-noise ratio at a well-known position of the tunneling tip above a surface feature. Even submolecular resolution can be achieved in spectroscopy mode.

The measured quantity is not primarily the I-V curve, but the derivative of the tunneling current with respect to the voltage (the differential conductivity dI/dV) in a typical energy interval of $\pm$2eV around E_F. Whenever STS measures the opening

of an additional tunneling channel, the dI/dV signal exhibits a well distinguishable peak [46].

Taking the derivative of the tunneling current (eq. (2.11)) with help of the lock-in technique, a signal proportional to the local density of states (LDOS) of the sample ρ_ν can be measured. The denominator serves as a normalization of the data. Details are discussed by Feenstra *et al.* in ref. [47]:

$$\frac{dI(V)/dV}{I/V} \propto \rho_\nu \left(\vec{r}_{x,y}, eV\right). \tag{2.12}$$

A modification of the STS measurement is the constant-current mode STS. Here, the tip is fixed in lateral, but not in vertical direction. The feedback loop controls the tip-sample distance to maintain the constant-current measurement. In that case, the measurement may not include zero bias voltage, because for small voltages the tip would approach closer to the surface until it crashes at V $= 0V$. When the constant-current technique is applied to each polarity, avoiding a small energy interval of e.g. $\pm$5meV it is possible to resolve spectroscopic features with great detail. For instance, semi-conducting molecular films may reveal their electronic structure in the gap region close to E_F, because the tip approaches close enough to detect even faint peaks in the LDOS. The highly conducting states at higher bias may be included in the same measurement, because the tip will retract accordingly. This makes the constant-current mode STS a versatile option.

Finally, it needs to be pointed out that the STS measurement of the dI/dV signal can also be conducted during scanning operation. In that case the resulting dI/dV images exhibit a contrast given by the sample's LDOS at the energy defined by the set bias voltage. High (bright) signals correspond to high density of states and low (dim) areas in the dI/dV maps resemble low density of states, respectively. In this manner, as an example, a molecular orbital can be imaged at a bias voltage close to its energetic position in the LDOS with spatial resolution. Provided that stable STM conditions are given, the dI/dV maps can be recorded for a series of energies, resulting in an energy dependent and spatially resolved data set on the sample's LDOS.

2.4. Technical Realization

2.4.1. The Probe

In principle, every thin metallic rod would be a suitable material to form a tunneling tip. As soon as high resolution is desired, the tip needs to be sharp. The metal atom at the apex of the tip is responsible for the imaging process. Due to a small decay constant in the exponential dependency of the tunneling probability on distance, a reduction of the tip - sample distance by the height of a single atomic step (about 2-5Å) raises the tunneling current up to three orders of magnitude [48]. Not only the sharpness of the tip, but also its stability is a requirement for successful experiments. For example, diffusing atoms at the tip, as well as mechanical vibrations and multiple tips are typical interference factors during STM operation. Several approaches have been developed to prepare and modify the front atoms of tunneling tips.

A very common tip material is tungsten (W) since it is very stiff. Another is the noble material platinum iridium (PtIr) which does not oxidize in air (but is mechanically less stable). Special purposes, such as spin-polarized STM, light emission STM, or contact tips for manipulation on the nanoscale, require different materials with specific magnetic (eg. Co), electronic (plasmons in Ag) or mechanic properties (soft gold tips).

Basically, there are two ways to produce a tunneling tip: to cut or to etch the wire. Cutting a wire with atomic precision is impossible to do, but practically 'there will always be some atom at the front'.[4] A PtIr wire can be cut in air, whereas less noble materials like tungsten oxidize. In addition, tungsten is brittle, so cutting a tip can result in a brush-like multi-tip inappropriate for STM imaging. In this case, etching e.g. with NaOH solution is a common technique (details in sec. 4.5).

After the tunneling tips have been transferred into a vacuum system, additional preparation steps may be performed before the STM experiments, e.g. sputtering (ion bombardment) or heating. Both techniques have the goal to to remove oxide layers from the tips.

Once a tip is used for STM operation it may experience accidental contacts to the sample surface or contamination. One straightforward procedure to enhance its quality is to apply

[4] A tautological bon mot by Maren Cottin from our every day life in the lab.

bias voltage pulses which may change the tip apex' configuration. Also intentional contacts with a metal substrate may help. The stiff tip material dips into a soft noble metal surface and eventually picks up one or several surface atoms forming a new tip apex.

For the tip preparation by field emission a high voltage is applied between tip and sample, when the tip is close to the surface, but not yet within the tunneling regime. At the tip and every micro-tip, the electric field will be enhanced so the electrons leave the tip at these positions and form the field emission current. Adsorbates desorb from the tip and the tip is reformed by material electromigrating to the apex. The field emission process is maintained with a current limited by a protective resistor. Details on field emission tip preparation controlled by a field ion microscope can be found in [49] and [50]. Further reading on tip preparation: [51, 52].

2.4.2. Mechanical Control on the Nanoscale Using Piezoelectrics

In the above introduction to STM [2.1] it was claimed that a probe and a sample can be brought together and stabilized in a distance as close as a few tenth of a nanometer. A distance so small, that quantum mechanics play a dominating role.

Piezoelectric crystals are used to accomplish the task to precisely control the tunneling gap. When the non-centrosymmetric polar crystals are deformed by external stress, the charge centers of the two types of ions are displaced with respect to each other. This displacement results in a voltage that can be measured between two sides of the crystal. Quartz and table sugar are examples for natural piezoelectric materials.
The inverse application of the piezoelectric effect is used for the mechanical control of the tunneling tip in STMs. Voltages up to a few hundred volts are applied to the piezoelectric crystals resulting in a small, but precisely controlled expansion or contraction. In order to control the position of the tunneling tip in three dimensions, several piezo elements may be combined. Compact designs use tube piezos with four outer segments electrically isolated from each other. The four outer as well as one inner segments are contacted separately. By applying a voltage between an opposing pair of outer contacts, the tunneling tip which is attached to the piezo can be moved within the surface plane. For the vertical contraction or expansion the same piezo tube is used and a voltage is applied in between the inner contact and all outer segments. The tube crystals used in this work are approximately sized

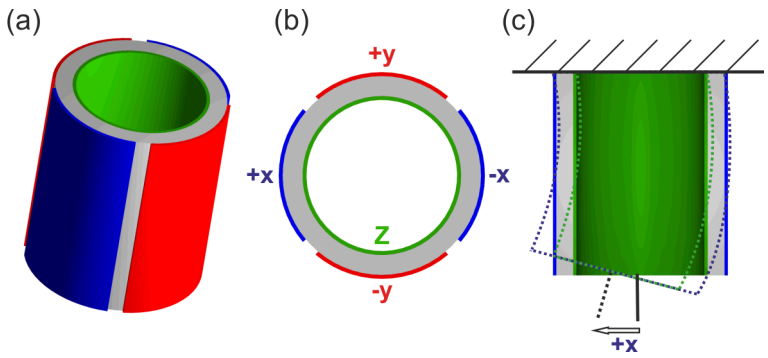

Figure 2.3.: Segmented piezoelectric tube. (a) 3D view and (b) top view: the four outer segments are pair-wise color-coded. (c) A cross section view for an exemplary (and by far exaggerated) deflection of the tube piezo along the $\pm$x direction. Realistic deflection ranges for a 1cm sized crystal are in the regime of 1...10μm. Figure reworked on the basis of [53].

2cm in height and 1cm in diameter with range of expansion and contraction in the regime of 2μm. A schematic view of a segmented tube piezo is given in Fig.2.3.

2.4.3. STM Feedback Loop

A feedback loop continuously controls the tip-sample distance (z) and keeps the tunneling current constant. The tunneling current depends exponentially on the tip-sample distance, with a decay constant in the order of 1Å. Hence, the system is very sensitive to small changes in the z direction. For the feedback loop, the tunneling current is converted to a voltage by an IVC (current-to-voltage converter). A typical amplification is 10^9V/A which means, that a tunneling current of 1nA is converted to 1V. From now on, this measurement voltage will be referred to as the the tunneling current signal.

To achieve a constant tunneling current, the logarithm of the tunneling current signal I_T is compared to a set value I_{set}. The logarithm of I_T is a linear function of the tip-sample distance and therefore an appropriate control parameter. Whenever the measured value rises (exceeds the set value), the tip will be retracted accordingly so that the tunneling current matches the set value again. On the other hand, an increasing tip-surface distance results in a drop of the current and the z piezo needs to be expanded. The control signals that adjust the z piezo while the surface is scanned are used to create topographic maps. It has to be stressed, that 'STM topographies' are maps of equal density of states of the sample. In many cases however, this corresponds well to the geometric topography.

2.5. Noise in Scanning Tunneling Experiments

In the present study, the characteristics of noise occurring in the tunneling current signal will be the observables that yield valuable information on dynamic processes of single molecules under the tip of a scanning tunneling microscope.

The four basic types of noise are *thermal noise*, *shot noise*, *telegraph noise*, and $1/f$-*noise*. They are summarized on the basis of reference [54] (german language).

Thermal Noise

The origin of thermal noise (Johnson-Nyquist noise) is the Brownian motion (random-walk) of charge carriers in equilibrium. Even in the absence of a force acting on the charge carriers [5], the statistical motion will lead to a finite standard deviation of the carrier flux while the total average current equals zero. The thermal noise originating from an idealistic resistor is called *'white noise'*. This means the power is equally distributed in frequency.[6]

Any experimental temperature will be above $0K$ allowing the carriers to diffuse within a conductor. The implementation of low-temperature experiments suppresses the occurrence of thermal noise to some extend (see also section 4.3).

Shot Noise

The term *'shot noise'* describes the inherent fluctuations in a signal caused by the discrete flow of charges (quantization). The measurement of a small current, with one electron or hole after another relies on counting discrete events. These random events are independent from each other and therefore described by a *Poissonian Distribution*. Whenever a current is small enough so that uncertainties within the distribution become significant, shot noise becomes important.

Shot noise is independent of temperature and frequency, i.e. it is a *'white noise'*, similar to the thermal noise.

$1/f$-Noise

The power spectral density of $1/f$-noise (pink noise) is inversely proportional to the frequency. $1/f$-noise is a widely found phenomenon in many fields of physics. However, the

[5] i.e. without any voltage applied

[6] This is valid for classical frequencies f up to $hf << kT$ (up to terahertz at room temperature).

physical source of $1/f$-noise is not conclusively clarified. The disorder of the investigated systems seems to play an important role for the occurrence of $1/f$-noise. For further reading the review article by Weissman [55] is recommended.

Telegraph Noise

A signal exhibiting telegraph noise (TN) switches between discrete levels. Often the terms burst noise, popcorn noise, or bi-stable noise are used equivalently.
In the simplest case, the number of levels is two, as depicted in Fig. 2.4.

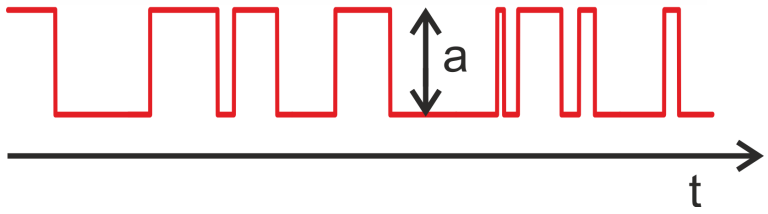

Figure 2.4.: Scheme of a two-level telegraph noise signal as a function of time (t); the measured quantity switches between discrete values which differ by the amplitude a.

The residence times of the two levels can be described statistically. A *'random telegraph noise'* (RTN) signal has constant probabilities for the transition from one level to the other. More explicitly this means, that such a signal has no memory, as it does not contain information about the past. The number of events as a function of life-times decays exponentially. A typical RTN signal is analyzed with respect to the decay of the life times in Fig. 6.6. Only in the special case of symmetric RTN, the two life times histograms decay with equal time-constants. Usually, the time-constants are different.

Noise in the Tunneling Current

In scanning tunneling experiments, the detection of small currents under the influence of mechanical, thermal and electrical disturbances is a challenge. Consequently, the intrinsic noise of tunneling currents was studied already in the early days of STM.

On highly oriented pyrolytic graphite, the noise was found to be dominated by a $1/f$ component at low temperatures (e.g. [56, 57]). Möller *et al.* reported, that the $1/f$-noise disappears for small tunneling currents on a silver sample, especially at a zero bias

voltage. Thermal noise of the tunneling resistance was measured and applied to realize an alternative feedback loop controlling the tip-surface distance [58].

Telegraph Noise in STM

Telegraph noise (TN) is a common observation in the field of dynamical processes on surfaces. Two or more levels of conductance at a specific position under the tip of an STM indicate switching processes in the tunneling junction. Welland and Koch reported on TN in the tunneling current in 1986, when they observed trapped charges on an oxidized silicon substrate [59]. A pioneering work on STM-based manipulation by Eigler *et al.* [60] presented an atomic switch realized with the tip of an STM, where Xe atoms were reversibly transferred between the tunneling tip and a nickel surface. The observation of the tunneling current signal yielded TN events whenever an atom was transferred back or forth. In the same year, Lyo and Avouris reversibly transferred silicon atoms between the tunneling tip and a silicon surface [61]. The rotation of single molecules of molecular oxygen on Pt(111) was reported to cause TN by Stipe *et al.* [62]. Stroscio and Celotta recorded random TN caused by Co adatoms on Cu(111) that were manipulated by the tunneling tip in between different adsorption sites and analyzed the transfer rates as a function on sample bias and tip-sample distance [63]. Pennec *et al.* presented silicon atoms to switch their buckling state in reconstructed dimer rows [64], also resulting in TN in the STM tunneling current.

Later, when organic molecules on surfaces attracted attention, the occurrence of TN coinciding with dynamics was reported for a large variety of (single) molecular switches in STM experiments. A few representative examples are given below. It is noteworthy, that the organic molecules studied show a broad spectrum of appearance and properties and the physics that drives the changes of molecular conductance is different from case to case. Among the examples from literature, tautomerizations are reported. A chemical tautomerization reaction is the conversion in between different isomers of the same organic compound, typically taking place via atom-hopping from one ligand to another. Another example for isomerization is the spatial rearrangement of molecules, for instance the folding of functional groups. Other studies report on molecular hopping between adsorption configurations or molecular rotations around specific symmetry axes within the molecule or

given by the adsorption configuration (e.g. adatoms). All of these processes were observed to cause telegraph noise (TN) in the tunneling current:

Examples of Telegraph Noise in STM Experiments on Organic Molecules

Gaudioso and Ho observed the motion of pyrrolidine-d_8 on Cu(100) [65, 66]. Pitters and Wolkow studied the TN jumps in the conductance of styrene molecules on Si(100) [67]. Iancu and Hla investigated a four-step molecular switch by analyzing RTN for Chlorophyll-a on Au(111) [68]. Liljeroth, Repp and Meyer induced the hydrogen tautomerization within naphthalocyanine molecules with the tunneling current and recorded the resulting TN as a function of bias and position [69, 70]. Henningsen *et al.* observed conductance jumps within bias dependent STM images of single phenyl rings of an azobenzene derivative on Au(111) [71]. Gao *et al.* reported on arrays of the anchored organic molecular rotor tetra-tert-butyl zinc phthalocyanine ($(t-Bu)_4$-ZnPc) on a Au(111) surface [72]. Later, Liu *et al.* found TN caused by rotating FePc molecules on the same substrate [73]. Wang *et al.* reported on an organic molecular switch driven by the controlled pushing and pulling of Sn atoms through the center of phthalocyanine molecules [9]. Nacci *et al.* analyzed the RTN signals for the conformational switching of single 1,5 cyclooctadiene molecules on Si(001) and identified current-induced switching [74]. Later, they studied the biconformational switching of COD molecules on the same surface and studied its temperature-dependence [75]. Tierney *et al.* observed TN stemming from the rotation of single dibutyl sulfide molecules (Bu_2S9 on Au(111) and found a threshold energy above which a C-H vibration excited the molecular motion [76]. Parschau *et al.* evaluated an inelastic tunneling current induced reaction yield as a function of current and bias voltage for a chirality switching of propene on Cu(211) from TN signals [77]. Simic-Milosevic, Meyer and Morgenstern assigned TN conductance jumps to a chirality change of chloronitrobenzene on Au(111) [78]. Wang *et al.* investigated a three-level TN resulting from a tunneling current stimulated molecular rotor (BTP-BCO) on Cu(111) [79]. Kühne *et al.* analyzed the rotation rate of individual molecules within a 2D supramolecular network as a function of temperature based on jumps in the tunneling current [80]. Jewell *et al.* studied the dynamics of thioether molecular rotors via the computer-assisted counting of TN switching events [81]. Auwärter *et al.* switched the nitrogen binding partners of the two central hydrogen atoms within free-base porphyrins with the tunneling current [82]. Recently, Hahne *et al.* studied the diffusion of CuPc on

Ag(100) [83].

3. Introduction to Density Functional Theory (DFT)

Among all quantum mechanical approaches to the simulation of matter, density functional theory (DFT) is now one of the most successful and widely used methods. It is an *ab initio* method, meaning that it does not make use of empirical input, nor does it possess any free parameters. DFT is formally exact in describing the interaction of electrons. However, its practical performance depends on the quality of the approximations made to fit the capabilities of today's computers when implementing the daunting task of numerically solving the many-electron problem.

This chapter introduces density functional theory with the aim of laying the foundations of a comprehensive description of the efforts made in the calculation of CuPc on Cu(111). The modeling of the system studied here will be explained in chapter 5 and chapter 7 is dedicated to the theoretical results. Parts of the following subsections in chapters chapters 3 and 5 are based on lectures and practical exercises given by Nicolás Lorente[1] and were summarized before in the diploma thesis by my student Andreas Sonntag (German language [84]), therefore resembling the following sections in terms of structure, notation and content. For further input the book by Martin [85] and the review articles by Payne *et al.* [86] and Capelle [87] as well as the VASP guide [88] were consulted together with the original research papers (where indicated).

3.1. The Concept

It is very demonstrative to remind oneself of the Hamiltonian for the many-body Schrödinger equation known from quantum mechanics lectures (eq. 3.1). It yields a full description of

[1] Centre d'Investigació en Nanociència i Nanotecnologia (CSIC-ICN), Campus UAB, E-08193 Bellaterra, Spain.

every quantum mechanical system such as molecules, solids or surfaces. The Hamiltonian contains all $3M$ coordinates of the nuclei $\vec{R}$ and the $3N$ coordinates of the electrons $\vec{r}$. The electron mass is m_e, the masses of the nuclei are named M, and proton numbers are Z. The five terms emphasized by brackets account for (a) the kinetic energies of the electrons, (b) the kinetic energies of the nuclei, (c) the electron-electron interaction, (d) the electron-core interaction, and (e) the core-core interaction.

$$\hat{H} = \underbrace{-\sum_i \frac{\hbar^2}{2m_e}\nabla_i^2}_{(a)} \underbrace{-\sum_\alpha \frac{\hbar^2}{2M_\alpha}\nabla_\alpha^2}_{(b)} + \underbrace{\frac{1}{2}\sum_{i\neq j}\frac{e^2}{|\vec{r}_i - \vec{r}_j|}}_{(c)} \underbrace{-\sum_{i,\alpha}\frac{Z_\alpha e^2}{\left|\vec{r}_i - \vec{R}_\alpha\right|}}_{(d)} + \underbrace{\frac{1}{2}\sum_{\alpha\neq\beta}\frac{Z_\alpha Z_\beta e^2}{\left|\vec{R}_\alpha - \vec{R}_\beta\right|}}_{(e)} \tag{3.1}$$

Unfortunately the Schrödinger equation for any system larger than the hydrogen atom is insolvable without making use of approximations.

The Born-Oppenheimer approximation was the first progress. It separates the degrees of freedom of the electrons from the nuclei part of the wavefunction. Thus, the electronic part can be calculated by treating 3N instead of 3N + 3M coordinates. Despite this achievement, there is still the remaining problem of the determination of the electronic wave function.

A choice of special techniques deal with the many-body problem. For example, methods like Hartree-Fock deliver approximative solutions of the Schrödinger equation. The main drawback of these *mean-field* theories is the treatment of the single electron. Each electron witnesses only a 'mean field' of all other electrons, thus, collective phenomena such as plasmons are not accounted for and the total energy of the calculated system is *a priori* augmented. Besides that, these methods (and also Green's function methods) demand for huge computational resources [87].

After the publication of the Hohenberg-Kohn theorems it became possible to solve the many-body Schrödinger equation with an acceptable computational effort.

The great success of the modern formulation of DFT as an *exact theory of many-body systems* originates from the 1964 landmark paper by Hohenberg and Kohn, proving that all

properties of a quantum many-body system can be expressed by functionals[2] of the ground state density [89]. Indeed, this radical idea only needs this one scalar function of position $n_0(\vec{r})$ to provide all information about the many-body wavefunctions. The wave functions for the $3N$ electron coordinates do not need to be calculated. This simplification lead to comparably low computational costs and consequently the quantum mechanical treatment of larger systems with several hundred atoms. DFT grew to a versatile and wide-spread technique yielding essential insights into many fields of physics, chemistry and biology. In honor of his work, Walter Kohn was awarded the *Nobel Prize* in Chemistry in 1998 [90] together with John Pople, who implemented DFT in computational chemistry.

3.2. Born-Oppenheimer Approximation

Back in 1927, Born and Oppenheimer published their successful approximation. It separates the electronic part from the nuclei part of the wave function [91]. Practically this means, that the wavefunction for N electrons with 3N coordinates can be calculated while the 3M coordinates of the nuclei are kept constant. Physically this means to treat the nuclei as spatially fixed particles which form an external potential for the electrons. This step is warranted by the fact that the masses of the nuclei exceed the electron mass by far, but the Coulomb forces acting on both are of the same order of magnitude. Hence, the nuclei will experience very small acceleration and speed as compared to the electrons, practically standing still during the time, in which the electrons react '*instantaneously*' to the potential created by the nuclei. The separated wave function can accordingly be written

$$\psi\left(\vec{r}_i, \vec{R}_\alpha\right) = \psi^{el}_{\left\{\vec{R}_\alpha\right\}}\left(\vec{r}_i\right) \cdot \psi^{nuclei}\left(\vec{R}_\alpha\right). \tag{3.2}$$

In the same way, the Hamiltonian can be separated into a nuclei part and an electronic part. In the following sections, just the electronic part will be considered:

$$H^{el}_{\left\{\vec{R}_\alpha\right\}} = \sum_i -\frac{\hbar^2}{2m_e}\nabla_i^2 + \frac{1}{2}\sum_{i\neq j}\frac{e^2}{|\vec{r}_i - \vec{r}_j|} + V^{ext}_{\left\{\vec{R}_\alpha\right\}}\left(\vec{r}\right). \tag{3.3}$$

The nuclei, on the other hand, create a (time-independent) external potential $V^{ext}_{\left\{\vec{R}_\alpha\right\}}\left(\vec{r}\right)$.

[2] In the calculus of variations, a functional can be seen as *'a function of a function'*. A typical aim is to find a function which minimizes a functional, e.g. the energy functional.

It includes both the Coulomb term for electrons and nuclei and the inter-nuclei interaction:

$$V^{ext}_{\{\vec{R}_\alpha\}}(\vec{r}) = -\sum_\alpha \frac{Z_\alpha e^2}{\left|\vec{r}-\vec{R}_\alpha\right|} + \frac{1}{2}\sum_{\alpha\neq\beta}\frac{Z_\alpha Z_\beta e^2}{\left|\vec{R}_\alpha-\vec{R}_\beta\right|}. \tag{3.4}$$

3.3. Hohenberg-Kohn Theorems

The first Hohenberg-Kohn theorem reads as follows (as phrased by R. Martin [85]):

Theorem I:

'For any system of interacting particles in an external potential $V^{ext}(\vec{r})$,
the potential $V^{ext}(\vec{r})$ is determined uniquely,
except for a constant, by the ground state particle density $n_0(\vec{r})$.'

This implies that the potential can be obtained from a functional of the ground state density. The external potential determines the Hamiltonian as well as all quantities derived from it. Thus, *all* properties of the system are given by the ground state density.

Theorem II:

'A universal functional for the Energy E[n] in terms of the density $n_{\vec{r}}$
can be defined, valid for any external potential $V^{ext}(\vec{r})$.
For any particular $V^{ext}(\vec{r})$, the exact ground state energy of the system is the
global minimum value of this functional, and the density $n(\vec{r})$ that minimizes the
functional is the exact ground state density $n_0(\vec{r})$.'

The second theorem answers the question how to identify the ground state density. For a known Hohenberg-Kohn functional $F_{HK}[n]$ the ground state density is the density, that minimizes the total energy of the system.

The proofs of both Hohenberg-Kohn theorems are can be comprehended with the help of introductory textbooks such as reference [85].

3.4. Kohn-Sham Equations

The Hohenberg and Kohn theorems facilitate the treatment of quantum systems by stating, that the electron density of the ground state completely describes a system.

However, the remaining challenge is to calculate this ground state density in the one or the other way.

The subtle approach proposed by Kohn and Sham circumvents the complex interacting many-body system which was the starting point of this chapter in eq. 3.1. Their *ansatz* replaces one problem with another; instead of dealing with the many-body problem, Kohn and Sham introduce an auxiliary **independent-particle** problem [92]. The new particles *'Kohn-Sham particles'* in the following replace the electrons and behave like non-interacting fermions, but strictly speaking do not possess any physical meaning. The same is valid for the *Kohn-Sham orbitals* and the *Kohn-Sham energies*. The *Kohn-Sham density* is assumed to share the same ground state density with the original interacting electron system. Thus, all information on the all-electron system can be derived also from the auxiliary system [92]. The difficult many-body interactions of the original problem are cumulated in an *exchange and correlation potential* V_{XC} together with one-body corrections that are necessary, because the Kohn-Sham theory enforces a single-particle Schrödinger equation.

At this point, we will begin to introduce approximations (see section 3.5). For the Kohn-Sham Hamiltonian $\hat{H}^{KS}$, we hide V_{XC} within the effective potential V^{eff} for the moment and come back to the exchange and correlation potential later:

$$H^{KS} = T + V^{eff} \tag{3.5}$$

$$\left(-\frac{\hbar^2}{2m_e}\Delta + V^{eff}\left(\vec{r}\right)\right)\psi_i\left(\vec{x}\right) = \epsilon_i\psi_i\left(\vec{x}\right). \tag{3.6}$$

H^{KS} now consists of the kinetic energy operator T for non-interacting particles plus an (so far unknown) effective potential V^{eff} (as yet unknown) with all the many-body physics inside. The resulting non-interacting *Kohn-Sham equations* are exactly - or at least numerically - soluble. The wave function of the ground state can be written in the style of a

Slater determinant

$$\Theta\left(\vec{x}_1, \vec{x}_2, \ldots, \vec{x}_N\right) = \frac{1}{\sqrt{N!}} \begin{vmatrix} \psi_1\left(\vec{x}_1\right) & \psi_2\left(\vec{x}_1\right) & \ldots & \psi_N\left(\vec{x}_1\right) \\ \psi_1\left(\vec{x}_2\right) & \psi_2\left(\vec{x}_2\right) & \ldots & \psi_N\left(\vec{x}_2\right) \\ \vdots & \vdots & & \vdots \\ \psi_1\left(\vec{x}_N\right) & \psi_2\left(\vec{x}_N\right) & \ldots & \psi_N\left(\vec{x}_N\right) \end{vmatrix}, \tag{3.7}$$

where the $\psi_i\left(\vec{x}\right)$ are the so called *Kohn-Sham orbitals* with $\vec{x}$ representing both the coordinates and the spin of the electrons. With help of the one-particle Schrödinger equation (eq. 3.6) the orbitals can be determined. In the ground state each of the N orbitals with the lowest eigenvalues ϵ_i are occupied with one electron for each spin until all electrons of the system are distributed. The Kohn-Sham density equals the sum of squares of the Kohn-Sham orbitals for each spin and we require it to equal the ground state density $n_0\left(\vec{r}\right)$:

$$n\left(\vec{r}\right) = \sum_{i=1}^{N} \sum_{s} \left|\psi_i\left(\vec{r}, s\right)\right|^2 \tag{3.8}$$

$$\stackrel{!}{=} n_0\left(\vec{r}\right). \tag{3.9}$$

The desired equality (eq. 3.9) is fulfilled only for an appropriate choice of the exchange and correlation potential V^{XC}, which is part of the effective potential

$$V^{eff}\left(\vec{r}\right) = e^2 \int \frac{n\left(\vec{r}'\right)}{\left|\vec{r} - \vec{r}'\right|} d^3\vec{r}' + V_{ext}\left(\vec{r}\right) + V_{XC}\left(\vec{r}\right). \tag{3.10}$$

Besides *Born-Oppenheimer*, we did not apply any approximations so far and thus all information on the system can be derived from the exact ground state density, if only V^{XC} is known.

3.5. Exchange and Correlation Functionals

In the last section, the Kohn-Sham equations and an iterative solution scheme were discussed. It was left an open question thus far as to find an appropriate-exchange (XC) and correlation potential V_{XC}. Among today's variety of sophisticated XC-potentials, the concepts of the two most widely used local and semi-local approximations shall be presented briefly.

3.5.1. Local Density Approximation

The local density approximation (LDA) is based on the idea of locally expressing the electronic system by the homogeneous electron gas. The exchange-correlation energy, E_{XC}, can than be written as a functional of the density, solely. E_{XC} is then computed simply by integrating all XC energies for the electrons $\epsilon_{XC}^{hom}\left(n\left(\vec{r}\right)\right)$ over space times the probability to find an electron at the position $\vec{r}$ [92, 93]:

$$E_{XC}^{LDA}[n] = \int n(\vec{r}) \cdot \epsilon_{XC}^{hom}(n(\vec{r}))\, d^3\vec{r}. \tag{3.11}$$

The underlying presumption is that the XC energy density equals that of the homogeneous electron gas at each point (hom). Any effect due to spatial inhomogeneities of the electron density on the XC energy are neglected. The total electron density n is a constant for a large system volume, V, with a large number of electrons, N. Hence, $n = N/V$. The interacting electrons experience a positive background charge resulting in an overall neutral system.

The LDA can equivalently be written in terms of two spin densities $n^{\uparrow}$ and $n_{\downarrow}$ (local spin-density approximation (LSDA) [94, 95]). To enhance the readability this is not done here since the DFT study presented in the further course of this work does not include spin-polarized calculations. In that case one simply obtains $n^{\uparrow} = n_{\downarrow} = n/2$.

The XC energy decomposes linearly into an exchange and a correlation term so that each can be treated separately:

$$E_{XC}[n] = E_X[n] + E_C[n]. \tag{3.12}$$

The exchange energy can be determined analytically for the homogeneous electron gas. According to the ansatz, this is the key advantage of the LDA. The correlation term can be calculated by quantum-mechanical Monte-Carlo methods [96].

The local density approximation will provide best results for solids in which the electronic system is close to a homogeneous electron gas, i.e. nearly-free electron metals. Nevertheless, the approach still works well in inhomogeneous cases [85].

When DFT results based on the LDA are quantitatively compared to experiment, an 'overbinding' tendency is inherent in geometry optimization calculations (LDA underestimates binding distances). In many cases, LDA is nevertheless a successful tool in surface science since the overbinding error compensates for the lack of (long range) van der Waals interaction in the simulations. Indeed, many systems of organic molecules on surfaces are

represented well by the local density approximation [97].

3.5.2. Generalized Gradient Approximation

Whereas the above local approximation (eq. (3.11)) represents the electron density locally by the constant density, $n(\vec{r})$, of the homogeneous electron gas, the generalized-gradient approximation (GGA) additionally considers the magnitude of the gradient of the density $\nabla n(\vec{r})$. Hence, the local treatment of the density in the GGA can be understood by the inclusion of the second term in a Taylor expansion of n at the position $\vec{r}$. The exchange-correlation functional reads in analogy to the previous section:

$$E_{XC}^{GGA}[n] = \int n(\vec{r}) \cdot \epsilon_{XC}(n(\vec{r}), \nabla n(\vec{r}))\, d^3\vec{r} \tag{3.13}$$

$$= \int n(\vec{r}) \cdot \epsilon_X^{hom}(n(\vec{r}))\, F_{XC}(n(\vec{r}), \nabla n(\vec{r}))\, d^3\vec{r}. \tag{3.14}$$

Again, the total density n was written instead of two densities corresponding to spin up and spin down. The exchange energy $\epsilon_X^{hom}(n(\vec{r}))$ for the (unpolarized) homogeneous electron gas can be used and the new analytic function $F_{XC}(n(\vec{r}), \nabla n(\vec{r}))$ contains the details of the particular GGA. It is called the enhancement factor. Numerous ways of implementing F_{XC} have been proposed. In the context of this work, the very popular Perdew-Burke-Enzerhof functional (PBE) was used [98, 99]. Other successful functionals are the PW91 by Perdew *et al.* [100, 101] and the BLYP derived from the names Becke for the exchange term [102] and Lee, Yang and Parr for the correlation term [103].
The major shortcoming of the LDA is its tendency to overbind. The problem of unphysical binding distances is reduced in the GGA. In contrast, although GGA meets closer the experimental values, it shows a slight tendency to yield binding distances that are too small.

Still, the DFT description does not account for long-range interactions, such as van der Waals. In the very recent years, theoreticians worked out several approaches to overcome this drawback starting from the GGA point of view [104, 105].

3.6. Periodicity, K-point Mesh and Cut-off Energy

Periodicity

Many DFT codes make use of plane-wave basis sets to express the wavefunctions. The Vienna ab-initio simulation package (VASP code) used in the framework of this thesis is one example (see section 5.1). In the case of plane-wave codes it is straight-forward to restrict the calculated model systems to periodic boundary conditions since this will result in a discrete set of plane waves. The wave functions (the corresponding expansion coefficients) depend on the Kohn-Sham orbitals and the wave vectors of the electrons, $\vec{k}$.

Many studied systems are a priori periodic, especially bulk solids. When it comes to surfaces, the periodicity is broken in one direction and if individual adsorbates shall additionally be studied then it is not obvious how to maintain a restricted basis set. The workaround is to create an artificial periodicity for those non-periodic systems by defining a supercell which will be repeated periodically to all directions. Three examples are displayed in Fig. 3.1.

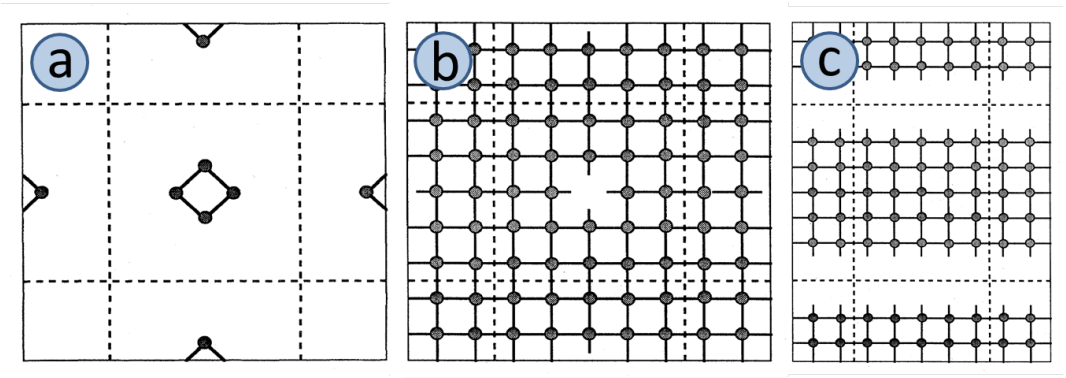

Figure 3.1.: Creating periodic model systems to study non-periodic phenomena with plane-wave basis set DFT codes [86].

The supercell chosen needs to be large enough in order to keep the self-interaction of the non-periodic system with its periodic representations to a minimum. In Fig. 3.1a molecule is placed in the middle of a supercell surrounded by vacuum. For simplicity the figure is restricted to two dimensions. The dashed lines indicate the borders of the supercell and the next neighboring periodic cells can be seen. The same construction is displayed in Fig. 3.1b for a defect inside a crystal. It can be regarded the inverse problem to (a). The supercell size in these directions is a multiple of the lattice parameter of the respective

material. In surface science (c), the supercells contain a few layers of the substrate which are extended in two directions (here: one). In the third direction (here: vertical) two surfaces are contained in the model. The cell-size perpendicular to the surface plane needs to be chosen large enough to add a vacuum gap clearly separating the two surfaces to guarantee that the interaction between the two is negligible. These kinds of model systems are called 'slab-models'. One of the surfaces may be chosen to add an adsorbate system like an organic molecule.

The solution of the stationary Schrödinger equation in a periodic potential (solid) is known to be representable by a plane-wave that is modulated by a function of the same periodicity as the solid (Bloch theorem). The wavefunctions may be expanded in plane-waves and the Kohn-Sham equations can be written as a linear system of equations. The Fourier transforms (e.g. for the effective potential) can be calculated quickly by todays computers and a numerical solution of the system of equations is within reach.

Only two more problems need to be addressed: Firstly, the infinite number of $\vec{k}$ vectors in the Brillouin zone cannot be included in a numerical calculation. Secondly, the number of lattice vectors has to be restricted from infinity to a numerically manageable number.

K-point Mesh

A very restricted k-point mesh is the practical answer to the latter problem. The periodic part of the wavefunction is nearly identical for points that are very close in k-space. Therefore, a 3-dimensional k-point mesh can be introduced in order to describe the Brillouin zone adequately. The Kohn-Sham equation only needs to be solved for these k-points. The VASP DFT code provides a feature, that automatically generates the k-point mesh by systematically exploiting symmetries. Equivalent k-points are found and the Kohn-Sham equation only needs to be solved for the irreducible number of k-points. To elucidate the practical implications of the k-point restriction, two examples shall be discussed: an individual molecule and a solid.

For a molecule in vacuum the energy levels are discrete. The 'band' structure exhibits perfectly flat states. As a consequence one k-point (the gamma point) is sufficient to describe the system.

In the case of a solid, many k-points are needed to represent the details of its band

structure. Metals especially require a dense set of k-points to represent their Fermi surface [86], thus more computational time is needed.

Cut-off Energy

In a plane-wave basis set, the waves with small kinetic energy are more important than the high-energy ones [86]. This can be understood by thinking of the Fourier transform of a periodic function. The basis set is truncated at a certain cut-off energy, E_{cut}, and only plane-waves with kinetic energies below E_{cut} are included. Together, the Bloch theorem discretization of the basis set and its truncation guarantee a finite basis set [86]. Typical cut-off energies are in the range a few hundred electron volts. The accuracy of plane-wave DFT calculations can be enhanced by raising E_{cut}.

3.7. Pseudopotentials

The concept of pseudopotentials deals with problems resulting from the oscillating wave functions of the tightly bound core orbitals. The rapid oscillations due to the deep ionic potential well in the core-region (e.g. Ψ_v in Fig. 3.2) complicate the convergence of the simulations. In addition, a rather large plane-wave basis set is needed to describe the wave functions with all their nodal points appropriately which again raises the demand for computational resources.
The electronic properties of typical studied systems depend on the valence electrons. Thus, the details of the atomic potentials close to the core do not need to be treated exactly and doing so would be a waste of resources. Consequently, the so called 'all-electron' potentials are replaced by pseudopotentials, which do not correctly describe the core electrons (e.g. V_{pseudo} in Fig. 3.2), but result in wave functions that exhibit as few nodal points as possible (Ψ_{pseudo}).

In the design of pseudopotentials it is crucial to set a meaningful minimal radius, r_c. Outside this radius the pseudoelectron and the all-electron potentials match (dashed vertical line in Fig. 3.2) and the potentials, and thus the wave functions, are indistinguishable.

Furthermore, the pseudopotentials are designed in a way, that yields meaningful scattering properties or phase shifts for the pseudo wavefunctions [86].

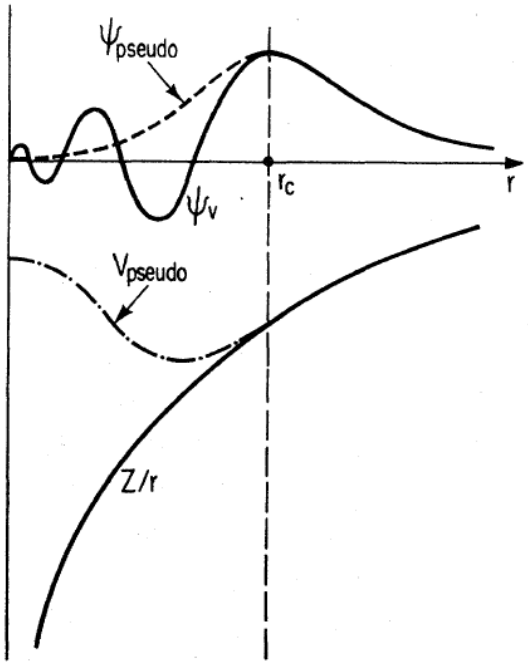

Figure 3.2.: Schematic illustration of the all-electron potential (bottom solid line) and the pseudopotential (dot-and-dashed line) as well as the respective wave functions for the electrons labeled Ψ_v and the pseudoelectrons Ψ_{pseudo}. The vertical line indicates the radius r_c at which the all-electron and the pseudoelectron approach match [86].

In the framework of this work, the so-called 'projector augmented wave' (PAW) pseudopotentials include the core electrons of the atomic potential. Hence, the core electrons, although present, are not part of the active electrons. This is a considerable improvement over the usual pseudopotential methods and was used as implemented in the VASP DFT code (see sec. 5.1) [106, 107].

3.8. Self-consistent Iteration Scheme

The Kohn-Sham equation (eq. (3.6)) is an implicit equation, because the density is its result but also an ingredient of the effective potential. A solution of the Kohn-Sham equation can be found in an iterative way as summarized in the flow chart Fig. 3.3.

As a starting point, an initial guess for the density is chosen; for instance a homogeneous

electron density. For this start-density the effective potential is calculated under the assumption that an appropriate XC-potential was chosen (sec. 3.5). The Kohn-Sham equation is solved with the resulting effective potential. The resulting density is calculated. The latter will differ from the initially guessed density. In other words, the result will not be self-consistent yet. We follow the arrow 'No' in Fig. 3.3.

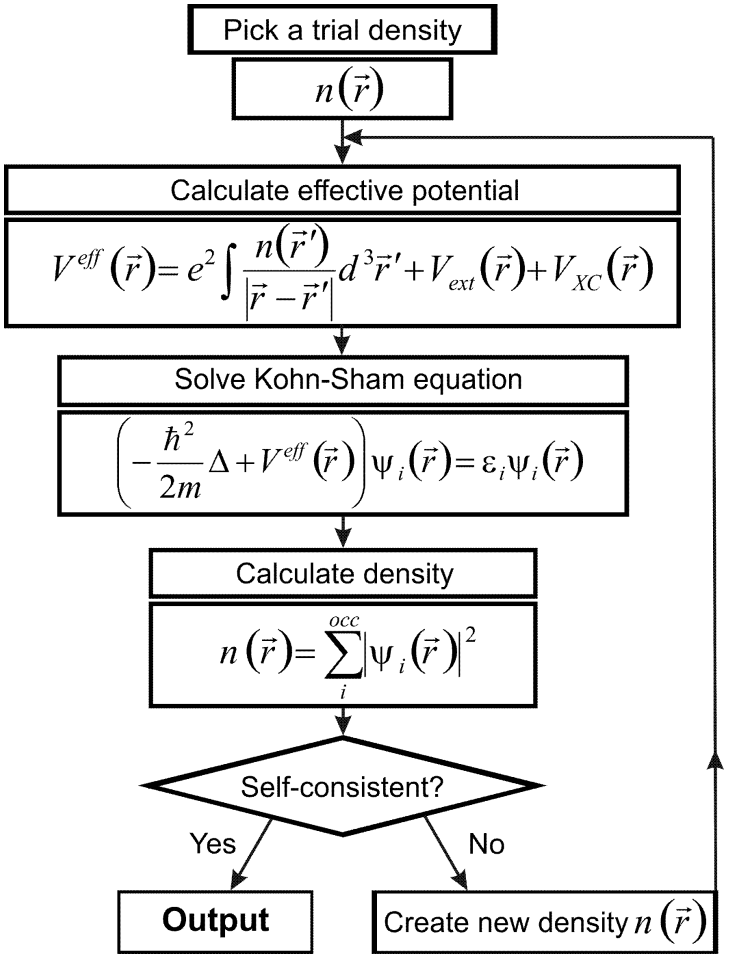

Figure 3.3.: Flow chart representation of the self-consistent iteration scheme for the numeric solution of Kohn-Sham equations. Based on [86].

The next step is to use a combination of the result density and the initial guess as the input for the next iteration loop. At this point the details of the so called density 'mixing' are crucial. For example, the use of the result density without mixing would completely change the effective potential of the next iteration, thus the electronic system would not

converge smoothly to a final density, instead suffering from dramatic changes and in many cases ending up in oscillations. On the other hand, a mixing that changes only very faintly the density will result in time-consuming calculations. Further reading, e.g. on the very effective Broyden mixing method: [108, 109, 110].

From iteration to iteration approximation of the electron density will become better and better until the difference between input density and output density vanishes (the resulting energy differences fall under a given threshold defining an accuracy limit). Once this situation occurs, the iterative loop is considered converged. In that case the output, e.g. the total energy, is created and the iteration stops.
As soon as the spin of the electrons is additionally considered, it is necessary to iterate two loops simultaneously. Each solution contains an effective potential for one spin direction which is again a functional of the total effective potential.

3.9. Ionic relaxation

In the previous sections, a strategy was introduced to solve the Schrödinger equation. However, as a prerequisite it was implicitly assumed, that the positions of the ions in space were given.

In the present study, an individual large organic molecule (57 atoms) is simulated on a Cu(111) surface. For this and similar systems the atomic coordinates are typically unknown. Therefore, many DFT studies start with an initial guess on the atomic configuration. For this specific guess, the iterative scheme summarized in the flow chart Fig. 3.3 is applied until convergence is achieved. The output total energy however, as well as all other data derived from the converged density will be far off reality. The reason is, that the geometric configuration of the system was kept fixed. Thus, molecule and surface, for example, were not allowed to relax reacting to the calculated electronic system.

As a consequence, a second iteration scheme is implemented to reach an energy-optimized atomic configuration, working as follows. On the basis of the output density of the above iteration scheme, the forces acting on each core are calculated. Then, the nuclei are allowed to slightly move their positions in the direction of the steepest descent. These updated coordinates are used as the input of a second run of the electronic convergence scheme. The electron system will adjust to the new potential given by the new core positions and after electronic convergence, the resulting forces will have changed. This change is not necessarily

an improvement. The nuclei might approach each other too close and experience a repulsion when evaluating the updated forces. Even dissociation of the model system may happen. Similar to the electronic iteration scheme and also in the case of the core coordinates, the atomic steps need to be small enough to prevent oscillating behavior whilst at the same time steps that are too small will waste computational resources. After several ionic relaxation steps, the core positions reach an energetic minimum and the forces fall below a set threshold. Then the geometry optimization iteration stops.
The force acting on the core (γ) with the coordinates $\vec{R}_\gamma$ can be written:

$$\vec{F}_\gamma = -\frac{\partial E}{\partial \vec{R}_\gamma} = -\frac{\partial}{\partial \vec{R}_\gamma} \langle\psi| \hat{H} |\psi\rangle \tag{3.15}$$

$$= -\langle\psi| \frac{\partial \hat{H}}{\partial \vec{R}_\gamma} |\psi\rangle . \tag{3.16}$$

The derivative with respect to the core coordinates can be written inside the expectation value, as guaranteed by the Hellmann-Feynman theorem (eq. (3.16)) [111]. The derivative of the hamiltonian (eq. (3.3) on page 27) equals the derivative of the external potential since only $V^{ext}_{\{\vec{R}_\alpha\}}(\vec{r})$ depends on the core coordinates (eq. (3.4)). Many possible expressions for the forces exist [85]. They have in common, that the forces can be calculated by integrating expressions including the density over space. The wave functions are not needed. It is noteworthy, that elaborate approaches implement the ionic relaxation by not only moving the nuclei but also some density within their proximity along with them (ref. [85] and appendix 'I' within).

3.10. Simulation of STM Images

Density functional theory simulations of surfaces yield information on the local density of states (LDOS). The LDOS, $\rho(\vec{r}, E)$ for a fixed energy E is accessed by evaluating and summing up the density of all Kohn-Sham orbitals at the energy E:

$$\rho(\vec{r}, E) = \sum_i |\psi_i(\vec{r})|^2 \, \delta(\epsilon_i - E). \tag{3.17}$$

The eigenvalue of the Kohn-Sham orbital ψ_i is ϵ_i.

As we know from chapter 2.2, the Tersoff-Hamann approach allows us to write the

tunneling current, I, as follows. Under the assumption of a constant tunneling probability it is proportional to the integral of the LDOS over energy, where the integration limits are the Fermi level and the Fermi level plus the electron charge times the applied sample voltage, V:

$$I\left(V\right) \propto \int_{0}^{eV} \rho_{\nu}\left(\vec{r}_{x,y}, E\right) T\left(E, eV\right) dE. \tag{3.18}$$

Inserting eq. (3.17) into eq. (3.18) we obtain an expression for the DFT tunneling current:

$$I_{sim}(V) \propto \sum_{\epsilon_i \in (E_F, E_f + eV)} \left|\psi_i(\vec{r})\right|^2. \tag{3.19}$$

The tunneling current $I_{sim}(V)$ is proportional to the sum of the electron densities of the occupied Kohn-Sham orbitals (absolute values of the ψ_i). The contributing occupied orbitals lie within the interval between Fermi level, E_F, and $E_F + eV$.

In order to create a simulated constant current STM images, it is necessary to choose a set electron density. For this value an electron density isosurface can be plotted from the DFT results.

It is important to stress that the Kohn-Sham orbitals are not physical orbitals and do not have informative value. Therefore, simulated STM data needs to be interpreted with caution.

Especially the influence of the tunneling tip is not part of this consideration (except for the Tersoff-Hamann approximation, which assumes a spherical tip).

In the book 'Computational Methods in Catalysis and Materials Science' the authors Bocquet, Lesnard, Monturet and Lorente introduce in detail the 'Theory of Elastic and Inelastic Electron Tunneling' including the derivation of the Bardeen approximation and the practical implementation on planewave codes (see ref. [112]).

3.11. Benefits and Limitations

A few points need to be made in order to briefly put in context the enormous benefits as well as the limitations of density functional theory.

Limitations

Firstly, it is important to remember that the Kohn-Sham equations do not describe the 'physical' electrons, but virtual particles. Strictly speaking, all statements derived from DFT results only apply for Kohn-Sham particles.

Kohn-Sham energies are in general incorrect to some extent. DFT needs to be benchmarked with the help of experimental data. In particular, bias dependencies extracted from DFT are typically off the experimental values. For example, STS and especially UPS[3] data are appropriate experiments that yield information on the energetic positions of (molecular) orbitals. Also bias dependent simulated STM images of organic molecules will tentatively show the expected orbitals with some energetic shift in comparison to STM data.

Kohn-Sham wave functions do not extend correctly into the vacuum. More explicitly, the wave functions do not decay exponentially. This is another problem for the simulation and the subsequent evaluation of STM images.

A priori, DFT is a ground state theory. In order to study excited states, the DFT results have to be interpreted with great care.

A general shortcoming of DFT is that it does not provide image potentials at surfaces. These phenomena and all physical consequences are thus not captured by the theory.

Van-der Waals (vdW) interaction is missing in standard DFT. This has a negative impact especially in surface science studies on adsorbates, as the binding distances will in general be underestimated. However, it was found, that for large organic molecules on metals, the LDA approximation with its intrinsic overbinding tendency produces decent results [97]. Furthermore, first vdW-corrected codes are available recently and the overcoming of this limitation is a current research goal. For example, within the latest version of the VASP-code a post-processing workaround can be implied to correct to some extent the results gathered within the GGA [104, 105].

Furthermore, band gaps computed from the Kohn-Sham levels are approximately 50%

[3] UPS = ultraviolet photoelectron spectroscopy

too small, and the band structure of semiconductors and Fermi surfaces can be evaluated only qualitatively.

Benefits

Geometries on the atomic scale are represented with excellent precision for solids (lattice constants) and molecules (bond length), with forces also being calculated. Also the vibronic frequencies within molecules can also be calculated with great precision.

DFT is capable of treating comparably huge systems. Several hundred atoms may be used to model a physical system. This is a prerequisite to study large organic molecules on metals within a periodic supercell.

The shape of orbitals resulting from DFT calculations is qualitatively correct.

DFT is a comparably cheap theory compared to Hartree-Fock methods. It depends on the three coordinates of each electron and therefore scales with N^3, where N is the number of basis functions. Ab initio methods like Hartree-Fock scale with N^4 thus being more expensive.

For many specialized purposes, the choice of appropriate functionals and the comparison to experiments helps to capture the physical properties of the studied system. In addition, many developments of DFT are very promising. For example, TD-DFT (time dependent DFT) allows to study atoms or molecules under the influence of time-dependent potentials such as magnetic or electric fields.

4. Experimental Setup and Studied System

In this chapter, the experimental setup shall be described. Section 4.1 treats the ultra-high vacuum system, followed by the cooling system needed for the low-temperature experiment. It is based on a commercial liquid helium flow cryostat, as in ref. [113]. In the framework of this thesis a low-temperature scanning tunneling microscope (LT-STM) was assembled. Details are given in section 4.3. A similar microscope was set up by Manfred Lange[1] with the additional capability to perform low-temperature atomic force microscopy experiments (LT-AFM). In principle, both models can be converted from LT-STM into LT-AFM and vice versa by transferring an exchange probe (tunneling tip (STM) or tuning-fork sensor (AFM)) into the microscope. The compact design by the Möller group was published by N. Wintjes, M. Lange, D. van Vörden, H. Karacuban and R. Möller in the *Journal of Vacuum Science and Technology B* [114]. The special electronics, designed for the analysis of noise in the tunneling current (sec. 4.4) as well as preparation techniques and the adsorption characteristics of CuPc molecules complete the experimental background section.

4.1. Ultrahigh Vacuum System

In surface science, reproducible experiments on well-defined samples require vacuum conditions. At ambient pressure, a freshly prepared clean surface, e.g. a metal sample would be covered by one monolayer of adsorbates within microseconds. At 1×10^{-6}mbar vacuum conditions this so called monolayer time is in the regime of one second. In contrast, clean surfaces that are prepared within the clean conditions of ultra-high vacuum (UHV, below 1×10^{-9}mbar) systems can be conserved for hours or days. Already in a worst-case scenario with a sticking coefficient of 1 (all impinging molecules stick to the surface), the

[1] University of Duisburg-Essen, Faculty of Physics, group of Prof. Dr. Möller, Lotharstr. 1, 47048 Duisburg, Germany

monolayer time exceeds 1 day for a pressure 1×10^{-10}mbar at room temperature. For further reading, ref. [115] is recommended.

If samples are cooled for low-temperature experiments, they act as cooling traps and attract adsorbates from the residual gas. Therefore, a good base pressure becomes even more essential.

The UHV system used here consists of four chambers, each of which is equipped with a set of vacuum pumps and valves allowing to operate the chambers individually (Fig. 4.2). When the respective valves are opened, neighboring chambers are interconnected and sample transfer between them becomes possible. The sample holders (*Omicron* design) are used to not only transfer samples, but can also be modified to carry tunneling tips and transferable molecular ovens. The handling of the sample holders between the manipulators, parking positions and the STM is done with wobble sticks (as an example, see item (3) in Fig. 4.1).

One analysis chamber of the UHV-system houses the LT-STM described in paragraph 4.3. The STM chamber is decoupled from the floor by pneumatic vibration isolation mounts (*Newport*). The neighboring parts of the UHV system are connected via flexible V-profile bellows for vibrational decoupling. The LT-STM chamber offers storage capacities for ten *Omicron*-type sample holders (see item (2) in Fig. 4.1).

For chemical surface analysis, ultraviolet and x-ray photoelectron spectroscopy (UPS and XPS) are available in a second analysis chamber. In addition, sample surfaces can be characterized by low energy electron diffraction (LEED). These methods provide complementary information to STM experiments and they can be used to control the different steps of sample preparation.

Sample preparation is done in the preparation chamber (Fig. 4.2). It is equipped with an ion gun for the sputter-cleaning of samples with Ar^+-ions. The manipulator exhibits a resistive heating filament allowing to anneal samples up to 1000K. In addition, semi-conducting samples can be annealed by direct current heating up to 1500K. A broad choice of seven Knudsen cells for the deposition of organic molecules and two metal evaporators are available.

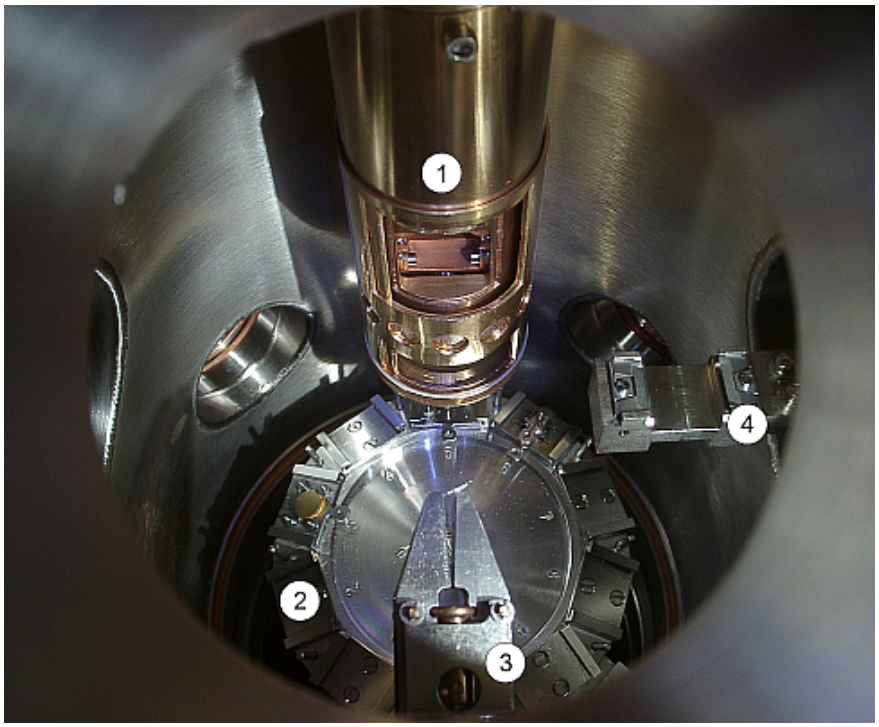

Figure 4.1.: Photograph of the LT-STM chamber as seen through a window flange. (1) The LT-STM; (2) rotatable sample storage capacities for up to ten samples or tip holders; (3) the pincer tool of the LT-STM chamber wobble stick; (4) the head of the magnetic driven transfer unit that connects the analysis chamber with the load-lock chamber and the preparation chamber [116].

A load-lock chamber allows for quick transfer of tunneling tips and samples from air into UHV and vice versa. Within a pumping time of one hour (reaching about 1×10^{-7}mbar), the objects can be transferred into the LT-STM chamber. Several (up to four) *Omicron* sample holders can be stored in the load-lock. One parking position offers a direct-current heating setup for the tunneling tips.

In order to achieve UHV pressure, bake-out procedures are mandatory after venting the chambers for maintenance or modifications. The chambers are kept at 100°C to 150°C for several days to remove water from the various surfaces. The initial vacuum is generated by turbomolecular pumps. After bake-out the ion getter pumps are used to reach the final pressure of about 1×10^{-10}mbar. The turbomolecular pumps are switched off, as they cause vibrations prohibiting STM operation.

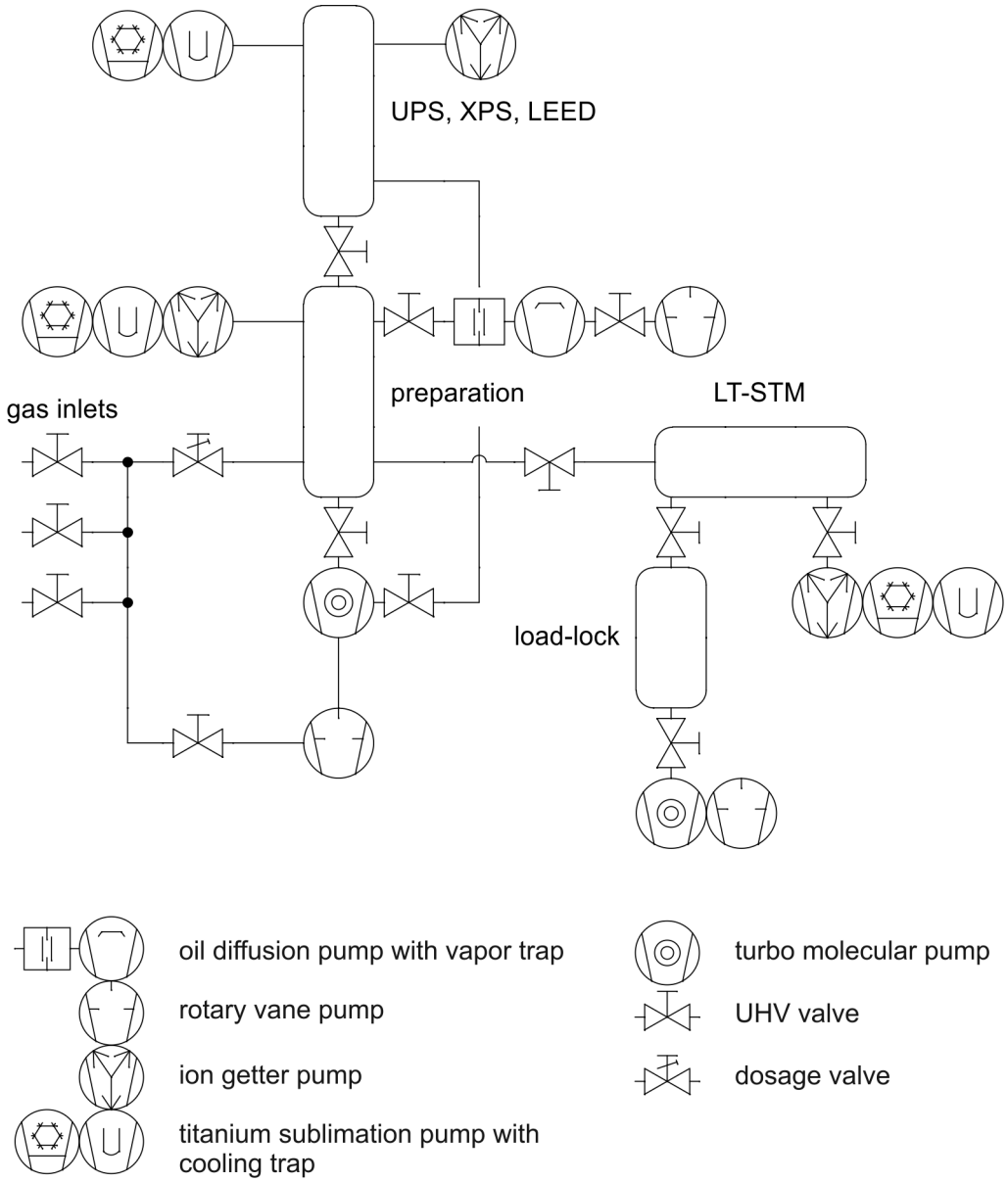

Figure 4.2.: Schematic view of the UHV system consisting of the LT-STM chamber, the preparation chamber, the photoelectron spectroscopy (UPS and XPS) and low electron energy diffraction (LEED) chamber and a load-lock. On the basis of [23]

4.2. Cooling System

Cooling of the LT-STM is achieved by using a cryostat (*LT3B-110* by *Advanced Research Systems*). It is operated with continuous flow of the coolant. The coolant (liquid helium (He-4) or liquid nitrogen (LN_2)) is permanently fed to the cryostat through a transfer line. In the cryostat, the coolant evaporates and the gas needs to be exhausted. A crucial point for the use of a flow cryostat in scanning probe applications is the mechanical noise caused by the flow of both, the liquid and the gas. Turbulences can lead to vibrations that interfere with the sensitive tunneling microscope. Valves for the coolant input as well as the gas output allow for precise regulation during STM operation. In Fig. 4.3 the cooling apparatus is schematically displayed. A pressure is applied to the dewar containing the liquid coolant reservoir (e.g. 0.2bar) to establish a constant coolant flow through the transfer line (blue and red arrows). The red arrows indicate gas phase helium used for the cooling of the transfer capillary containing the liquid coolant (blue). After the absorption of heat by the phase transition from the liquid (blue) to the gas phase (green), the gas is directed to the exhaust.

A major advantage of the flow cryostat as compared to bath-cryostats are the short cool-down and warm-up times for compact microscopes with a small thermal mass. From the start of the cool-down process only two hours are necessary until stable tunneling conditions are reached. A built-in heater may be used additionally, facilitating variable-temperature operation by a temperature controller (*Lakeshore*).

Once stable conditions are reached, the temperatures at the central parts of the STM (close to the sample) do not vary by more than $1/100K$ for several hours and up to a few days. The final temperature at the sample is about $6.5K...7.2K$. The maximum operation time at low temperature is limited by the capacity of the liquid helium dewar. A maximum of 4 days was reached with a consumption of 80 liters of liquid helium (consumption: $\approx 0.8l/h$). When cooling with liquid nitrogen ($78K$), the coolant can be refilled interrupting the experiments for approximately one hour.

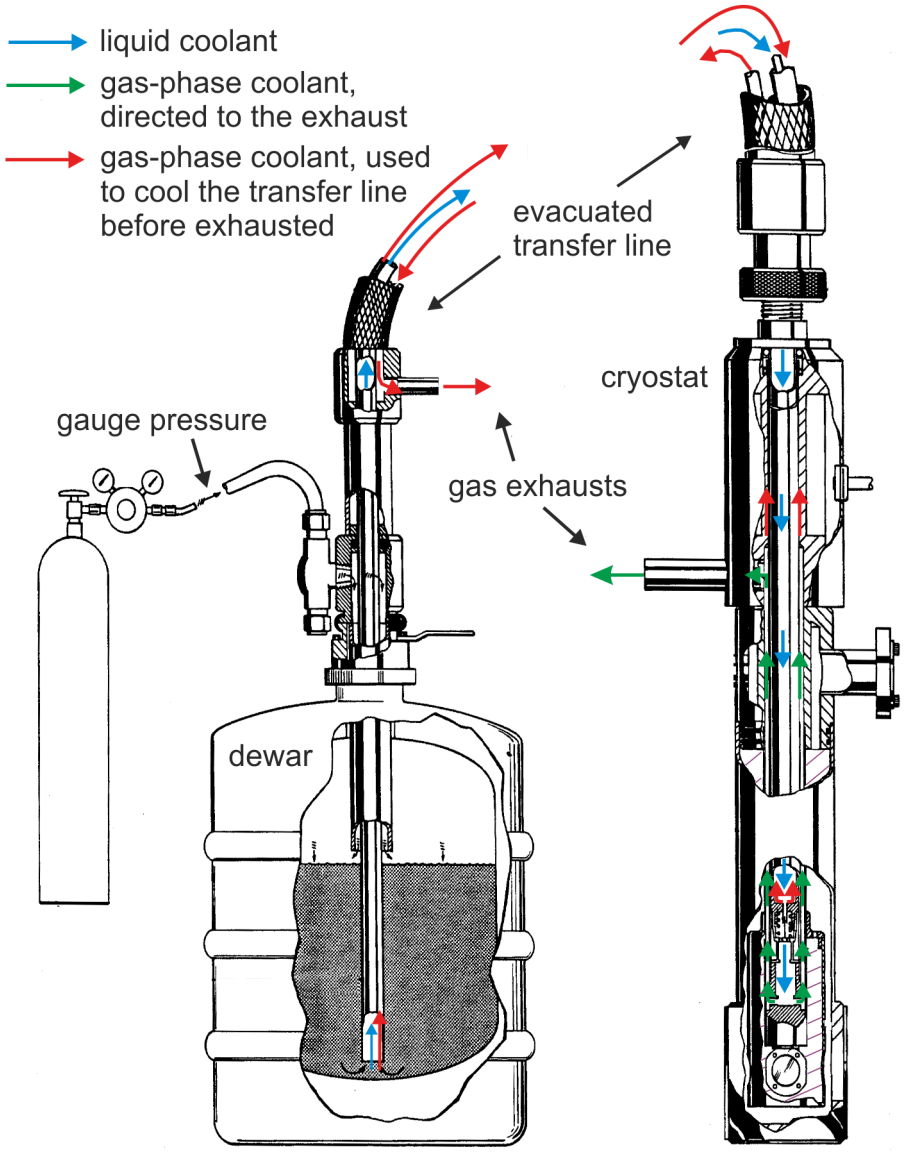

Figure 4.3.: The LT-STM cooling apparatus. An evacuated liquid helium or liquid nitrogen transfer line connects the dewar with the cryostat (*LT3B-110*, *Advanced Research Systems*). The coolant flow is depicted by arrows indicating the liquid phase with blue color. The gas phase coolant is marked green for the gas flow to the exhaust and colored red for the gas flow used for cooling of the transfer line. Based on [117, 118]

4.3. The Möller Design LT-STM

The invention of the STM revolutionized surfaces science by imaging the atomic structure of surfaces in real space. However, the stability of the measurements remained a limitation to this powerful technique. With the development of the low-temperature STM (LT-STM) many shortcomings of the room temperature microscopes could be overcome [119, 120, 121, 122, 123, 113]. The thermal drift of the piezo crystals can be substantially reduced and the thermal noise is reduced such that the signal-to-noise ratio (s/n) is enhanced (s/n $\propto \sqrt{T}$).
The stability of the microscopes depends on temperature. The temperature stability of a LT-STM can be in the regime of 0.01K during 1 day [113], thus the drift in the distance between tip and sample can be as low as 0.02nm/hour [123] and even 0.006nm/hour [113]. This allows to operate spectroscopic measurements with fixed tunneling tip and disabled feedback loop for several minutes. Furthermore, specific positions on a surface, for example single molecules, can be investigated for several days in contrast to typical room-temperature microscopes.

Also the stabilities of the tunneling tip and the sample surface including adsorbates profit from low temperatures. Thermal activated diffusion processes of atoms and molecules are frozen out. This allows to study adsorbates (e.g. CuPc molecules) that are highly diffusive and cannot be imaged at room temperature. Furthermore, low-temperature phenomena such as structural phase changes, superconductivity and Kondo physics may be studied.

In order to maintain stable LT-STM conditions and to prevent heat input by radiation or heat conductance, special care has to been taken at various details of the setup:

The Möller design LT-STM is housed within a thermal shielding system (see Fig. 4.4) screwed to the cryostat. An inner shield reaches the same minimal temperature as the STM (6.5K...7.2K) and blocks thermal radiation. In addition, it serves as a cryogenic pump reducing the adsorption of residual gas on the sample surface. It interacts with the outer shield via heat radiation, which is cooled by the reflux helium or nitrogen gas.

The central part of the STM including the piezo scanning unit, sample and tip (Fig. 4.4) is suspended from the cryostat by four springs. The combination of the springs and the mass of the STM results in a very low resonance frequency (≈3Hz) in order to decouple as effectively as possible from the vibrations of the building (typical frequency ≈20Hz).

Integrated magnets damp the oscillations of the suspended microscope with respect to its housing via eddy current damping. For the initial cool-down, a locking screw (Fig. 4.4) deactivates the spring suspension and thermally couples the STM to the inner housing. This helps to cool down the STM quickly. The screw is operated with a wobble stick.

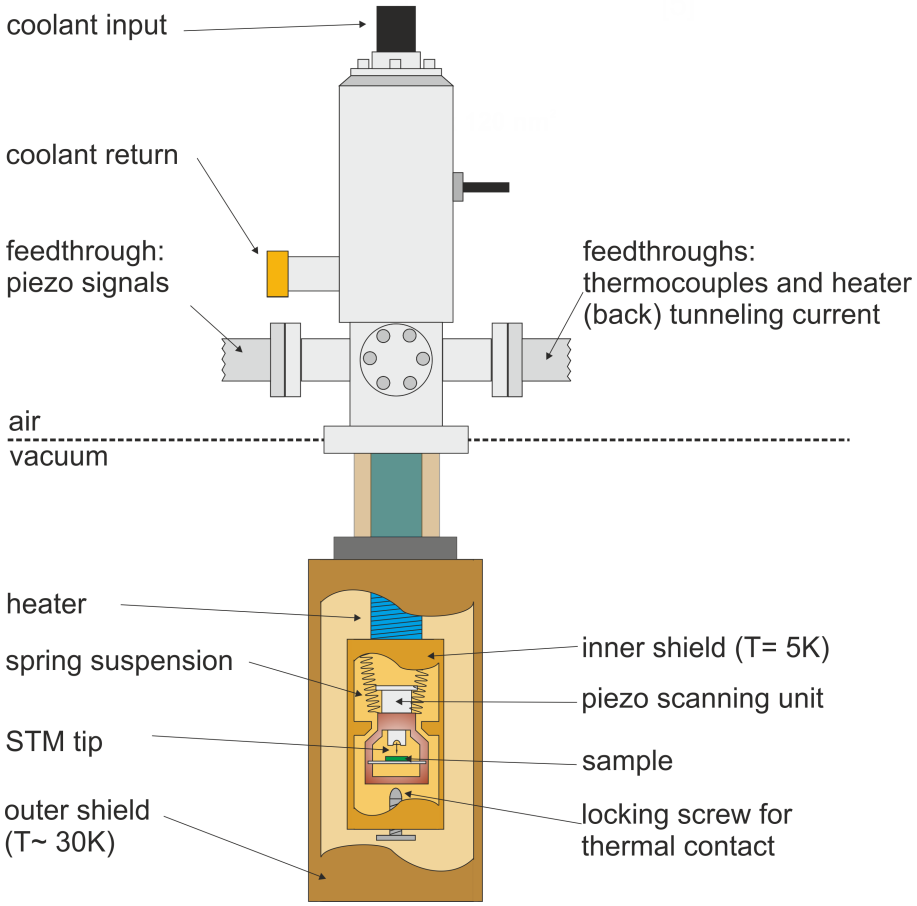

Figure 4.4.: Schematic representation of the cryostat together with the Möller design LT-STM. Figure based on [118, 114].

During measurements the springs are a thermal contact between the STM and the cryostat thus they are used for cooling. The necessary electronic wires are a constant thermal bridge, too, connecting the room temperature feedthroughs with the STM. To effectively diminish this inevitable addition of heat, the wires are cooled in several intervals in between the feedthroughs and the STM. Sapphire rings are used to thermally contact the STM housing with the wires and at the same time to electrically isolate one from the other.

Among the possible isolating materials for UHV application, Sapphire (Al_2O_3) has an excellent heat conductivity. For the wiring from the feedthroughs (room temperature) to the outer shield, and from the outer shield to the inner shield, the low-temperature wire *KAP-14* (Caburn) is used. It is made from stainless steel to reduce the heat conduction as compared to copper wires. From the inner shield to the piezo actuator inside the STM, more flexible copper wires are used. The wires are cooled by the sapphire contacts and can therefore be used to cool the STM during operation. This wiring strategy was applied to all ten contacts: the tunneling current, the bias voltage, a diode for temperature measurement at the central part of the STM, one ground-signal and all contacts of the piezo scanner.

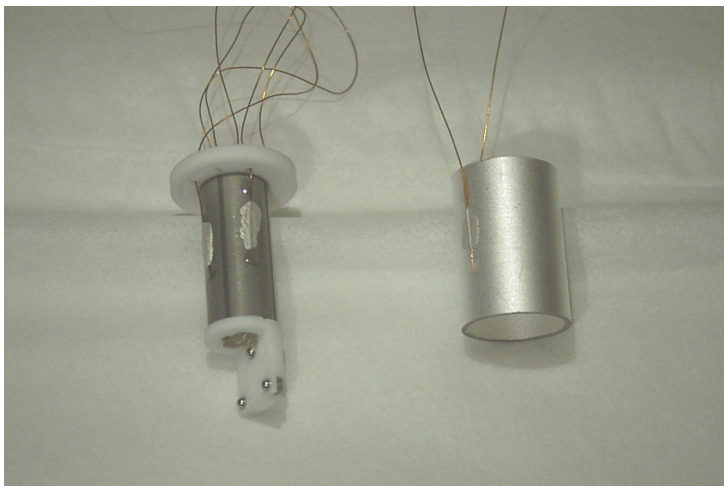

Figure 4.5.: The inner and outer piezo tubes before assembly; left hand side: the inner piezo with its segmentations; the triangular set of spheres with magnets behind them is glued to *Macor* parts; right hand side: the un-segmented outer piezo. Contacting pads made from conductive silver.

The piezo scanner unit consists of an outer and an inner piezo tube (Fig. 4.5). The outer piezo is used to perform vertical (z) movements only while one face of the inner piezo is segmented and can be contacted with four outer and one inner contacts to realize horizontal ($\pm$x and $\pm$y) and vertical ($\pm$z) motion of the tunneling tip. The two z piezos additionally provide the possibility to split fast z signals and slow signals. The outer piezo may be used to perform slow z ramps for the compensation of slopes between tip and sample while the inner piezo uses the fast signals from the feedback loop that react on topographic details, like atomic steps.

The piezo tubes are glued to a contact area made from *Macor*, with an triangular

arrangement of three small spheres made from steel that have magnets behind them (Fig. 4.5). The triangular arrangement of magnets holds the tunneling tip carriers, which can be transferred into the STM and can be exchanged by manually attaching and de-attaching the tip carriers to or from the magnetized spheres. The spheres are additionally used for contacting the tip carrier, i.e. to measure the tunneling current. The tunneling tips are spot-welded to the tip carriers (Fig. 4.6). A stick-slip motion of the tip carrier relative to the piezo actuator takes place in between hardened steel contact areas and their counterparts, the magnetized spheres. A cycloid signal applied to the piezos actuates this stick-slip motion. It is noteworthy, that the triangular assembly of the magnetic tip positioning allows not only to move the the tip in vertical direction, but also a tilt motion in e.g. x direction parallel to the surface is possible by applying the cycloid signal to the respective segments of the piezo tube. The tip exchange, coarse approach and tilt motion are monitored by a camera.

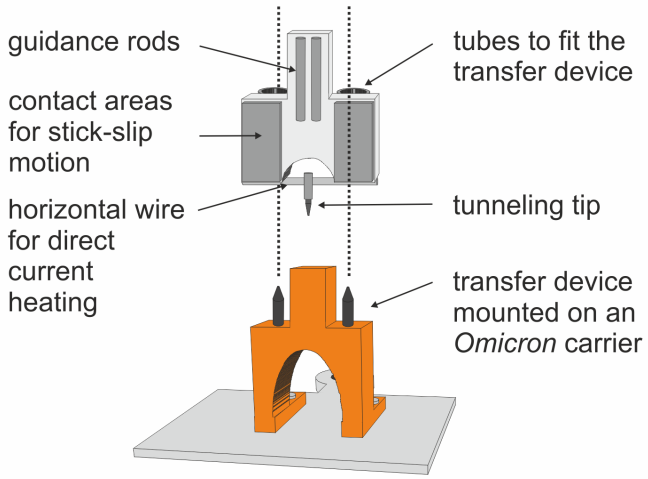

Figure 4.6.: Schematic representation of the tunneling tip carrier which can be inserted to the STM or re-positioned on the transfer device with the piezo actuator.

The tip can be exchanged *in-situ* at every temperature of the microscope. The transport unit designed for an *Omicron* carrier is shown in Fig. 4.6. The piezo motor can move the tip carrier onto the transport unit. For this purpose, it exhibits two metallic rods which fit into two tubes on the backside of the tip carrier. In Fig. 4.6 this is indicated by the dotted lines.

Approaching tip and sample

After the tip is transferred into the STM and the tip carrier is removed using a wobble stick, the sample can be inserted into the STM. A webcam is used to monitor the coarse approach from a tip-sample distance of several mm to a distance in the 1/10mm regime (as described above). The mirror image of the tip reflecting in the surface helps to visually control the coarse approach. Afterwards the locking screw is loosened and the radiation shields are closed.

For the further approach into the tunneling regime the following automated procedure is repeated sequentially. Starting from its fully retracted state, the z piezo is slowly expanded while the feedback loop waits for the onset of the tunneling current. Once the full z range of $\approx 5\mu$m is expanded without reaching a tunneling current, the z piezo is retracted again and the piezo drive performs a step forward. It is crucial here, that the step size needs to be smaller than the maximum range of the z piezo ($<5\mu$m) to prevent accidental tip-surface contacts.

At the new position of the tunneling tip relative to the surface, the procedure is repeated and the sequence stops as soon as tunneling conditions are found.

4.4. Automated Real-Time Noise Analysis

This section explains details on the technical realization of a new signal analysis procedure, which is also described in a publication in the article *Scanning Noise Microscopy* in *Review of Scientific Instruments* [124] [2].

The major goal of this work is to analyze dynamic processes under the tip of an STM. This means to accomplish a task, that the STM is not capable of at normal operation, as it is an intrinsically slow technique. This problem could be solved by designing an electronic setup dedicated to the analysis of random telegraphic noise (RTN) [see section 2.5] observed in tunneling current signals. The new setup can be used simultaneously to standard STM operation.

The method presented here will be called *scanning noise microscopy (SNM)* in the following. It provides the amplitude, the rate and the duty cycle of telegraphic noise in the tunneling current in real-time. These three new channels can be measured during the topographic STM imaging of a surface. Thus, amplitude maps, rate maps and duty cycle maps become available, which may carry valuable information about dynamic processes, e.g. switching processes on the nanoscale, with unprecedented spatial resolution.

The new method is also applicable to point probe experiments (*scanning noise spectroscopy, SNS)*. Here, the quantities described above can be evaluated as a function of electron energy or as a function of the tip-sample distance.

4.4.1. The design of the electronics

The analogue electronics presented here extracts a full characterization of current switching processes from current traces as given in Fig. 4.8a. The exemplary trace exhibits two distinct levels and switches randomly between them with constant probabilities for

[2] The term *scanning noise microscopy* was first used by Möller *et al.* in 1990 (see refs. [125] and [126] in the context of a scanning probe technique that is capable of adjusting the tip-sample distance in the absence of a tunneling voltage by measuring thermal current noise.

The technique presented here focuses on the characterization of telegraph noise, nevertheless, the general term *scanning noise microscopy* is preserved.

Independently, Sung *et al.* use the same terminology to refer to a conceptually different technique based on an atomic force microscope with a tip in contact to a sample. It is used to analyze the power spectral density of a current flow through micrometer-sized circuit paths on a substrate [127].

switching events, thus fulfilling the definition of random telegraph noise (RTN). In the following, the highly conductive level will be referred to as the on-state, and the less conductive level will be referred to as the off-state. The respective average life-times of the on- and the off-state will be called τ_{on} and τ_{off}.

Random telegraph noise can be fully described by the three quantities:

$$\text{switching rate} \qquad r = \frac{1}{\tau_{on} + \tau_{off}},$$

$$\text{duty cycle} \qquad d = \frac{\tau_{on}}{\tau_{on} + \tau_{off}},$$

$$\text{amplitude} \qquad A.$$

The duty cycle always refers to the probability for the system to be found in the on-state.

The SNM electronics' signal processing is given schematically in the block diagram Fig. 4.7.

For clarity, several steps of the signal processing are displayed for an exemplary measurement in Fig. 4.8.

The logarithm of the tunneling current $log(I)$ is used as the input signal (Fig. 4.8a). Assuming that the amplitude is a linear function of the average current $A/I_{average} = const$, this ensures equal amplitudes of the jumps independent from the particular set current. After passing the differential input amplifier, the $log(I)$ is differentiated with respect to time resulting in a signal exhibiting a peak at the position of every switching event (Fig. 4.8b). For further processing, the signal is split.

The signal path in the upper part of the block diagram shows the measurement of the amplitude. The peaks of the derivative signal is rectified and averaged over time by low-pass filtering. Since the output amplitude $\tilde{A}$ depends linearly on the rate of events r, it should be normalized by the rate: $A = \tilde{A}/r$.

For the measurement of the rate and the duty cycle, the differentiated signal is evaluated with respect to its sign. For each polarity of the peaks, adjustable thresholds can be set. As an example, Fig. 4.8b showcases the detection thresholds indicated by dotted black

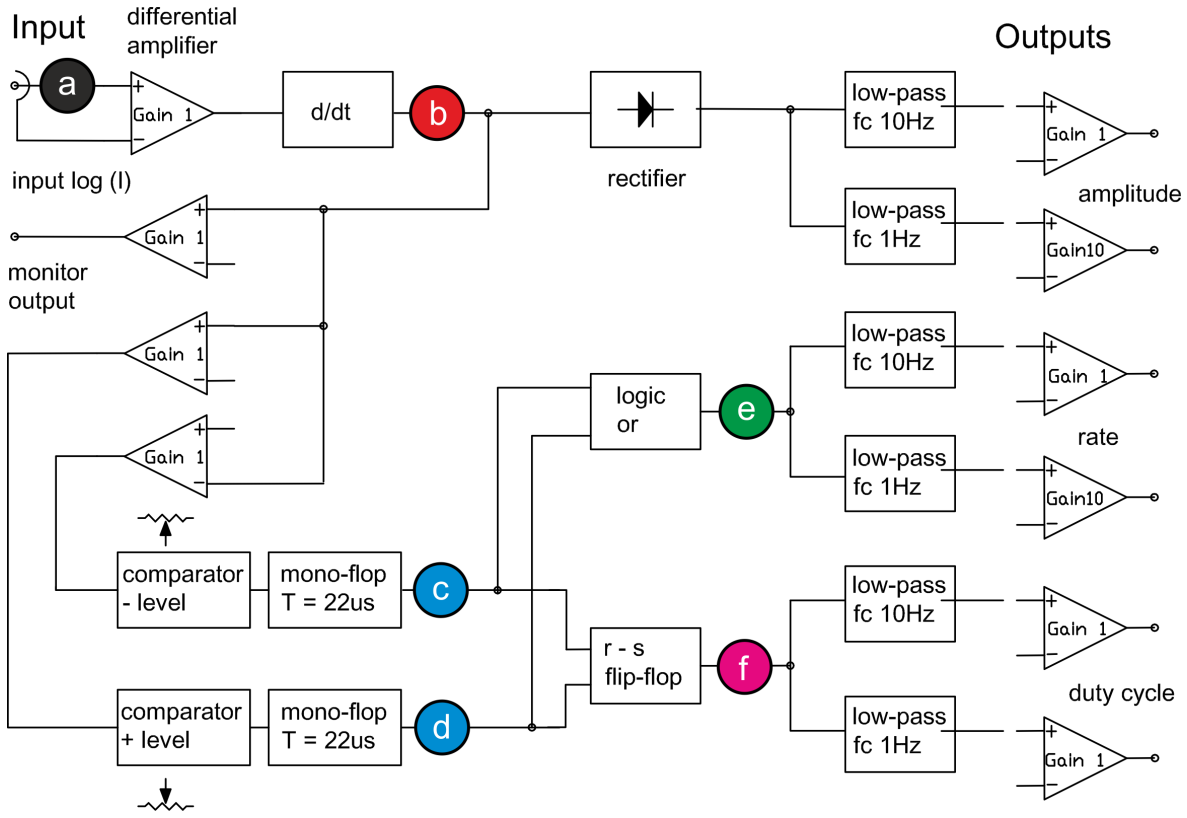

Figure 4.7.: Block diagram of the scanning noise microscopy electronics. The letters (a) to (f) mark different steps of the RTN signal processing. They can be linked to the signals plotted in Fig. 4.8. fc = cutoff frequency, T = time constant.

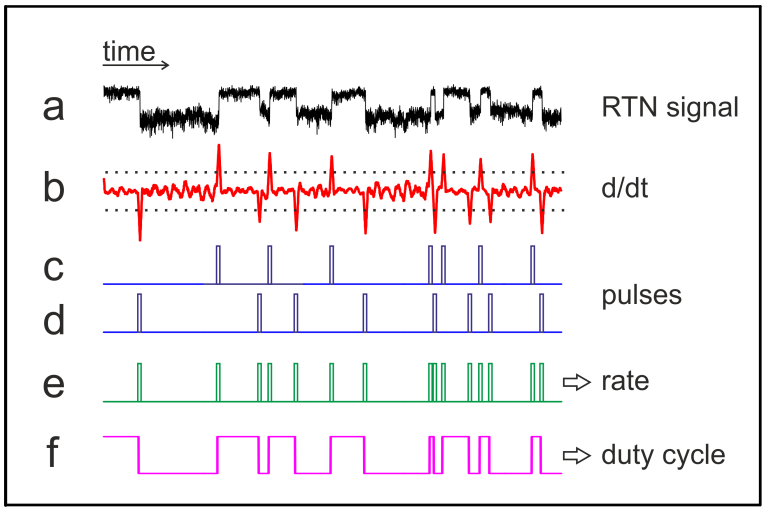

Figure 4.8.: Stepwise scheme of the RTN signal processing in Scanning Noise Microscopy (SNM).

lines. If these thresholds are exceeded, a switching event is detected. The thresholds ensure that noise in the tunneling current, which is not related to the conductance switching is neglected. At the begin of a measurement, these thresholds are set manually. By means of a function generator a reference input signal simulating a well defined switch may be generated. An oscilloscope is used for monitoring. With this procedure the sensitivity of the noise detection can be calibrated accounting for the tunneling conditions during the particular experiment.

For every detected event mono-flops generate a pulse with a defined width (here 22μs). The signals can be seen in Fig. 4.8c+d. Subsequently, the rate is determined by a logical *or* taking into account both, *on* and *off* events (Fig. 4.8e). A low-pass filter integrates the signal over time resulting in an output voltage. The output voltage scales linearly with the rate. For the outputs a choice of two low-pass filters with different time constants (0.1s and 1.0s) was implemented followed by output amplifiers. This allows to adjust the detection range of the SNM-electronics coarsely to the observed rates.

To obtain the duty cycle the pulses for the *on* and *off* events are used to trigger an RS flip-flop. By this, the original tunneling current signal is reproduced in a binarized manner. In Fig. 4.8f this can be seen by a comparison with the input signal (a). Integrating the duty cycle over time finally results in the duty cycle output which represents the average

occupation of the on-state. A value of e.g. 0.3 means, that there is a chance of 30% to observe the on-state during the observation time.

The presented setup works reliably within the range of 1Hz to several kHz. The circuit can easily be adapted to higher or lower switching frequencies.

4.4.2. Limitations of the SNM Technique

Low Current Limit

The signal-to-noise ratio is a limiting factor in the analysis of switching processes within the tunneling current. If the observed states of conductance can be distinguished well from the background noise, our SNM electronics can be operated reliably. For example, the choice of very low average currents e.g. 1pA or below, will typically lead to a poor signal-to-noise ratio. Applying higher tunneling currents, e.g. 10...100pA, may help to improve the signal-to-noise ratio such that the above described detection thresholds can clearly be set between on-state and off-state.

High Frequency Limit

As soon as two consecutive events occur within the duration of one pulse, the detection will fail and the measured rate will show a saturation for high frequencies. In case of applications in the regime of more than 1 kHz, the generation of pulses with shorter time constants (e.g. 1μs) can be realized. However, the extension of the frequency range of the setup to higher frequencies will at some point require a current-to-voltage converter (IVC) with sufficient bandwidth.

The IVC used for the experiments presented here is self-built and offers a bandwidth of 5kHz at an amplification of 10^9V/A.

Stability Limit

The choice of the scanning parameters crucially influences the quality of the statistics describing the rate. The scan speed and number of pixels determine the time per pixel used for averaging. Therefore, equivalent to standard STS, slow measurements will yield more significant data at a given excitation probability and at a given stability of the STM.

Nevertheless, the statistical significance for the amplitude and the duty cycle images scales with the number of events measured at every pixel, not with averaging time. Therefore non-switching areas in the duty cycle maps will not exhibit defined data, as the duty cycle will stick to either 1 or 0, reflecting the absolute absence of detected events. In the duty cycle map this results in meaningless white (1) or black (0) lines, which may be discarded, e.g. by masking with a neutral color.

2-level Restriction

The measurement scheme given in Fig. 4.7 is designed to study two-level conductance switches. For organic molecular switches with three or more states of conductance, the setup must be extended in a more sophisticated manner. One simple way of proceeding with the given circuit is to use several SNM setups which accumulate several levels in the first place and to subsequently subtract the output signals to distinguish the different levels of molecular conductance.

4.5. Preparation of Tunneling Tips

For the experiments of this thesis, tunneling tips (see section 2.4.1) made from platinum iridium (PtIr) and tungsten (W) wire were prepared in the following procedures.

Ex-situ Preparation

PtIr is cut from a wire of $100\mu m$ diameter and spot-welded to the tip holders (see Fig. 4.6). In order to prepare a tunneling tip at the end of the wire, it is cut again before it is placed inside the vacuum chamber. The wire is cut diagonally and is at the same time tightened by pulling the wire cutter. The concept behind this procedure is to cut the major part of the diameter and to rupture the remaining micrometers. By this, a sharp tip shall be produced.

In order to etch the $100\mu m$ W wire (purity 99.95%), it is dipped into 3-molar sodium hydroxide (NaOH) solution. The wire acts as the cathode during etching. An anode formed from PtIr wire is also placed in the etching container. A DC voltage (2V...5V) is applied in between the electrodes. The W wire narrows down at the electrolyte surface during the etching process (see Fig. 4.9).

The resulting current is monitored by electronics. As soon, as the wire is divided in two parts, the current drops and the electronics instantly shuts down the voltage supply. This prevents the tunneling tip from being over-etched (loosing sharpness). Once the etching process has stopped, the upper part of the wire is cautiously removed from the etching setup and rinsed with de-ionized water. Subsequently the wire is spot-welded to a tip-carrier and shortened.

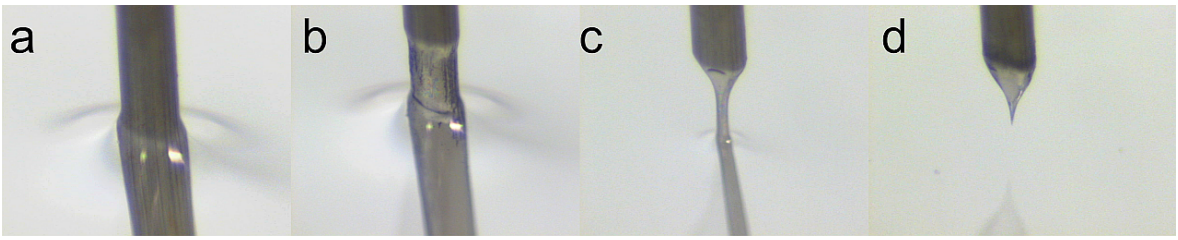

Figure 4.9.: A tunneling tip is etched from a tungsten wire in NaOH solution. During the process (several minutes pass during the sequence a - d), the diameter of the wire narrows down at the electrolyte surface until it is divided into two parts. Photographs from [128].

In-situ Preparation

In the load-lock chamber at a pressure of 1×10^{-5}mbar to 1×10^{-7}mbar, the tunneling tips are annealed to remove oxides and adsorbates and to enhance crystallinity. The tips are spot-welded to a PtIr wire, which can be heated by a current. The tips are heated until they reach orange glow for about one second. The glow is controlled visually. The cleaned tips are used for STM operation.

To improve the tunneling tips within the STM, techniques described in section 2.4.1 are used. Field emission at a tip-surface distance slightly above the tunneling regime is carried out with typical sample bias voltage of 300V and 5-30μA for half an hour.

4.6. The Cu(111) Surface

All experiments presented here were conducted on a single crystalline copper (111) sample. Copper (Cu) is a transition metal with a wide range of application in electronic devices due to its high electrical and thermal conductivity.

The electron configuration of copper is $[Ar]3d^{10}4s^{1}$. The band structure and density of states are shown in Fig. 4.10. The d-bands (formed by the superposition of d-orbitals) carry the major part of the density of states and are found between -2eV and -5eV below the Fermi level. Closer to the Fermi level the electronic structure of Cu is dominated by s-orbitals.

Copper crystals exhibit a face-centered cubic (fcc) structure (Fig. 4.11a) with a lattice constant of 0.361nm [130, 131]. Cutting the fcc lattice along the (111)-plane (blue) results in a hexagonal surface as can be seen in the top-view image shown in Fig. 4.11b. The next-neighbor distance equals 0.255nm. The Cu(111) atomic step height is 0.208nm. Based on atomically resolved STM images the piezo actuator can be calibrated.

The underlying 2nd and 3rd layer are indicated in dark gray and light gray, respectively. The layer stacking sequence is ABC. For later discussion the black arrows point to preferred adsorption sites on Cu(111). There are two hollow sites, where an adatom can sit centered in between three surface atoms. The hcp adsorption site coincides with the position of an atom from the 2nd layer (dark gray hollow sites). The fcc hollow site corresponds to

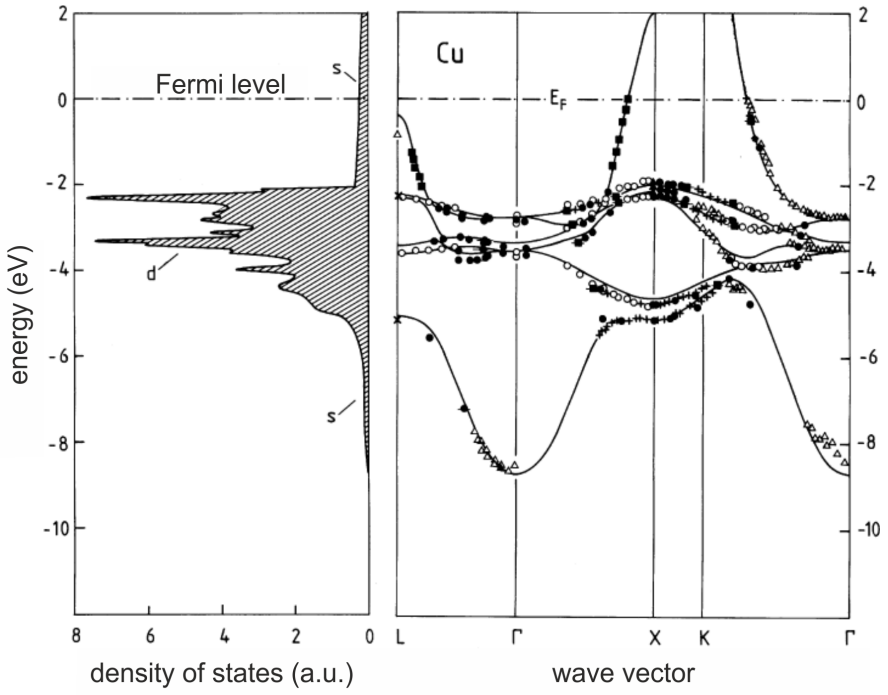

Figure 4.10.: The band structure (right) and the density of states (left) of copper [129].

the lateral position of an atom from the 3rd layer. Another typical adsorption site is a bridge position (in between two next-neighbor atoms). Finally, on-top adsorption sites are also possible. In the latter case, an adsorbate is observed centered above a surface atom.

4.6.1. electronic properties

The electronic structure of the Cu(111) surface is different from that of the bulk shown above. When projecting the Cu band structure to the Brillouin zone of the (111) surface, a band gap occurs at the Γ-point. In this gap a Shockley-type surface state evolves. The electrons in this surface state can be described within the model of a two-dimensional free electron gas (parabolic dispersion relation) localized in the surface and decaying exponentially into both, vacuum and bulk. The Shockley surface state electrons exhibit an effective mass of 0.412 electron masses [132]. The position of the band minimum of this state is 435meV below Fermi level [132]. In the density of states (e.g. scanning tunneling spectroscopy measurements) the onset of the surface state is observed as a step function.

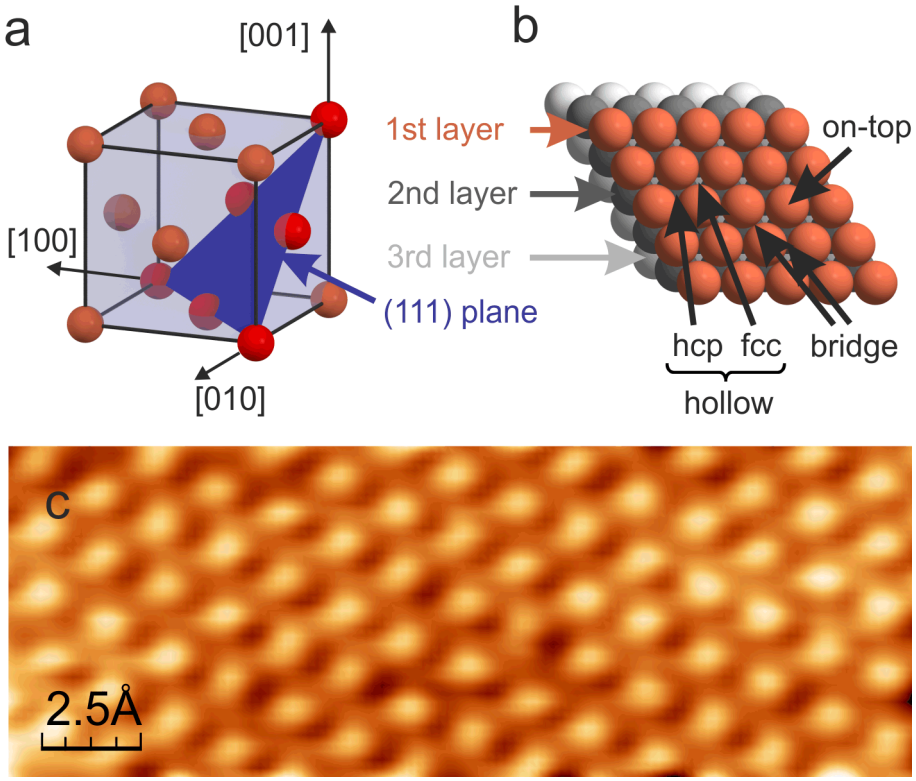

Figure 4.11.: a) The face centered cubic crystal structure of copper and the (111) plane marked blue. b) Top view of a (111) surface. The surface atoms are in hexagonal configuration. Arrows point to possible adsorption positions for adatoms or molecules. c) STM scan of the hexagonal Cu(111) surface ($U_{sample} = -1V, I = 40pA$).

In STM images the range of the absolute value of the k-vector is defined by the tunneling bias voltage. The surface state electrons are scattered at surface defects [133]. A modulation of the local density of states emerges from the interference of the electrons within the surface state. The interference patterns can be observed as standing wave images in STM [134, 135] for e.g. the (111) surfaces of gold, silver, or copper.

For the theoretical studies in this work it will be important to thoroughly model the copper surface so that the electronic structure of the substrate including the Shockley surface state is appropriately represented.

4.6.2. preparation

The copper (111) single crystal was cleaned by repeated cycles of argon ion bombardment (sputtering) and annealing steps.

For sample preparation the ion getter pump of the preparation chamber was shut down and vacuum was achieved by an oil diffusion pump with a liquid nitrogen cooled cryo trap. Via a dosing valve argon gas was let into the chamber. The ions created in the sputter gun were accelerated to an energy of 2.5kV towards the sample, which is mounted to a manipulator. An ion current of 10μA...30μA was maintained for approximately 30min per preparation cycle. The ion current depends on the applied voltage and on the partial pressure of argon in the preparation chamber which was held at 1×10^{-5}mbar.

To anneal the sample, it was radiatively heated by a filament until it reached deep red glow. The glow was controlled visually and maintained for 5min. Afterwards, the preparation was repeated a second time to thoroughly remove organic or carbon residues. The quality of the resulting surface was confirmed by STM. Following this preparation recipe, Cu(111) terrace widths of up to 500nm were observed.

4.7. The Organic Molecule Copper-Phthalocyanine (CuPc)

Phthalocyanine molecules are a very popular class of organic semiconductors with a wide spectrum of applications. Their popularity is based on the flexibility of the electronic properties.

Phthalocyanines are for example used for organic light emitting diodes (OLEDs) [136]. Furthermore, CuPc was mixed with C_{60} molecules to form graded donor-acceptor heterojunctions for an organic photovoltaic cell application (OPVC) [137, 138, 139] in which a power conversion efficiency of $\approx 2\%$ was realized [140]. In the field of organic field effect transistors (OFETs) [141] a promising heterojunction film consisting of CuPc on PTCDA was reported [142].

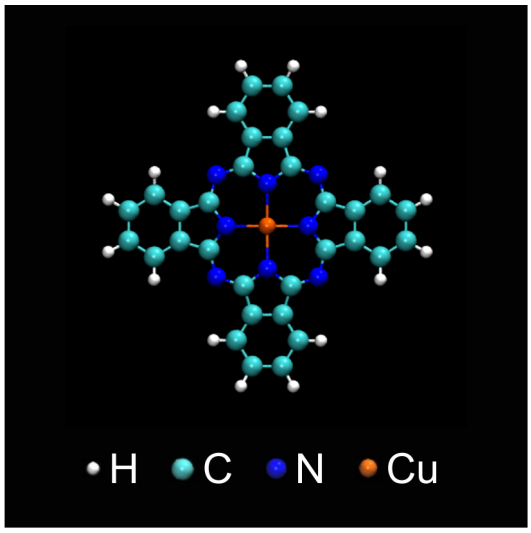

Figure 4.12.: Structural model of copper phthalocyanine (CuPc) [143]. The flat molecule consists of a copper core in its center, surrounded by nitrogen atoms, followed by carbon and hydrogen atoms.

The high thermal stability of phthalocyanines allows to prepare samples under UHV conditions by the thermal vacuum sublimation from crystalline powder without decomposition [144].

Phthalocyanine is a planar molecule with C_{4h} symmetry consisting of four pyrrole rings forming a tetrapyrrole macrocycle. Four outer benzene rings are bound by two C-C-bonds

each. The π-conjugated electron system is extended over the pyrrole and benzene macrocyclic structure resulting in a homogeneous charge distribution.

Free-base phthalocyanine (H_2Pc) has the molecular formula $C_{32}N_8H_{18}$. The specialty about phthalocyanine is, that it can carry a double ionized metal or transition metal atom in its center, substituting the two central hydrogen atoms. As a consequence, the different metal phthalocyanine molecules (MPcs) offer a rich variety of physical properties for scientific or industrial application.

This work focuses on copper phthalocyanine (CuPc). Its molecular formula reads $C_{32}N_8H_{16}Cu$. The mass of CuPc is 575 or 577 atomic mass units (amu), depending on the embedded copper isotope (^{63}Cu or ^{65}Cu). Due to its absorption maximum between 600nm and 800nm, it is used as a blue dye in industry.

4.7.1. electronic properties

The electronic structure of CuPc [145] around the Fermi level is determined by its bandgap. The optical bandgap (1.7eV for the molecular solid [146]) is displayed in Fig. 4.13 (third from right) in comparison to other organic molecules [147].

The molecular orbitals closest to the Fermi level are usually named HOMO for the 'highest occupied molecular orbital' and LUMO for the 'lowest unoccupied molecular orbital'.

It is noteworthy, that the transport bandgap, which is relevant to describe charge carrier transport processes, is a little larger than the optical bandgap ($\geq$2.1eV [148]).

In the gas phase, CuPc molecules possess two degenerate LUMO orbitals. Each of them is localized at one pair of opposing benzopyrrole rings and the phthalocyanine center. The two LUMO orbitals plotted in Fig. 4.14 are Kohn-Sham orbitals resulting from a gas phase DFT calculation and were found 3.87eV below the vacuum level. With the aim to correctly describe the magnetic properties as well, the energy optimization calculation was carried out within the local spin-density approximation (LSDA) and the positions of the atoms were relaxed until the maximum forces fell below 0.01eV/Å.

Despite the fact, that each LUMO is asymmetric with respect to a central axis connecting the benzopyrrole rings, the mirror symmetry of the full LUMO system is not broken. This

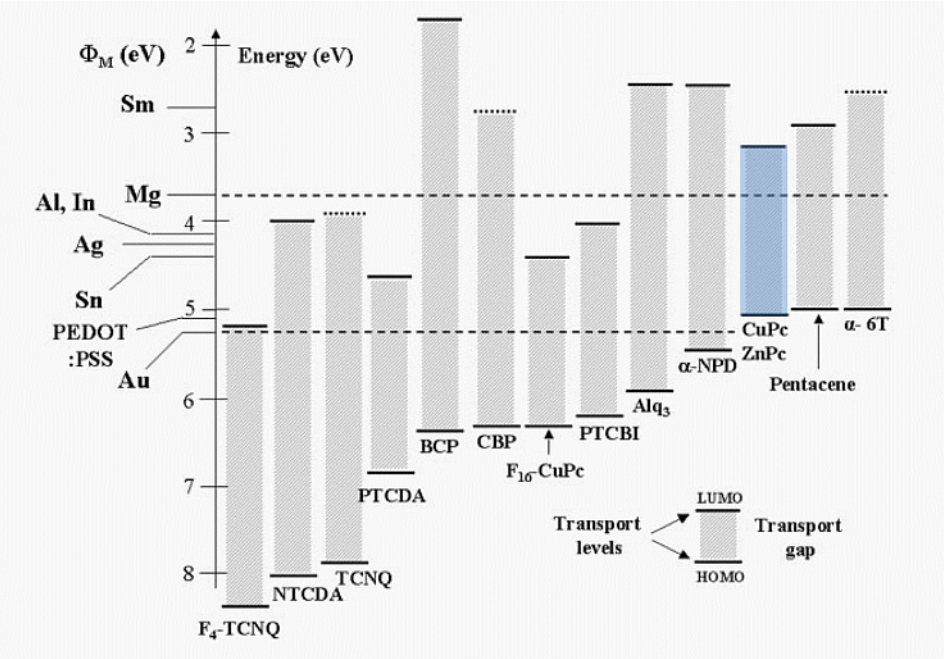

Figure 4.13.: Comparison between the energetic positions of the highest occupied molecular orbitals (HOMO) and the lowest unoccupied molecular orbitals (LUMO) defining the optical bandgap, as determined by ultra-violet and inverse photoelectron spectroscopy (UPS, IPES) for different organic molecules. The blue dye CuPc is marked in blue color; for a heterogeneous organic system consisting of CuPc and PTCDA (4th from left) see the appendix B. The energy scale in eV is fixed by the common vacuum level (zero). As a reference, several metal work functions are given [147].

can be understood by a close inspection of Fig. 4.15, where the LUMO and the LUMO* charge densities are summed up.

In addition, Fig. 4.15 shows the HOMO orbital, which was found at an energetic position of 5.32eV below the vacuum level and the SOMO (singly occupied molecular orbital). The SOMO is only half occupied because its energetic position differs for the two spin components (4.93eV and 4.15eV below the vacuum level [84]). The one electron in the SOMO determines the magnetic properties of CuPc. The magnetism of CuPc can be explained as follows. The Cu atom is positively charged since the electronegative N atoms accumulate approximately two electrons. The unfilled d-shell of the copper atom and with that, the whole molecule has spin $1/2$.

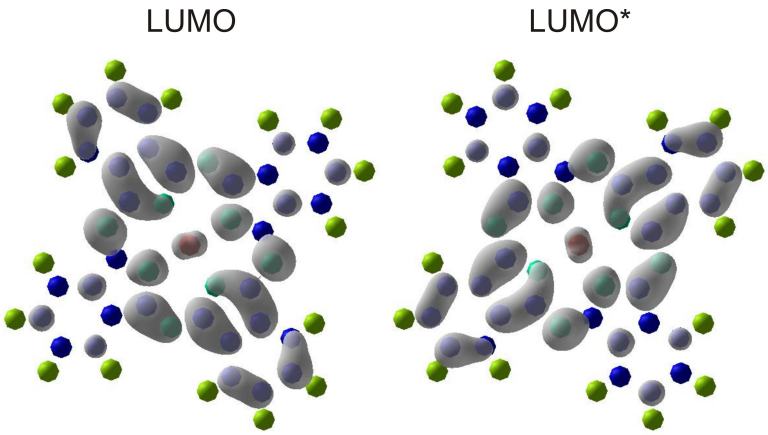

Figure 4.14.: Copper phthalocyanine possesses two degenerate lowest unoccupied molecular orbitals (LUMO) in its gas phase. The electron densities of the orbitals labeled LUMO and LUMO* are each localized over a pair of opposing benzopyrrole rings and the phthalocyanine center [84].

In surface science CuPc was investigated intensely on a broad choice of substrates: The monolayer and multilayer growth on Cu(111) and Cu(100) was studied by LEED [149] in 1977. The first STM images of CuPc were measured on polycrystalline silver surfaces in 1987 [36]. The internal structure, i.e. the fourfold symmetry of CuPc on Cu(100) was successfully resolved by STM [150]. Since then, the model molecule was studied on Au(111) [151, 152, 153], Ag(111) [154, 155, 156], Ag(110) [157, 158], and Ag(100) [97], Cu(100) [150, 159] and Cu(111) [24, 159], platinum modified Ge(100) [160], hydrogen passivated Si(100) [161] and Si(111) [162], TiO_2(011)-(2×1) [163], as well as thin films of Al_2O_3 grown on NiAl(110) [164] and Ni_3Al(111) [165].

CuPc has furthermore been combined with other organic molecules on surfaces, for example CuPc on C_{60} on a Au(111) film [166], CuPc on a precovered monolayer of PTCDA on HOPG [167], CuPc in a heterostructure with PTCDA on Cu(111) [168, 169], CuPc as a guest in a two-dimensional molecular host network on highly oriented pyrolytic graphite (HOPG) [170]. Very recently, Krull and coworkers reported on the controlled doping of CuPc with up to six Li atoms on Ag(100) [171] and a few weeks later, Uhlmann *et al.* charged CuPc on NaCl/Cu(100) with Ag and Au atoms [172].

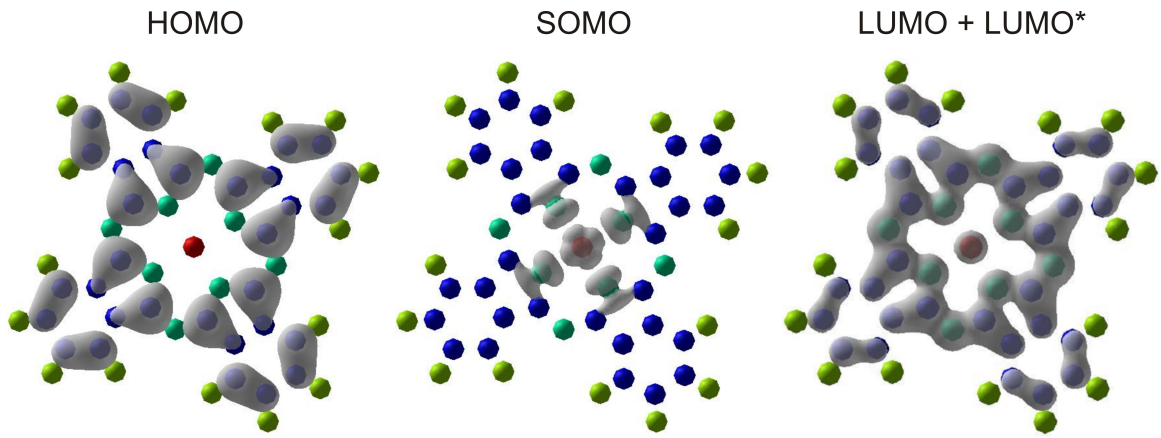

Figure 4.15.: The shapes (charge density isosurfaces) of the molecular orbitals HOMO, SOMO, and LUMO+LUMO* for CuPc in the gas phase as calculated by DFT [84].

4.7.2. preparation

For the deposition of CuPc on the samples, crystalline CuPc powder was filled into crucibles and brought into UHV conditions. The molecule oven underwent a bake-out procedure at 120°C. After bake-out the crucible was heated by a surrounding filament and the residual gas was monitored by a quadrupole mass spectrometer. CuPc was sublimated at 320°C. Before sample preparation, the crucible was kept slightly below that temperature in order to degas the molecular powder. During this procedure the partial pressures of fragments of CuPc decrease until a steady level is reached. After approximately one day, the remaining partial pressures of fragments are assigned to a cracking of the molecules due to the electron bombardment for ionization. STM was used to calibrate the deposition process for submonolayer coverages and confirmed, that only a negligible amount of decomposed molecules adsorbed on the surface. Sample preparation was carried out with the samples held at room temperature.

5. Implementation of DFT Calculations

5.1. The VASP code

The theoretical part of this thesis comprises extensive first-principles studies within the framework of density functional theory (DFT) as implemented by the Vienna ab initio simulation package (VASP) [173, 174, 107].

VASP is a software that is designed to fulfill a broad spectrum of tasks. Besides the electronic structure calculations, quantum mechanical molecular dynamics can also be addressed from first principles. It optionally allows one to solve the many-body Schrödinger equation via the Hartree-Fock approach or in terms of 'hybrid functionals' mixing Hartree-Fock and DFT [175].

In the plane-wave treatment of this work, pseudopotentials on the basis of the projector augmented-wave (PAW) were used [106, 107]. VASP also offers norm-conserving or ultrasoft pseudopotentials [175].

For the exchange-correlation functional, we choose the local density approximation (LDA) as soon as the adsorption of the large organic molecule CuPc on Cu(111) comes into play. Please find the discussion on this topic in chapter 8.2.

5.2. Optimizing a Model within the DFT Framework

In the following chapters, DFT results on CuPc/Cu(111) will be presented. Beyond that the results will be applied to an approach from the electron scattering point of view, simulating the excitation of a molecular motion by tunneling electrons. However, it goes without saying, that the starting point has to be the careful modeling of the studied system in order to develop the prerequisites for the more sophisticated studies.

The Copper Crystal

With the aim of creating a DFT compatible representation of the Cu(111) surface (see sec. 4.6), the DFT lattice constant of the bulk material - which may be a little different from the experimental value - needs to be determined first.

It is important to find a well-converged lattice constant within the chosen exchange and correlation potential in order to perform subsequent simulations without surface stress. For this reason, the corresponding total energy optimization of the surface is more important than the actual value of the resulting lattice constant as compared to experimental literature.

In Fig. 5.1, the intrinsic energy of the Cu bulk model is plotted as a function of the lattice constant. The fcc models were set up with lattice constants close to the expected values from literature and the results were fitted to parabolas. The red curve shows calculations within the GGA and the blue curve shows calculations for within the LDA flavor, both for a cut-off energy of 400eV and 11x11x11 k-points. Despite differences being small, it can be directly seen that LDA has the tendency to 'overbind'. The LDA lattice constant is 3.53Å compared to the experimental value of 3.616Å [176]. The GGA lattice constant is higher than the value from literature; it measures 3.64Å.

For the determination of the lattice parameter of copper, a k-point grid (see sec. 3.6) of 11x11x11 points was used. The next two figures (Fig.5.2 and 5.3) rationalize that this computational effort was sufficient to adequately describe the copper bulk within the DFT framework.

For repeated simulations including different numbers of k-points, the resulting internal

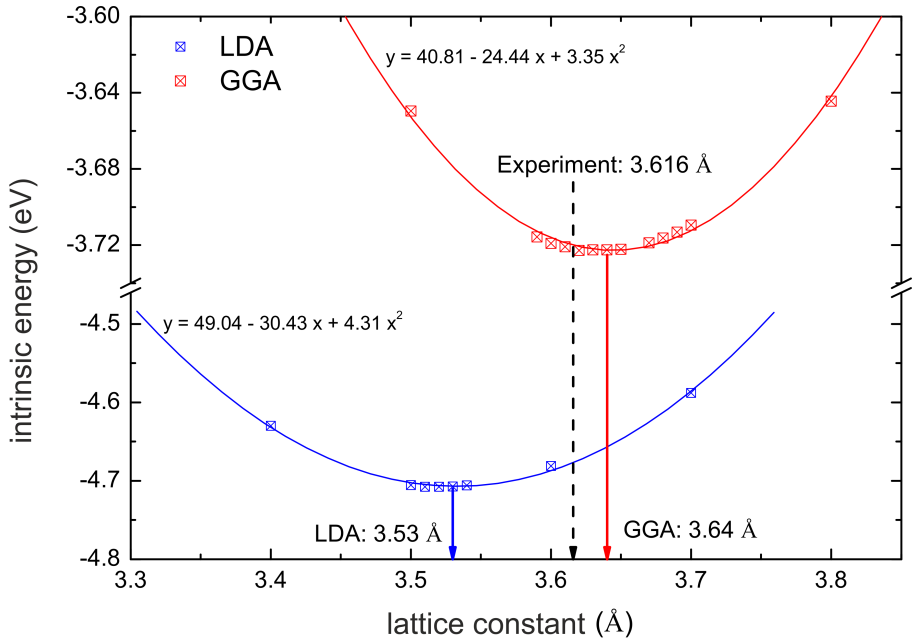

Figure 5.1.: Determination of the Cu lattice constant. The intrinsic energy is plotted as a function of the lattice constant for a set of Cu bulk models calculated within the local density approximation (LDA, blue) and the generalized gradient approximation (GGA, red). The minima correspond to the lattice constants chosen for further calculations. For comparison, the experimental value is indicated in black [176]. Based on [84]. $E_{cut} = 400eV, k-grid : 11 \times 11 \times 11$.

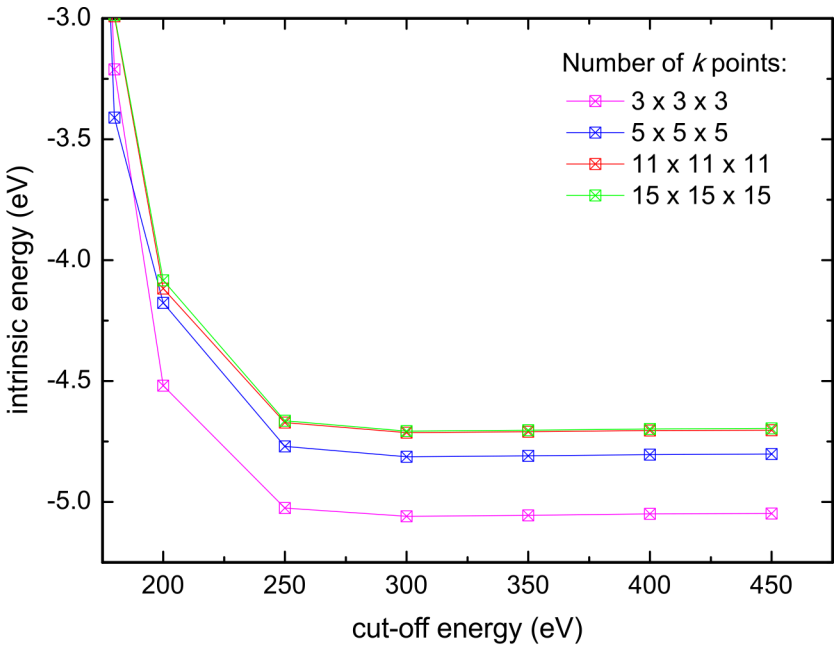

Figure 5.2.: The choice of the k-point mesh for the simulation of the copper bulk. The intrinsic energy is plotted as a function of the cut-off energy and the number of k-points. Cut-off energies of 300eV and higher are high enough to not affect the intrinsic energy of the studied system. 11x11x11 k-points produce an equally accurate result as the larger number of 15x15x15 k-points comparing the total intrinsic energy (LDA, lattice constant = 3.53Å) [84].

energy of the bulk-model is given as a function of the cut-off energy (see sec. 3.6) in Fig.5.2. The intrinsic energy is independent from the cut-off energy from energies above 250...300eV. This means that the choice of 400eV used for the calculation of the lattice parameter is appropriate. Furthermore, the intrinsic energy curves do not change when taking into account 15x15x15 instead of 11x11x11 k-points.

How the number of k-points affects the result of the lattice constant calculations can be seen in Fig. 5.3. The intrinsic energy converges for k-point grids with 11x11x11 points or higher. However, the resulting lattice constants (the minima of parabolic fits in the central parts of the wells) are practically equal also for 7x7x7 k-points and even 5x5x5 k-points.

This indicates that the lattice parameter calculation (Fig. 5.1) was carried out with a k-point grid of reasonable size.

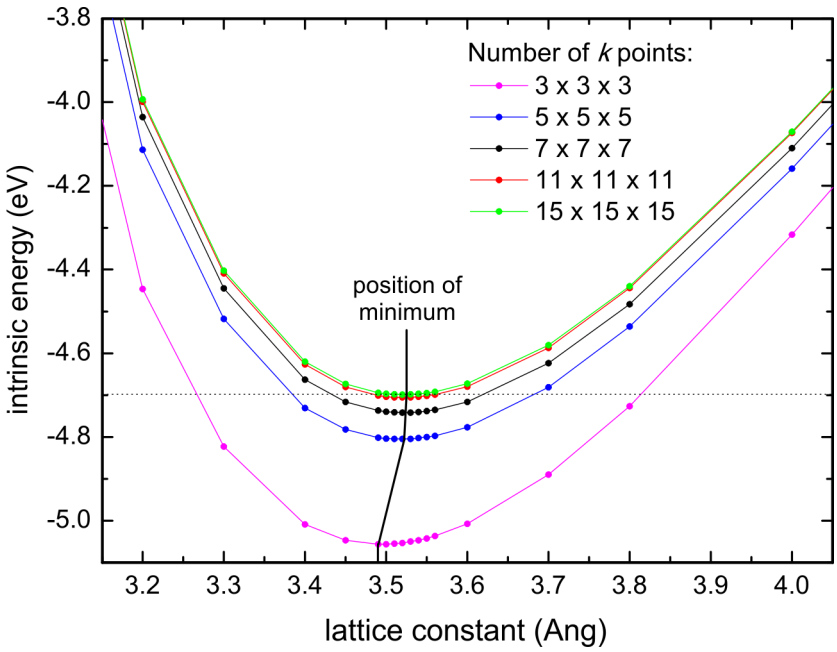

Figure 5.3.: Intrinsic energy of the LDA copper bulk calculations as a function of the lattice constant for different sized k-point grids consisting of 9 (pink) ... 3375 (green) points. The position of the minima of parabolic fits in the centers of the wells determines the copper lattice constant to be 3.53Å for 5x5x5 k-points or more. $E_{cut} = 400eV$ [84].

From Bulk to Surface

Due to periodic boundary conditions, surface models need to be constructed as a building block from atoms together with some free space above and below, thus representing the vacuum. These kind of models are called *slab models* or *supercell models* and were introduced in chapter 3.6. They are chosen as small as possible to reduce the computational effort but large enough to contain all the physics necessary. Especially, in the case of adsorbates like organic molecules, a few Å of extra space between adsorbate and the slab borders have to be added to prevent the adsorbate from interacting with the periodic replica of itself.

The Cu(111) surface exhibits a Shockley-type surface state with a quasi free two-dimensional electron gas smeared out within the surface plane [177, 132] (see sec. 4.6) . The localization of the Shockley surface state is spread over several Cu(111) lattice constants perpendicular to the surface even extending into the vacuum. For this reason, the model system must comprise several atomic layers to reliably reproduce the electronic

properties of this surface.

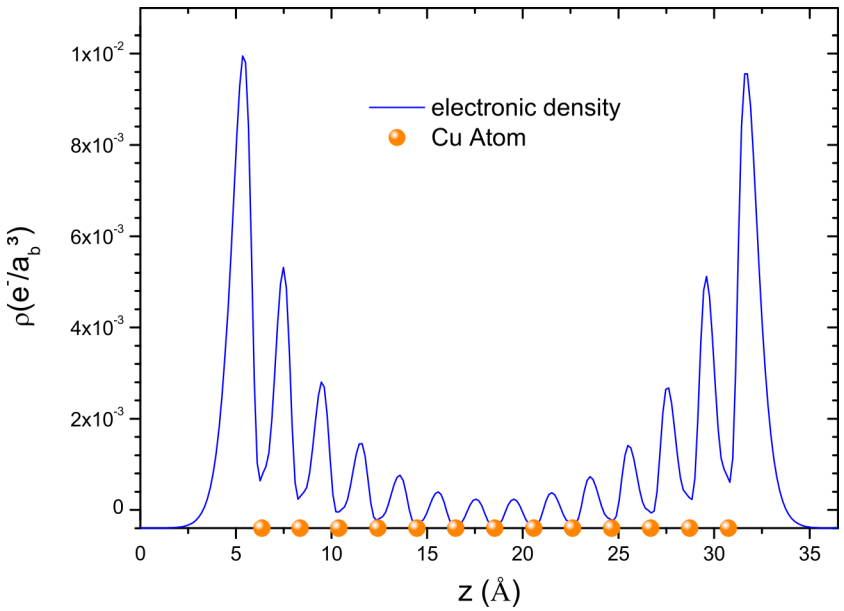

Figure 5.4.: Lateral average of the Cu(111) Shockley-type surface state electron density ρ at the Γ point as a function of z, the coordinate perpendicular to the surface plane. Each orange dot represents one atomic layer of copper. The maxima of ρ are located in between the atomic layers. The electron density is given with respect to a volume defined by the Bohr radius $a_b \approx 0.5$ Å. $E_{cut} = 280eV, k-grid : 11 \times 11 \times 1$ [84].

In Fig. 5.4 it can be seen how the Shockley surface state electron density is localized in between the atomic layers of the copper substrate and outside the first metal layer. Each orange dot represents one layer of copper. Outside the solid, the Shockley electron density exhibits its maximal value. It decays exponentially both into the bulk and into the vacuum.

Next, the size of the vacuum gap, which separates the copper slab and its next periodic representation shall be chosen. For very small distances, the two surfaces of the slab model will interact and degrade the results. Needlessly large vacuum gaps, on the other hand, will cost valuable computation time. In Fig. 5.5 the intrinsic energy of a test system as a function of the gap size is plotted. The slab consists of eight copper atoms and one hydrogen atom, which passivates one surface of the slab. The intrinsic energy of the test slab decreases when the bulk is split by a very small vacuum gap ($<$1Å). The reason for this is the loss of the energetically preferred bulk condition. The actual value of the

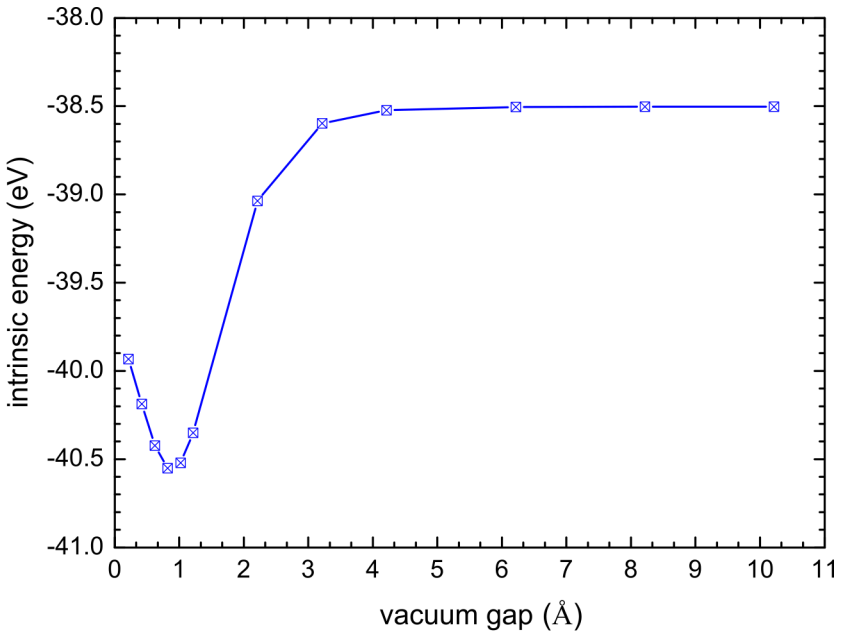

Figure 5.5.: Intrinsic energy of a test slab model as a function of the vacuum gap in between the two surfaces of the periodically repeated slab $LDA, E_{cut} = 280eV, k-grid : 11 \times 11 \times 1$ [84].

minimum is only about an angstrom, because the hydrogen atom is now in between the copper layers. For further increased gap sizes the system enters a 'repulsive regime' and the intrinsic energy converges for vacuum gaps of 5Å and higher. For vacuum gaps of this minimal size, the slab's surfaces may be assumed non-interacting. In the case of adsorbates (and geometric relaxation calculations of adsorbates), extra space needs to be incorporated.

With the aim to thoroughly simulate the electronic properties of the Cu(111) surface, the Shockley surface state has to be considered when determining the number of atomic layers in the slab. The test slab was now consecutively varied in its number of atomic layers. The resulting energetic positions of the Shockley surface state with respect to the Fermi level, E_S-E_F are plotted in Fig. 5.6. Starting from five layers, the position does not change much, even when the model is extended to more than ten layers. The surface state is found at 0.65eV below Fermi level. Compared to the experimental value from literature, 0.435eV below Fermi level [132], the calculated value is more than 200meV off.

For the extensive set of DFT calculations that will produce a rotational potential energy sur-

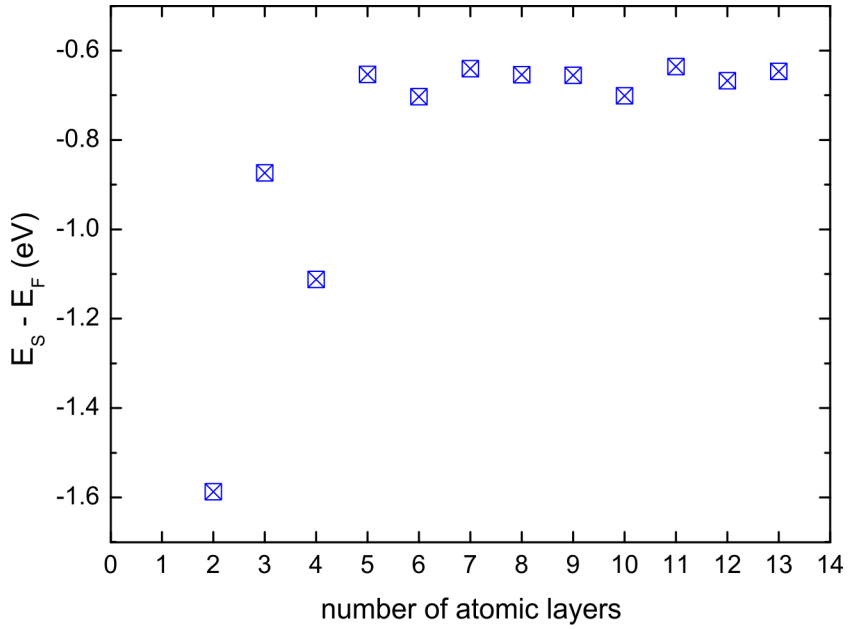

Figure 5.6.: The energetic position of the Cu(111) Shockley surface state E_S with respect to the Fermi level E_F calculated for different slab sizes. $LDA, E_{cut} = 280eV, k-grid : 11 \times 11 \times 1$ [84].

face for CuPc on Cu(111), the slab model needs to be constructed in a minimal meaningful configuration in order not to waste computation time.

With four layers of copper and each layer consisting of 9×10 atoms, this guarantees that the adsorbate CuPc will not interact in-plane with its periodic replica. The substrate supercell ends up with 360 atoms. The CuPc molecule (57 atoms) is placed on-top of the surface, resulting in a 417 atom model. A slab model of this size is close to capabilities of today's computers. The additional inclusion of more atomic layers of copper, for instance, would therefore be expensive in terms of computational time and demand for lower precision calculations. The 417 atom model is sized 22.5 Å $\times$ 21.6 Å with a substrate thickness of 6.0 Å plus a vacuum gap of 19.0 Å (including the flat-lying molecule).

Complete Model System

All calculations on the completed model system CuPc/Cu(111) were performed using the local density approximation (LDA) and pseudopotentials based on the projector augmented-wave method (PAW) [106, 107]. For the plane wave basis set, a kinetic-energy cut-off of 300 eV was chosen.

The orientation of the molecules with respect to the substrate is known from our STM studies showing the individually adsorbed molecules to be in alignment with one substrate axis (see Fig. 5.7). In fact it will be seen in the results chapter, that our DFT study predicts this alignment when analyzing an angle-dependent potential energy surface.

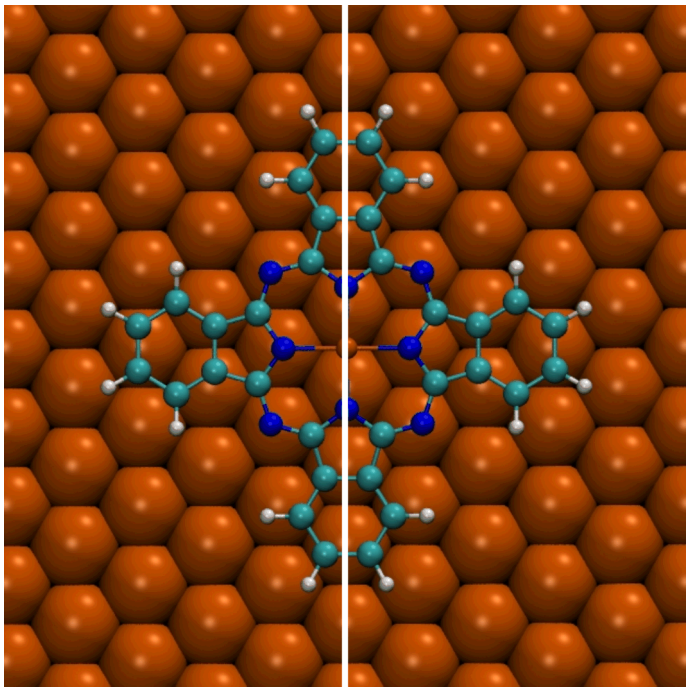

Figure 5.7.: Adsorption configuration of a singly adsorbed CuPc molecule on Cu(111). The molecule is in alignment with the [-110] or equivalent direction, as indicated by the white line. It is adsorbed with its central copper atom over the highly symmetric bridge position.

With the experimental information as a starting point, a set of DFT simulations for different adsorption sites was performed, enhancing and extending the work started in [84]. The DFT adsorption study identified the highly symmetric bridge position shown in Fig. 5.7 to be the most favorable adsorption site. This geometry was found to be energetically preferred by 114meV as compared to the hollow-site configuration. Here, the hcp (ABA packing) hollow site was chosen. A noteworthy energetic difference stemming from the second layer of substrate atoms is not expected for the adsorption at the fcc (ABC packing) hollow site [178] which was not considered here in analogy to comparable

	LDA	DFT+D2
z	2.574	2.805
E_{chem}	4.21	5.08

Table 5.1.: Computed binding distances, z, between the molecular Cu atom and the Cu(111) surface as well as the molecular chemisorption energy, E_{chem}, obtained with LDA and DFT-D2 [181].

DFT studies [179, 180]. A second bridge configuration with lower symmetry (with the dotted white line (molecular axis) in Fig. 5.7 **not** centered on a densely-packed row of substrate atoms) was also considered, but was found to be disadvantageous by 670meV. Finally, an on-top configuration resulted in a total energy which is unfavored by 1142meV as compared to the highly symmetric bridge position.

The molecule was initially placed within the vacuum gap at a distance of 2 Å above the surface. After reaching the full relaxation, the molecule sits at 2.57 Å above the Cu(111) surface. This result is in close agreement with calculations of CuPc on Ag(100) by Mugarza *et al.*, who report a binding distance of 2.46 Å between the central phthalocyanine atom and the Ag atom below [97].

For comparison with our LDA results, the adsorption configuration was additionally computed with a van der Waals correction [104] as implemented in the VASP code (DFT+D2). The numbers for the adsorption distances, z, measured between the central Cu atom of the molecule and the surface plane as well as the adsorption energies, E_{chem}, are printed in table 5.1 [181]. The adsorption energy is 16% higher in the van der Waals corrected calculation. The respective adsorption distance is 8% larger in that case.

6. Experimental Results

All STM data presented in this thesis were measured using the software provided by the *GXSM* project. *GXSM* is an open source software for scanning probe microscopy and other applications [182]. It was designed by P. Zahl *et al.*. In the Möller group, minor contributions were made in terms of co-development and testing [183]. STM images were processed with the free software *WSxM* [184]. Spectroscopy data are plotted with the spreadsheet program *Origin 8* [185].

6.1. Starting-Point: CuPc on Cu(111)

Small amounts of CuPc were evaporated onto the Cu(111) sample at room temperature (chapters 4.6 and 4.7) and studied with the STM at 7K. For coverages in the regime of about 0.1 monolayer (ML) the flat-adsorbing CuPc molecules are found to be randomly distributed on the Cu(111) terraces (overview scan Fig. 6.1a). In addition, the atomic Cu steps are decorated with molecules. At this low coverage CuPc is not found to form dimers, trimers, clusters, or islands. An exception is the adsorbate-induced cluster-formation where several molecules are bound to the same surface defect or adsorbate (Fig. 6.1b, bottom right corner).

No diffusion of the molecules is observed at $7K$, even after many hours of repeated scanning with different tunneling parameters[1].
The four benzene rings, or lobes, that yield the 'cloverleaf' appearance of CuPc show interlobal contrast: The molecules appear in a two-fold symmetry, as can be seen for every single molecule in the zoomed-in STM image in Fig. 6.1b. Pairs of opposing benzene rings

[1] The home-built low-temperature STM can in principle be operated with variable temperatures. However, the singly adsorbed CuPc molecules were found to be highly diffusive on the Cu(111) surface. Already starting below $20K$, the molecules can not be imaged reproducibly without inducing motion. At 80K, the molecules cannot be imaged by STM at all.

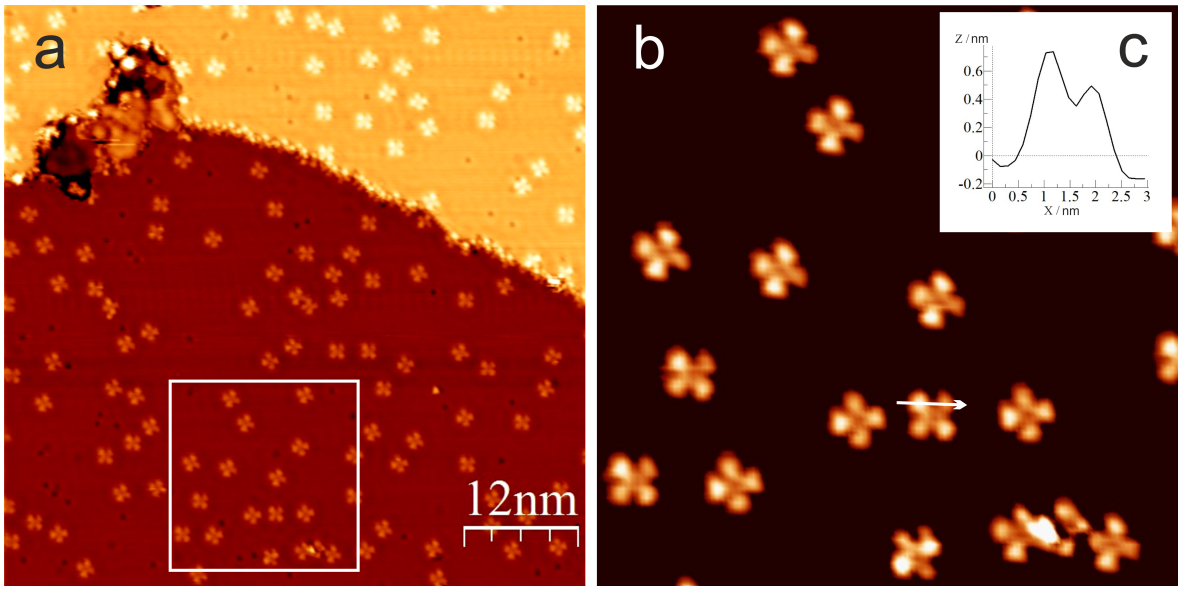

Figure 6.1.: Overview STM images of CuPc on Cu(111) for a coverage of 0.1ML observed at $7K$. (a) The STM overview scan shows the random distribution of molecules on the terraces. (b) High resolution image of the area marked by the white square in (a). The two-fold symmetry of the molecules becomes obvious. (c) This is highlighted by the line profile as indicated by the arrow in (b). $V_{sample} = 0.4V, I = 20pA$ [23].

exhibit an identical apparent topographic height. In the images, they appear brighter than the remaining two benzene rings. As an example, the inset (c) in Fig. 6.1 displays a line profile across two molecular lobes of different apparent height.

Three equivalent adsorption geometries are found, rotated by $120°$ with respect to each other. Each orientation corresponds to one symmetry axis of the (111) surface. A statistical evaluation on the adsorption angles was done in [186]. High resolution STM data with atomic resolution of the substrate prove this alignment. In Fig. 6.2 the hexagonal structure of the surface atoms can be identified. A dashed line indicates one of the three densely packed rows of the (111) surface (e.g. [-110]) to highlight the molecule-substrate alignment.

The coverage dependent initial growth of CuPc on Cu(111) (growth of molecular chains and islands) was studied in more detail. At higher submonolayer coverages the growth of short molecular chains occurs. For coverages above 0.5 monolayers, the first CuPc islands were found. The corresponding STM data were reported in *Surface Science* 603 (2009) [24] and discussed in the diploma thesis Ref. [186] as well as the doctoral thesis by Hatice

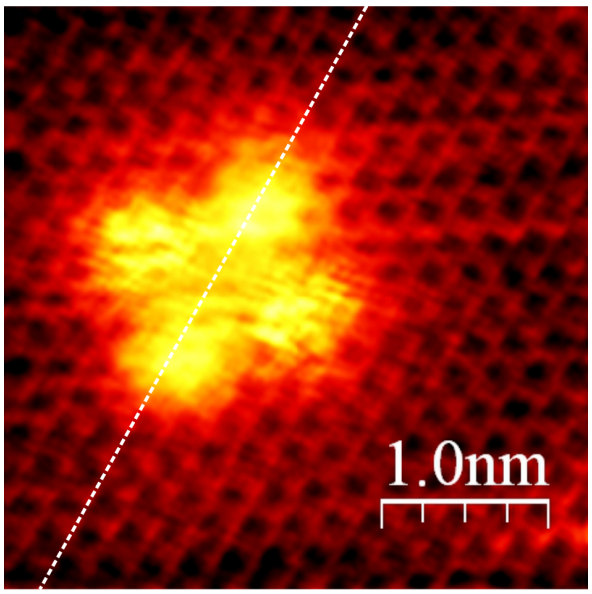

Figure 6.2.: A single CuPc molecule on Cu(111) observed at $7K$. The color scale is optimized to highlight the atomically resolved hexagonal substrate so that the alignment of the molecule with one of the three densely packed rows of the substrate becomes obvious. The aligned opposing pair of benzene rings is marked by the dashed line. $V_{sample} = -0.7V, I = 50pA, T = 7K$.

Karacuban [23] (both german language). Details on the closed monolayer growth of CuPc on Cu(111) were reported in references [149] and [159].

The focus of the present work is set on single molecules and the following phenomenon: During observation of the occupied states with the LT-STM, all individually adsorbed molecules show fluctuations (or noise) in the tunneling current signal mainly located on two opposing benzene rings.

The noisy parts of the molecules always correspond to a dim appearance in the STM images at positive sample bias (empty states). The two noisy lobes are orthogonal to the densely packed rows of copper atoms marked by the dashed line in fig. 6.2.

A zoom of an occupied states measurement presented in Fig. 6.3 shows the typical appearance of a single CuPc molecule on Cu(111). The strong fluctuations in the tunneling current result in bright dots in the STM topography. Interestingly, the fluctuations exceed the topographic border of the molecular lobes. This detail will become important later. The two smooth lobes are not completely free of the fluctuations in the

tunneling current. Very rarely, events can also be observed on the smooth lobes in the STM images (Fig. 6.3), but the contrast is inverted: the dots appear dark instead of bright.

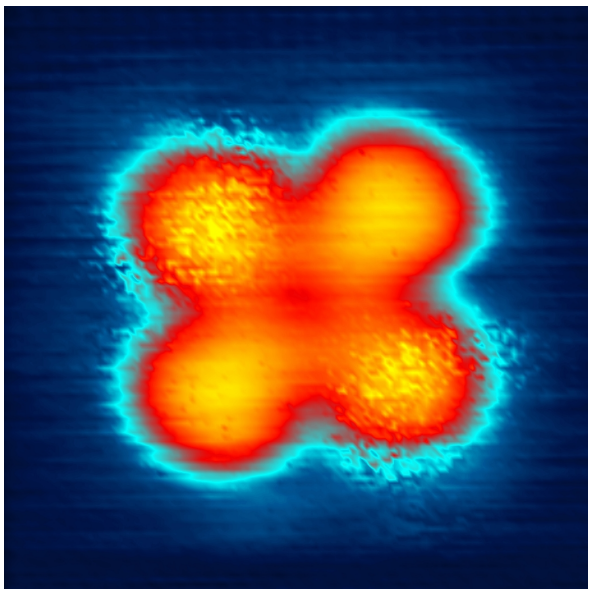

Figure 6.3.: The noisy appearance of CuPc on Cu(111): Strong fluctuations of the tunneling current result in bright dots in the STM topography. The fluctuations are localized on two out of the four lobes and occur in an area a bit larger than the topographic borders of the molecule. Rarely, switching events can also be observed on the smooth lobes, but the respective dots in the image appear dark. $2.3 \times 2.3nm^2, V_{sample} = -1.5V, I = 100pA, T = 7K$.

Before focusing on the characteristics of the noisy tunneling current signals, the symmetry of the observed phenomenon is summarized in Fig. 6.4.

The coordinate system corresponds to the vectors [100], [010] and [001] that span the (111) Miller index plane. The densest packed directions are represented by the arrows [-110], [0-11] and [10-1]. Every molecule is aligned with one of these, here [-110] was chosen. The two molecular lobes, perpendicular to [-110], exhibit fluctuations in the tunneling current represented by the dotted areas. The noisy lobes are adsorbed parallel to the direction [-1-12] (or its negative counterpart [11-2]).

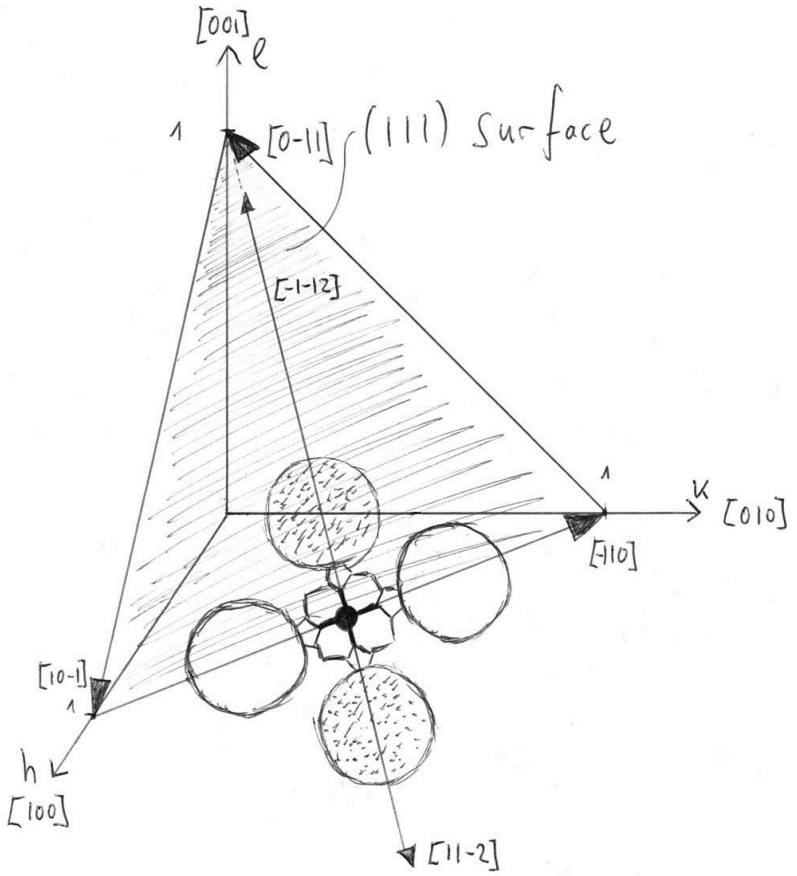

Figure 6.4.: A 3D chart illustrating the alignment of CuPc on Cu(111). The (111) Miller index plane is spanned by the h-, k- and l-vectors [100], [010] and [001]. The most densely packed directions on a Cu(111) surface are represented by the arrows [-110], [0-11] and [10-1]. Two smooth lobes of the molecule are in alignment with the exemplary chosen [-110] direction. The perpendicular noisy (here: dotted) lobes are parallel to the [-1-12] direction.

6.2. Identifying Random Telegraph Noise

The STM observation of fluctuating molecules at 7K could be assigned to specific noise patterns in the tunneling current signal. An oscilloscope showed sudden jumps of the tunneling current around its set point between a high-conducting level (on-state) and a low-conducting level (off-state), thus indicating a bistable system. The height of these jumps was surprisingly large: a factor of almost two (1.5 ... 2) was measured in between the two levels. The low background noise level of the LT-STM allowed the two levels to be clearly distinguished.

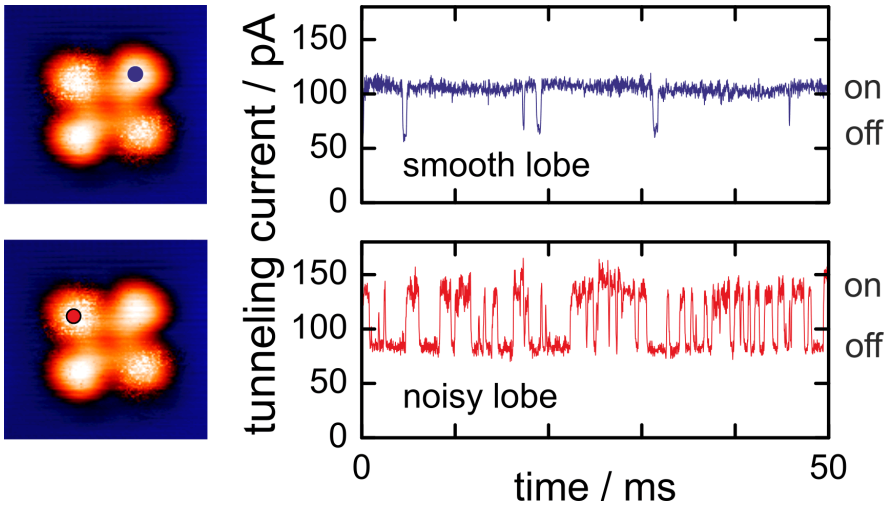

Figure 6.5.: The noise in the tunneling current measured with the tunneling tip positioned as indicated by blue and red dots corresponding to the equally colored current traces. Blue curve: the tip is placed at fixed distance above a smooth lobe at an average tunneling current of 100pA. Occasionally the current drops to roughly half its value for a short time (≈1ms). Red curve: with the tip placed over a noisy lobe (100pA, fixed distance), the strong current fluctuations between two levels are observed. A factor of almost two in current separates the on-state and the off-state.

The red curve in Fig. 6.5 shows a typical tunneling current trace measured with the tunneling tip placed at fixed tip-sample distance over a fluctuating lobe. In the lower level the current equals approximately 80pA, while the high level reaches almost 150pA. Starting with an average tunneling current of 100pA, the distribution of the two current levels around this value is not symmetric, because the lifetimes for the low-conducting

state are longer than the lifetimes of the high-conducting state in this example.

For comparison, the blue curve shows a tunneling current trace measured on a smooth lobe for comparison. As stated above, the smooth lobe only rarely shows conductance switching events. Here, the initial set current of 100pA is maintained except for five sudden and very short-lived drops of the molecular conductivity within the 50ms observation time. The current drops to about half its value, i.e. the amplitude is the same as in the case of the noisy lobes.

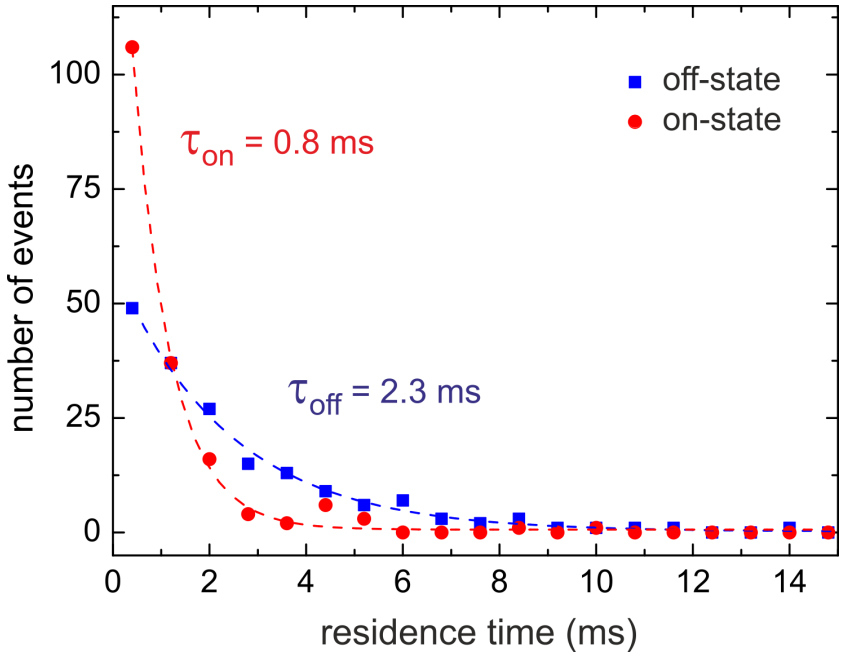

Figure 6.6.: The residence times of the two levels of conduction observed for a noisy lobe of CuPc on Cu(111) can be described by exponential decays, thus fulfilling the definition of random telegraph noise. The average lifetimes of the two states are in the millisecond regime and were measured for the sample bias voltage of V = -0.5V. The data have been published in the supplementary information to ref. [143], available online.

In order to verify that the observed signal is a random telegraph noise (RTN) signal, the distributions of the lifetimes of the on-state and the off-state are plotted in Fig. 6.6. For a series of time-traces recorded for the noisy lobes at a sample bias voltage of -0.5V the residence times for on-state and off-state were measured and sorted into time bins. The number of events is plotted as a function of the residence time.

An exponential decay function was fitted to the data points for each state, perfectly describing the data, i.e. fulfilling the definition of RTN. The two decay constants resulting from the fit yield the average lifetimes of the on- and off-state: $\tau_{on} = 0.8$ms and $\tau_{off} = 2.3$ms.

6.3. Lateral Resolved Mapping of Molecular Switching

When the molecular fluctuations were identified to cause random telegraph noise (RTN) in the tunneling current, the idea came up to analyze the signals with a new electronic setup [124]. This setup is capable to count the conductance switching events automatically during standard STM operation in order to supersede the post-experimental data analysis. The new measurement provides a full characterization of RTN resulting in the three additional data channels 'rate of events', 'amplitude of the current jumps' and 'duty cycle' (relative occupation of the on-state). Details on the design of this technique 'scanning noise microscopy' (SNM) are explained in section 4.4.

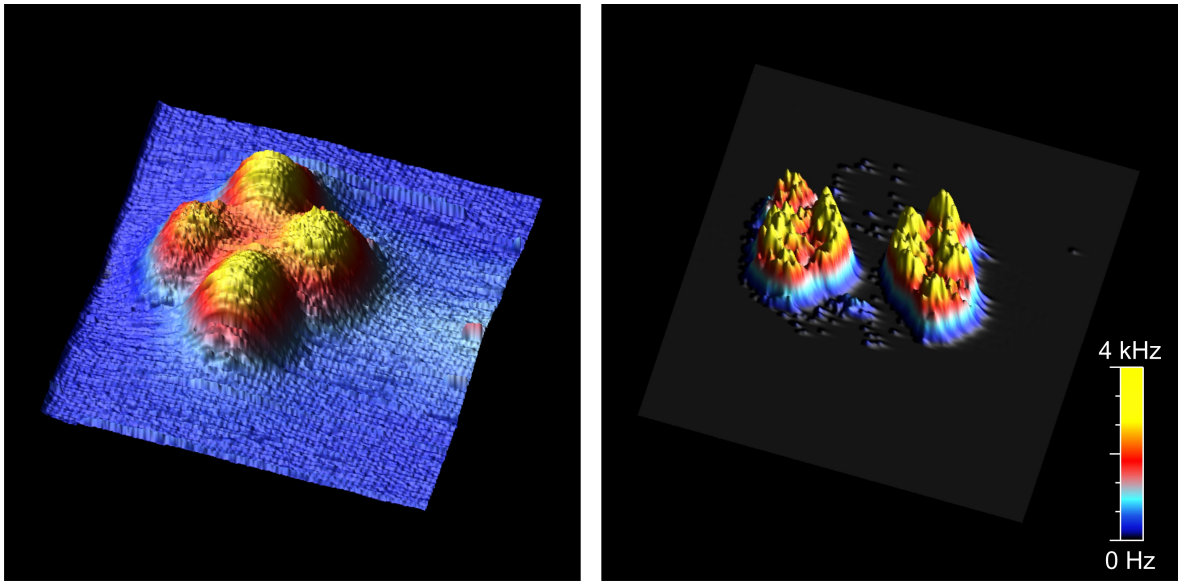

Figure 6.7.: Topography (left) and rate image (right) of a CuPc molecule on Cu(111) at $7K$, measured with the special electronics presented in chapter 4.4. $V_{sample} = -0.6V, I = 100pA$.

The experimental results obtained by the SNM method feature the same lateral resolution

as the STM topography that is measured simultaneously. Therefore, the SNM data can be instantaneously compared to the topographic information.

In the left panel of Fig. 6.7 the topography of a CuPc molecule on Cu(111) is shown in a 3D view. No filtering was applied to the raw data in order not to lose information. Hence, the raw data topography appears less ideal than usually found in literature since often some image processing is used to reduce noise or to enhance the general accessibility of the data to a broader readership. Although the left and right lobe appear somewhat fuzzy, the RTN can hardly be recognized. The right hand panel of Fig. 6.7 presents the lateral distribution of the switching rate as measured by SNM for the same molecule. The false-color code does not correspond to topographic height as in standard STM, but the switching rate is color-coded for frequencies ranging from $0s^{-1}$ (black) to $4000s^{-1}$ (yellow). The rate image exhibits an appearance that is drastically different from the topography: the two noisy lobes produce high contrast, whereas the smooth lobes almost completely disappear. On the copper surface no events were counted. At the positions of the smooth lobes, a very low switching rate is observed for some pixels of the scan. Interestingly, these rare events are often located at the borders of the benzene rings.

A full data set also including an amplitude map and a duty cycle map is displayed in Fig. 6.8. The data set starts with an overview topographic scan in panel (a). To guide the eye, white arrows indicate the surface base vectors [-110], [0-11] and [10-1]. Each molecule is aligned to one out of the three base vectors (marked by white dotted lines). The corresponding rate information is shown in (b).

Again, every molecule shows the pronounced RTN only on the two lobes that are orthogonal to one of the substrate's symmetry axis. The overview scan characterizes a group of several molecules. It took about eight hours of measurement time.

The overview rate scan yields important information on the uniform switching behavior of the molecules. This information can not be derived from (faster) topographic overview measurements. In Fig. 6.8b all molecules randomly switch within the same frequency range of up to $500s^{-1}$ at -1V sample voltage and 40pA set current. There is no broken, inactive or externally influenced molecule (e.g. by adatoms or defects) amongst the eight CuPc molecules imaged here. Thus, every molecule can be chosen for further investigation.

Subsequent zoomed measurements focus on individual molecules that are imaged with greater information density (number of pixels, time per pixel). The molecule marked by the

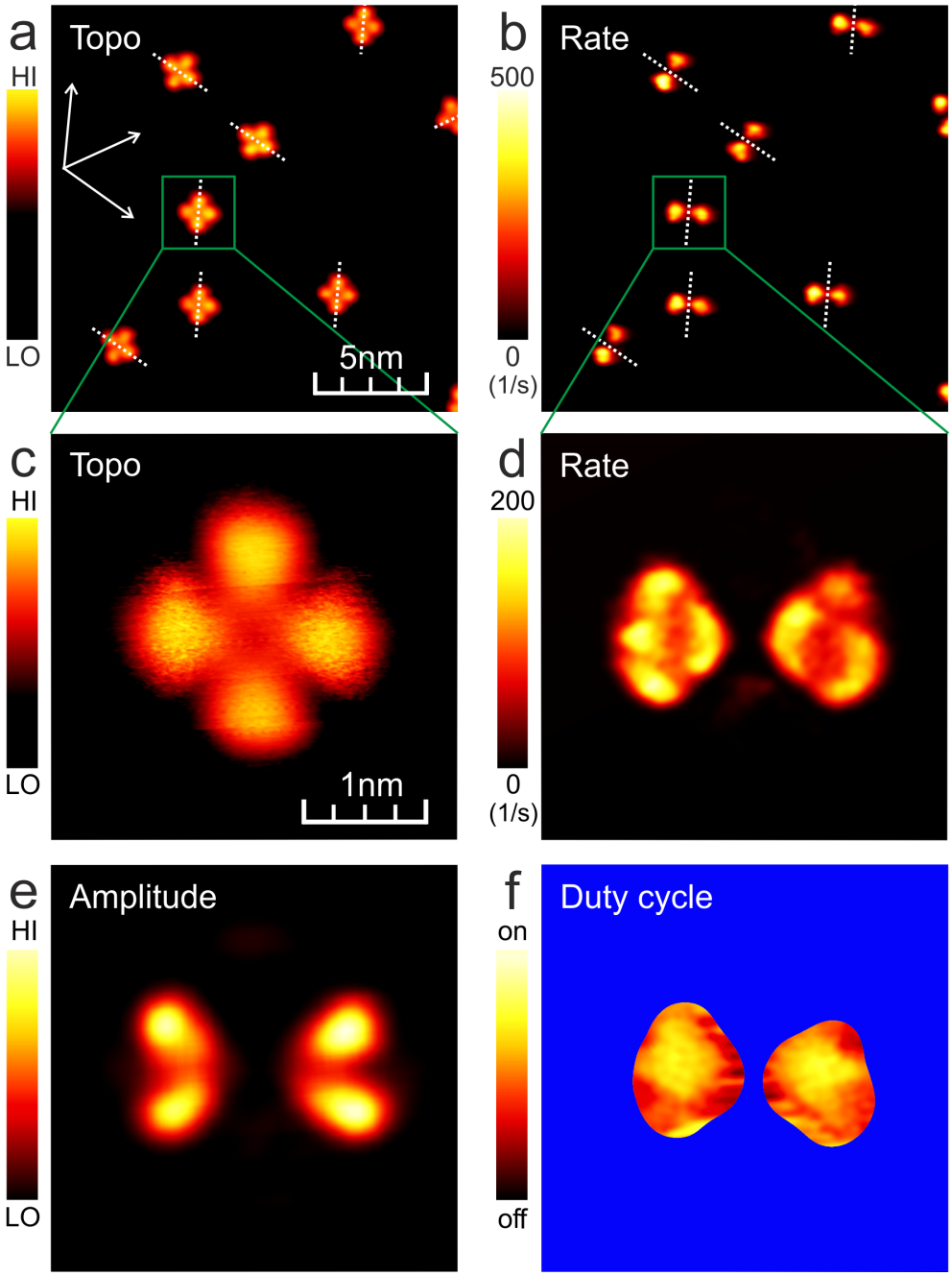

Figure 6.8.: Scanning noise microscopy study of CuPc on Cu(111). a) topography: eight individual molecules $V_{sample} = -1V, I = 40pA$. b) Simultaneously measured rate map; dotted lines (a+b) indicate the molecular alignment to the surface base vectors (white arrows). (c-f) Full SNM data set of a single molecule measured at $V_{sample} = -0.4V, I = 40pA$. (c) Topography. (d) The rate map provides high-resolution information on the molecular conductance switching. (e) The amplitude map reveals that the maximum difference between the two states is localized at the benzene-ring borders. (f) The duty cycle map shows a preference of the high-conducting state when probing the centers of the lobes. Undefined data are masked blue. Published in [143].

green squares was chosen arbitrarily. The full data set is plotted below and starts with the topography (c). In comparison to the overview scan, the data were recorded with a smaller sample voltage (-0.4V) resulting in smaller maxima in the rate image (d). Frequencies occur in the range of 0s^{-1} to 200s^{-1}. It is noteworthy, that the borders of the molecular lobes are very sharp in the rate image, exceeding the sharpness of the STM topography. Furthermore, SNM provides intramolecular details even within the four molecular lobes: In the high-resolution data the central parts of the noisy molecular lobes exhibit switching rates of only about 100s^{-1}, half of the maximum values.

The amplitude image (e) provides information on where the fluctuations cause the largest changes in conductivity. In comparison to topography, these spots are clearly located at the upper and lower borders of the noisy lobes. The outer borders however do not show amplitude maxima.

Finally, the duty cycle map analyzes the relative occupation of the on-state as a function of tip position. When the tip is placed over the central parts of the noisy lobes, the molecule will be preferably found in the on-state (65%, yellow). At the outer regions of the benzene rings the duty cycle tends to reveal an equal occupation of the on-state and the off-state (50%, red). The rest of the image is masked by blue color since the duty cycle is not a defined observable in the absence of switching events.

A voltage-dependent SNM study is depicted in Fig. 6.9. The four columns are from left to right, the standard constant-height STM topography images, the rate maps, the amplitude maps and the duty-cycle maps. The sample voltages range from -1.0V (occupied states) to $+$0.5V (unoccupied states). In the STM images, the left and the right lobe appear noisy, corresponding to the active lobes in the second column. The rate maps are in this case printed with scale bars indicating the events per incident electron. This electron yield ranges between 1x10^{-7} to 1x10^{-6} events per electron. Hence, the plots are independent of the set current. At positive bias the topographic images show the symmetry reduction of CuPc/Cu(111). The lobes that appear dim at positive bias (left and right in the images) are those showing random telegraph noise. At the positive voltages, very faint RTN activity is still observable on the noisy lobes. The amplitude images again show maxima on the borders of the active lobes. The duty cycle maps exhibit their maxima at the centers of the active lobes. It is noteworthy, that the SNM rate images (second column) are very highly resolved with submolecular details and sharp borders of the active areas in the data.

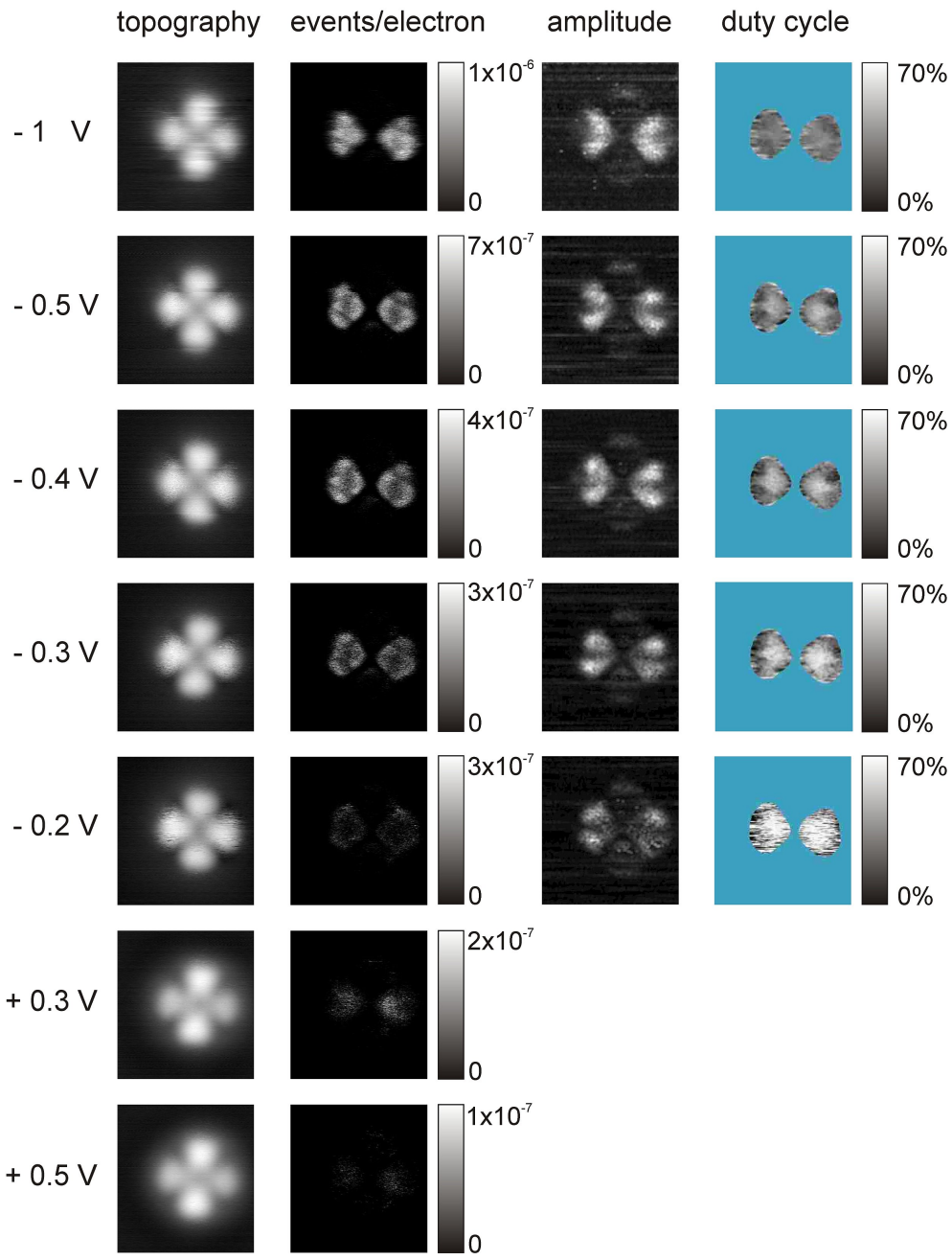

Figure 6.9.: Scanning noise microscopy (SNM) study of an individually adsorbed molecule of CuPc on Cu(111) at 7K for different bias voltages. First column: standard STM topography (constant current). Second column: Random telegraph noise rate maps (scale bars: events per electron). The electron yields range from $1x10^{-7}$ to $1x10^{-6}$. Third column: spatial distribution of the switching amplitude. Fourth column: Duty cycle maps (undefined data masked blue). At positive sample voltage, the detected events are so infrequent, that except for the rate map the SNM outputs do not yield meaningful information. Imaged at 40pA tunneling current. Figure published in the supplementary information to reference [143].

6.4. Orbital Mediated Switching Analyzed by Noise Spectroscopy

The scanning noise microscope (SNM, see sec. 4.4 and reference [124]) permits to perform new spectroscopic methods. Similar to scanning tunneling spectroscopy (STS) the tunneling tip is kept at a fixed lateral position in order to investigate the properties of a specific position on the surface.

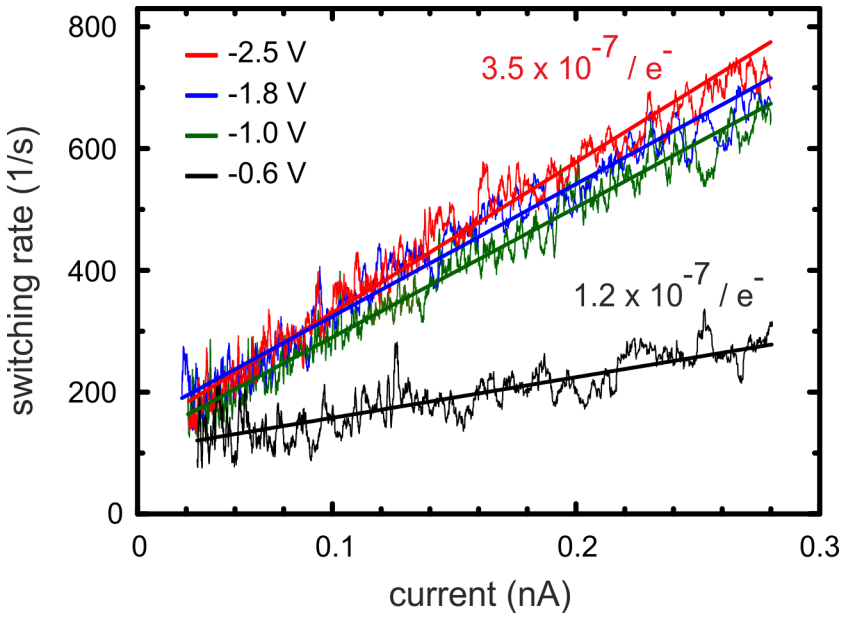

Figure 6.10.: Molecular switching rate as a function of tunneling current. A linear response is observed in a z-spectroscopy random telegraph noise measurement. The slopes of the straight lines vary with tunneling voltage and are found to be in the regime of 1×10^{-7} events per electron. Figure published in [143].

The first spectroscopic RTN measurement on the system CuPc on Cu(111) presented in Fig. 6.10 analyzes the molecular switching rate as a function of the tunneling current. To ramp the tunneling current, the LT-STM was used in the so called z-spectroscopy mode: The tip-surface distance is varied. The molecular switching rate is measured as well as the resulting tunneling current. The experiment was repeated for different sample voltages, represented by different colors. The data can be fit well by linear regression. It can be seen that also for tunneling currents higher than 10pA...100pA as in the previous section,

the switching rate depends linearly on the current.

The slopes of the straight lines increase with increasing negative sample voltage. Using the elementary charge $e_0 \approx 1.602 \times 10^{-19}$C the events counted as a function of current can be expressed as events per electron: The rate is multiplied by the elementary charge and divided by the current. For the voltage of -0.6V the slope corresponds to 1.2×10^{-7} events per electron, whereas for the highest of the four plotted voltages (-2.5V) the slope corresponds to 3.5×10^{-7} events per electron.

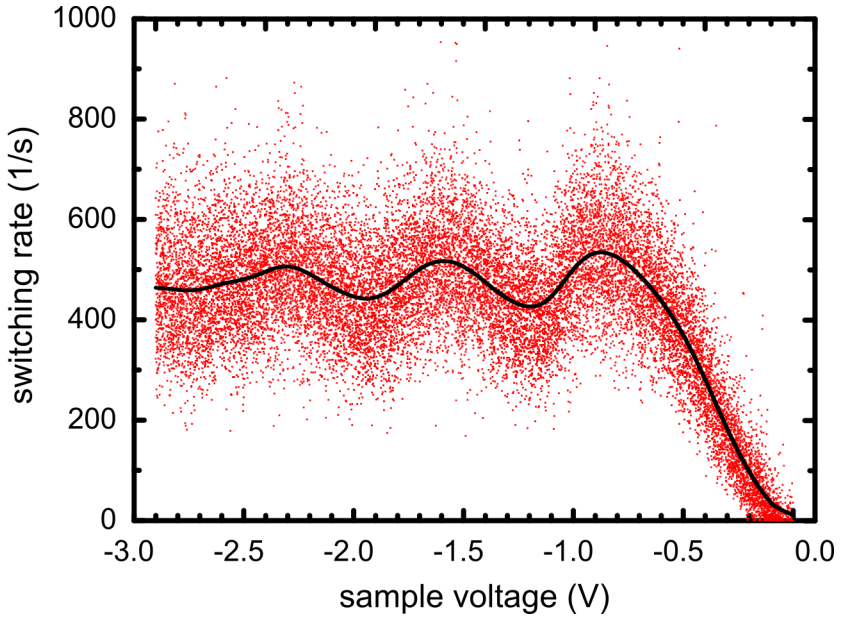

Figure 6.11.: Molecular switching rate as a function of tunneling electron energy (sample bias voltage). Close to Fermi level (0V) the studied CuPc molecule is almost inactive whereas increasing the bias to -0.9V leads to an increase of the rate to 500s^{-1}. Two more rate maxima are found at -1.6V and -2.3V bias voltage.

The linear fits in Fig. 6.10 can be extrapolated to zero current leading to finite switching rates. However, the SNS measurement fails for very small tunneling currents, as the events per measurement time become very rare. In consequence, the statistics analyzed by the SNM electronics (sec. 4.4) worsens in the limit of small currents. Due to the limit of accuracy, the extrapolation to zero current will not be evaluated quantitatively. Nevertheless, a finite background switching rate cannot be excluded.

The dependence of the switching rate on the sample bias is investigated in detail by ramping the voltage at constant tunneling current as shown in Fig. 6.11. The red data points are raw data of a typical ten times repeated measurement. For every voltage ramp, 1000 data points were recorded for both, increasing and reducing the voltage, resulting in $1000 \times 2 \times 10 = 20.000$ data points. The black curve is a smoothed representation of the data (Savitzki-Golay algorithm [187]).

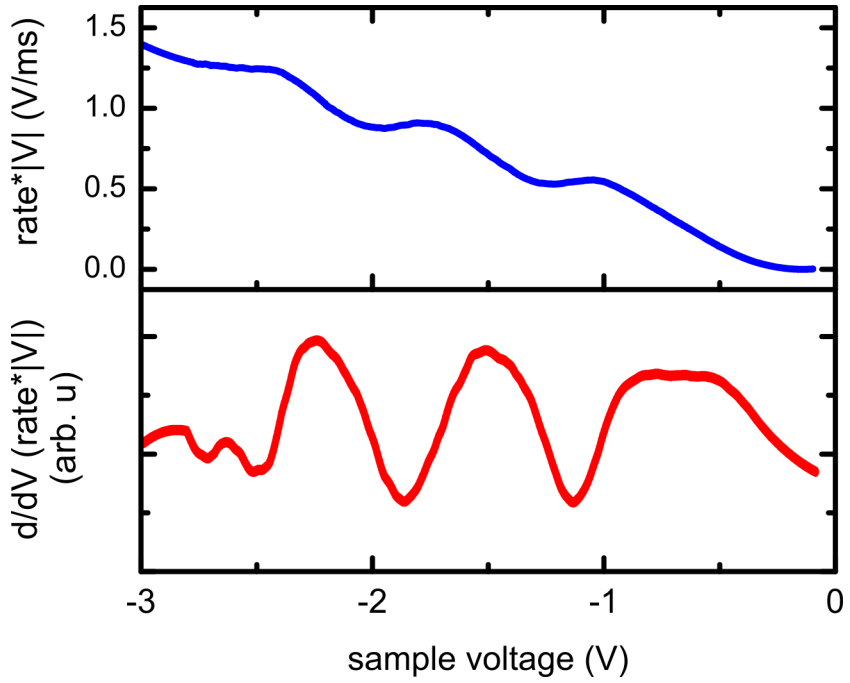

Figure 6.12.: Data analysis of scanning noise spectroscopy (SNS) in analogy to standard scanning tunneling spectroscopy (STS): Upper part: The rate from fig. 6.11 is multiplied by the sample bias voltage in order to compensate for the varying tip-surface distance during the rate measurement, providing a 'pseudo constant-distance' signal. Lower part: The resulting spectrum is differentiated with respect to the bias voltage. The maxima correspond to the energies of the steepest slopes in the original rate measurement (Fig. 6.11) in analogy to STS, where the derivative of the signal reveals the steepest slopes of the I-V curve.

Going down from the Fermi level (0V) the rate increases from practically zero to a value of approximately 500 events per second at -0.9V where it reaches a maximum. The scattering of the raw data points give an impression for the statistical behavior of the molecular switch: The data points scatter by $200 s^{-1}$ around the average value. The distribution of

the life times of the two-level system was shown earlier in Fig. 6.6 on page 87. For higher sample voltages the rate decreases by $100s^{-1}$ and then rises again and reaches another maximum at -1.6V. A third maximum can be found at -2.3V.

In order to analyze the rate data of Fig. 6.11 in analogy to standard STS, the rate information was subsequently treated in the following way (Fig. 6.12).

Assuming a linear I-V curve, the rate measured at constant current was multiplied by the tunneling voltage V with the aim to obtain spectra at constant tip-surface distance (blue curve) as it is commonly plotted in STS. Then the derivative with respect to the bias is calculated (red curve).

We know from Fig. 6.10 that the rate is proportional to the current. Hence, the resulting spectrum can be interpreted in analogy to STS: With increasing bias, new tunneling channels open. The additional tunneling channels are represented by the steps in the blue curve. These result in peaks in the derivative of the constant-height tunneling current (STS), or the constant-height rate in this case. In the following d(rate*V)/dV signals (like the red curve in Fig. 6.12) will be referred to as scanning noise spectra (SNS).

In Fig. 6.13, the SNS results are assigned to the electronic system of CuPc/Cu(111). A very broad maximum is found around -0.7V (LUMO). Further maxima are observed at -1.5V (HOMO) and -2.2V (HOMO-1). The maxima correspond to the energetic positions of the steepest positive changes in the rate measurement. Their energetic positions allow to extract information on the electronic properties of the adsorbed organic molecule (see discussion sec. 8.1).

One more new spectroscopic method that can be performed with the SNM electronics is the duty cycle spectroscopy shown in Fig. 6.14. In the present study, the duty cycle spectra yielded an interesting hint on the dynamics of the studied system.

The duty cycle signal in Fig. 6.14 starts with a value close to one at the Fermi level. This means, the molecular switch is almost exclusively observed in the on-state. When the negative sample bias is increased the duty cycle drops within the first 700meV to a value of approximately 0.35. In that regime it saturates. For high bias voltages duty cycle saturation levels between 0.2 and 0.4 have been observed for all molecules studied. The curve resulted from a Savitzki-Golay smoothing of the raw data similar to Fig. 6.11.

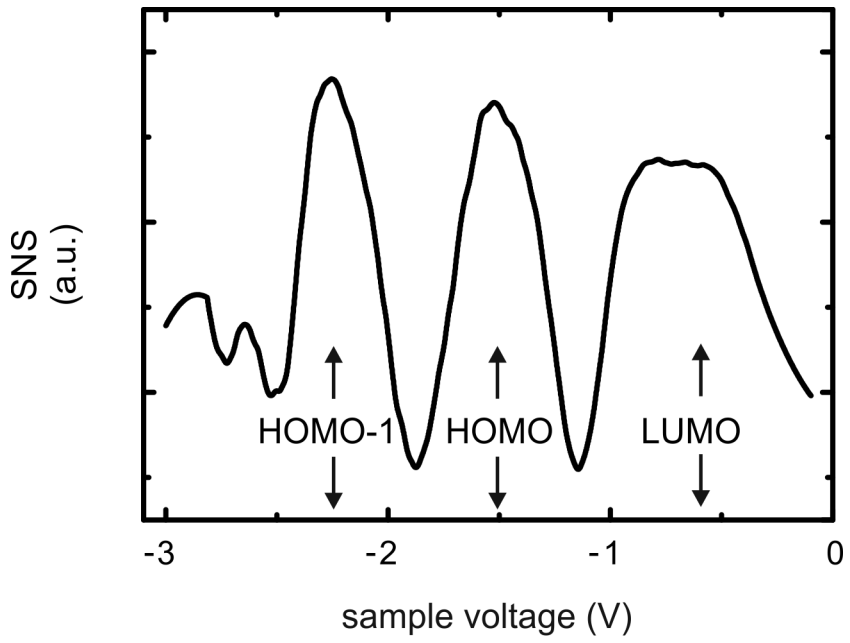

Figure 6.13.: Scanning noise spectroscopy (SNS) data for an individually adsorbed CuPc molecule on Cu(111): The maxima in the SNS curve are assigned to molecular orbitals. The (partially filled) LUMO has its onset at -0.4eV; the HOMO is found at -1.5eV, and the HOMO-1 sets in at -2.3eV.

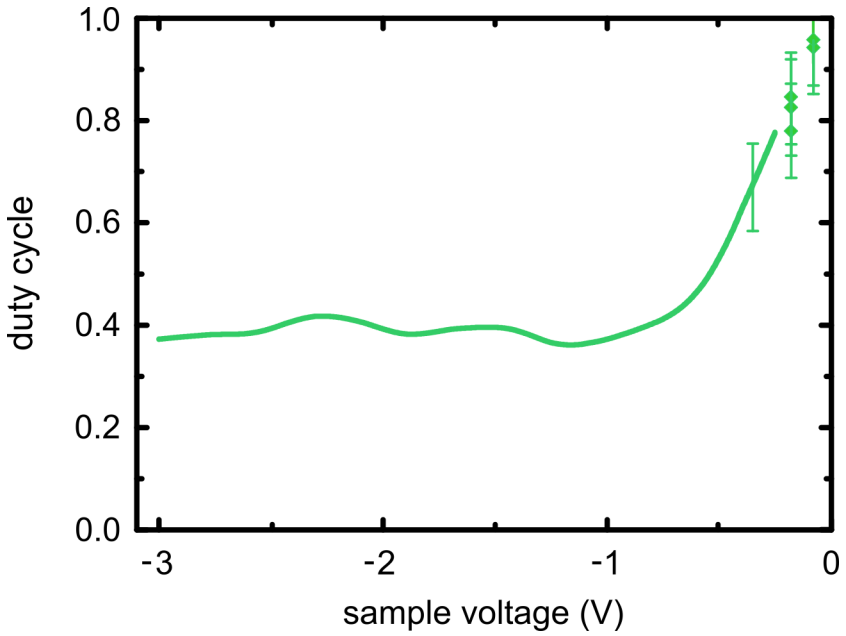

Figure 6.14.: Duty cycle spectroscopy data for an individually adsorbed CuPc molecule on Cu(111)]. Close to the Fermi level the conductance switching molecule is found in its on-state almost exclusively (duty cycle close to one). With increasing negative sample bias the duty cycle drops to roughly one third and saturates. The discrete data points at low voltages were added by a manual analysis of current-time-traces to assure reliable data in the regime of the low-frequency limit of the RTN electronics (sec. 4.4) [143].

The additional data points at very low bias have been added by manually counting switching events in the tunneling current traces recorded over a time of 10s each. Although, the RTN electronics were designed to supersede the manual data analysis it was double-checked in this case that the duty cycle can be extrapolated to the value one at Fermi level. This was necessary, since the duty cycle is not a defined measure in the absence of events (explained in sec. 4.4). From Fig. 6.11 we learn that bias voltages $<$100meV lead to very small numbers of events per time. Therefore the duty cycle output does not yield reliable information in the case of small voltages and was complemented by the additional data points.

6.5. Scanning Tunneling Spectroscopy

Several month before the SNM and SNS data (chapters 6.3 and 6.4) were recorded, standard low-temperature scanning tunneling spectroscopy (STS, see sec. 2.3) was measured on the system CuPc/Cu(111). Unfortunately, STS turned out to not resolve information on the molecular orbitals no matter how many attempts and tunneling tips were tried. It was only after SNS had shown convincingly pronounced features that we re-evaluated our STS data to check whether the molecular orbitals might have faintly been included, but overseen so far.

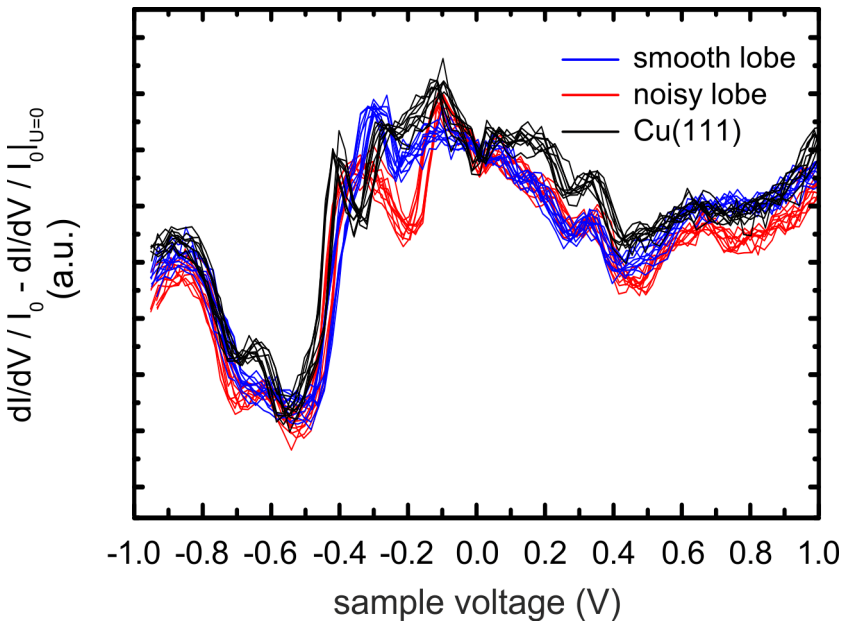

Figure 6.15.: Conventional low-temperature scanning tunneling spectroscopy (STS) data for CuPc on Cu(111) measured at constant tip-surface distance. At -0.4V sample bias voltage the onset of the Shockley surface state can clearly be recognized. The molecular spectra (red and blue) appear very similar to the substrate reference spectrum (black). Measured at 7K, spectra normalized and offsets equalized at 0V.

Prior to each STS measurement, the tunneling tip has to be well characterized. On Cu(111) the electronic properties of the tips and sample were routinely checked by measuring the Shockley surface state at approximately -0.4eV sample bias voltage (see sec. 4.6). The sharp onset of the surface state at that energy can be seen in Fig. 6.15. The successful resolution of this state is a good reference to confirm a clean metal tip and a

clean Cu(111) sample. We applied the same routine to check the quality of the tunneling tips prior to all SNM and SNS measurements. The dI/dV data (see sec. 2.3) is plotted for ten spectroscopic measurements on each the smooth and the noisy lobes and on the clean substrate, respectively.

The spectra were recorded at 7K and normalized by the current. In addition, the offsets were equalized at zero sample bias voltage. There are only faint differences between the curves for the smooth and the noisy lobes.

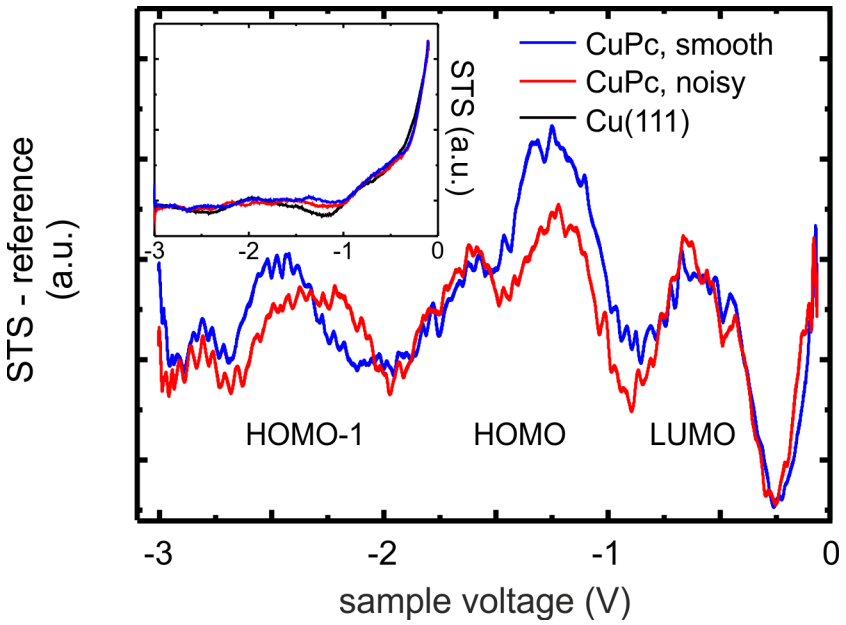

Figure 6.16.: STS data for CuPc on Cu(111) measured at constant current. The inset shows the raw data for the clean substrate (black), above a smooth (blue) and a noisy lobe (red) of CuPc. The main diagram displays the spectra obtained by subtracting the spectrum of Cu(111) from the other two. The LUMO, HOMO and HOMO-1 can be identified [143].

With the well-characterized tunneling tip, STS was performed to access information on the molecular orbitals of CuPc (Fig. 6.16). For this task, the measurement was performed in constant-current mode (at 100pA set current). As discussed before (sec. 2.3), the constant-current mode helps to resolve faint features in STS as low current conditions are avoided resulting in an enhanced signal to noise ratio. Nevertheless, the raw data presented in the inset of Fig. 6.16 for the smooth and noisy

lobe and the substrate appear rather similar and reveal no molecular features at first glance.

However, by subtracting the reference spectrum of the clean Cu(111) surface, the molecular states appear. The orbital shapes are still not strikingly pronounced (compared to SNS in sec. 6.4) but clearly present. Starting from Fermi level (zero bias voltage), the partially filled LUMO, the HOMO and the HOMO-1 are labeled in the plot. The results will be compared to SNS, UPS and DFT in the discussion section 8.6.

7. Theoretical Results

The results of our DFT calculations are presented in this chapter (see chapters 3 for basics on DFT and 5 for the modeling of the studied system). In the following, we explore the potential energy surface (PES) of the CuPc molecule as it rotates around its central atom on the Cu(111) surface and how the rotation affects the binding geometry. The electronic structure calculations allow to simulate constant current STM images and learn about the underlying molecular electronic system by analyzing the contribution of its molecular orbitals to the total density of states. Finally, we model the rotational excitation of the adsorbed molecule by tunneling electrons using a scattering theory approach.

7.1. Potential Energy Surface

For the rotation of CuPc on Cu(111), a one-dimensional PES shall be derived from DFT calculations as a function of the rotation angle, ϕ, as introduced in Fig. 7.1. The preliminary studies are described in chapter 5. The adsorption ground state is derived from STM measurements and from DFT calculations for different high-symmetry adsorption configurations. The molecule is centered in a highly symmetric bridge position with two opposing benzene rings aligned with the substrate's densely packed rows, e.g. the [-110] direction.

From this ground state, the molecular coordinates are stepwise changed in terms of slight rotations around the central Cu atom of the molecule within the surface plane. For each slight rotation, the molecule (x and y within the surface plane, and z perpendicular), the first copper layer (x, y, and z) and the second copper layer (z only) are structurally optimized albeit the molecular axis, which needs to be fixed in order to prevent back-rotation into the ground state. The rotational fixing is realized in the following way. First, two opposing N atoms from the phthalocyanine core are fixed in their x and y coordinates. Then, after relaxation, the calculations were repeated, fixing another (perpendicular) pair of N atoms. Due to this procedure, the molecule and the substrate are allowed to find a configuration without stress so the forces reach very low values, indicating a good convergence of the

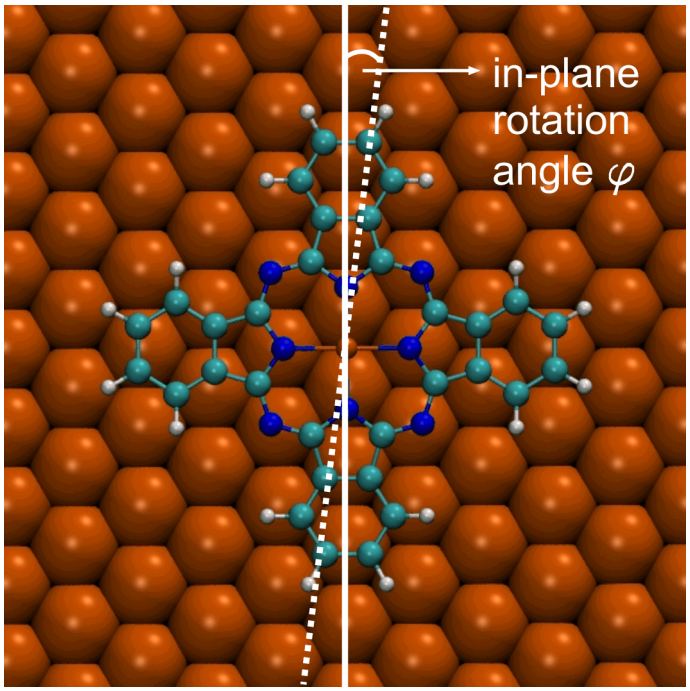

Figure 7.1.: The in-plane molecular rotation angle of CuPc on the Cu(111) surface. The ground state adsorption configuration of CuPc is marked by a white line which is aligned with a densely packed row of Cu atoms (e.g. [-110]). The dotted line indicates an exemplary rotation of the molecule, which will be described in the following by the angle ϕ.

simulations. Ionic convergence is assumed to be achieved as soon as the maximal force within the full system falls below 0.02eV/Å. After all ionic relaxation steps have converged successfully, a more accurate electronic convergence is obtained by one more computational run for each final configuration. This procedure is repeated for every point in the PES. The PES is obtained using one k-point. Once stable potential wells are localized, the barrier height is computed with higher precision using nine k-points.

The difference of the total energy of the system with respect to the ground state's energy is plotted as a function of the rotational angle in Fig. 7.2. Three minima are found for rotation angles of $0\,^\circ$ and $\pm 7\,^\circ$. The overall minimum at $0\,^\circ$ is the symmetric bridge position. The barrier for rotational excitation from the rotational ground state into one of the side-well states is about 50-70meV. To guide the eye, a polynomial fit is given as a solid blue line although the fit has the tendency to underestimate the barrier height.

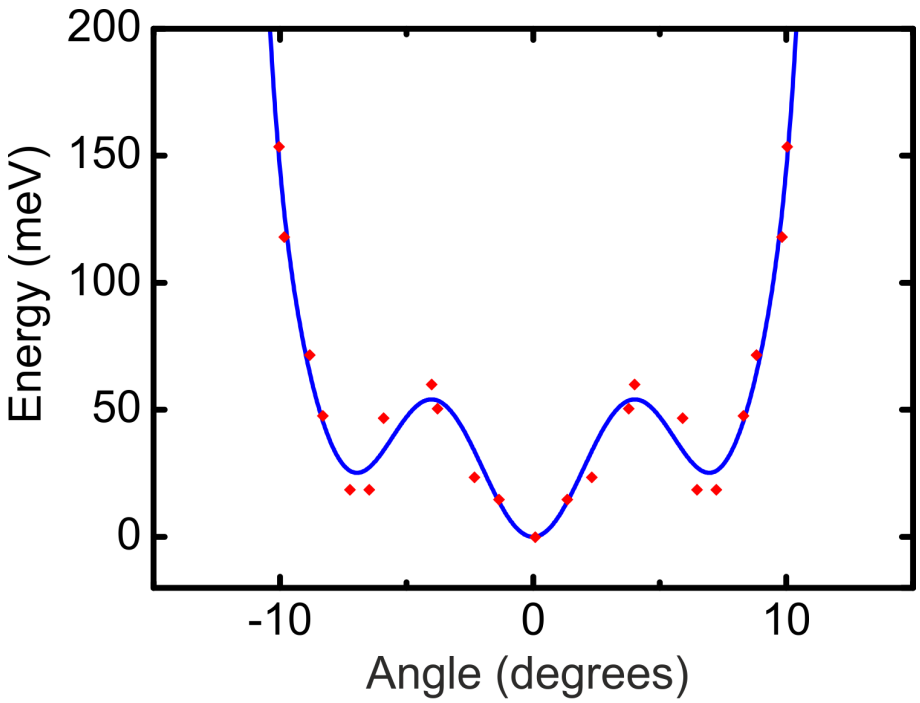

Figure 7.2.: Adiabatic potential energy surface (PES) as a function of the molecular rotation angle around its core Cu atom within the surface plane. The data points display the results of the DFT study, the blue line is a polynomial fit. The potential side wells are found to be located at $\pm 7^\circ$. The barrier for rotational excitation is about 50-70meV.

7.2. Binding Distance Analysis

In order to rationalize the existence of the side wells in the potential energy surface, the dependency of the DFT binding distances on the molecular rotation angle shall be analyzed. For this purpose, a simple C++ code was written to calculate the respective distances in the VASP-code output files.

The molecular copper core exhibits a vertical distance of 2.06Å with respect to the surface in the rotational ground state. In average (all atoms), the molecule is adsorbed in a distance of 2.16Å.

For the rotated configuration the relaxed geometries yield a binding distance of the molecular copper core to the surface of 2.14Å. The full molecule in average, however, is found at the same vertical distance (only about 1pm further away) from the surface after rotation.

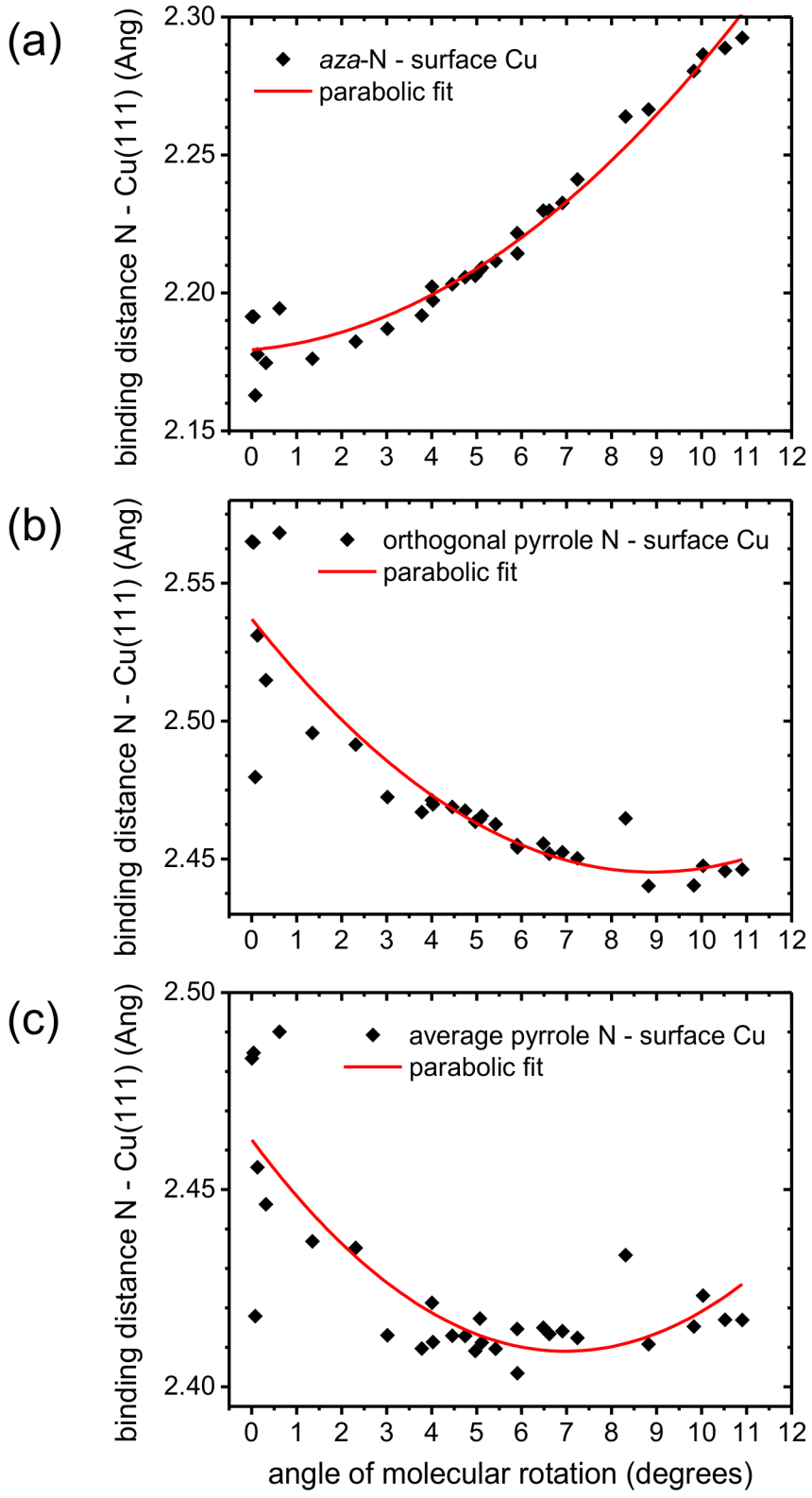

Figure 7.3.: Analysis of the calculated binding distances of the N atoms of the CuPc molecule to the Cu(111) surface under rotation.

The *aza*-N atoms[1] dominate the binding and with that the orientation of the molecule on the surface. For the most stable configuration, with the CuPc molecule in alignment with one of the Cu(111) densely packed directions, the *aza*-N atoms are found in a binding distance of about 2.18Å from the closest Cu atom within the surface (not from the vertical position of the surface, as before). When the molecule rotates away from its ground state configuration, this distance grows larger, as plotted in Fig. 7.3a. Parabolic fits (red curves) are added to the figure to guide the eye.
Interestingly, the behavior is not found for the pyrrole-N atoms. In contrary, the pyrrole-N atoms approach their next-neighboring Cu atom on the surface during the molecular rotation. This is effect is obvious for the two pyrrole-N atoms of the molecular lobes aligned orthogonal with respect to the densely packed Cu(111) directions (Fig. 7.3b). Measuring the average binding distances over all pyrrole-N atoms results in the following observation. The N-Cu bonds shrink for the first seven degrees of molecular rotation and then show a tendency to grow again (Fig. 7.3c).

The inflection point of the parabolic fit corresponds to an angle of about seven degrees, the same angle where the PES side wells were found (see Fig. 7.2).

The benzene rings (the outer parts of the four lobes) show a minimal rearrangement under rotation. The aligned pair and the orthogonal pair react in the same way on the rotation. The benzene-surface binding distances increase by about 3pm in average in between the rotational ground state (0 degrees) and the rotated state (7 degrees). However, the aligned pair of benzene rings starts at a binding distance 10pm higher than the orthogonal pair. After rotation, the difference measures 8pm.

[1] The phthalocyanine molecule consists of four benzopyrrole rings bound by four *aza*-nitrogen bridges (compound ligands). In the following, the '*aza*-N atoms' refers to the outer four N atoms in the structural model Fig. 4.12. The inner four N atoms will be referred to as the 'pyrrole-N' atoms, respectively.

7.3. Calculated STM images

With the help of a code developed by Nicolás Lorente, STM images can be simulated based on the results of the DFT calculations for the adsorption of CuPc on Cu(111).

The method of calculating STM images takes advantage of the Tersoff-Hamann treatment of the tunneling current (see section 2.2). Tersoff and Hamann employ a spherical symmetry (an s-orbital) to simplify the representation of the tunneling electron from the tip, while the surface is treated exactly.

The tunneling current is known to decay exponentially with increasing tip-surface distance, z. Thus, for the implementation of the STM simulation code, the wave functions are forced to decay exponentially from a minimal distance, z_0, from the surface.

The code by Nicolás Lorente is a finite-bias extension of the Tersoff-Hamann theory, where the LDOS is integrated for an energy window between the Fermi energy, E_F, and the Fermi energy plus the applied bias voltage times the electron charge, $E_F + e\,V$. Thus, it allows to compare simulated STM images for different bias voltages whereas the standard Tersoff-Hamann theory provides the local density of states (LDOS) only at the Fermi level, which corresponds to STM imaging at zero bias voltage.

In the following, the term 'bias' refers to the voltage, V, that defines the energy window of the integration of the LDOS. This is also the value that is given for the simulated images: In analogy to experiment, all electrons between Fermi level and $E_F + e\,V$ may contribute to the tunneling process.

The Unoccupied States

The results of the Tersoff-Hamann calculation for the unoccupied states are displayed in Fig. 7.4. For the ground-state image at 200meV, a two-fold symmetry of the adsorbed molecule becomes obvious from the first-principles calculations. With increasing energy, the two-fold symmetry lasts, but the contrast diminishes. The rotated configuration does not show a comparable inter-lobe contrast. The molecule appears in a four-fold symmetry. At all energies plotted in Fig. 7.4, the clockwise rotated molecule shows some faint, but clearly recognizable chirality. In general, no dramatic change occurs as a consequence of

high or low sample voltage.

The Occupied States

Simulated STM images of the occupied states of CuPc on Cu(111) can be seen in Fig. 7.5 on page 111. The setup of the chart is similar to the data above, except the sign of the tunneling bias voltage is inverted. Again, three exemplary energies are chosen. The energy dependence of the molecular appearance is small. For the ground state at an energy close to the Fermi level (-200meV), the two-fold symmetry is still faintly present. For larger bias voltages, four-fold symmetry is observed.

The rotated state generates a higher resolved image. The shape of the four molecular lobes as well as the central depression at -200meV are more pronounced compared to the ground state. The general appearance of the rotated state is less chiral than that of the unoccupied states.

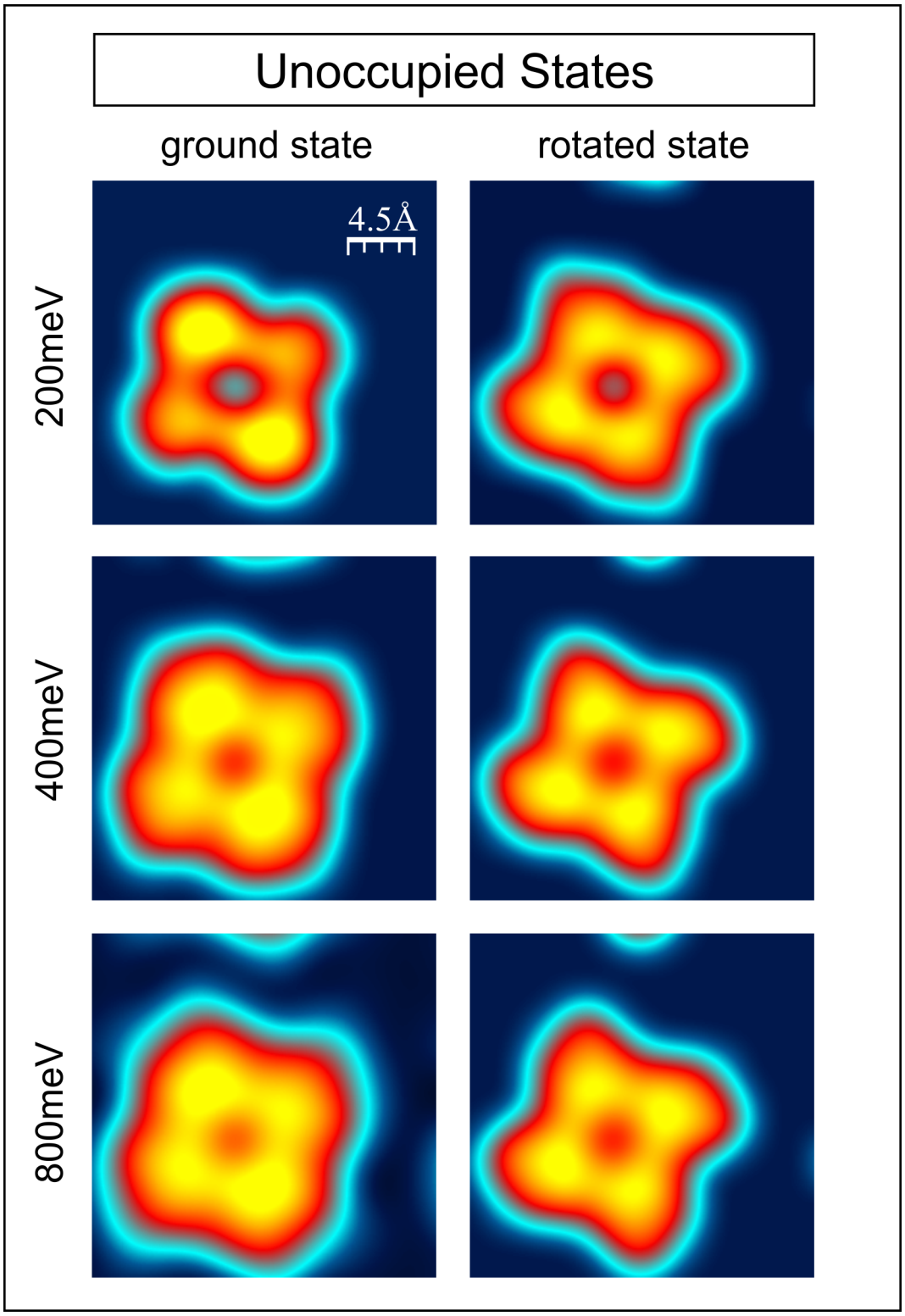

Figure 7.4.: Simulated unoccupied states STM images resulting from a Tersoff-Hamann treatment of the DFT calculations of CuPc on Cu(111). The left (right) column displays the ground state (rotated state) for three positive sample bias voltages.

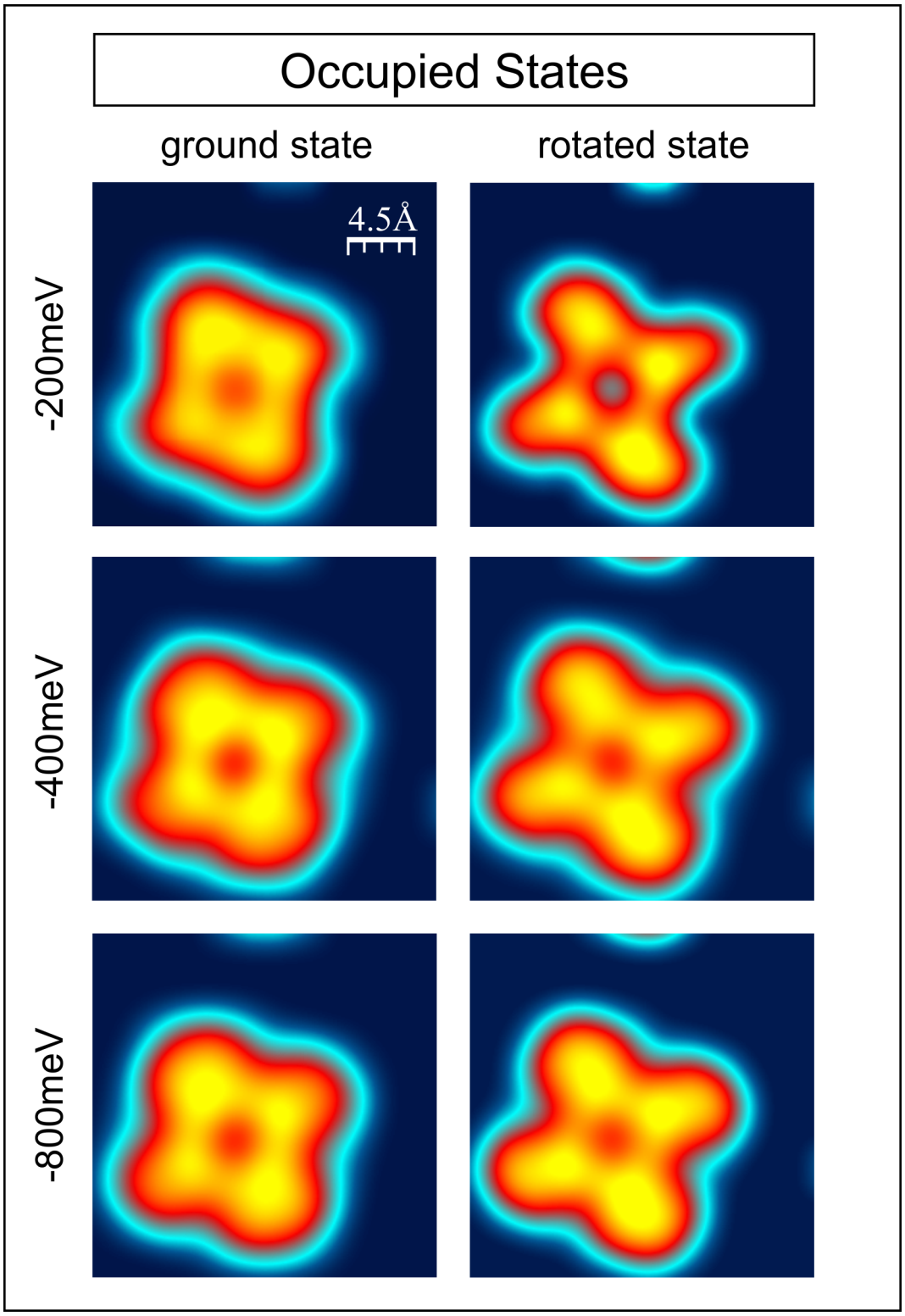

Figure 7.5.: Simulated occupied states STM images resulting from a Tersoff-Hamann treatment of the DFT calculations of CuPc on Cu(111). The left (right) column displays the ground state (rotated state) for three negative sample bias voltages.

7.4. Projected Density of States

The projected density of states (PDOS) is a function of the electron energy that represents the density of electronic states (DOS) per unit energy weighted by the contribution of a chosen orbital on the total electronic structure. In this way, the DOS can be analyzed in terms of different orbitals that are chosen by their physical meaning.

Here, we take the orbitals of the free molecule (from gas phase calculations) evaluated for the geometrical conformation of the adsorbed molecule. In this way, only the electronic hybridization of the molecular and substrate orbitals is considered in the PDOS. If the PDOS of a given orbital shows a very sharp peak, the chosen orbital is a good representation of an eigenstate of the system, since its energy is well-defined. On the other hand a very broad PDOS structure means, that the chosen orbital has little to do with the actual electronic structure of the system. In the case of weakly bound species, the molecular orbitals are expected to be good approximations to some of the states of the combined molecule+substrate system, hence sharp peaks are expected. In strongly chemisorbed systems however, the covalent bonds lead to strongly hybridized states that lead to a broad PDOS. In this way, the PDOS gives direct information about the type of molecular binding, but it also gives information on the charge transfer by showing whether the structures originating in the molecular orbitals are above or below the substrate's Fermi energy. If the projection on an initially empty gas phase orbital leads to a PDOS below the Fermi level, it can be concluded that there is charge transfer from the substrate into the molecule, since the electronic structure of occupied levels has a strong character of the initially empty orbital.

The resulting PDOS as a function of energy is plotted in Fig. 7.6 for the molecular orbitals indicated in the color-coded legend. The calculation was carried out for both, the ground state adsorption configuration (perfect alignment of one molecular symmetry axis with a densely packed row of copper atoms (0°)) and for the second configuration, rotated by 7°.

As a result of a Bader charge analysis [188], a net charge transfer of about two electrons from the substrate to the molecule was found. The formerly unoccupied molecular states become partially filled when adsorbed onto the copper surface.[2] Furthermore, it can clearly

[2] In literature, 'former lowest unoccupied molecular orbitals' that are actually (partially) filled under adsorption, are sometimes called 'FLUMO' or 'F-LUMO'. In this work, the acronym LUMO is retained despite the fact, that the two LUMO orbitals are not completely unoccupied on Cu(111).

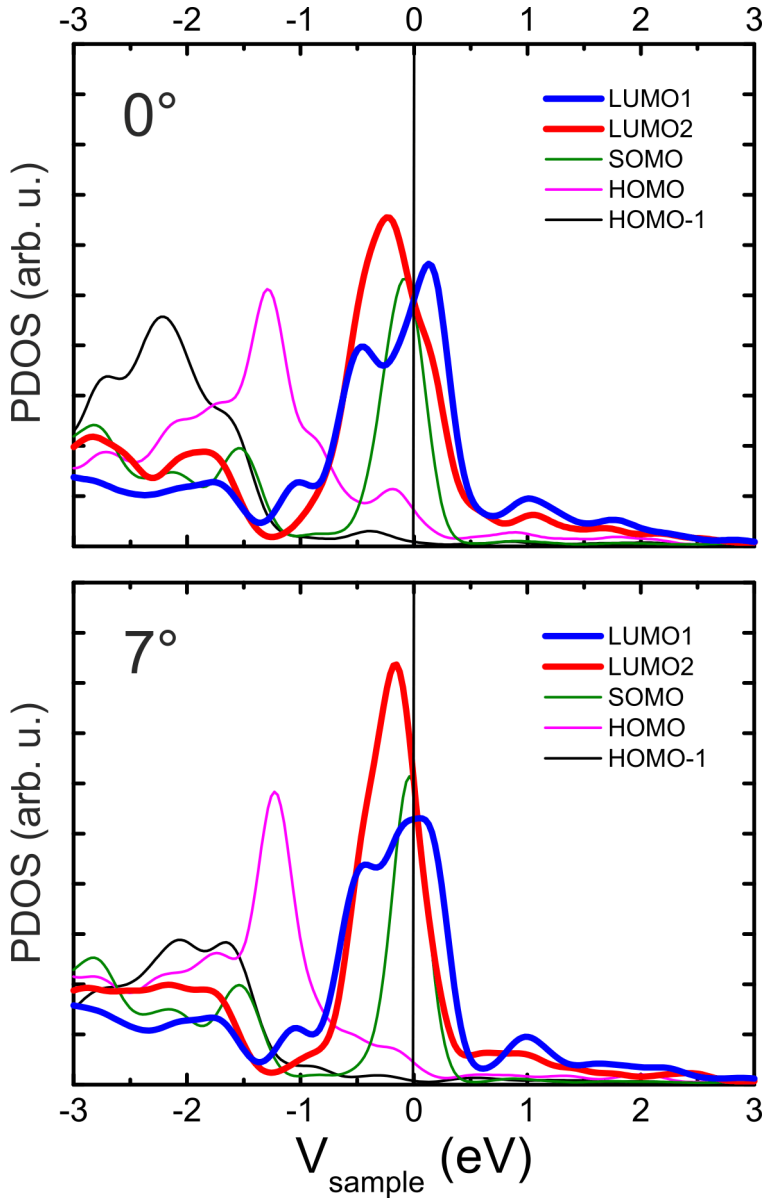

Figure 7.6.: The projected density of states (PDOS) as a function of sample bias voltage for CuPc on Cu(111) for the adsorption configuration in alignment with a densely packed row of substrate atoms (0°) and for the rotated state, with an angle of 7°. The LUMO orbitals are partially filled upon adsorption and dominate the electronic structure of the system (bold red and blue lines). Data published in the supplementary information of reference [143] (available online).

be seen in the plots (Fig. 7.6), that the degeneracy of the two LUMO orbitals is lifted upon adsorption: For the zero degree calculation the bold red and blue lines differ near the Fermi level (zero bias voltage). The LUMO orbitals dominate the electronic structure close to Fermi level, with the majority of their spectral weight at the occupied states regime. The distribution of the LUMO1 is localized along the [-110] direction of the Cu(111) surface. The HOMO orbital is found at -1.25eV and the HOMO-1 is found at -2.2eV below the Fermi level. All spectra appear broadened due to the interaction with the substrate plus a numerical broadening of 0.25eV, which was added to artificially create more realistic orbital shapes.

When the density of states for the rotated configuration is projected onto the gas phase molecular orbitals, the spectral weight of the LUMO2 orbital below Fermi level is slightly enhanced, whereas the LUMO1 orbital appears rather unchanged. The HOMO orbital does not shift in energy, but appears less broadened as compared to the zero degree calculation. The HOMO-1 loses its formerly pronounced peak and appears washed out after rotation.

7.5. Rotational Schrödinger Equation

Once the PES (Fig. 7.2) resulting from several DFT calculations is available, it not only serves as illustrative material proving the existence of side wells, but the Schrödinger equation can be given. The numerical solution yields the rotational levels for the CuPc molecule that rotates in the potential.

To accomplish this task, several simplifications are needed. We start with the Schrödinger equation:

$$-\frac{\hbar^2}{2I}\left(\nabla^2 + V(\vec{r},t)\right)\ \Psi(\vec{r},t) = E\,\Psi(\vec{r},t). \tag{7.1}$$

The momentum of inertia of the CuPc molecule, *I*, with respect to its center, $\vec{r_0}$, is needed. It is calculated by summing up the distances of every atom to the central copper atom weighted by the atomic masses of the respective elements m_i (7.2)

$$I = \sum_{i=1}^{N} m_i(\vec{r_i} - \vec{r_0})^2. \tag{7.2}$$

Then, we use the ∇^2 operator in cylindric coordinates:

$$\nabla^2 f(r,\psi,z) = \frac{1}{r}\frac{\partial}{\partial r}\left(r\frac{\partial f}{\partial r}\right) + \frac{1}{r^2}\frac{\partial^2 f}{\partial \phi^2} + \frac{\partial^2 f}{\partial z^2}, \tag{7.3}$$

and restrict the Schrödinger equation to one dimension, that is, the rotational degree of freedom, ϕ, of the molecule within the surface plane. The potential, V, within eq. (7.1) is replaced by a polynomial fit-function describing the one-dimensional PES, $V(\phi)$.

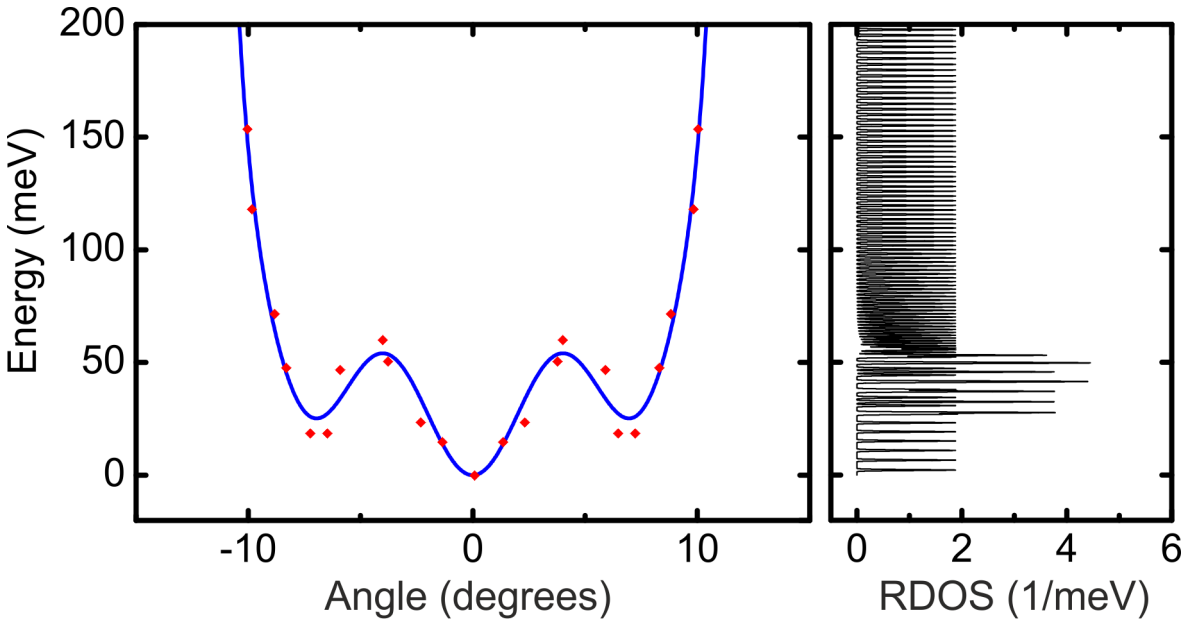

Figure 7.7.: The potential energy surface (left) as presented in section 7.1 together with the rotational levels (right) resulting from a one-dimensional Schrödinger equation for the in-plane rotation of CuPc on Cu(111).

The numerical solution of eq. (7.1) provides the rotational levels of the molecular rotation in the potential given in Fig. 7.2. The levels are plotted in Fig. 7.7 next to the PES to facilitate the assignment with the shape of the potential. The first levels are roughly equally spaced with rotational energy quanta of 3meV. With increasing energy, it can be seen how the rotational density of states (RDOS) shows the double degeneracy of states as soon as the energy reaches the potential side wells. When the rotational energy exceeds the side wells, this degeneracy decays and every level is occupied with the same rotational density as in the low-lying ground state regime.

7.6. Resonant Angular Momentum Transfer - Simulation of Excitation Maps

The excitation of the rotational motion reported above proceeds via resonant scattering of inelastically tunneling electrons at the molecular orbitals. The mechanism of resonant angular momentum transfer from the electrons to the molecule is discussed in detail in section 8.7.

In this chapter, the numerical approach based on the above DFT results will be depicted, paving the way for a simulated excitation map which will be compared to the rate images measured by scanning noise microscopy.

The results presented here were published in [143]. Further details on the theoretical treatment will be summarized in an additional publication based on this chapter in co-operation with and under supervision of Nicolás Lorente[3] and Jean-Pierre Gauyacq[4], who developed the presented approach [181].

Nomenclature

An electron will be transferred from an initial state, $|\psi_i\rangle$ with the energy, ϵ_i, to a final state, $|\psi_f\rangle$, with the energy ϵ_f. The process may be inelastic such that $\epsilon_i \neq \epsilon_f$. The excess energy is transferred to a rotational degree of freedom of the target molecule. The excited rotational level will, in this case, be one of those resulting from the solution of the one-dimensional Schrödinger equation for the potential energy surface in paragraph 7.5. When the molecule changes its rotational state from $|R_0\rangle$ to $|R_n\rangle$, the energy stored in the excitation equals $E = E_n - E_0$, where E_0 and E_n are the initial and final rotational state energies.

The full system is initially described by the state $|i\rangle = |R_0\rangle \otimes |\psi_i\rangle$ with an energy given by $E_i = E_0 + \epsilon_i$. The final state is represented by $|f\rangle = |R_n\rangle \otimes |\psi_f\rangle$ with the energy $E_f = E_n + \epsilon_f$, respectively.

[3] Centre d'Investigació en Nanociència i Nanotecnologia (CSIC-ICN), Campus UAB, E-08193 Bellaterra, Spain.

[4] Institut des Sciences Moléculaires d'Orsay, CNRS-Université Paris-Sud, UMR 8214, Bâtiment. 351, Université Paris-Sud, F-91405 ORSAY Cedex, France.

Fermi's Golden Rule and the T-Matrix

The excitation rate (probability of transition per unit time) is given by the extension of *Fermi's Golden Rule* (FGR) to all orders. As FGR only contains the connecting potential to lowest order, the transition rate will be expressed in terms of an operator, the T-matrix, that includes higher orders of the connecting potential:

$$T_{i,f} = \langle \psi_i | \hat{T} | \psi_f \rangle. \tag{7.4}$$

In general, it is difficult to determine the connecting potential, i.e. the T-matrix for a given position of the molecule. It depends parametrically on the molecular rotational degree of freedom, here expressed by the angle, φ.

Tersoff-Hamann Approximation

The *Tersoff-Hamann Approximation* [30, 31] allows us to express the T-matrix proportional to the substrate's final wave function evaluated at the position of the tip apex, $\vec{r}_0$:

$$T_{i,f} = \langle \psi_i | \hat{T} | \psi_f \rangle \approx C \psi_f(\varphi, \vec{r}_0), \tag{7.5}$$

with C being a constant. $\hat{T}$ is inserted into the following expression for the transition rate (inverse time) as follows from the extended FGR:

$$\frac{1}{\tau_{ine}} = \frac{2\pi}{\hbar} \sum_{i,f} |T_{i,f}|^2 \delta(E_i - E_f). \tag{7.6}$$

Each quantity may now be replaced by its value:

$$\begin{aligned} \frac{1}{\tau_{ine}} &= \frac{2\pi}{\hbar} \sum_{i,f} \sum_{n > N_R} f_{tip}(\epsilon_i)[1 - f_{sub}(\epsilon_f)] \\ &\times |\langle R_0 | \langle \psi_i | \hat{T} | \psi_f \rangle | R_n \rangle|^2 \delta(E_0 + \epsilon_i - E_n - \epsilon_f), \end{aligned} \tag{7.7}$$

with f_{tip} and f_{sample} representing the Fermi functions of tip and sample and $\hbar$ being the reduced Planck constant. The state N_R is the first rotational level that needs to be excited to cause a molecular rotation with a probability clearly above zero. The

direction of the tunneling current can be set by the signs of the Fermi factors. Since the experiment observes electrons flowing from the occupied states of the sample, the product $f_{tip}(\epsilon_i)[1 - f_{sub}(\epsilon_f)]$ is used, where the tip's Fermi energy is displaced by eV with respect to the substrate's Fermi energy, ϵ_F. V represents the STM tunneling bias.

Zero Kelvin Approximation

The expression can be further simplified by implying the zero Kelvin approximation for the Fermi distribution function, which is a Heaviside theta function, $\Theta(\epsilon_F - \epsilon)$. In the same step, the Tersoff-Hamann approximation (eq. (7.5)) is used, so eq. (7.7) can be written as

$$\begin{aligned} \frac{1}{\tau_{ine}} &= \frac{2\pi}{\hbar} \sum_{i,f} \sum_{n>N_R} \Theta(\epsilon_F + eV - \epsilon_i)\Theta(\epsilon_f - \epsilon_F) \\ &\times |C|^2 |\langle R_0|\psi_f(\varphi, \vec{r}_0)|R_n\rangle|^2 \delta(\epsilon_i - \epsilon_f - E). \end{aligned} \tag{7.8}$$

Homogeneous Tip Approximation

The tunneling tip, i.e. the initial state, is still part of the expression. For tunneling tips made of a material with electronic properties which can be summarized in a density of states function, $D_{tip}(\epsilon)$, using that

$$\sum_i = \int D_{tip}(\epsilon) d\epsilon,$$

we can abandon the summation over i. Later, when the inelastic fraction will be calculated, D_{tip} will cancel out completely.

Excitation Rate

The final expression for the excitation rate over the rotational barrier reads

$$\begin{aligned} \frac{1}{\tau_{inelastic}} &= \frac{2\pi}{\hbar} \sum_{n>N_R,f} D_{tip}(\epsilon_f + E)|C|^2 \\ &\times |\langle R_0|\psi_f(\varphi, \vec{r}_0)|R_n\rangle|^2 \Theta(\epsilon_F + eV - \epsilon_f - E)\Theta(\epsilon_f - \epsilon_F). \end{aligned} \tag{7.9}$$

The Inelastic Fraction

Based on this result, it is possible to express the *inelastic fraction* of the tunneling current consisting of only those electrons that provoked a molecular rotation. The key advantage is that this value is observable in SNM experiments. The total tunneling current, I, is given by $I = e \times \frac{1}{\tau_{total}}$, where $\frac{1}{\tau_{total}}$ is given by a similar expression to eq. (7.9), except that the total current has no restriction in the sum over n:

$$\begin{aligned} \frac{1}{\tau_{total}} &= \frac{2\pi}{\hbar} \sum_{n,f} D_{tip}(\epsilon_f + E)|C|^2 \\ &\times |\langle R_0|\psi_f(\varphi, \vec{r}_0)|R_n\rangle|^2 \Theta(\epsilon_F + eV - \epsilon_f - E)\Theta(\epsilon_f - \epsilon_F). \end{aligned} \tag{7.10}$$

The *inelastic fraction*, η, is straight-forwardly given by the ratio of inelastic to elastic current. It is noteworthy that all unknown constants stemming from the Tersoff-Hamann approximation as well as the tip's density of states cancel out. As a function of the tip location, $\vec{r}_0$, and the tunneling bias, we get:

$$\eta(\vec{r}_0, V) = \frac{\sum_{n>N_R,f} |\langle R_0|\psi_f(\varphi, \vec{r}_0)|R_n\rangle|^2 \Theta(\epsilon_F + eV - \epsilon_f - E)\Theta(\epsilon_f - \epsilon_F)}{\sum_{n,f} |\langle R_0|\psi_f(\varphi, \vec{r}_0)|R_n\rangle|^2 \Theta(\epsilon_F + eV - \epsilon_f - E)\Theta(\epsilon_f - \epsilon_F)}. \tag{7.11}$$

Large Bias Approximation

One further simplification can be carried out for the assumption of a tunneling bias much larger than the typical rotational energies. In this case, the product of the Θ functions will always equal one and the denominator becomes:

$$\begin{aligned} \sum_{n,f} & |\langle R_0|\psi_f(\varphi, \vec{r}_0)|R_n\rangle|^2 = \\ \sum_{n,f} & \langle R_0|\psi_f(\varphi, \vec{r}_0)|R_n\rangle\langle R_n|\psi_f^*(\varphi, \vec{r}_0)|R_0\rangle = \\ \sum_{f} & \langle R_0||\psi_f(\varphi, \vec{r}_0)|^2|R_0\rangle, \end{aligned} \tag{7.12}$$

since $\sum_n |R_n\rangle\langle R_n| = \hat{1}$ is the closure relation.

We get the following expression for the *inelastic fraction*:

$$\eta(\vec{r}_0, V) = \frac{\sum_{n>N_R,f} |\langle R_0|\psi_f(\varphi, \vec{r}_0)|R_n\rangle|^2 \Theta(\epsilon_F + eV - \epsilon_f - E)\Theta(\epsilon_f - \epsilon_F)}{\sum_f \langle R_0||\psi_f(\varphi, \vec{r}_0)|^2|R_0\rangle}. \quad (7.13)$$

The denominator is basically a constant, since the sum extends over all possible electronic states, giving another closure relationship. However, this constant is important to correctly normalize the inelastic fraction.

The *inelastic electron* fraction does not yield the number of electrons that actually rotate the molecule, but it refers to the fraction of electrons that excite the molecule over a certain rotational level, N_R.

In order to estimate the fraction of excitations that will successfully rotate the molecule to one of the side wells of the PES, for example the righ well, we will calculate the so called 'branching ratio', p_R, as follows. The value of the branching ratio is based on the geometric evaluation of the weight of the rotational wavefunctions (eq. (7.14)). The weights of the wavefunctions in the angular regime of one side well are integrated for an angular interval from a critical angle φ_c to 15°. The lower integration limit represents the maximum of the barrier of the PES. By inspection of the PES, $\varphi_c = 5°$ was chosen for this estimation. The upper limit reflects the fact, that the molecule is not allowed to rotate freely, but within a ±15° rotational PES for the frustrated rotation. Angles beyond this PES belong to an equivalent adsorption configuration aligned with another symmetry axis of Cu(111). The probability of the trapping in the left well can be assumed to be similar.

The fraction of molecules excited to a given excited rotational level n that is trapped in one of the side wells is then given by:

$$p_R(n) = \int_{\varphi_c}^{15°} |R_n(\varphi)|^2 d\varphi / \int_{-15°}^{15°} |R_n(\varphi)|^2 d\varphi. \quad (7.14)$$

Figure 7.8 shows the de-excitation probability that leaves the molecule in one of the rotated configurations (also called 'the branching ratio'). For small energies, the system cannot be excited into one of the side wells and yet, no probability for a de-excitation into one of the side wells can be found. For energies in the range of the barrier height, alternating probabilities for all three states can be found. The result of this consideration

can be seen for high energies within the figure: The branching ratio approaches the value of $1/3$ for energies clearly above the barrier height.

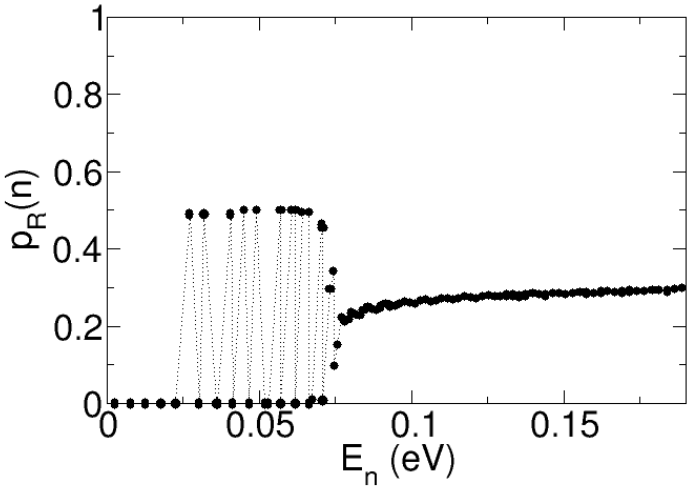

Figure 7.8.: The probability of de-excitation into one of the rotated states or: 'the branching ratio' p_R as a function of energy. For the very small energies, the molecule cannot be rotated. For higher levels, but still below the barrier (70meV), the system is alternatingly found in one of the three states. For energies above the barrier however, the de-excitation probability is found to approach the value of $\approx 1/3$. This number coincides with the model of a heavily excited rotor in the high-frequency limit, as stated in the experimental section, where the duty cycle saturates at $1/3$. The figure is taken from ref. [181].

Final Expression for the Inelastic Fraction

Finally, the inelastic fraction η_{rot} of electrons that successfully rotate the molecule is given by:

$$\eta_{rot}(\vec{r}_0, V) = \frac{\sum_{n>N_R,f} 2p_R(n)|\langle R_0|\psi_f(\varphi,\vec{r}_0)|R_n\rangle|^2\Theta(\epsilon_F + eV - \epsilon_f - E)\Theta(\epsilon_f - \epsilon_F)}{\sum_f \langle R_0||\psi_f(\varphi,\vec{r}_0)|^2|R_0\rangle}. \tag{7.15}$$

In the following, the inelastic fraction, η_{rot}, will be referred to as the excitation *efficiency*. It depends on the position of the tunneling tip ($\vec{r}_0$) and on the bias voltage, V. It is important to emphasize that the excitation is independent of the resonance lifetime. This is a result of the *sudden approximation* by Abram and Herzenberg which applies when the resonance lifetime is short compared to one rotational period [189].

Access to Density of States Information

To compare the experimental SNM data, it is interesting to show that the derivative of the efficiency with respect to the bias yields direct information on the density of states. We approximate the sum over the substrate's electronic structure by an integral weighted by the DOS and in addition, assume that the bias is larger than the rotational energies. Hence, the derivative of eq.(7.15) can be calculated:

$$\begin{aligned}\frac{\partial \eta_{rot}(\vec{r}_0, V)}{\partial V} &\approx \frac{eD_{sub}(\epsilon_F + eV)\langle R_0||\psi_f(\varphi, \vec{r}_0)|^2|R_0\rangle}{\sum_f \langle R_0||\psi_f(\varphi, \vec{r}_0)|^2|R_0\rangle} \\ &\propto D_{sub}(\epsilon_F + eV)\langle R_0||\psi_f(\varphi, \vec{r}_0)|^2|R_0\rangle.\end{aligned} \tag{7.16}$$

Hence, we assumed that $2p_R(n)$ is a constant, allowingthe use of the above closure relation. The result shows that for the very localized function R_0, the derivative of the efficiency with respect to the bias $\frac{\partial \eta_{rot}(\vec{r}_0,V)}{\partial V}$ is proportional to the local density of states at the chosen bias voltage.

Numerical implementation

Despite the simplification resulting from the Tersoff-Hamann approximation, the numerical implementation of the *inelastic fraction*, η_{rot} (eq. (7.15)) remains challenging. The main difficulty is the φ-angular integration $\langle R_0|\psi_f(\varphi, \vec{r}_0)|R_n\rangle$ which incorporates all Kohn-Sham eigenfunctions of the DFT calculation. Furthermore, it has to be performed for each spatial position, $\vec{r}_0$. As the slab model for the studied system is rather large in terms of DFT simulations, data files over 20 GB have to be dealt with for each angle, φ. The integration becomes even more difficult with increasing n, because the

number of nodes of the $R_n(\varphi)$ increases. This can be directly seen for the exemplary wave functions plotted in Fig. 7.9. The number of bands included in the simulation is fixed by setting a sample bias voltage, and for the present calculation, $-0.5V$ was chosen.

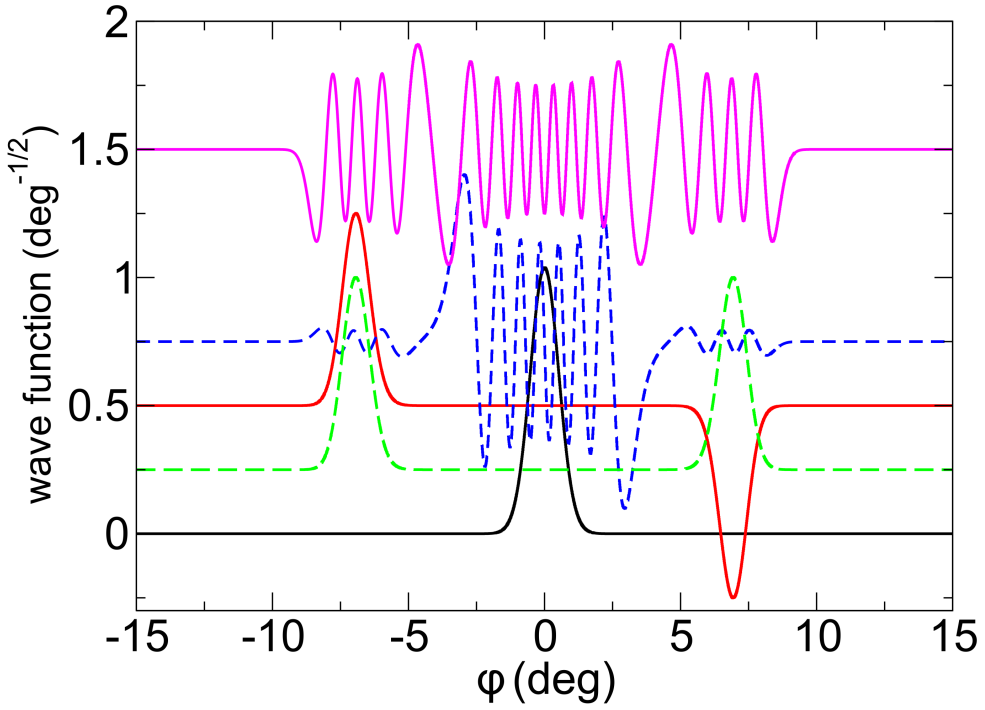

Figure 7.9.: Rotational wavefunctions for the potential energy surface shown in Fig. 7.2. The ground state, R_0, is the black curve. The local minimum-energy state, R_7 for the side well potential is shown in green and has been arbitrarily displaced. The basically degenerate second well state is shown in red, further displaced. The first state leading to a significant rotational excitation probability corresponds to R_{25}, shown in blue. The magenta curve corresponds to the rotational state R_{33} which has an energy well above the barrier.

As an approximation to the electronic wave function, $\psi_f(\varphi, \vec{r}_0)$, the DFT Kohn-Sham eigenfunctions are used. $\psi_f(\varphi, \vec{r}_0)$ is assumed to be a continuous function of φ that can be evaluated via interpolation among a set of particular points. Fig. 7.9 shows the

extension of $R_0(\varphi)$. For angles beyond $\pm 2\circ$, $R_0(\varphi)$ is negligible. Hence, the following ensemble of points was chosen for linear interpolation:

$$\varphi_0 = -15.0^\circ,\ \varphi_1 = -2.0^\circ,\ \varphi_2 = -1.5^\circ,\ \varphi_3 = -1.0^\circ,\ \varphi_4 = 0.0^\circ,$$
$$\varphi_5 = 1.0^\circ,\ \varphi_6 = 1.5^\circ,\ \varphi_7 = 2.0^\circ,\ \varphi_8 = 15.0^\circ. \tag{7.17}$$

The interpolation of the wave function, $\psi_f(\varphi, \vec{r}_0)$, results in the following expression for the matrix element from eq. (7.15):

$$\langle R_0|\psi_f(\vec{r}_0;\varphi)|R_n\rangle \approx$$
$$\int_{\varphi_0}^{\varphi_1} d\varphi R_0^*(\varphi) \left\{ \frac{\varphi-\varphi_0}{\varphi_1-\varphi_0} \left[\psi_f(\vec{r}_0;\varphi_1) - \psi_f(\vec{r}_0;\varphi_0)\right] + \psi_f(\vec{r}_0;\varphi_0) \right\} R_0(\varphi)$$
$$+ \ldots + \int_{\varphi_7}^{\varphi_8} d\varphi R_0^*(\varphi) \left\{ \frac{\varphi-\varphi_7}{\varphi_8-\varphi_7} \left[\psi_f(\vec{r}_0;\varphi_8) - \psi_f(\vec{r}_0;\varphi_7)\right] + \psi_f(\vec{r}_0;\varphi_7) \right\} R_0(\varphi) \tag{7.18}$$

Map of Excitation Efficiency

The theoretical treatment of the excitation of the molecular rotation provides a map of the spatial distribution of the inelastic fraction of electrons triggering the molecular switch. The probabilities of all states above the rotational barrier are summed up and a branching ratio (explained above) of $p_R = 1/3$ is applied for the de-excitation into a side well of the PES from Fig. 7.2.

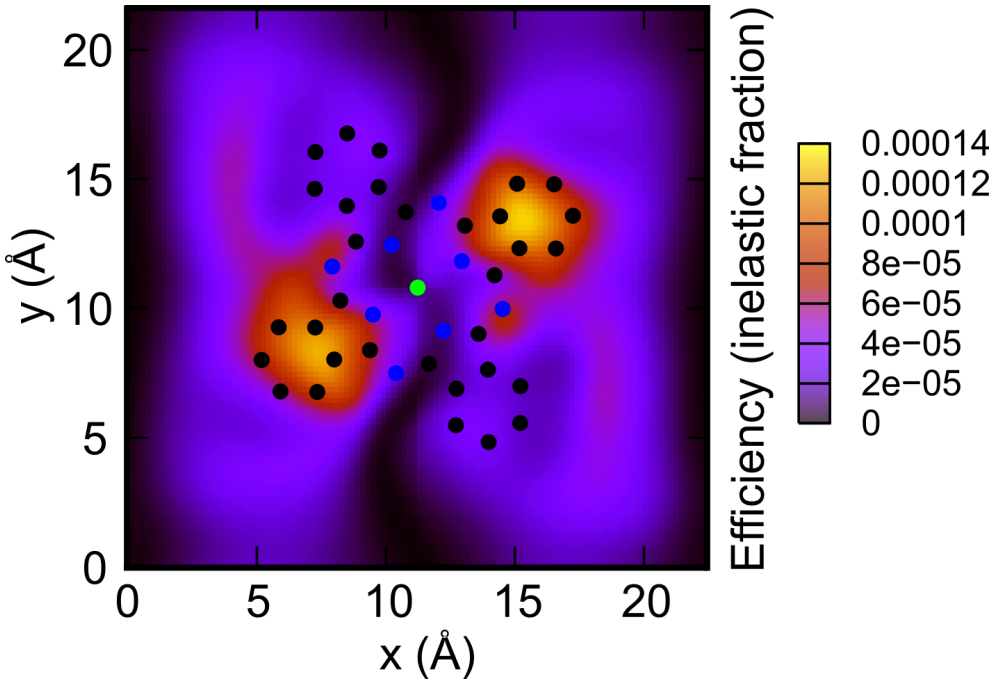

Figure 7.10.: Inelastic fraction of electrons exciting the molecular rotation of CuPc on Cu(111). The probabilities of all states above the rotational barrier are added and a factor of $1/3$ is used for the branching ratio of the de-excitation into a side well of the PES [143].

The resulting excitation map presented in Fig. 7.10 shows the inelastic fraction of electrons which successfully provoke a rotational motion. The map clearly exhibits maxima in the excitation efficiency located at the two benzene rings aligned with the [1-10] direction of the substrate. In the center and at the inactive lobes of the molecule the simulated excitation probability vanishes.

To guide the eye, a schematic model of CuPc is given as an overlay with the green dot representing the central Cu atom, blue dots being the N atoms and black dots representing

the C atoms, respectively. The H atoms are not plotted.

The maximum value of the color coding corresponds to an efficiency of approximately 2.5×10^{-5} for a tunneling bias of -0.5V.

Due to artifacts from the periodic boundary conditions of the DFT slab model, some unphysical maxima occurred far off the molecule at the borders of the unit cell. A gaussian function centered at the molecular Cu atom suppresses these meaningless data and thus prevents distracting features.

8. Discussion

8.1. The Information on Dynamics is in the Noise

When CuPc molecules were initially studied on the Cu(111) surface with the low-temperature STM at 7K, their partially fuzzy appearance in the STM topography could not be understood at first glance. Although the overall image quality was high (Fig. 6.1), zoomed in images of individually adsorbed molecules on the clean terraces of Cu(111) always revealed that two of the four molecular lobes (benzopyrrole rings) exhibit noise when probing the occupied states. An example is shown in Fig. 8.1, where the gray arrow marks a noisy lobe. The noisy lobes of the molecules were found on an axis perpendicular to the [-110] direction of the substrate (Figs. 6.2, 6.4 and 6.8a+b).

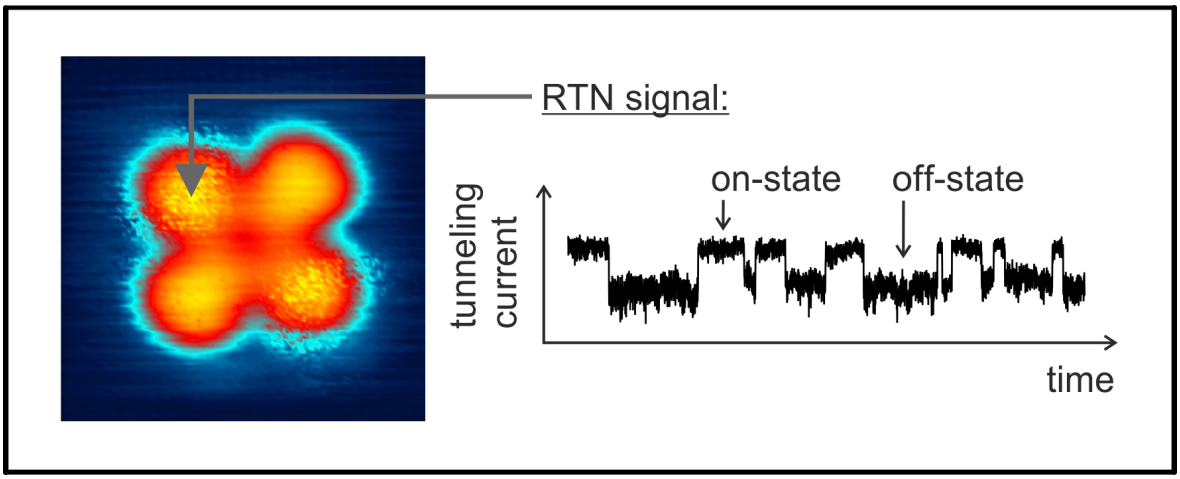

Figure 8.1.: The noisy appearance of CuPc on Cu(111) in STM topography at low temperatures. When the tunneling tip is placed over a noisy part of the molecule, the tunneling current is found to jump between two discrete levels. The signal could be identified as random telegraph noise (RTN); $2.3 \times 2.3nm^2, V_{sample} = -1.5V, I = 100pA, T = 7K$.

For the following discussion of experimental indications on the dynamical process that causes the jumps in the tunneling current it is noteworthy that the noisy area in the STM images actually exceeds the topographic edges of the molecule slightly (Fig. 8.1).

The jumps in the tunneling current occur between two discrete levels within the limits of experimental accuracy (Fig. 8.1). We name the high current state the 'on-state' and the low current state the 'off-state'. The residence times in the on- and the off-state are in the regime of milliseconds for typical scan parameters (e.g. 1V and 100pA). In order to determine the type of noise the residence times of the two levels are measured and sorted into 'time bins'. The resulting distribution of the residence times τ_{on} and τ_{off} (Fig. 6.6) can be perfectly described by exponential decay functions. The system has constant probabilities for a current jump. However, they may differ for a jump up or down, resulting in two decay constants (Fig. 6.6). The conductance switching system has no memory; the observed noise is thus identified as random telegraph noise (RTN, see sec. 2.5).

It was not possible to temporarily disable the switching molecular system with the STM, for example by applying voltage pulses, or to reactivate it. However, the switching characteristics could be controlled by continuously ramping the sample bias voltage or the tunneling current (see SNS results in chapter 6.4).

To gain insight into the observed dynamic process, scanning noise microscopy (SNM) was developed. The technique was designed to measure the noise amplitude, the hopping rate, and the relative occupation of the on-state (duty cycle). These three SNM outputs can be used to fully describe the RTN signal in time average. The details, advantages, and shortcomings of our new technical approach are described in chapter 4.4 as well as in reference [124].

The SNM results yield unprecedented maps of the molecular switching characteristics with the same high lateral resolution as the STM topography (Fig. 6.8). In the rate image 6.8d for instance, the lateral detail of the rate map even exceeds that of the topographic data, which was measured simultaneously. Especially the edges of the two lobes in the rate map appear very sharp.

In addition, the data provide key indications on the relevant dynamic process. The

amplitude map replotted in Fig. 8.2 shows the height of the current jumps, i.e., it reveals the positions of maximum difference between the on- and the off-state. These are located at the edges of the active molecular lobes. A comparison of Fig. 6.8c and 6.8e shows that the main change upon switching does not occur at the center or the outer edge of the noisy lobes. The maxima of the amplitude are however found at the inner edges of the lobes, where the noise exceeds the molecule in the topographic images.

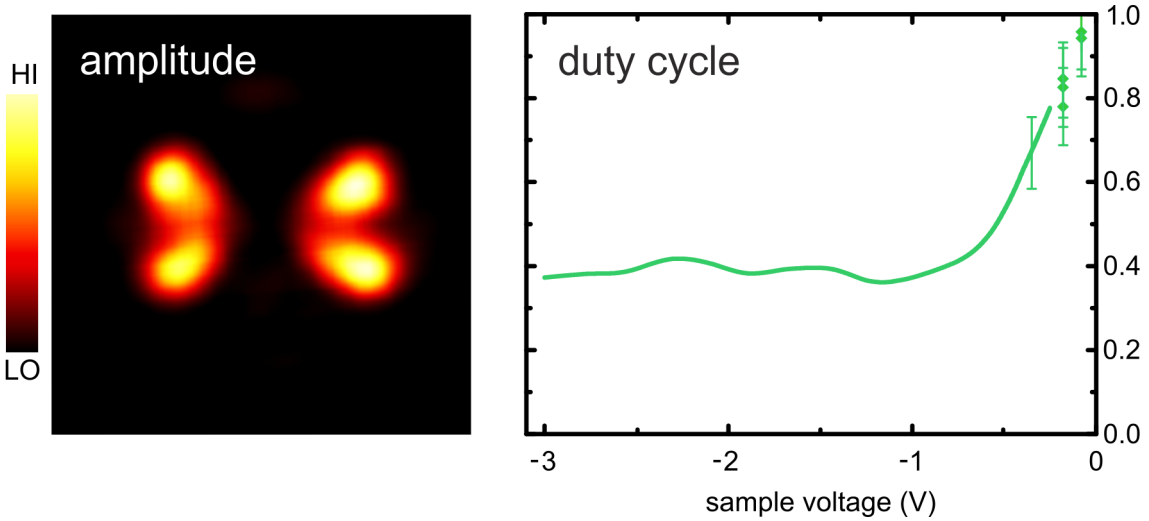

Figure 8.2.: Experimental indications leading to the model of a frustrated rotational motion of CuPc on Cu(111). Left: The amplitude map exhibits two maxima per fluctuating molecular lobe. Right: The duty cycle spectroscopy shows that probing the molecule close to the Fermi level leads to a preference of the on-state with a duty cycle of almost one. For increased sample bias, the duty cycle drops and saturates at about one third. The data were published in [143].

The inner edges of the lobes would highly affect the tunneling current for an in-plane rotation of the molecule by a small angle, as the tunneling tip would sense an enhanced interaction whenever the molecule rotates into the tunneling junction. When the molecule rotates away from the tip, the interaction would drop back to its initial state. The rotation angle must be small, as we can still image the molecule in its cloverleaf-like appearance, whereas a free rotation would result in a ring-shaped STM topography. Such a rotation by a small angle in between the equilibrium states of a given potential, that does not allow free rotation, is called frustrated rotation or libration. With this model in mind, one can roughly estimate a rotation angle of 5°-10° from the amplitude maps. A schematic view of

the rotation model is given in Fig. 8.3. The white arrow indicates the in-plane character of the molecular motion.

It is important to note that the observed rotational motion exhibits three states, one ground state with the molecule in perfect alignment to the densely packed rows of underlying substrate atoms (solid model in Fig. 8.3(b)) plus two states for a clockwise and counterclockwise rotation (transparent models in Fig. 8.3(b)). However, the two rotated states are symmetric and result in equivalent electronic properties and configurations. Therefore the two-level noise in the tunneling current can actually be caused by a three-state rotational switch.

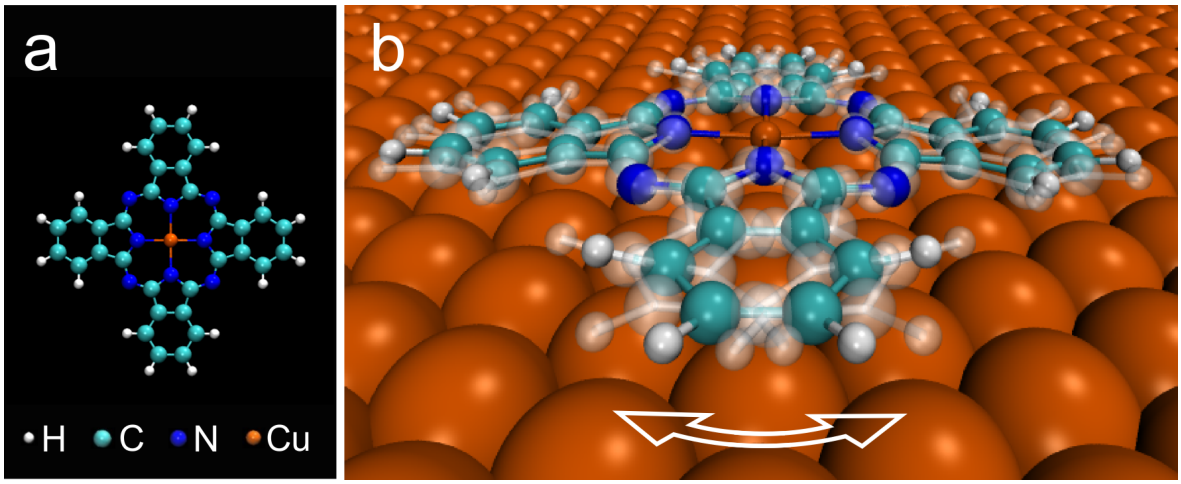

Figure 8.3.: (a) Ball-and-stick model of CuPc. (b) Sketch of the frustrated rotation of CuPc on Cu(111). The solid model represents the rotational ground state of the molecule in alignment with the substrate's [-110] (or equivalent) direction; the transparent models indicate the two rotated configurations [143].

The noise spectroscopy results support the proposed rotational motion of the molecule. The duty cycle measurement (replotted in Fig. 8.2) shows that close to the Fermi level the molecular switch is mainly found in its on-state (high current level). The on-state is the favored state in the absence of inelastic processes. This reflects in the fact that we find the duty cycle to be almost one in the limit of small current and small voltage. Hence we assign the on-state to the ground state of the molecular switch. When increasing the negative sample bias, the duty cycle is drastically reduced until it reaches roughly one third and saturates for high switching rates. For the frustrated rotation this means that

the saturation value of the duty cycle represents a three-state rotor in the limit of high excitation. In this case, the switch is continuously forced to change its position resulting in an average occupation of one third for each rotational state. The observed saturation value is thus another experimental indication corroborating the model.

To further understand the experimental results found so far, we discuss the result of a second spectroscopic experiment (scanning noise spectroscopy (SNS), section 6.4). The switching rate as a function of the tunneling current is analyzed in Fig. 6.10. For this type of experiment the height of the STM tip is ramped (z-spectroscopy) to vary the average tunneling current, whereas the SNM electronics characterize the RTN signal. The results show a linear response.

Therefore it can be concluded that the molecular switches are driven by the tunneling current via an one-electron process.

The slopes of the fits in Fig. 6.10 reveal the electron yield: Depending on the sample bias about every 10^{-7}th electron excites a switching event. We call this fraction of the electrons the 'inelastic fraction'. This term will be used in the discussion of the theoretical results.

Due to limitations of the measurement accuracy, the SNS measurement does not lead to accurate results for the limit of very small tunneling currents. Therefore the rate vs. current measurement was not shown for currents smaller than 40pA in Fig. 6.10. The reason for this shortcoming is that, for this specific conductance-switching system, the rate nearly vanishes (1Hz regime) for small currents (and small voltages) and thus the statistics evaluated by the SNM electronics (chapter 4.4) worsen. Hence a small finite background of the switching rate for tunneling currents extrapolated to zero cannot be excluded.
Under the assumption that the molecules rotate by a few degrees forth and back around a ground state configuration, the question arises, why there are only two active lobes observed in the experimental data. At this point we recapitulate the data acquisition of this scanning probe method. As stated, the switching events are triggered by the the tunneling electrons. At the same time, the STM experiment is based on the tip-sample interaction which manifests in the tunneling current. This means that the molecules are excited by the measurement. The excitation and detection of events are inseparable!

In consequence the SNM rate maps can be regarded as excitation maps. In fact, this term helps to point out that (black) areas exhibiting a rate of zero do not imply missing dynamics at these positions. Rather, black areas in the rate maps (e.g. Fig. 6.8b+d) are due to the local absence of excitation. Despite the two-fold appearance of CuPc in the rate maps, the model of rotating molecules assumes the rotation of the full molecule.

The planar phthalocyanine molecules (structural model: Fig. 8.3a) are very stable and the tetrapyrrole macrocycle is mechanically extremely stiff so that internal vibrational modes are by far higher in frequency (in the terahertz regime [190, 178]) than the Hz ... kHz reported here. Repeated molecular deformations (e.g. bending perpendicular to the surface) can consequently be ruled out as possible switching mechanism (see also the discussion on the symmetry reduction in section 8.3).

Similarly, the observed switching cannot be attributed to the temporary charging and discharging of the molecule, as it experiences a strong hybridization with the metal substrate which results in short lifetimes of the electronic states. Charges cannot be trapped at the highly conducting surface. The intense interaction with the copper surface is reflected in the large binding energy of about 4-5eV, as calculated in chapter 5.2 (table 5.1). We conclude that the current jumps must be attributed to molecular dynamics that stabilize the tunneling current at the two observed levels. The stabilization is long enough to be captured by STM [143].

During SNM scans the external scan parameters, like set current, voltage, scan speed, etc. are kept identical. Thus there has to be a reason why the impinging electrons can only excite the dynamical process at two out of the four molecular lobes. Interestingly topographic STM images also showed a two-fold symmetry of CuPc molecules when adsorbed to the Cu(111) surface (Fig. 6.1 and references [24, 23]). In the gas phase CuPc exhibits a perfect four-fold symmetry with two degenerate LUMO orbitals located on opposing pairs of benzopyrrole rings. When it adsorbs to the six-fold symmetric Cu(111) surface, the symmetry is reduced and the degeneracy of the LUMOs is lost due to the interaction with the substrate (charge transfer, see section 8.3).

We assign the 2-fold symmetry in the excitation maps to the electronic structure of the CuPc/Cu(111) complex. Obviously the LUMO orbitals, which are found at energies slightly below the Fermi level, are involved in the tunneling process. Due to the broken degeneracy the two orbitals exhibit different tunneling conductances. This explains that both, the

topography and the excitation probabilities, differ for the two pairs of molecular lobes.

We have now seen experimental indications originating from noise measurements that led to the deduction of a model of a frustrated rotational motion of CuPc on Cu(111). The experimental findings were discussed in this light. However, the excitation process itself, i.e., how the tunneling electrons interact with the orbitals, cannot be unraveled by the experiment alone. The following chapters will draw a consistent picture by completing and discussing the experimental findings in the context of the theoretical results.

8.2. How Theory Models the Experiment

The theoretical treatment of the studied system presented in chapter 5 started with the modeling of a slab model for the Cu(111) surface. The slab consists of four layers of copper atoms (a total number of 360 atoms). This large model was necessary to achieve a meaningful representation of the electronic properties of the surface. Especially the lateral extension of 22.5 Å $\times$ 21.6 Å offers enough space for a CuPc molecule to be adsorbed individually and prevents the self-interaction with its periodically repeated representations.

For the electron exchange and correlation functional, the local density approximation (LDA) was chosen. The motivation behind this decision is to benefit from the LDA 'overbinding' effect. One essential shortcoming of the LDA is that it produces too small binding distances. This is exploited by surface scientists with the aim to compensate the disregard of the van der Waals interaction to some extend. The DFT binding distances of adsorbates like organic molecules are represented by the LDA with acceptable precision despite the lack of van der Waals. Depending on the specific molecule and substrate combination, more decent results may be obtained using the LDA rather than the GGA (generalized gradient approximation, see section 3.5). This was recently proven by Mugarza *et al.* for the same molecule CuPc on the Ag(100) surface [97].

In order to compare our LDA results with those of a van der Waals corrected calculation, the binding distances between the molecular Cu atom and the Cu(111) surface as well as the molecular chemisorption energy were recomputed within DFT+D2 [104], as implemented in the VASP code. As can be seen in table 5.1, the adsorption energy calculated in LDA is 16% higher in the van der Waals corrected calculation and the adsorption distance is

8% larger [181]. It can be concluded that for the present adsorbate system, as well as for related systems [97], LDA compares fairly well with the more advanced DFT+D2 method.

The adsorption configuration of CuPc on Cu(111) was addressed by comparing the total energies of several possible adsorption sites within the local density approximation. The alignment of one molecular axis to a densely packed row of substrate atoms is known from the experiment as schematically drawn in Fig. 6.4. This knowledge was consequently applied to all adsorption configurations calculated (chapter 5.2). The favored adsorption configuration shown in Fig. 5.7 is a highly symmetric bridge configuration.

A similar result was found by Heinrich *et al.* for the closely related system cobalt phthalocyanine (CoPc) on Cu(111). Heinrich *et al.* used an adsorption-site-tracking technique realized by lateral manipulation of ad-atoms to unravel the exact adsorption configuration of the Pc molecule. This technique creates a lateral scale within the STM images by experimentally marking the hollow sites with the manipulated adatoms. Similar to this work Heinrich *et al.* confirmed their result with a DFT study in the local density approximation [191].

Cuadrado *et al.* performed a van der Waals corrected DFT study on the same system and also found the highly symmetric bridge position with the densely-packed row alignment as the most favorable adsorption configuration [179].

Thus our calculations are in good agreement with the experimental and theoretical findings by Heinrich *et al.* and Cuadrado *et al.* [191, 179].

8.3. Symmetry Reduction of CuPc on Cu(111)

Our STM studies on copper phthalocyanine (CuPc) on the Cu(111) surface reveal a symmetry reduction from the four-fold (C_4) symmetry in the gas phase to a two-fold (C_2) symmetry on the surface. One pair of opposing lobes appears brighter in the STM images (see for instance Fig. 6.1). This reduced symmetry compared to the molecular gas phase was published in a previous work by Karacuban *et al.* [24].

Similar observations were reported for numerous STM studies on metal-core phthalocyanine (MPc) molecules adsorbed on hexagonal surfaces: A reduced symmetry of adsorbed MPc molecules was first shown in STM and STS data by the Ho group for a fraction of the

observed CuPc molecules on an ultrathin Al_2O_3 film grown on NiAl(110) [164]. A C_2 symmetry was also found for CoPc, CuPc and FePc on Cu(111) [192, 24, 191, 179, 193]. The same is valid for SnPc [193] and H_2Pc [194] on Ag(111). In addition, a symmetry reduction was also reported for PbPc on HOPG measured by two photon photoemission experiments (2PPE) [195].

Possible explanations for the observed symmetry reduction of adsorbed CuPc are largely based on the electronic properties of MPcs [164]. In the gas phase, is exhibits two degenerate lowest unoccupied molecular orbitals (LUMOs), each of them localized at a pair of opposing benzopyrrole rings [196]. Upon adsorption this degeneracy is assumed to break due to the interaction of the molecule with the substrate. Once the LUMO levels are shifted with respect to each other as a consequence of charge transfer processes, their electronic properties differ. Both LUMOs are partially filled by charge donation from the substrate but the level alignment favors one LUMO in this process resulting in different levels of occupation.

However, a theoretical approval of this explanation was missing for the studied system and needed to be confirmed by our DFT study.
In general, it is not easy to capture the symmetry reduction of a large adsorbed molecule on a metal surface by DFT [197, 178, 179]. The energetic positions of molecular orbitals as calculated by DFT (Kohn-Sham orbitals) are usually misleading to some extend. Especially an energy shift with respect to the Fermi level is a typical shortcoming of DFT calculations while the positions of the orbitals relative to each other are represented more reliably.

Cuadrado *et al.* addressed the symmetry reduction for the system CoPc on Cu(111)via DFT calculations. They report that the symmetry reduction could only be reproduced when a van der Waals correction was applied [179].

In 2012, Baran and Larsson concluded from their DFT study, that the symmetry reduction found for SnPc on Ag(111) is due to 'electronic, rather than geometric effects' [180]. Upon adsorption the molecule interacts with the substrate via a charge transfer process, which results in the loss of the double degeneracy of the LUMO orbitals. Although the splitting is small, the two states will be unequally populated due to the different adsorption configurations of the molecular lobes with respect to the hexagonal substrate. This conclusion corroborates the explanation as described above. A bending of two molecular lobes with respect to the other was found to be negligible in this case of a non-planar MPc molecule as well (the Sn atom points out of the phthalocyanine plane)

[180].

In the framework of this work on CuPc/Cu(111), an almost perfect resemblance of theory and experiment is found.

This can be seen in the calculated STM images in chapter 7.3. The key features found in the STM images are clearly reproduced. Firstly, the center of the molecule appears as a dip. Secondly, the symmetry reduction of the adsorbed CuPc (as compared to its gas phase) was successfully reproduced: one pair of opposing benzopyrrole rings appears brighter than the other. This agreement of DFT and STM data confirms that the theoretical description captures the experimental findings from our STM experiments.

In addition, it can be concluded, that the symmetry reduction results from an electronic effect. A saddle-shape deformation of the molecule can be ruled out, since all carbon atoms of the four benzene rings are found within 10pm (picometers) around their average vertical binding distance of 0.21nm measured from the first layer of surface atoms. Not the absolute value of the binding distance is the subject of discussion here, but rather the result, that the planar structure of CuPc is not substantially distorted upon adsorption to the Cu(111) surface. More specifically, the pair of bright lobes is not significantly bent with respect to the surface. The bright lobe's C atoms have an average binding distance of 216pm as compared to 206pm for the dim lobes.

Our results coincide with the work by Mugarza *et al.*, who found that CuPc remains planar after the adsorption on the Ag(100) substrate [198] and with Baran and Larssons results for SnPc on Ag(111) [180].

It is noteworthy, that the two-fold symmetry of CuPc on Cu(111) is also observed by STM, when the molecules are self-assembled in a binary molecular monolayer composed of PTCDA and CuPc. This was shown earlier by the Möller group [168] and has been confirmed by recent work in our group [169]. Details on the latter study will be summarized in the appendix (B) of this thesis.

8.4. Potential Energy Surface

The hindered rotation of a molecule on a surface or in more general terms, the evolution of a dynamic physical system calls for the description by a potential energy surface (PES).

Every observed state will be represented by a potential well with barriers in between. These can be linked to the measured occupation levels and excitation probabilities.

The energy optimized DFT calculations that were necessary to obtain a one-dimensional PES for the rotation angle of the molecule were carried out within the local density approximation (LDA). Particularly, in the present case, the LDA (no van der Waals interaction included) is regarded as a meaningful approach to the adiabatic PES. Since the van der Waals force is a long-range interaction it is hardly affected by atomic details such as the small changes in the adsorption configuration under a small-angle in-plane rotation of the molecular axis. In addition, we have checked the applicability of LDA to the system CuPc/Cu(111) by comparing to a van der Waals corrected benchmark calculation. The result presented in table 5.1 on page 80 is, that the LDA binding distance as well as the chemisorption energy differ only by 8% and 16%, respctively [181].

Therefore, it can be concluded, that the LDA compares fairly well with the more elaborate DFT+D2 method - at least for the present system.

A similar conclusion is drawn for closely related systems in a recent publication by Mugarza *et al.*, who compare the center metal ion binding distances to the surface for FePc, CoPc, NiPc, and CuPc on Ag(100) for LDA, GGA and GGA plus van der Waals correction.

The results from an extensive set of DFT calculations (see 7.1) are displayed in Fig. 7.2 on page 105. It can be seen that the total minimum of the PES is located at a molecular rotation angle of zero degree. This means, that our angle dependent DFT study predicts the molecular axis to be aligned with one of the surface's densely packed rows (e.g. the [-110] direction). This geometric result is in perfect agreement to the experimental findings. In addition, two side-well states are found at $\pm 7^{\circ}$. These states coincide to the clockwise and anti-clockwise rotation of the molecule as expected from the proposed model in the previous discussion of the experimental results (see 8.1).

It is important to point out, that the DFT calculations include the geometry optimization for every data point of the PES. In this sense, the computational result of Fig. 7.2 represents an adiabatic PES. The curve follows equilibrium states and does not necessarily describe the physical PES that the molecule interacts with under rotation. For every rotated configuration of the simulations the molecular axis had to be fixed with respect to

the substrate to prevent the molecule from rotating back to its ground state. To achieve this, two N atoms were fixed laterally for a geometry optimization run. Subsequently, the calculations have been repeated without this constrain, now laterally fixing a perpendicular pair of N atoms. Thus, for every point of the PES, the ions were allowed to converge to a (local) minimum energy configuration, which is far from a realistic description.

Hence, any realistic excitation barrier can be expected to be higher than what is fitted to the calculated PES here. The physical motion may involve more complicated reaction coordinates than given by the adiabatic approximation, since the physical system does not have time for geometrical relaxation during rotation.

In addition, the polynomial fit to the PES is by no means physically justified, but rather reflects a certain uncertainty of the data points. The continuous fit has the tendency to underestimate the barrier height, as the maxima are washed out (see Fig. 7.2). Barrier heights of 50meV and 70meV are both consistent with our results. As a consequence of the smoothing effect of the polynomial fit to the data points, the barrier height of approximately 70meV is regarded more realistic and was used for the resonant scattering approach (sec. 7.6, 8.7).

The PES (Fig. 7.2) describes the studied system for rotation angles up to $\approx 10^\circ$. Due to the symmetry of the system, a rotation by 30° would result in an adsorption configuration equivalent to the 0° ground state. Unfortunately no number can be given to estimate the barrier height for a molecular rotation by 30° in between two of these alignments. The reason is, that the barrier height for a 30° rotation is given by the total energy of the most unfavorable rotation angle of 15°. This state was found to be completely unphysical. The VASP code could not converge the system for this situation due to large forces acting on the ions and therefore, a precise number for the total energy of the unphysical geometry would no be meaningful, anyway. Nevertheless, from our calculations we can conclude, that the height of a purely rotational barrier in between 0° and 30° is larger than 300meV. In addition, the STM experiments never observed a free rotation of CuPc on Cu(111). It can be concluded, that the PES triple well is very deep, thus protecting the molecule from rotational motions other than the libration described in this work. This is an information that could not be derived from the STM and SNM experiments, where a 30° rotation (or a rotation by multiples of 30°) would have led to identical levels of conductivity and thus would not be captured by our technique.

An analysis of the binding distances of the CuPc molecule before and after rotation yielded an interesting result for the N atoms (see Fig. 7.3 in sec. 7.2). While the outer four N atoms (aza) within the phthalocyanine molecule depart from the nearest neighbor atom in the surface when the molecule rotates, the contrary happens with the inner (pyrrole-)N atoms. In average, they approach a surface Cu atom for the first 7 degrees of an in-plane molecular rotation, until a minimum is found. From this rotation angle forward, the N-Cu distances increase again.

The coincidence with the angle of the PES side-wells suggests that the pyrrole N atoms have a stabilizing impact on the rotated (7 degree) configuration, while the aza N atoms determine the ground state alignment of the molecule with respect to the substrate. The extra chemical activity of the (inner four) pyrrole N atoms as compared to the outer N atoms has its origin in the electron lone pair [1] localized in these atoms which enhances the adsorbate-substrate interaction [178].

In real systems, the van der Waals interaction is expected to play an important role in the binding of phthalocyanines to metal substrates, especially determining the overall vertical binding distance. Nevertheless, the N atoms still dominate the rotational orientation of the molecules with respect to the high-symmetry axes of the substrate, since the long range van der Waals interaction does not affect the more localized interplay between e.g. the N atoms and their nearest neighbors in the surface.

8.5. The Factor of Two in the Tunneling Current Jumps

In chapter 7.3 simulated constant current STM images of CuPc on Cu(111) are presented. The agreement between the experimental results as well as the theoretical corroboration of the symmetry reduction has already been discussed. Moreover, the computational data could be analyzed by means of cross sections through the local density of states (LDOS) at a fixed tip height. This approach helps to explain the experimental factor of two in between the two current levels of the observed random telegraph noise.

The resulting LDOS cross sections are displayed in Fig. 8.4a. The red/blue curve corresponds to the on/off or in other words the aligned/rotated state. The tip height was chosen 8.1Å above the Cu(111) surface. This distance is assumed to represent a typical

[1] The 'lone pairs' mentioned here are two electrons in the outermost shell of the nitrogen atoms that are not involved in the chemical bonding within the molecule.

tip-surface distance in STM experiments. Fig. 8.4b+c show corresponding simulated STM images for a sample bias voltage of -0.4V. The energy is chosen arbitrarily, since the amplitude difference found experimentally can be described by the factor of approximately two independent of the bias voltage. The dotted lines in b and c indicate the position of the cross section analysis.

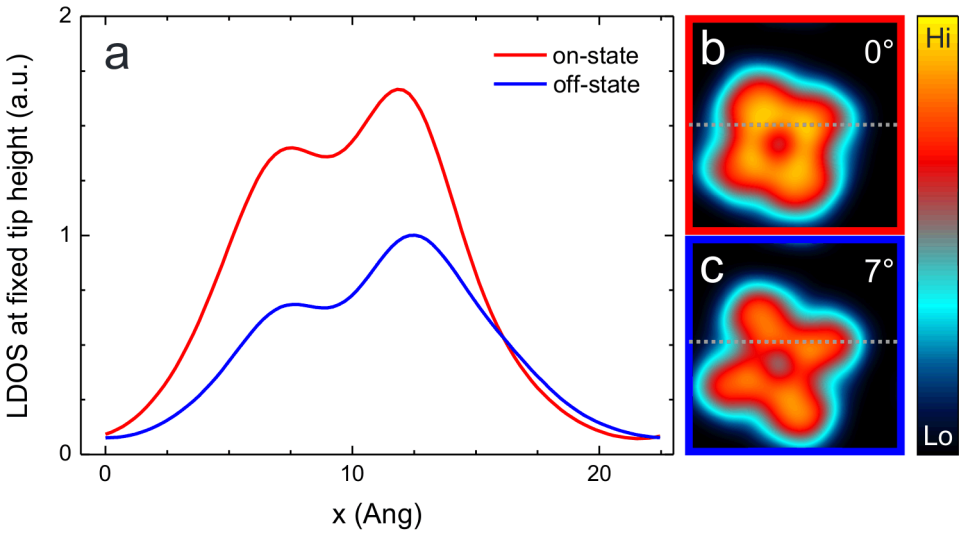

Figure 8.4.: The factor of two in between the telegraph noise current levels. (a) Two cross sections through the local density of states (LDOS) for the on-state (red) and the off-state (blue) at a fixed tip height (8.1Å) above the Cu(111) surface. The factor of two is reproduced in this theoretical result. The positions of the cross sections are shown in calculated STM images (b) and (c) for the two states as indicated by the colored frames. The on-state LDOS clearly exceeds the off-state by a factor between 1.5 and 2, in agreement to the experimental observation. The data was published in the supplementary information of reference [143].

The on-state exhibits a clearly enhanced local density of states as compared to the off-state. This is valid for the full length of the cross section. The slightly more protruded LDOS of the off-state at the right border of the molecule, as well as the slight shift of the blue line towards the right hand side, are due to the rotation of the molecule. This can be comprehended by the comparison of b and c.

The LDOS of the on-state exceeds the off-state value by a factor between 1.5 and 2. Thus, the LDOS cross-section analysis reproduces the experimentally observed factor of

two in the random telegraph noise amplitude with an outstanding agreement.

It is noteworthy, that the density of states projected to the gas phase molecular orbitals (PDOS) presented in chapter 7.4 indicated a higher density for the off-state. This can be explained by the slightly reduced adsorbate-substrate interaction after the molecular rotation from the ground state to the rotated state. This minor reduction of interaction is reflected in slightly larger binding distances for the rotated configuration found by the binding distance analysis in section 7.2. Interestingly, the more STM-oriented analysis of the LDOS cross-sections at constant height perfectly meets the experiment and elucidates the origin of this phenomenon. A careful study of the electronic structure of the adsorbate + substrate system by Nicolás Lorente confirmed that the on-state wavefunctions protrude further into the vacuum and enhance the tunneling current due to a stronger overlap with the wavefunctions of the tip. This explains the why the LDOS cross sections in a realistic tunneling distance perfectly reproduce the experimental findings while the PDOS yielded a higher density for the off-state ([178], supplementary information for ref. [143]).

Therefore it can be concluded, that the 'factor of two' is a consequence of the change of the electronic properties of the studied system under rotation [143].

In addition, a simple estimation highlights this result by excluding a molecular deformation. We have seen in the theoretical results section 7.2 that the noisy benzene rings bend upwards only by 2pm un rotation. We can now use the expression for the tunneling current from eqns. (2.10) and (2.6) for exemplary tunneling distances of 3Å ... 10Å and a work function of about 5eV [199]. We find, that a change in the tunneling distance of 2pm results in a change of the tunneling current in the order of 0.25% ... 0.1%. In comparison to the experimental random telegraph noise signals, such a small change is negligible compared to the drastic jumps (factor of two) observed in the tunneling current.

8.6. Comparison: Molecular Orbitals Determined by SNS, STS, UPS, and DFT

In this thesis, the scanning noise spectroscopy technique (SNS) was established as a new approach to probe the electronic structure of surface complexes that provoke telegraph noise. In Fig. 6.12 it is explained, how the SNS results are analyzed in analogy to STS. In STS, the opening of additional tunneling channels results in maxima in the spectra. The maxima are then assigned to electronic states that participate in the tunneling process. For SNS the same argument is valid, as the (molecular) electronic system is involved in the tunneling process. Thus, we derivate the rate data for 'pseudo-constant-height' noise rate measurements with respect to the bias voltage in order to investigate the changes in the voltage dependent rate spectra.

For CuPc on Cu(111) the SNS spectra reveal pronounced peaks at the energetic positions -2.3eV, -1.5eV, and a broad peak setting in at -0.4eV below Fermi level and spanning to -1.0eV (chapter 6.4). We assign these features to the molecular orbitals HOMO-1, HOMO, and LUMO as indicated in Fig. 8.5.

The broadening of the orbitals results from a strong hybridization of the phthalocyanine and the metal surface[2]. The LUMO is found in the occupied states[3]. This is due to a partial filling of the LUMO orbitals upon absorption. As a result, the LUMOs dominate the electronic structure around the Fermi level (zero sample voltage) and the molecules (at least in the first layer) become practically metallic. Similar strong substrate-adsorbate interaction was reported for a number of metal phthalocyanines and other organic molecules on metal surfaces [200, 201, 202].

The charge donation in the system CuPc/Cu(111) was analyzed first in a recent ultraviolet photoelectron spectroscopy study by Stadtmüller *et al.* [202]. The authors name the filled orbital F-LUMO ('former LUMO') as shown in the UPS spectrum in Fig. 8.6. The energetic position of this LUMO peak is -0.4eV below Fermi level[4]. Similar to the SNS

[2] In addition, one may assume, that the broad LUMO peak involves a vibronic satellite peak (for example a C-H stretch mode).

[3] In this work, 'LUMO' refers to the lowest unoccupied molecular orbitals of CuPc in the gas phase and is still used after adsorption, even if the orbitals may be partially filled due to charge transfer processes.

[4] The binding energies given in the UPS data Fig. 8.6 correspond to negative sample voltage in the scanning probe results in this work.

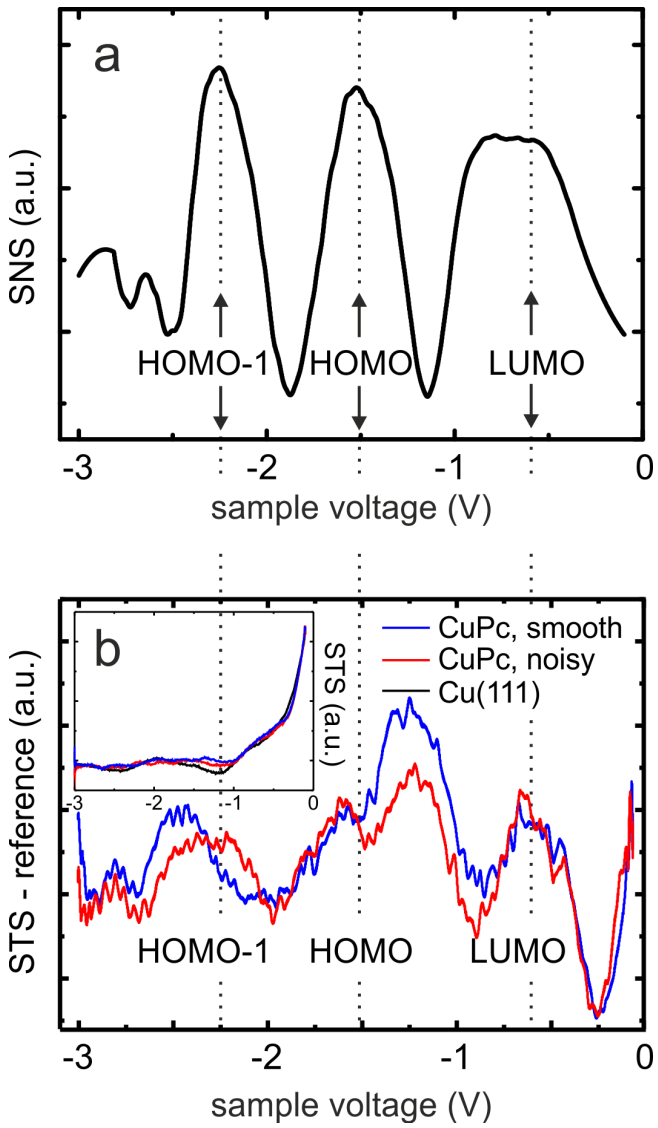

Figure 8.5.: (a) Scanning noise spectroscopy (SNS) reveals the electronic structure of individual CuPc molecules on Cu(111). The partially filled LUMO (broad peak) has its onset at -0.4eV and spans several hundred meV; the sharper HOMO peak is found at -1.5eV, and the HOMO-1 peak sets in at -2.3eV. (b) The scanning tunneling spectra (STS) were measured at constant (average) current. The blue curves represent the smooth lobes and the red curves represent the noisy lobes. A reference spectrum measured above the clean Cu(111) surface was subtracted to reveal the STS peaks, which are very faint compared to the SNS results. The inset shows the raw STS data [143].

results, it appears broader than the HOMO, which is reported at -1.46eV for a coverage of 0.85 monolayers. Thus, the UPS data reported by Stadtmüller *et al.* are in perfect agreement with the SNS results presented here.

The DFT results (chapter 7.4) further confirm the interpretation by Stadtmüller *et al.*. The charge transfer from substrate to adsorbate could be derived from our DFT study through a 'Bader charge analysis' (chapter 7.4). The net charge transfer was calculated to be the equivalent of about 2 electrons. Upon adsorption this charge is transferred into the formally degenerate LUMOs. The maxima of the LUMOs' projected density of states (PDOS) (Fig. 7.6) is found at about -0.25eV. The LUMOs dominate the electronic structure around the Fermi level. This is corroborated by the good agreement of STM images of CuPc on Cu(111) with the simulated STM images presented in chapter 7.3. Thus, the STM images are determined by the contribution of the two LUMOs to the electronic structure.

In the PDOS spectra the HOMO-1 is found at -2.2eV and the HOMO is found at -1.25eV below the Fermi level. The spacing of the energetic positions agree well with our experimental findings keeping in mind that the absolute values of the PDOS features obtained from LDA need to be interpreted with caution as they may be shifted by several hundred meV as compared to experimental values.

The molecular rotation coincides with a slight reduction of the molecule-substrate interaction which manifests in a slight sharpening of the PDOS peaks (compare upper and lower part of Fig.7.6). The change of the HOMO and LUMOs is small, but noticeable. An exception is the HOMO-1 peak, which appears washed-out after rotation.

Finally, the SNS data shall be compared to standard scanning tunneling spectroscopy (STS, chapter 6.5). The low-temperature STS experiments on the system CuPc on Cu(111) yield a poor signal-to-noise ratio, such that no obvious information on the molecular orbitals could be deduced from the data. This is due to a very strong interaction of the copper surface with the organic molecule. In contrast to adsorbate systems on thin insulating layers for example, the organic adsorbate shows almost metallic behavior on the Cu(111) surface. That means, the I-V curves measured with the tip placed over CuPc is practically linear just like the I-V curve of the clean substrate and therefore, the STS spectra appear featureless within the limits of detection.

The STS raw data in the inset in Fig. 8.5b demonstrate the featureless molecular spectra (red and blue) which appear quite similar to the substrate spectrum (black). The

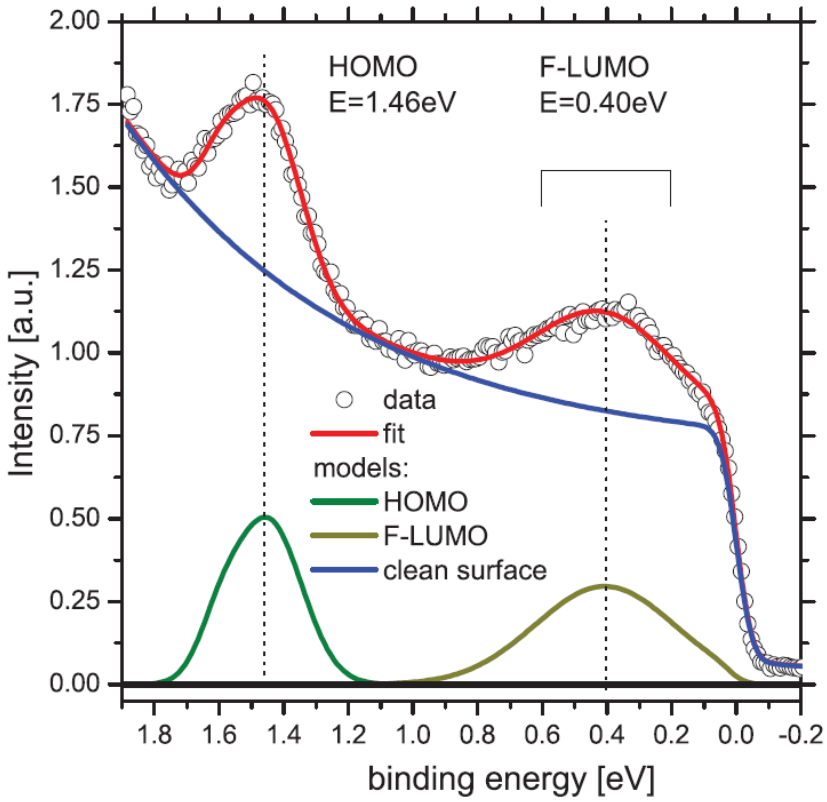

Figure 8.6.: Ultraviolet photoemission spectrum (UPS) for 0.85ML CuPc on Cu(111) at T = -140°C (emission angle 45°). The gas-phase LUMO orbital is partially filled upon adsorption and called F-LUMO. Its energetic position equals a binding energy of 0.4eV. The HOMO is found at approximately 1.5eV binding energy [202]. In the SNS and STS data (Fig. 8.5) the binding energy corresponds to negative sample voltage.

measurement was carried out in constant (average) current mode in order to receive the maximum possible signal at all energies. Still, it was necessary to subtract a reference signal (measured at the clean substrate) to obtain spectral features (main graph). The dotted lines in Fig. 8.5 help to compare the SNS data and the faint and noisy STS result. Indeed, a resemblance is found. Without the very pronounced features in the SNS data, the weak STS signals would not have been interpreted with confidence.

It can be concluded, that SNS opens a pathway to studying in detail the electronic structure of systems that cause TN in the tunneling current, even if standard STS fails. The molecular orbitals of CuPc/Cu(111) could be accessed resulting in very pronounced features in the spectroscopy data. A comparison to standard STS, as well as UPS and DFT confirms our results.

8.7. Resonant Angular Momentum Transfer

Resonant scattering of electrons at molecules was already studied intensely in the 1960ies - more than twenty years before the development of the STM. Electron scattering at molecules could be studied in the gas phase by electron energy loss spectroscopy measurements. For example, slow electrons (1-10eV) were used for the rotational excitation of H_2 molecules by single collisions [203].

Abram and Herzenberg successfully describe the observed rotational excitation within the *sudden approximation* which assumes that the time of interaction of the projectile electron with the target molecule is short as compared to one rotational period [189].

It took quite some time until the theory of resonant angular momentum transfer was applied to molecules adsorbed on surfaces. Teillet-Billy, J.P. Gauyacq and M. Persson showed, that the three-fold rotational hopping of O_2 molecules on a Pt(111) surface observed by the group of W. Ho, could be interpreted as the result of the resonant inelastic scattering of tunneling electrons by the molecules [62, 204]. It was shown, that 'low-energy resonant electron scattering, in particular the need to take into account angular momentum conservation, can lead to a very efficient rotational excitation of the adsorbed molecules, even in the case of a short-lived resonance' [204].

In the following, the recoil character of the excitation mechanism shall be explained. The

corroborating mathematical derivation can be found in chapter 7.6.

As a simplistic analogy to the angular momentum transfer, the linear momentum transfer is sketched in Fig. 8.7 in order to illustrate the recoil character of the resonant momentum transfer. Electrons, represented by green dots, pass a molecular orbital with the energy E and the momentum $\vec{p}$. The orbital (blue circle) picks one electron with a kinetic energy that allows the transient capture into the state E. The resulting compound (blue circle in (b)) is called a resonance. The chosen electron is marked yellow. The vast majority of the electrons follows its trajectories without interacting with the orbital. During the capture step, no matter how short lived it is, the initial momentum, mv_i, brought by the electron is stored within the molecule.

With the reemission of one electron, the resonance decays. Two scenarios are given in Fig. 8.7 c1 and c2. The first scenario showcases the idealized case of backscattering at a massive target ($M >> m$). The emitted electron takes away the correspondent kinetic energy of the state E, such that the resulting recoil deposited in the molecule is exactly twice the initial momentum $2mv_i$. This is the maximum possible transfer of momentum.

In general (Fig. 8.7 c2), all possible combinations of incoming and outgoing trajectories have to be considered. As a result, the finite net momentum transfer is the vector subtraction of incoming and outgoing momenta. The net transfer can range between zero and twice the initial linear momentum of the impinging electron.

For the case of angular momentum transfer a simple demonstrative sketch is not straightforward. However, the same logic applies. The resonant molecular orbital establishes selection rules for the captured electron. The electron must offer well defined characteristics (energy plus well defined symmetries including spin and angular momentum) and the orbital picks an electron from the incoming flux to fit the symmetry of the intermediate state. Due to angular momentum conservation, the electron deposits its angular momentum in the molecule and in the same way, it takes away some angular momentum, when the resonance decays by electron emission.

In fact, the amount of transferred angular momentum by a single electron can be in the same order of magnitude as the momentum of a target atom or molecule, despite the huge

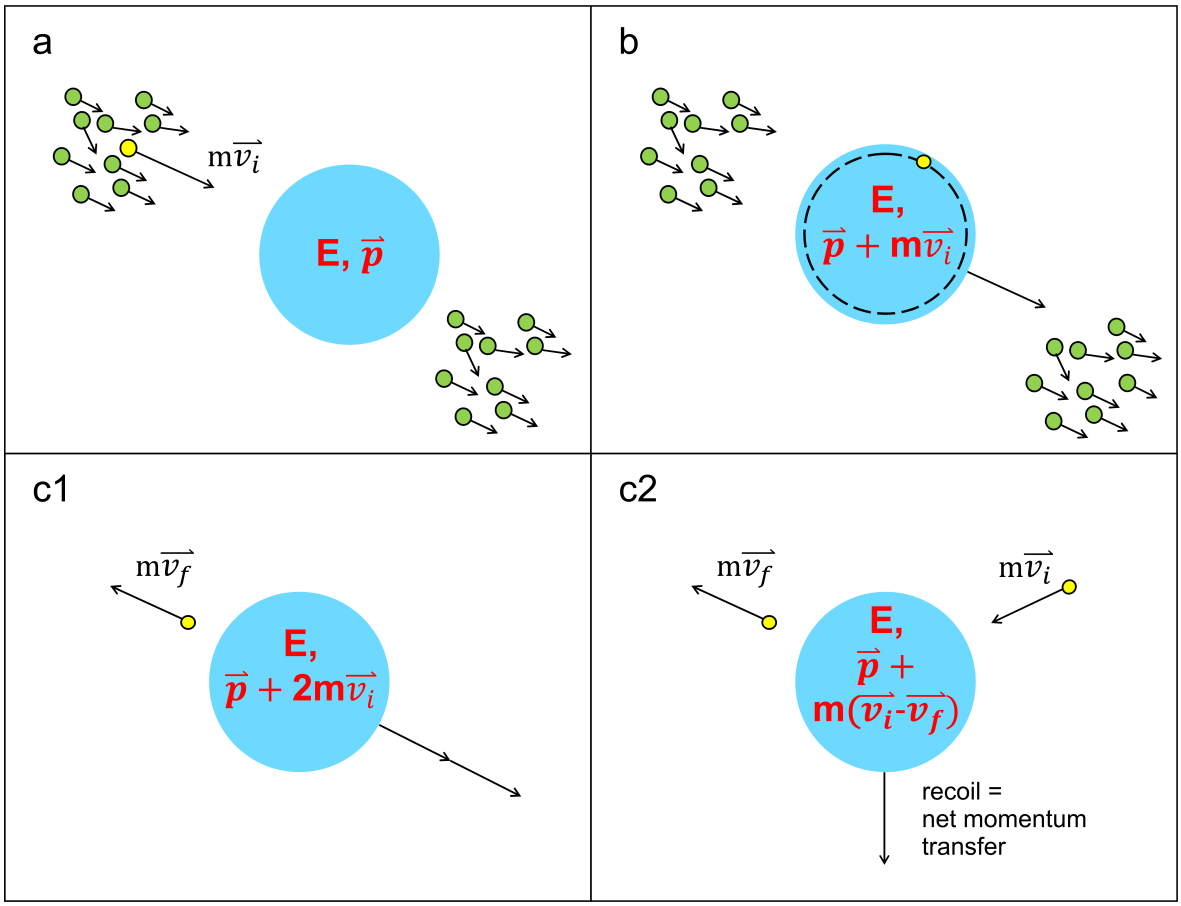

Figure 8.7.: The analogy to linear momentum transfer: (a) In a simplistic linear picture, the electrons impinge on the molecular state with the energy E. (b) The vast majority of the electrons do not fit to the given energy E. The electron marked with yellow color carries the kinetic energy E that allows the orbital to transiently capture it for a short time. The recoil mv_i is deposited in the molecule. (c1) When the resonance decays by the reemission of an electron, the maximal momentum transfer equals the double recoil of the capture step. This corresponds to back-scattering at a massive target ($M >> m$). (c2) In general, all possible combinations of incoming and outgoing electron trajectories have to be considered, which yield a net momentum transfer smaller than $2mv_i$.

difference in size and mass. The linear momentum mentioned before is usually extremely small as compared to the linear momentum of the heavy targets and is not capable of efficient excitation. The difference in the case of angular momentum is, that it is quantized. Consequently, this allows for efficient excitations due to a considerable deposition of rotational recoil.

It is important to note, that neither the projectile electrons nor the target molecules can be associated with angular momentum eigenvectors. Rather, both have to be associated with a distribution of angular momentum. The rotational excitation probabilities remain very high [204].

The same logic applies to the resonant transfer of (quantized) spin momentum [205] and helped to understand magnetic transitions in FePc molecules on Cu(110)(2×1)-O and CoPc on Pb(111) [206, 207].

For the case of CuPc/Cu(111), the excitation of molecular dynamics was observed for the filled states of the molecules. I.e. the tunneling electrons flow from the sample to the tip. In principle, both directions of the current (from the tunneling tip to the surface or vice versa) can be described equivalently. What changes when the current is reversed, is whether the (molecular) orbital involved in the tunneling process is filled or empty. Instead of electrons, we might think of holes or we might replace the term 'transient capture' by 'transient loss'. Both current directions result in the same picture of angular recoil from the resonant scattering point of view.

In chapter 7.6, the mathematical treatment of the rotation excitation yields an interesting side product. In the experimental results (SNS) the derivative of the excitation rates is given as a function of energy and the spectroscopic features are assigned to molecular orbitals.

Indeed, it is straightforward to show, that the derivative of the excitation efficiency is proportional to the local density of states (LDOS) of the sample (see eq. 7.16). This result further confirms the interpretation of the SNS data (see chapter 6.4 and 8.6) from the theoretical point of view.

The main result of chapter 7.6 is the successful calculation of the spatial distribution of the fraction of tunneling electrons that excite the molecular rotation. This 'inelastic fraction' is re-plotted in Fig. 8.9. Until now, this theoretical excitation map for the resonant angular momentum transfer from inelastic tunneling electrons is unprecedented for an adsorbate

system of this size and complexity.

The relaxation process from an excited state into one of the three rotational levels may be very complex and was not tried to be studied in detail. The de-excitation may occur in a direct manner or via one or many intermediate states, as indicated schematically in Fig. 8.8.

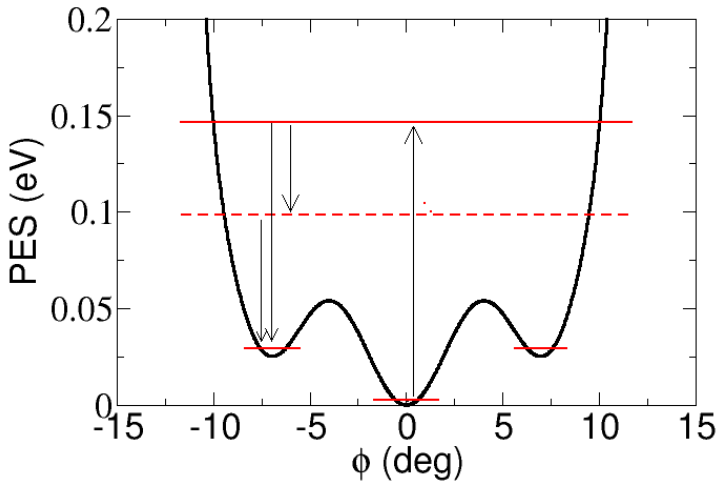

Figure 8.8.: Scheme of the excitation and de-excitation in between rotational levels of CuPc/Cu(111). The excitation from the ground state (medium potential well) to an arbitrarily chosen highly excited state (red solid line) is indicated by the black arrow (pointing upwards). Here, the de-excitation into the left side well is depicted. It may happen directly or via an intermediate state, as indicated by the red, dashed line. Similarly, several intermediate states may be involved. The figure is taken from ref. [181].

For the quantitative treatment of the de-excitation of the molecule from an excited rotational state into one of the wells of the PES, a so called 'branching ratio' is needed. This number gives the probability of the de-excitation into one of the rotated configurations (for example the right potential well). We estimated the branching ratio by evaluating the weight of the rotational wavefunction of a given excited state as a function of the rotation angle (eq.(7.14)). For angles between 5° and 15° we assumed the system to undergo the frustrated rotation into the respective side well.

As can be seen in Fig. 7.8 on page 121, the branching ratio approaches a value of one third for energies clearly above the rotational barrier. Interestingly, this number coincides with the model stated in the experimental results chapter, where the duty cycle spectra also saturate at $1/3$. This was assigned to a heavily excited three-state rotor in the high-frequency limit, with a probability of $1/3$ to find the system in each of the states. Thus, we consider the use of the value of $1/3$ for the branching ratio to be meaningful.

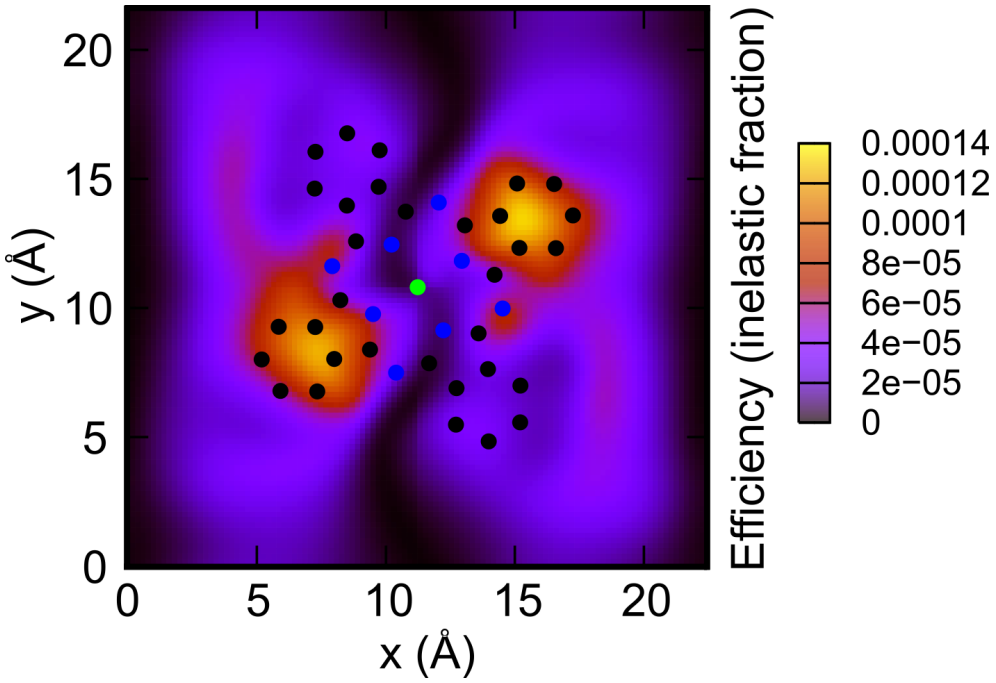

Figure 8.9.: The laterally resolved inelastic fraction of electrons that excite the molecular rotation of CuPc on Cu(111). The probabilities of all states above the rotational barrier are added and a factor of $1/3$ is used for the branching ratio of the de-excitation into a side well of the PES (see chapter 7.6) [143].

The excitation map shown in Fig. 8.9 clearly exhibits the main features observed in the experiments. Two out of the four molecular lobes exhibit maxima in the excitation probability. The orientation with respect to the substrates' densely packed rows of atoms reproduces the STM findings (the noisy lobes are perpendicular to the [-110] direction). The center as well as the remaining two lobes are inactive under the tunneling electron flux. While the lateral information perfectly meets the experimental data, the absolute values of the inelastic fractions resulting from the calculations are larger than the experimental ones by two to three orders of magnitude. In consideration of the challenging theoretical

treatment with several numerical approximations (chapter 7.6) and a most probably underestimated barrier height (see 8.4), the inelastic fraction is still regarded to be in agreement with experiment.

The resemblance between the calculated and the experimental lateral excitation distribution highlights that the model of resonant angular momentum transfer correctly describes the frustrated rotational motion of CuPc on Cu(111).

9. Summary

The observation of telegraph noise in the tunneling current gave rise to the here presented study on the dynamics of adsorbed molecules. Focusing our investigations on the noise and developing a new method of detection led to a new pathway for exploring atomic and molecular dynamics on surfaces using conventional STM setups equipped with additional electronics. From the experimental results based on this development we established a model of the observed dynamics of CuPc molecules on Cu(111). Parts of the individually adsorbed CuPc molecules appeared noisy in the STM images (Fig. 6.3) at very low temperatures (7K). The noisy appearance was manifested in sudden jumps in the tunneling current. The origin of the observed switching phenomenon was unknown and only speculations existed with regards to the underlying dynamical process. The framework of DFT was chosen to simulate the adsorbate system, validate our model and understand the excitation mechanism, which could not be deduced from experimental data alone.

In general, STM experimentalists regard noise as a nuisance. Its origin often remains unknown and the noise is disregarded as being a source of information. However, when telegraphic noise is found as jumps in the tunneling current (Fig. 6.5), it is rewarding to draw attention to this phenomenon since it documents a bi-stable tunneling conductance and may therefore carry valuable information on switching processes on the nanoscale.

The information contained in telegraph noise signals has not yet been consequently accessed and a substantial improvement of the detection method is required. The technical approach presented in this work deals with this task; and to provide a full characterization of random telegraph noise (RTN) signals, special electronics were developed (chapter 4.4). The 'scanning noise microscopy' technique (SNM) detects and analyzes the current jumps - or conductance switching events - in an automated way as a function of time, and all parameters that can be controlled by the respective experimental setup such as (average) current, voltage, temperature, and illumination [124].

In this study we converted the detected events into well-defined pulses, which makes them suitable for automated processing. From these pulses the SNM electronics generated three additional sources of information: 1) The rate of current switching events, 2) the amplitude of the jumps in the tunneling current and 3) the relative occupation of the states (the duty cycle). Averaged over time, these three quantities fully describe an RTN signal.

A key advantage of the SNM technique is that it provides noise characteristics with the same lateral resolution as the STM. This allows the dynamic properties of organic molecules or even single atoms to be observed in great detail. The noise maps (Fig. 6.8) reveal, with submolecular resolution, where the highest rates of switching events are detected and where the difference between the two observed levels of conductance has its maxima.

This information is a considerable improvement when compared to the previously common analyses as those were mainly limited to the observation of switching events at a fixed tunneling tip. Such 'point-probe' experiments did not only lack STM resolution, but also required the post-experimental evaluation of the data. In contrast, SNM characterizes the noise on-line without interrupting the ongoing STM study. The three output signals are measured simultaneously with the STM topography: the measurement software creates the STM image and the three noise maps at once. This real-time availability of the noise characteristics enables the experimentalist to directly react to his or her observations in an unprecedented way.

A key challenge in point probe measurements is to exclude changes of the tunneling tip in between the experiments. Such experiments therefore have to be repeated several times e.g. at the positions of two molecules to achieve the comparability of the data. A strength of the SNM technique is that an area of a surface can be characterized within a single measurement, i.e. with the same tunneling tip. This allows for a reliable comparability of several conductance switching systems at once.

Nevertheless, the new SNM electronics can also be used to analyze the RTN in point-probe measurements as well. This mode is advantageous for the quick measurement of noise spectra (sec. 6.4). We call this type of experiment 'scanning noise spectroscopy' (SNS) in analogy to standard scanning tunneling spectroscopy (STS). In fact, the two techniques are very closely related.

As a matter of fact, the detection of noise could be exploited to gather information on the electronic structure of CuPc on Cu(111). The SNS spectra yield very pronounced maxima (Fig. 6.13) indicating specific energies for which the excitation probability is clearly enhanced. Since it can be assumed that the inelastic tunneling electrons interact with the molecular orbitals we assigned the maxima to the following electronic states: 1) the LUMO (lowest unoccupied molecular orbital, setting in at -0.4eV and spanning to -1.0eV), 2) the HOMO (highest occupied molecular orbital at -1.5eV) and 3) the HOMO-1 at -2.3eV. The former LUMO appears below the Fermi level due to a partial filling of this orbital when CuPc is adsorbed on Cu(111) (DFT result: approx. two electrons). The molecular orbitals revealed by SNS have been discussed in sec. 8.6 and compared to STS as well as the complementary technique UPS and the density functional theory. All of them confirmed the SNS assignment.

Thus, SNS is capable to access the molecular electronic structure. The SNM electronics extracts solely the jumps from the tunneling current signal. The information on the molecular orbitals is still included in this purely inelastic part of the signal. As a result, SNS may be regarded as a 'filter' for the detection of molecular fingerprints of fluctuating systems.

Two key indications have been found in the experimental data for CuPc on Cu(111) that helped to unravel the dynamics that take place under the tip of the STM:

1. The noise slightly exceeds the edges of the fluctuating molecular lobes (Fig. 6.3) and the amplitude maps exhibit maxima at these positions (Fig. 6.8e).

2. The duty cycle saturates at a value of about one third for large negative sample bias (Fig. 6.14).

These two findings strongly suggest, that the molecule performs a frustrated rotation (or 'libration') between three quasi-stable positions within the adsorption plane: 1) The change upon a small-angle rotation will be most dramatic when the tunneling tip resides at the edge of a lobe. 2) The duty cycle saturation at $1/3$ can be understood in terms of a heavily excited three-state switch in its high-frequency limit. The molecule is found in each of its three configurations with equal probabilities.

The rate vanishes for small bias voltages while the duty cycle approaches the value of 1. Thus, the high-conducting state is the favored state in the absence of inelastic processes and it can be concluded that it corresponds to the ground state. We additionally know from STM images, that this state is aligned with one of the base vectors of the substrate (Figs. 6.2, 6.4, 6.8a). The two meta-stable states are rotated clockwise and counterclockwise (Fig. 8.3b), respectively. The rotated states are perfectly symmetric with respect to each other, energetically degenerate and lead to an identical current.

The model of a frustrated rotation could not be conclusively proven by experiment only. Rather, a corresponding potential energy surface resulting from ab-initio calculations was highly desirable. Our DFT study yielded the exact adsorption configuration of CuPc on Cu(111) (Fig. 5.7) and reproduced the symmetry-reduction of CuPc on Cu(111) [24] in terms of simulated STM images (sec. 7.3).

Subsequently, a one-dimensional potential energy surface was calculated by simulating various rotated configurations of the molecule. It confirmed the model that was established experimentally: A three-well potential was found with an energetically favored ground state in the center and two additional side wells (Fig. 7.2). The rotated states are rotated by approximately $\pm 7^{\circ}$ with a barrier in the order of 50-70meV in between ground state and rotated states.

The rotation excitation mechanism can be described as follows. An inelastic tunneling electron lifts the system to a highly excited rotational state above the side wells of the PES. Only one inelastic electron is needed (one-electron process) as was established from SNS, where a *linear* dependency of the switching rate on the tunneling current was observed (Fig. 6.10). The relaxation may take place directly or may be mediated by one or a cascade of many intermediate states (Fig. 8.8). From the excited state the system relaxes into one of the three potential wells with a branching ratio of about one third for each well (Fig. 7.8). The inelastic fraction of impinging electrons that successfully shift the system to a rotational state above the barrier was evaluated within the sudden approximation. This treatment is justified by the slowness of the molecular rotation compared to the fast collision of an electron and the molecule, which can be regarded as a *sudden* process. The reason for the rotation is the deposition of momentum in a kind of recoil process during the collisions: After each electron-molecule scattering event, some amount of angular momentum from the incoming distributions of angular momenta of the electrons remains in the target.

In the simpler case of linear momentum transfer, the large mass discrepancy between electron and molecule makes recoil mechanisms very inefficient. In contrast, a recoil mechanism can be highly efficient in the case of rotational excitation, since the momenta of projectile and target are in the same order of magnitude due to the quantization of the angular momentum [189]. What has been established for many years in the field of electron scattering at gas-phase molecules has also been shown to remain an efficient process in the rotational excitation [204] and the magnetic excitation [205, 207] of adsorbed species.

Since the excitation probability depends on the position of the tunneling tip an excitation map was calculated within the Tersoff-Hamann approximation (Fig. 7.10). It clearly reproduces the key feature of the experimental rate maps: The excitation maxima are located at those molecular lobes that are aligned perpendicular to a substrate base vector.

In conclusion, it was possible to disentangle the initially unknown molecular dynamics of CuPc on Cu(111) by the implementation of a new experimental technique that provides additional information on bistable systems from the exploitation of noise. The new channels of information led to the model of a frustrated rotation of the organic molecule on the surface which was supported by an accompanying theoretical study. Not only did the potential energy surface for the molecular dynamics prove the existence of the experimentally deduced ground state and two rotated states, but furthermore, the excitation mechanism via a resonant angular momentum transfer from single, inelastic tunneling electrons to the target molecule was be explained. The theoretical treatment allowed the simulation of an excitation map and its resemblance to the experimental observations completed this study.

10. Future Prospects

The power of the SNM technique could make a significant impact in the field of switching processes on the nanoscale. In general, the SNM electronics are not limited to the usage in combination with scanning probe microscopes alone. Instead, any arbitrary input signal that exhibits two-level telegraph noise can be analyzed.

An example for a complementary experimental approach is the so called *break-junction technique*. When only one molecule bridges the gap between the two electrodes in this setup, transport measurements through the smallest organic building blocks are possible [208]. Hence, the technique is a candidate to study conductance switching processes within single molecules. First studies on noise from the break junction have already been reported, e.g. the measurement of shot noise from a single molecular (D_2) junction [209]. As soon as telegraph noise is observed, it could be processed with the help of the SNM electronics presented here.

For further study of the specific system CuPc on Cu(111), the employment of low-temperature scanning force microscopy experiments (LT-AFM) would be an interesting approach, since this microscope does not need to drive a current through the adsorbed molecules. The feedback controls the tip-sample distance by measuring a force gradient, as for example in the tuning fork AFM setup [210, 211, 114]. As a consequence, the AFM enables the analysis of CuPc on Cu(111) avoiding the dominating rotation excitation by inelastic tunneling electrons. This approach might help to separately image the molecule in both rotational states. Eventually, the rotors could also be stabilized in one of the states in a controlled manner by temporarily (1ms) driving a tunneling current through the molecules and subsequently imaging them without a current. The lobe-selective measurement of the force, frequency shift and dissipated energy might yield interesting complementary information [**?**].

As an extension to the presented work, other metal core phthalocyanines could be studied, with the aim to eventually find and characterize their (frustrated) rotation dynamics. In addition, ligated or double-decker phthalocyanines [212] may be taken into account and the substrate could be changed in order to alter the organic-metallic interface. A priori, it is not known if other adsorbate/substrate combinations would show comparable dynamics. However, varying the tunneling current, the voltage and, for example, the temperature between 7K and room temperature may be regarded as promising approaches to eventually find dynamic behavior of the studied systems.

In the appendix B of this work, an exemplary heterogeneous system will be presented. The system CuPc + PTCDA forms highly ordered intermixed islands up to several hundred nanometers in size. However, the conductance switching of CuPc, which was treated in the main part of this work is based on the frustrated rotation of the molecules and was not observed for the highly ordered hetero-system, since the neighboring molecules act as a steric hindrance for the molecular rotors.

Nevertheless, the large variety of organic compounds appears to provide unlimited combinations of molecular species and SNM is an ideal tool to also investigate molecular switches embedded in hetero-systems. We know for example from earlier experiments in the Möller group that CuPc acts as an eccentric rotor when adsorbed on top of C_{60} islands [166, 213]. This hetero-system could be used as another benchmark for the SNM technique.

First successful measurements by other groups using the SNM setup for scanning probe experiments were already conducted by E.P. Smakman *et al.* in the group of P. Koenraad at the Technische Universiteit Eindhoven (Eindhoven, Netherlands) [214]. Instead of studying single organic molecules adsorbed on a surface, the authors analyzed single dopant atoms embedded within a semiconducting surface [215]. The charging of these dopants by tunneling electrons is currently investigated using our experimental approach. Only small adjustments of the integration times of the electronics have been made to account for the smaller switching frequencies that were observed for the studied system.

The theoretical part of this work can be extended to obtain information on the behavior of different metal-core phthalocyanines on Cu(111). As a starting point one might slightly modify the model system by replacing the central MPc atom. This would allow to systematically study binding energies, binding distances and barriers for rotational motion

of different phthalocyanines. As a result of such extensive calculations, predictions on the observation of noise, stemming from the rotation of Pc molecules on Cu(111) or other substrates could be made.

Finally, new excitation mechanisms could be tested. For instance, the illumination of the sample might be a different type of stimulus to inject energy into the adsorbate system. Light, originating from the tunneling junction, can be detected in a separate experiment. The latter experimental setup was already realized in the Möller group and will be presented in the PhD thesis by Maren Cottin. It might open the opportunity to detect an energy dissipation channel of dynamic systems on the surface, i.e. the characteristic light emitted from individual molecules would present distinctive fingerprints of molecular switching phenomena.

A. Appendix: Iron-Octaethyl-Porphyrin Chloride on Cu(111)

Among the most studied organic molecules in surface science, the porphyrins together with the phthalocyanines are two outstanding classes of quasi-planar complexes. Both pigments are available in many different appearances exhibiting a large variety of properties. Porphyrins and phthalocyanines have in common a pyrrole network, which is able to carry a (transition) metal ion as the molecular core. Another possibility to modifying the properties of the molecules is to substitute carbon atoms by nitrogen. In addition, the compounds can be ligated to functional groups like phenyl rings [82, 216].

Figure A.1 gives an impression of the close relation between phthalocyanine (left) and porphyrin (right). Besides the substitution of four carbon atoms by nitrogen, the ligation of benzene rings converts porphyrin into phthalocyanine. As a consequence, phthalocyanines can also be described by the term 'tetrabenzotetraazaporphyrin'.

Surface scientists appreciate the great choice of metal-core porphyrin and phthalocyanine derivatives to tailor the desired physical properties on the nanoscale. Among other molecular compounds, metal porphyrins have attracted considerable attention in the field of molecular magnetism [217, 218, 8, 219, 220, 221, 222].

This chapter contains both experimental and theoretical work on 2,3,7,8,12,13,17,18-octaethylporphyrin Fe(III) chloride (in the following FeOEP-Cl) adsorbed to the Cu(111) surface. The structural formula is given in Fig. A.2. FeOEP-Cl ($C_{36}H_{44}ClFeN_4$ (Hill system), atomic mass: 624.08u[1]) consists of a porphyrin with eight ethyl groups attached. In

[1] u = unified atomic mass units = one twelfth of the mass of an unbound neutral atom of carbon-12 in its ground state = $1.660538921(73) \times 10^{-27} kg$

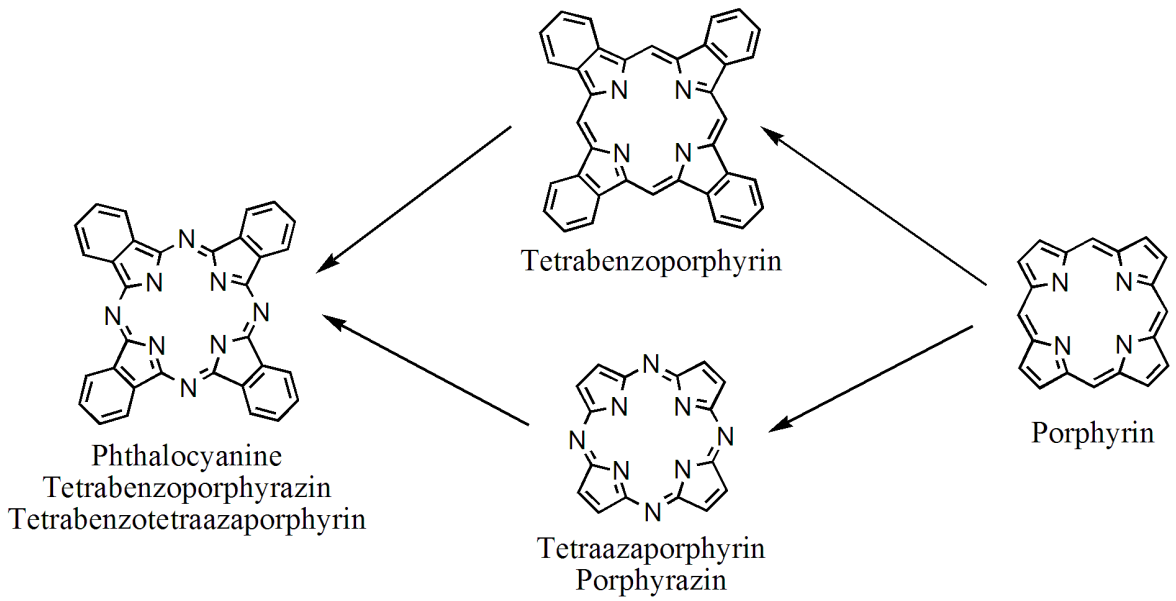

Figure A.1.: Structural formulae displaying the relationship of porphyrin (right) and phthalocyanine (left). The substitution of carbon by nitrogen and the additional ligation of benzene rings converts porphyrin to phthalocyanine. Therefore the latter can also be named tetrabenzotetraazaporphyrin.

addition, a Cl atom is ligated to the central Fe atom and points out of the porphyrin plane[2].

The Cu(111) single crystal was cleaned by several cycles of Ar^+ ion sputtering and annealing as described in chapter 4.6. The deposition of a submonolayer FeOEP-Cl was carried out with the sample held at room temperature by thermal evaporation. The molecule furnace was heated to 236°C and the sample was held into the molecular beam for 120s.

In addition, small amounts of Co was adsorbed to some of the samples forming small triangular islands with the goal to create additional organo-metallic systems on the very same sample. Here, the LT-STM experiments performed at 7K focus on the organic molecules adsorbed on the clean Cu(111) surface with no Co islands in the close vicinity. The LT-STM data measured at 80K were conducted for FeOEP-Cl adsorbed onto clean Cu(111) samples.

[2]Supplier: *Porphyrin Systems* GbR, Maria-Goeppert-Str. 1, D-23562 Lübeck, Germany.

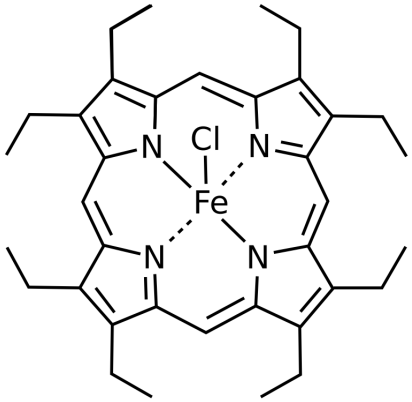

Figure A.2.: Structural formula of 2,3,7,8,12,13,17,18-octaethylporphyrin Fe(III) chloride (FeOEP-Cl). The chlorine atom points out of the drawing plane.

A.1. Experimental Results

Low-temperature STM studies on the system FeOEP-Cl/Cu(111) evidenced a rather high mobility of the molecules on the surface even at cryogenic temperatures (79K). When interacting with the tunneling tip, the molecules showed some likeliness to diffuse or even to bind to the tip. Especially the unoccupied states (positive sample bias voltage) were hardly observable with reproducible imaging quality[3].

In the series of experiments it was attempted to adsorb FeOEP-Cl on cobalt on Cu(111). However, the adsorption of the molecules on the Co islands was experienced to be even weaker, so that STM experiments could not successfully image single molecules on the cobalt islands. In contrary, the molecules were manipulated by the tunneling tip and picked up by the tip, so that the image quality was degraded for both, positive and negative sample bias voltages. The small triangular Co islands were decorated by molecules at their borders. Here, we focus on individually adsorbed molecules on the clean Cu surface. The availability of large clean Cu(111) terraces yields the opportunity to study single FeOEP-Cl molecules (about $0.05ML$).

The overview scan shown in Fig. A.3 gives an impression of the prepared surface. As

[3]This was also verified by Manfred Lange and Dennis Van-Voerden, who repeated the experiments with several tunneling tips and several sample preparation cycles in the LT-STM/AFM laboratory (AFM = atomic force microscope).

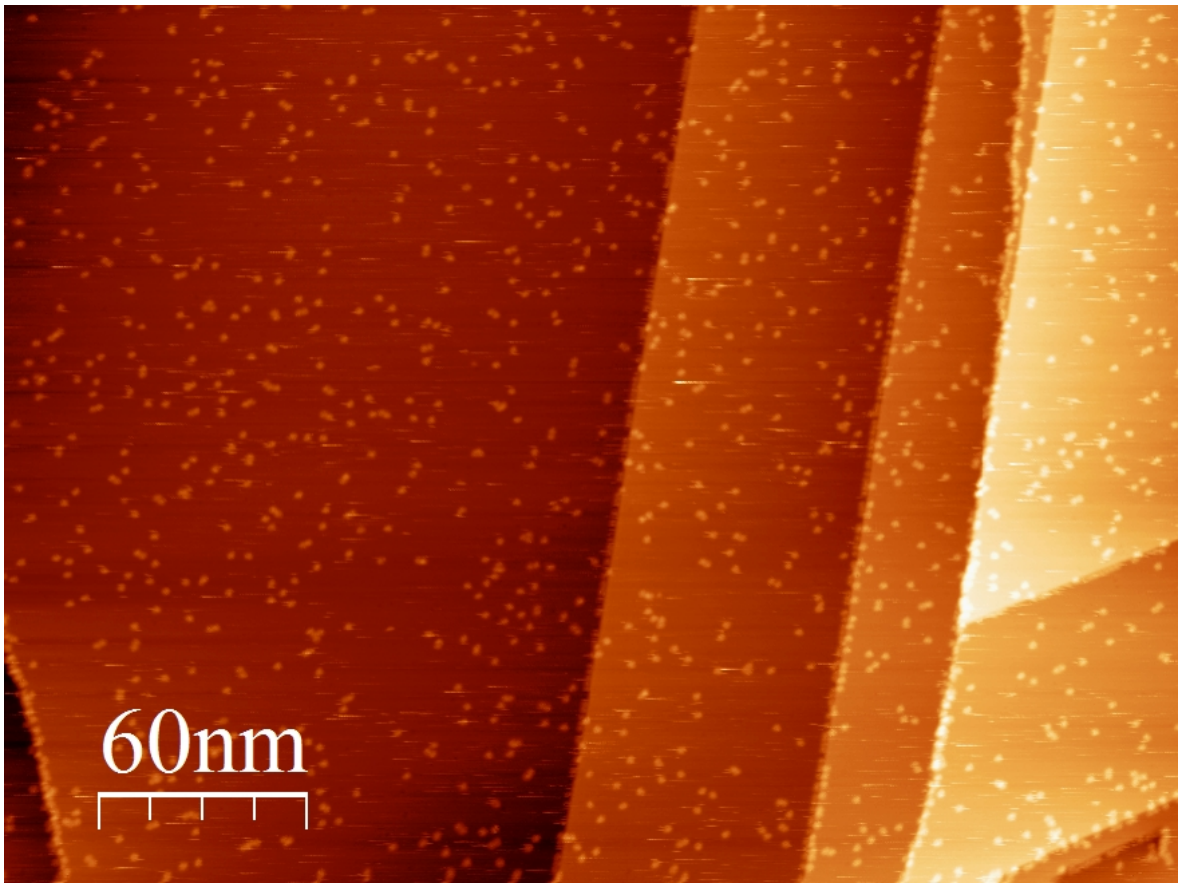

Figure A.3.: A submonolayer of FeOEP-Cl on a Cu(111) surface. All step edges are decorated with molecules. On the large terraces, FeOEP-Cl is found to be adsorbed individually or to form small complexes consisting of two or more molecules (not more then 10). No ordered island growth is observed. $T = 79K, 350x250nm^2, U_{sample} = -2V$.

seen before for the CuPc molecules, also the FeOEP-Cl molecules are predominantly found individually on the Cu(111) surface while the atomic steps are decorated more densely. The formation of dimers, trimers, short molecular chains and small clusters is rarely observed at this low coverage. The growth of ordered islands was not observed. Small horizontal bright lines in the STM data witness the temporary interaction of molecules with the STM tip or the interaction of molecules, that have contaminated the tunneling tip, with the surface.

When zooming-in to a surface area with a side length of about one tenth of the overview scan, the molecules can be seen in more detail. Fig. A.4 displays two consecutive scans of the very same surface area exhibiting 18 molecules. Ten single molecules, two dimers

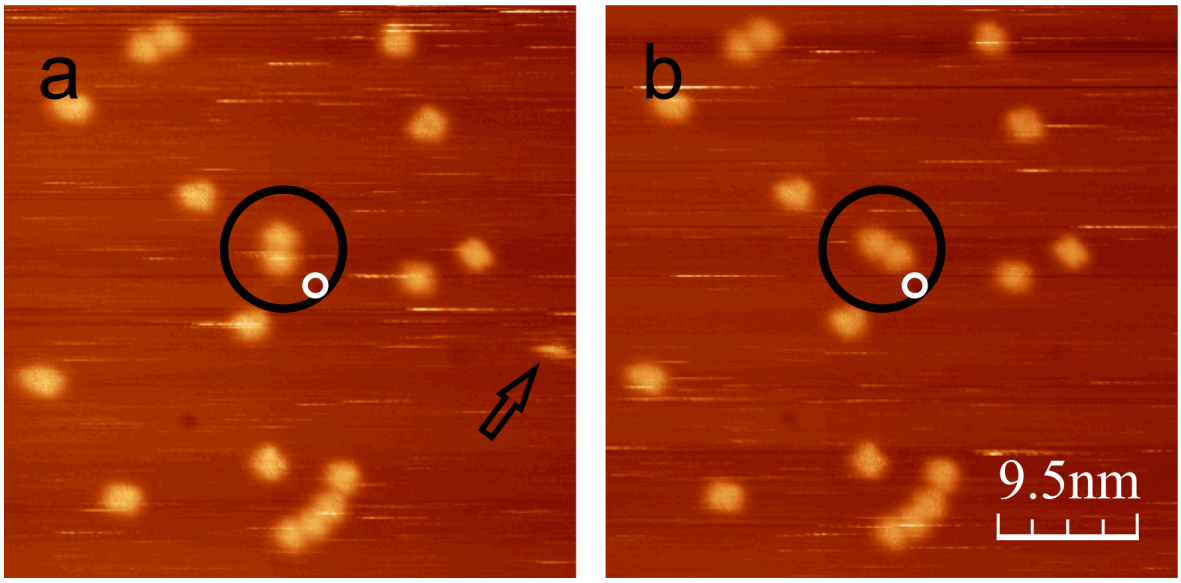

Figure A.4.: Motion of FeOEP-Cl on Cu(111) at $T = 79K$: Two successively scanned STM images show a FeOEP-Cl dimer (marked by circles), which changes its orientation in between the two measurements (a) and (b). A surface defect is highlighted by the white circle. It serves as a lateral reference point for the rearrangement of the dimer in the circle. In addition, a 'truncated' molecule is imaged at the right border of (a) as marked by the arrow. It was removed from the scan area by the interaction with the tunneling tip. $38x38nm^2, U_{sample} = -2V$.

and one molecular chain consisting of four molecules can be seen. Again, horizontal bright lines are noticeable. They indicate the tip-molecule interaction. On the right hand side of Fig. A.4a a 'truncated' molecule is imaged at the mid-right border of the scan. It is marked by the black arrow. The tip removed this molecule during the measurement. It cannot be determined, where the manipulated molecule has moved to: Either it diffused out of the scan area or it sticked to the tunneling tip.

Another evidence of molecular motion can be seen in the center of the two scans. A dimer of FeOEP-Cl is marked by the black circles. In the second STM scan, the dimer is imaged in a different orientation on the surface. From the distances of the dimer to the surrounding molecules and a surface defect marked by the white circles it can be concluded, that the lower of the two molecules has moved around its dimer partner by $90°$ and found another stable dimer configuration.

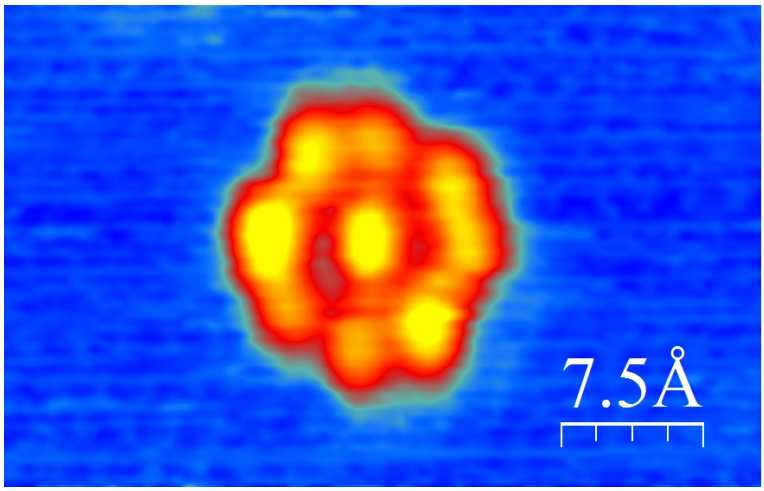

Figure A.5.: Closeup STM image of a single FeOEP-Cl molecule on Cu(111) at $T = 79K$. In this high-quality data, submolecular features are unraveled. Eight outer protrusions plus one central protrusion can be observed. $U_{sample} = 850mV, I = 0.5nA$. Data provided by D. Van-Vörden and M. Lange.

Eight outer protrusions were found, when D. Van-Vörden and M. Lange collected high-resolution STM data that can be seen in Fig. A.5. The eight outer protrusions in the STM image appear in pairs of two and the overall molecule appears in a round shape.

After the preliminary measurements at 79K, it can be concluded, that after depositing a small amount of FeOEP-Cl (<1ML) on the terraces of the Cu(111) surface the individually adsorbed molecules could successfully be imaged.

Thus, an experiment at very low temperature (7K) was initiated in order to enhance the STM stability and to reduce the mobility of the molecules on the sample at the same time.

Single molecules could now be investigated in more detail. Fig A.6a+b shows, that the appearance of the FeOEP-Cl still changed during the measurement. When this molecules was first resolved in STM at a small negative sample voltage (-0.1V) it appeared in a triangular shape. After switching the bias voltage between -2V and 2V it appears in a rectangular shape with four protrusions. The four 'molecular lobes' slightly differ in STM contrast with a pair-wise resemblance of opposing lobes.

The manipulated molecule exhibited an enhanced stability and thus offered the opportunity to study it as a function of energy (bias voltage) by recording dI/dV maps (spectroscopic

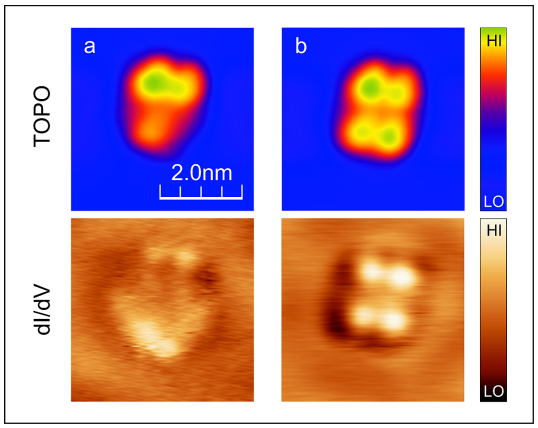

Figure A.6.: (a+b) STM topography: An individually adsorbed FeOEP-Cl molecule on Cu(111) was modified by STM-manipulation at a temperature of 7K. Lower part: corresponding dI/dV maps. $U_{sample} = 500mV, I = 300pA, T = 7K$.

imaging, see section 2.3).

The stabilized molecule kept its position and characteristics long enough (several hours) to perform an energy-dependent series of dI/dV-maps ranging from -800meV to +800meV as can be seen in Figs. A.7 and A.8.

The data in Fig. in Figs. A.7 are plotted in a pseudo-3D view where the protrusions (bright color) correspond to a high local density of states and depressions (dark color) correspond to a low local density of states (LDOS). The 3D representation was chosen to highlight the changes in the dI/dV intensities for the different scans. The maximal lateral resolution of the data can be seen in the (standard) 2D plots (Fig. A.8).

The molecule is centered in these images. Wave-like protrusions and depressions outside the molecule stem from the Shockley surface state of the Cu(111) surface (sec. 4.6). In addition, a row of four small defects can be seen as depressions at the top of the scans and two small defects can be seen at the bottom border of the scans.

The dI/dV maps for the filled states (negative bias) show four protrusion located in the molecule. From -700meV to -400meV the maxima evolve more and more as compared to the LDOS of the environment (Fig. A.7). The four maxima can be clearly seen, as the rest of the porphyrin produces a dark background in the LDOS images. The shapes of the four maxima change from a roundish appearance (-700meV) to a stripe-like appearance

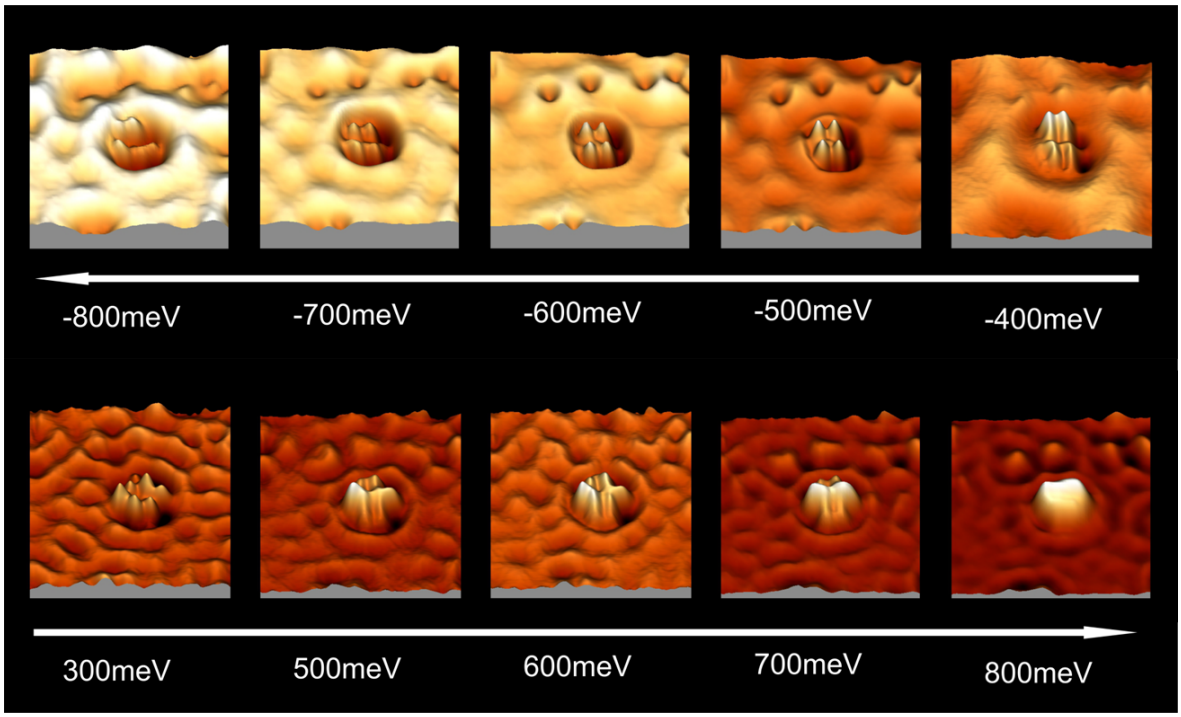

Figure A.7.: 3D representation of low-temperature (7K) dI/dV maps of FeOEP-Cl on Cu(111) for the filled states (upper series) and the empty states (lower series). The gradual increase/decrease of the main features in the density of states can be seen as a function of sample voltage are highlighted by the 3D representation. For the full lateral detail see Fig. A.8. I = 300pA, 10nm × 10nm, 10min per scan.

(-400meV). Starting from small negative sample voltage (Fig. A.8) throughout the data measured with positive sample voltage the Shockley surface state of Cu(111) (see chapter 4.6 and refs. [132, 133, 134, 135]) causes the typical standing-wave pattern, due to the scattering of the surface electrons at the adsorbates.

At positive bias, relative to the respective maxima outside the molecule, the molecular features become more and more protruded as the bias voltage is increased. While the 300meV image shows no clearly resolved symmetry, but a flourish appearance (Fig. A.8), the 500meV data exhibits the stripe-like maxima that was observed at -400meV, too. In addition, a perpendicular stripe is found. This new feature crosses the other two at the center of the molecule. With increasing bias voltage it becomes the dominating maximum. Finally, at 800meV no submolecular resolution is found in the dI/dV data; the molecule

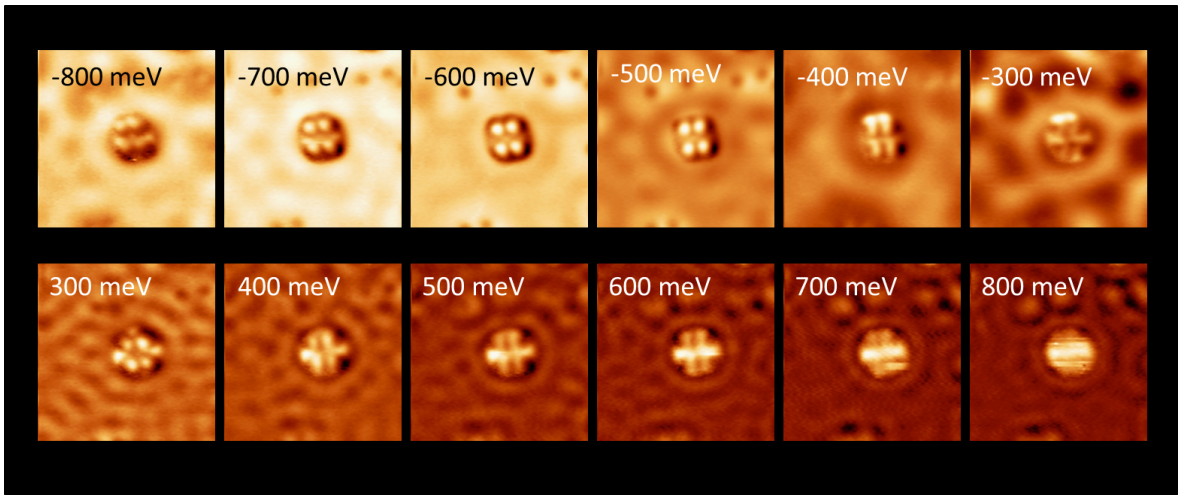

Figure A.8.: 2D (standard) representation dI/dV maps of FeOEP-Cl on Cu(111) for the filled states (upper series) and the empty states (lower series). Here, the focus is on the lateral detail while the relative increase/decrease of the features can be compared in Fig. A.7. I = 300pA, 10nm × 10nm, 10min per scan.

exhibits one single maximum. Energies higher than 800meV reduced the data quality and could therefore not be chosen.

After the measurement of the dI/dV-maps, more voltage pulses (±2V) were applied to the very same FeOEP-Cl molecule. Interestingly, it could be changed again. This time, the symmetry was reduced. The two upper lobes approached each other during the STM manipulation. Fig. A.9 shows the initial appearance (left), the stabilized appearance (middle), and the final appearance (right).

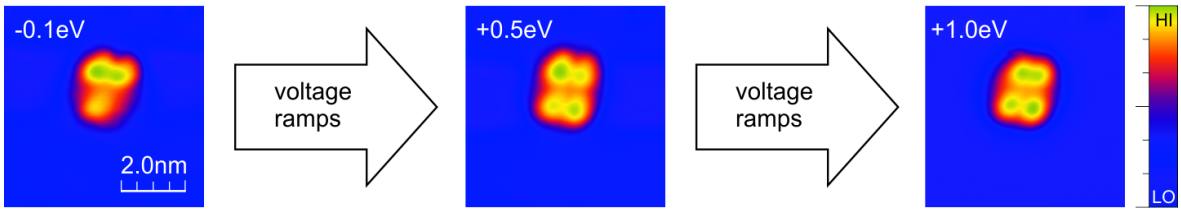

Figure A.9.: STM-manipulation of FeOEP-Cl on Cu(111) at 7K: The molecule was first transformed from its initial, triangular appearance (left) to a highly symmetric rectangular appearance (middle) by applying ±2V sample voltage pulses to the molecule. After a series of dI/dV measurements (Figs. A.7 and A.8) the procedure was repeated and the molecular appearance was changed again. The final appearance (right) exhibits a closer distance of the two upper lobes.

A.2. Cl-FeOEP on Cu(111) - Theoretical Approach with DFT

The molecular coordinates for the porphyrins treated in this chapter were constructed 'manually' with the help of a spreadsheet program. Subsequently, ionic relaxation in the gas phase was achieved with the *VASP* DFT code.

Albeit the fact, that the absence of a surface reduces the number of atoms in the model drastically, reaching good ionic convergence still is a complex task. Especially large organic molecules with singly-bonded side groups like the eight ethyl groups in this study, exhibit additional degrees of freedom. The side groups and parts of the side groups may rotate and, depending on their position, interact with neighboring side groups. This can lead to the dissociation of the molecule due to strong repulsive forces that may occur at a specific relaxation step. Until the DFT code finally converges the ionic coordinates into a stable energetic minimum, a costly series of calculations has to be performed. The so called 'good guess' for the initial coordinates is very important and in addition, the ionic steps must be chosen small. The latter ensures that the ions perform careful relaxation steps which do not overcompensate the calculated forces from the previous position. Otherwise, atoms approach each other too close, resulting in even larger forces for the next step and often causing the dissociation of the model.

In special cases, depending on the specific goals of DFT studies, organic molecules are simplified in a drastic way. If it is physically justifiable, side groups can be neglected completely and the bonds are saturated by single hydrogen atoms to reduce computational effort. Examples are studies on magnetic properties and the interaction to the substrate, where the predominant magnetic characteristics are given by the porphyrin core, i.e. the central transition metal atom and the nitrogen atoms within the carbon network [223, 221, 222].

A goal of this study is to obtain simulated STM images within the Tersoff-Hamann approximation in order to identify the molecular orbitals mapped with dI/dV-STM measurements. Thus, a full representation of the large molecule has to be achieved.

A stepwise, careful setup of the model system resulted in the successful relaxation of the following molecules in the gas phase (please compare to Fig. A.10):

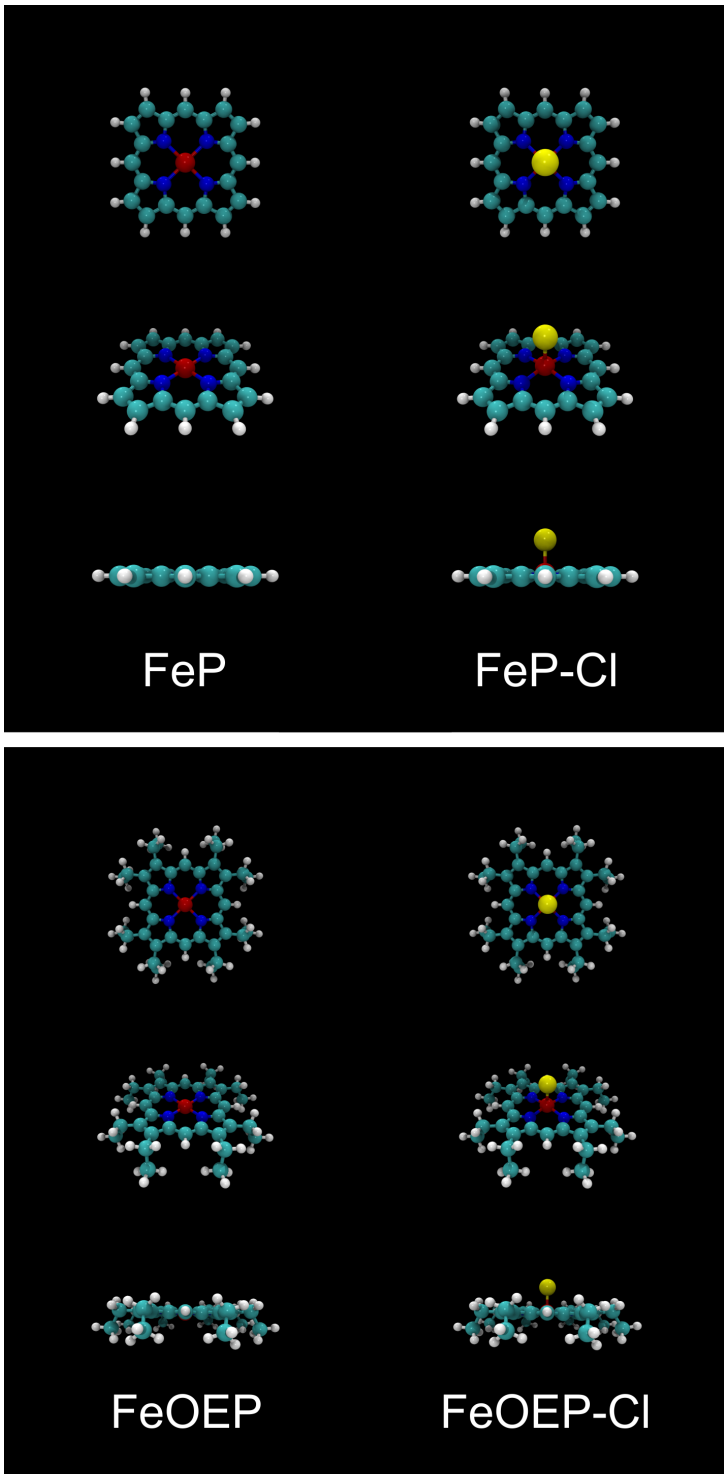

Figure A.10.: Ball-and-stick models of FeP, FeP-Cl, FeOEP, and FeOEP-Cl. From top to bottom, a top view, a perspective view, and a side view of the planar molecules are provided. The ionic coordinates were optimized for the gas phase with *VASP* and visualized by ball-and-stick models with *vmd* [224].

Molecule	Abbreviation	Conformation
Iron-Porphyrin	FeP	porphyrin with central Fe (III) core
Iron-Porphyrin-Chloride	FeP-Cl	chlorine atom ligated to the Fe core
Iron-Octaethyl-Porphyrin	FeOEP	eight ethyl groups ligated to FeP
Octaethyl-Iron-Porphyrin-Chloride	FeOEP-Cl	chlorine atom ligated to the Fe core

Table A.1.: The four porphyrin species modeled in this work. Stable configurations for the gas phase could be found and serve as a basis for ongoing studies including the Cu(111) surface.

In a second step, the Cu(111) surface of the studies on CuPc (main part of this thesis) was used in its original, relaxed state. The slab model was kept the same and the pre-relaxed porphyrin molecules from the gas phase calculations were added resulting in a 446 atom model for the case of Fe-OEP-Cl. This large number of atoms challenges todays standard computer clusters. With calculations running for several weeks, the number of simulations has to be kept low and the parameters of convergence have to be chosen with caution.

The orientation on the surface was chosen with the central molecular plane (given by the four nitrogen atoms) parallel to the surface. Angle-dependent near-edge X-ray absorption fine-structure spectra (NEXAFS) for Fe-OEP-Cl on Co and Ni films on Cu(100) published in the supplementary information to [223], as well as the STM investigations on Cu(111) shown above reveal a planar adsorption configuration. An initial vertical distance between the nitrogen plane and the surface atoms of 2Å was used. The lateral adsorption position was chosen with the central Fe atom placed in the highly symmetric bridge position. As a result of a series of geometry optimization calculations, the ethyl groups point away from the copper surface with an angle of approximately 120°. The complete model system was handed over to the collaborating DFT specialist Roberto Robles, who compared the bridge position to an on-top configuration. The bridge position turned out to be energetically favored by 180meV compared to the on-top site.

A calculation with the Cl pointing towards the surface instead of the vacuum resulted in a very unfavorable increase of the total energy of 1.65eV as compared to the bridge position with the Cl atom pointing towards the vacuum. Furthermore, the ethyl groups were set to another configuration, facing towards the sample, while the Cl atom pointed to the vacuum. For this case, the total energy increased by 1.03eV [197]. Thus, the latter two configurations were excluded.

A.3. Discussion

The room-temperature deposition of a small amount (<1/10ML) of FeOEP-Cl onto the Cu(111) surface resulted in predominantly individually adsorbed molecules on the copper terraces. In addition, groups of 2-4 molecules have been observed by STM at 79K, too (Figs. A.3 and A.4).

When probing with the STM, the molecules show a tendency to rotate or diffuse. This molecular motion is reflected by the short white lines in the STM data. The direction of these lines corresponds to the fast scan direction. The maxima (white lines) are due to molecules, that occur within the tunneling junction, enhancing the tunneling current. They may be caused by FeOEP-Cl molecules that interact with the STM tip.

The white lines not always start or end at the position of an individually adsorbed molecule. It might be possible, that a fraction of the molecules on the surface diffuse more easily and cannot be resolved in the above data (Figs. A.3 and A.4). The diffusive molecules might appear 'suddenly' under the tunneling tip and provoke the white lines. The reason for the motion of a fraction of the molecules would be thermal activation in combination with a reduced binding energy compared to those molecules that are clearly resolved.

A difference in binding energy can be due to the stabilizing influence of surface defects (e.g. adatoms) below the adsorption site of the fixed molecules.

Another scenario is, that more than one molecular species is present on the surface as a consequence of a (partial) dissociation of the large organic compound. For example, the eight ethyl groups, which possess many degrees of freedom, might be affected by chemical reactions (dissociation, rearrangements). The side groups of the molecule and also the ligand (Cl) may be lost during adsorption. At this point, based on the preliminary data, a conclusive explanation for the observed mobility of the adsorbates cannot be given.

When the experiment was repeated at even lower temperatures (7K), the molecules could be studied in more topographic detail. However, the FeOEP-Cl still changed during measurement (Figs. A.6 and A.9). Possible scenarios for the reason of this observation include the STM-induced rearrangement of the ethyl groups. For example, ethyl groups that point towards the sample might be lifted under interaction with the tip. As a result, the molecule might reach an energetically favored state with all ethyl groups pointing out of the surface plane. Each of the four outer protrusions of the molecule imaged by STM would then

consist of two ethyl groups.

This explanation coincides with the geometries of FeOEP-Cl and FeOEP, that were found in the gas-phase DFT simulations (Fig.A.10). Also for this data set, possible scenarios include chemical reactions as mentioned before leading to a reduced number of molecular lobes (topic of ongoing studies, see below). Here, the interaction of the tunneling current with the molecule might have led to chemical reactions like the dissociation of side groups. The small defects found in the close proximity of the studied molecule can be assumed to be CO molecules that adsorbed to the Cu(111) surface. Or, they might result from a dissociative STM-induced manipulation. In that case, STM cannot any more be regarded a minimal invasive technique and great care has to be taken on the the interpretation of the experimental data as long as it is not clarified which species has exactly been studied. With this uncertainty in mind it needs to be emphasized that the experimental data presented in this appendix have a preliminary character and cannot serve for a conclusive analysis, yet.

The dI/dV maps of FeOEP-Cl on Cu(111) show orbital shapes with submolecular resolution. The data may be used to compare with future DFT simulations and additional experimental studies in order to clarify the actual identity of the molecule that was manipulated and subsequently studied here. However, the SPM-based study of the adsorbed species is a delicate task, as the molecules react sensitive to specific voltages and likely interact with the tunneling tip.

As a result of the theoretical treatment within the framework of DFT including the surface (in collaboration with Roberto Robles) it can be concluded that the adsorption of FeOEP-Cl on Cu(111) prefers a highly-symmetric bridge position. First DFT results suggest, that all eight ethyl groups, as well as the Cl-atom point away from the surface.

However, FeOEP-Cl with its 86 atoms and - even more important - the many rotational degrees of freedom of the ethyl groups, is also a challenging object to study within DFT. This is also reflected by the fact, that in literature, the molecules are drastically simplified by cutting off the eight ethyl groups and replacing them with H atoms in order to facilitate the theoretical treatment. For the studies on magnetism of the molecules on surfaces this procedure is justified since the magnetic central atom and the porphyrin center dominate the magnetic properties [223, 222]. In contrast, the ansatz of the present work was to include the full system in the DFT model and to aim for the comparability to our STM studies. So far, the exact (possible) configuration(s) of FeOEP-Cl on Cu(111) could not

be clarified with final conclusiveness.

It is noteworthy, that the preliminary experiments presented here are continued in the Möller group and the theoretical modeling of the large organic molecule was used as the basis of ongoing extensive studies by Roberto Robles [197]. Both, the recent experimental and theoretical approaches already yielded new results that will be discussed in detail in upcoming publications [225, 226, 227].

B. Appendix: CuPc Embedded in a Self-assembled Heterogeneous System on Cu(111)

B.1. Heterogeneous Organic Molecular Systems

In its main part, this thesis treats the dynamics of CuPc molecules adsorbed on a Copper(111) substrate. As a matter of course, CuPc on Cu(111) is not the only system studied in the context of this work. Quite some approaches have been made to prepare and investigate different combinations of substrates and adsorbates always accompanied by the question, whether or not the organic molecules might be found to switch in the one or the other way.

The results presented in this appendix are part of the diploma thesis by Maren Cottin [116] (german language) and have been published in the journal 'Applied Surface Science' in 2012 [169].

B.1.1. Motivation

Organic molecules offer a broad variety of e.g. electronic, optical, or magnetic properties and are therefore regarded promising candidates for future devices. Especially self-assembling behavior might help to tailor thin films on surfaces with well-defined properties for future applications. For this kind of bottom-up approaches, the variety of possible properties can be by far extended when heterogeneous systems are taken into account. Two or more species of molecules that interact with each other in a heterogeneous system may result in a thin film that exhibits completely new properties, independent from the

properties of single species molecular films consisting of its respective ingredients.

Charge transfer complexes are mixed molecular systems that exchange charge from one species to the other. One molecular species is the donor, the other one the acceptor. Therefore, such systems are often called donor-acceptor systems. The amount of charge transferred is determined by three factors: (1) the electron affinity of the acceptor, i.e. the energy that can be gained by the filling of the lowest unoccupied molecular orbital (LUMO); (2) the energy needed to ionize the donor molecule and (3) the energy gain due to the electrostatic interaction of donor and acceptor. One self-assembled prototype charge transfer complex will be investigated in this appendix.

The optical properties of organic donor-acceptor systems typically include strong absorption bands. Thus, they may be used to produce intense colors and thus to design organic electronic devices like organic solar cells or displays.

B.1.2. Examples of Organic Heterogeneous Systems

Phthalocyanine molecules are candidates for the application in organic photo voltaic cells (OPVCs) for example in combination with perylene derivatives or fullerenes. The power conversion efficiency for such systems reached about 1% in 1986 [228][1] in a planar heterojunction design.

More recently, in 2012, a power conversion efficiency of 4.56% could be achieved [11][2]. Nowadays, the so called dispersed heterojunction design is used, where the donor and the acceptor are intermixed, resulting in layer thicknesses in the order of the diffusion length of the excited electron-hole pair (exciton). This is desirable, since one has to deal with the so called 'exciton bottleneck': The OPVCs need to be designed to meet the requirements of both, high optical absorption and exciton diffusion [140]. The organic compounds offer high absorption but the exciton diffusion length for typical compounds are only in the order of nanometers (5-20nm [229], 8±3nm for CuPc and 40±5nm for C_{60} [138]). Another approach is the so called graded donor-acceptor heterojunction, which combines the advantages of planar heterojunctions with reduced diffusion length [140].

[1] under an illumination of 75mW/cm^2
[2] under an illumination of 100mW/cm^2 (= 1 sun)

In each case, planar layer stacking or intermixed compounds, the growth of the organic domains for technological applications takes advantage of the self-assembling behavior. The fundamental properties of inter-molecular interaction as well as molecule-substrate interaction need to be addressed by basic research in order to understand its crucial interplay in the scope of future application. A few examples for promising studies shall be given here:

The organic donor compound di-indenoperylene (DIP) and the acceptor fluorinated CuPc (F16CuPc) were reported to show long-range self-assembled binary monolayers on Au(111) and Cu(111) at ratios of DIP:F16CuPc = 1:1 and 2:1 [230, 231, 232].

Free base tetraphenylporphyrins (2HTPP) together with cobalt and iron centered tetraphenylporphyrin molecules (CoTPP and FeTPP) were intermixed on Ag(111) and studied as a function of the bias voltage by STM [216].

CuPc was used as the donor compound in a heterojunction with fullerene as the acceptor for the generation of OPVCs in combination with indium-tin oxide (ITO) as well as coated ITO substrates [139].

Further heterogeneous systems were prepared from Perylene and PTCDA [233], ZnPc and metalloporphyrins [234], CuPc and DIP [235], and CuPc and PTCDA [168].

B.1.3. The organic compound PTCDA

As an example, this appendix summarizes on LT-STM experiments on a heterostructure consistent of the well-characterized CuPc on Cu(111) with additional PTCDA molecules.

PTCDA (3,4,9,10-perylene-tetracarboxylicacid-dianhydride, $C_{24}H_8O_6$, Fig. B.1a) is another archetype molecule, which has already been intensely studied in surface science (review paper by F.S. Tautz: [236]). Just as CuPc, PTCDA is a planar species and typically adsorbs flat on a surfaces [237, 236]. Therefore, the π-orbitals of PTCDA maximize their overlap with the electronic structure of the surface resulting in a robust molecule-substrate bonding [238]. The strength of the bond to the surface increases in the sequence Au(111), Ag(111), Cu(111) [239]. The energetic positions of the highest occupied molecular orbital and the lowest unoccupied molecular orbital of PTCDA can be found in Fig. B.2 as highlighted by the red color. As a reference, the optical bandgaps several common organic compounds as well as several metal work functions are given [147].

On many surfaces, PTCDA reliably assembles in the so called 'herringbone' structure. This zig-zag arrangement growth in large and highly ordered 2D islands. Figure B.1b helps to understand why PTCDA prefers to grow in the herringbone structure. The electro-negative oxygen atoms attract charge and leave the borders of the perylene core positively charged. Therefore, the molecules tend to arrange in a pattern that allows them to minimize the distances in between the charges of opposite sign. The resulting herringbone arrangement can for example be seen in Fig. B.3c.

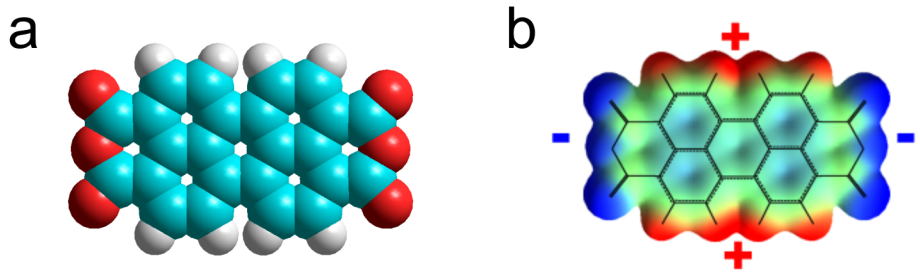

Figure B.1.: 3,4,9,10-Perylene-tetracarboxylicacid-dianhydride (PTCDA). (a) Model (blue: carbon, red: oxygen, white: hydrogen). (b) Charge distribution as calculated with 'hyperchem' [240]. The electronegative oxygen atoms attracts electrons (blue) from the borders of the perylene core which remains positively charged (red).

The self-assembled growth of PTCDA has been studied for example on graphite [241, 242], Au(111)[243], Ag(110) [244, 245], Ag(111) [246, 247], Cu(111) [248], InAs(001) [249] and KBr(001) [250, 251].

Furthermore, PTCDA is a candidate for the application in organic electronics, for example organic light emitting diodes (OLEDs) [252, 253] or OPVCs [254].

B.1.4. The Heterogeneous System CuPc + PTCDA

Lunt *et al.* reported on an organic heterojunction consisting of a CuPc film on top of a PTCDA film on a KBr substrate [142]. These films have a thickness of several hundred Angstroms and therefore it remains an open question how the intermixing of CuPc and PTCDA can be controlled in a bottom up approach, starting from islands or clusters in the monolayer.

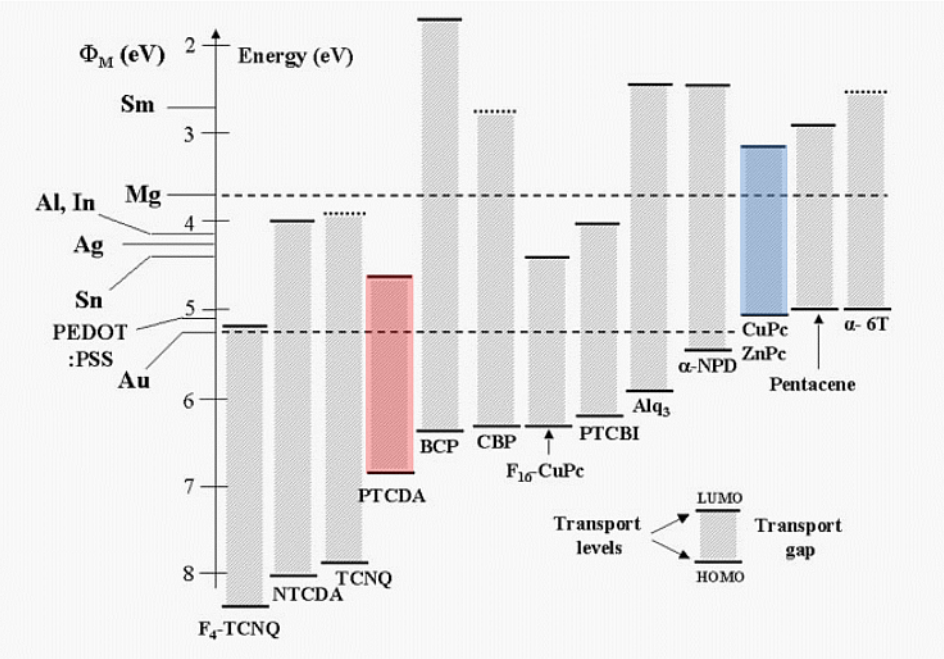

Figure B.2.: Comparison between the energetic positions of the highest occupied molecular orbitals (HOMO) and the lowest unoccupied molecular orbitals (LUMO) defining the optical bandgap, as determined by ultra-violet and inverse photoelectron spectroscopy (UPS, IPES) for different organic molecules. The red dye PTCDA is marked red and the blue dye CuPc is marked in blue color. The energy scale in eV is fixed by the common vacuum level (zero). As a reference, several metal work functions are given [147].

The experiments presented here focus on this aspect: the initial growth of the heterogeneous system CuPc + PTCDA on Cu(111).

From earlier work by the Möller group it is known that a CuPc + PTCDA heterostructure can be grown on Cu(111) [168]. Interestingly, it was reported, that a mixed phase with the stoichiometric ratio 1 PTCDA : 2 CuPc could be prepared only if CuPc was deposited first on the clean surface. The inverse preparation sequence did not result in the observation of a mixed structure [168].

Here, we want to transform a pre-patterned PTCDA submonolayer on the Cu(111) surface into a heterogeneous mixed structure. To accomplish this task, we include thermal annealing steps after the additional deposition of CuPc.

B.2. Experimental Results

The self assembly of the heterogeneous organic system CuPc + PTCDA on a Cu(111) surface (sec. 4.6) was studied using our home-built LT-STM (sec. 4.3) at 7K sample temperature. The experiments were started from a PTCDA pre-covered sample with a coverage of about 0.75ML (monolayers). On Cu(111) PTCDA assembles in single-layer thick islands. Onto this sample, small amounts of CuPc were deposited in several steps. Prior to each of the subsequent deposition steps, the sample was removed from the cooled STM and transferred into the preparation chamber at room-temperature. There, the sample was slightly annealed to about 100°C in order to remove adsorbates from the residual gas that sticked to the cold surface. Subsequently, CuPc was deposited onto the sample, at room-temperature or slightly above (20°C...70°C).

The STM data for the first stoichiometric ratio of 0.75ML PTCDA : 0.03ML CuPc can be seen in Fig. B.3. At this low coverages of CuPc, and without an annealing step after the CuPc deposition, no intermixed phases have is observed.

Two different types of PTCDA islands are found. In the following, the two phases are referred to as 'I' and 'II', as indicated in Fig. B.3. Structural models are given in (b) and (c) and zoom images are given in (d) and (e).

The unit cell for phase I contains eight molecules. The structure is closely related to the well-known herringbone pattern, which can be seen in phase II. The herringbone structure consists of zig-zag rows of PTCDA, with a two-molecule unit cell. As compared to this arrangement, the molecules of phase I are slightly rotated and form two groups of four molecules within the eight molecule unit cell.

In the following, we will focus on the interplay between PTCDA and CuPc. In contrast to the PTCDA molecules, the CuPc molecules are found randomly distributed on the free Cu(111) terraces and in addition, decorating the PTCDA island borders. The free CuPc molecules appear to repel each other as they are observed to spread out on the Cu(111) terraces with maximal distances to the next CuPc molecules. Neither PTCDA, nor CuPc molecules are observed in the second layer.

For the subsequent experiment, the sample was annealed to about 400K and the CuPc coverage was raised to about 0.1ML. The result is plotted in Fig. B.4.

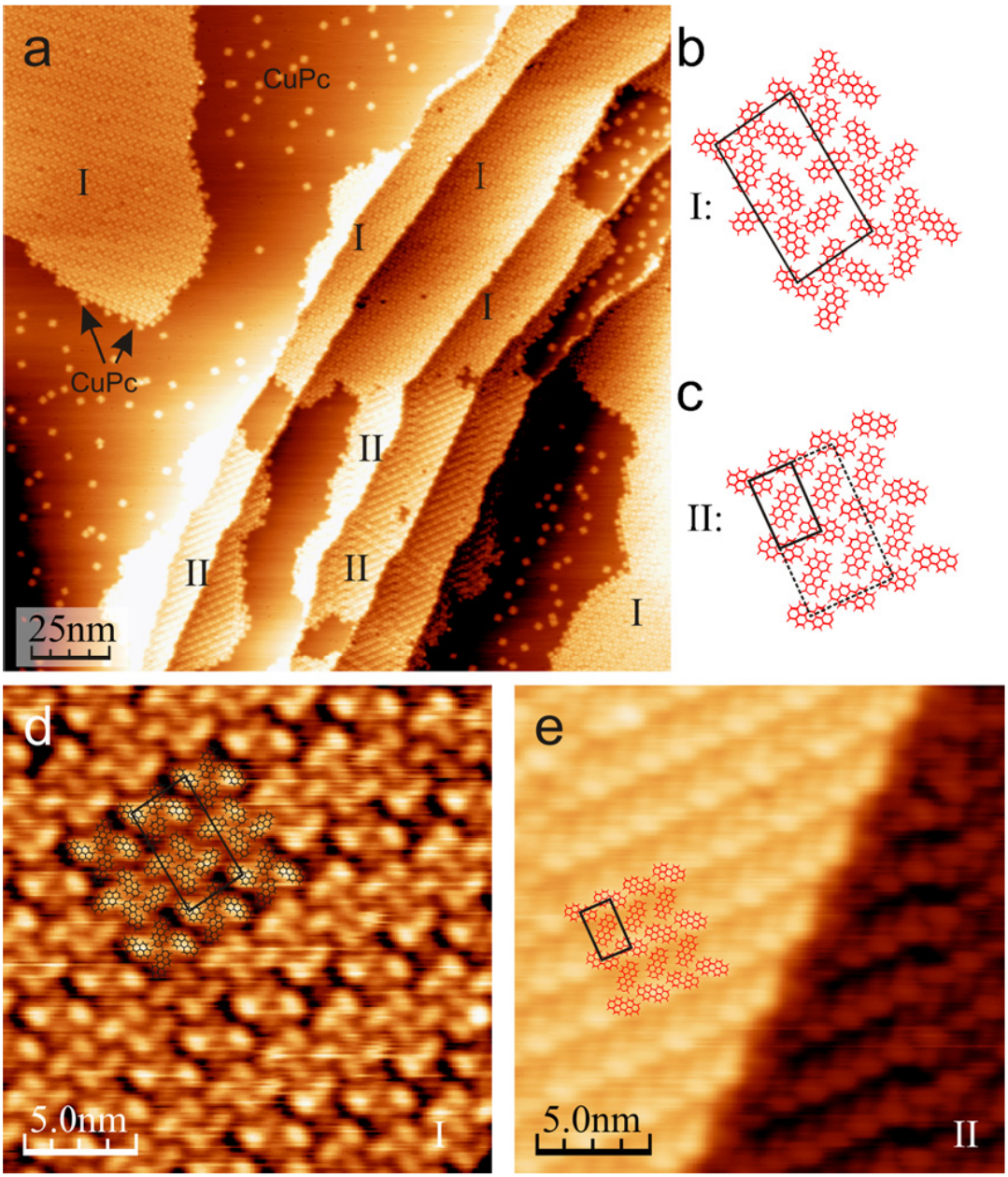

Figure B.3.: Low-temperature STM data showing 0.75ML PTCDA + 0.03ML CuPc on Cu(111). (a) PTCDA was deposited first and self-assembles to highly-ordered islands exhibiting two types of reconstructions: (I) and (II). CuPc decorates the island borders or adsorbs on the free Cu(111) terraces. (b+c) Structural models of the two PTCDA structures including the eight molecule unit cell (phase I) and the two molecule unit cell (phase II). For comparison with phase II, the four times larger unit cell of phase I is plotted as a dashed rectangle, indicating the close resemblance of the two phases. (d) Zoomed STM image of phase I. (e) Zoomed STM image of phase II. $V_{sample} = -0.5V, I = 320pA, T = 7K$ [169].

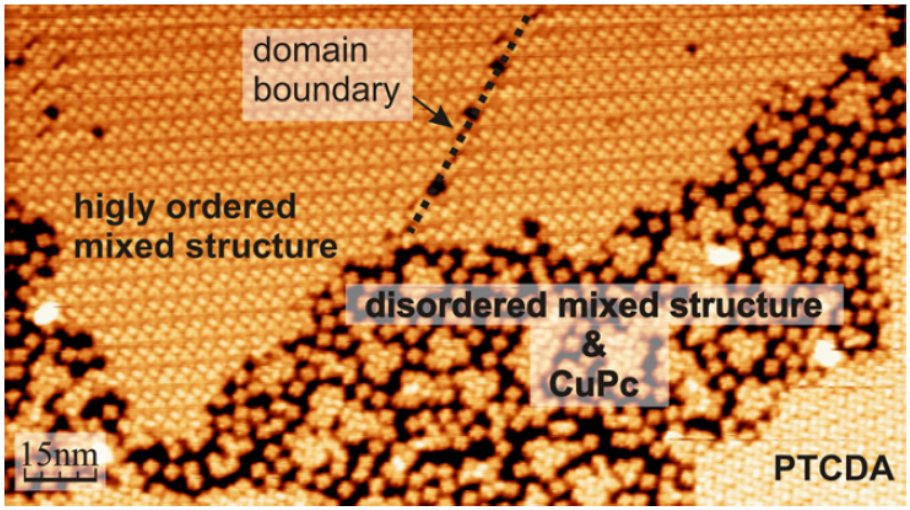

Figure B.4.: STM image of the same system after an annealing step to about 400K and the subsequent deposition of CuPc, resulting in the stoichiometric ratio of 0.75ML PTCDA : 0.1ML CuPc. A mixed structure consisting of both molecular species can now be observed. The mixed islands exhibit high order and extend over more than one hundred nanometers. Pure PTCDA phases are still observed, too. In addition, groups of PTCDA molecules are now found in a disordered structure, entirely surrounded by CuPc molecules. $V_{sample} = 2V, I = 20pA, T = 7K$ [169].

Interestingly, a highly ordered mixed phase of CuPc and PTCDA is now observed. Two PTCDA molecules and one CuPc molecule now form a unit cell in which a zig-zag row of PTCDA molecules is conserved, while these herring-bone like rows are interconnected by the CuPc molecules. The comparably large island containing the self-assembled mixed structure in Fig. B.4 exhibits a domain boundary as marked by the arrow. Despite this, only a few defects due to missing molecules can be found in the observed island. The long-range order is typically as high as it was in the pure PTCDA islands before the preparation step. A structural model for the heterostructure is given in Fig. B.5c+d.

In addition to the mixed phase, pure PTCDA islands still exist on the sample. Also, there are still individually adsorbed CuPc molecules left on the Cu(111) terraces. It can be seen, that the symmetry reduction, which was discussed in the main part of this thesis, is still present in the data. The individual CuPc appear with a two-fold symmetry and even when arranged in the mixed phase, two out of the four molecular lobes appear brighter in the STM topography.

In contrast to the first investigated stoichiometric ratio, small groups of typically three or more PTCDA molecules are found on the terraces as well, and all of them are entirely surrounded by CuPc. The most frequently observed clusters consisting of 3 PTCDA + 6 CuPc can be seen in Fig. B.5a+b.

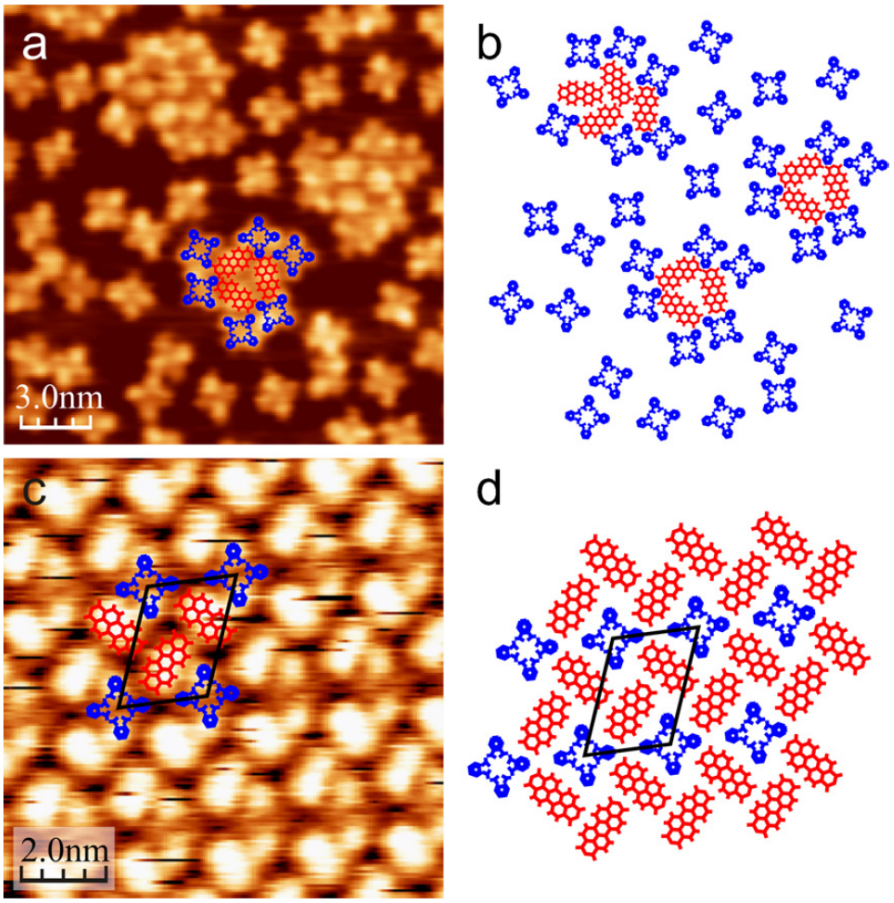

Figure B.5.: (a) STM image and (b) model of the disordered mixed phase exhibiting typical clusters of 3 PTCDA and 6 surrounding CuPc molecules as highlighted by the structural models. The remaining CuPc molecules are distributed randomly on the Cu(111) terraces. $V_{sample} = 2V, I = 10pA$. (c) STM image and (d) model of the highly ordered mixed phase with a stoichiometric ratio of 2 PTCDA : 1 CuPc including a unit cell (black). $V_{sample} = 1V, I = 30pA$. $T = 7K$ [169].

In order to quantify the areas covered by the self-assembled phases found for this stoichiometry (0.75ML PTCDA : 0.1ML CuPc) we evaluated two large STM scans with

the size of 500nm × 500nm, which could be measured over-night at stable tunneling conditions. The PTCDA herringbone structure still covered 70% of the investigated surface area, while the highly ordered mixed phase covers 8% of the area and the remaining 22% is dominated by the disordered mixed structure and individual CuPc molecules.

Afterwards, the sample was again annealed to 400K and the amount of CuPc molecules was increased to about 0.17ML. Unfortunately, a close inspection by STM became impossible, since organic clusters and/or other adsorbates grew in 3D and inhibited the analysis of larger areas of the surface. In small scans in between these 3D defects however, the mixed phase was mainly observed. We used low-energy electron diffraction (LEED) as a complementary method to identify the dominating phase on the surface. The results which were obtained at room-temperature are shown in Fig. B.6a.

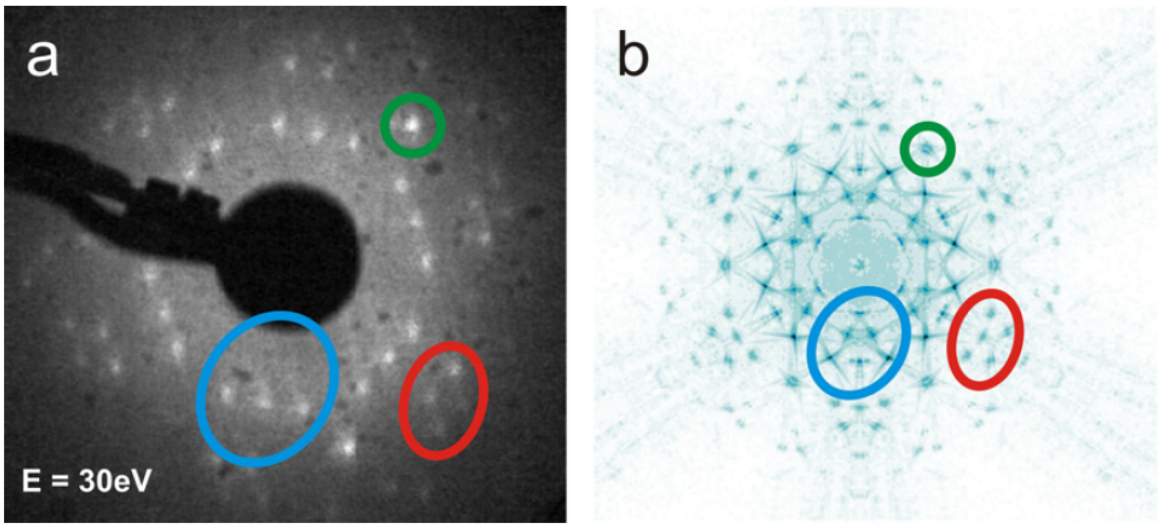

Figure B.6.: (a) Low-energy electron diffraction (LEED) pattern measured for the stoichiometric ratio of 0.75ML PTCDA : 0.17ML CuPc on the Cu(111) surface. (b) Corresponding simulated diffraction pattern derived from STM images of the highly ordered mixed Phase. Qualitative resemblance is found, indicating that the mixed phase covers substantial parts of the sample [169].

For comparison, we simulated the diffraction pattern by calculating the fast Fourier transform (FFT) of STM data of the mixed phase. As the self-assembled islands are expected to grow in alignment with one of the three symmetry axes of the underlying substrate, we duplicated the resulting pattern and rotated the duplicates according to the symmetry axes

of the sample. The measured and the simulated diffraction patterns can be seen in Fig. B.6.

Indeed, the LEED spots (a) coincide with the FFT pattern derived from the STM data (b). In the LEED data, groups of three maxima with a very faint underlying triangular pattern can be seen. One of these groups is marked by the blue circle and identified in the simulated pattern as well. The bright spot marked by the green circle and the spot group marked in red can also be recognized at the corresponding positions, although the relative intensities of the LEED spots are by no means comparable to the FFT data derived from STM.

B.3. Discussion

After the first preparation (0.75ML PTCDA + 0.03ML CuPc), no binary phase was observed. Nevertheless, already for the smallest dosage of CuPc a strong intermolecular interaction is observed. The PTCDA island borders are entirely decorated by CuPc molecules. The remaining CuPc molecules on the Cu(111) terraces repel each other [255] since they compete for the so called donation/backdonation process of charge from the substrate to lowest unoccupied molecular orbitals and from the filled molecular states to the substrate. However, the two processes (the donation and the backdonation of charge) do not cancel out completely resulting in an accumulation of negative charge as demonstrated by Stadler *et al.* for the exemplary system SnPc/Ag(111). The authors report that for CuPc the molecule substrate interaction is basically the same with a weaker donation effect due to a smaller orbital overlap [255].

The observed pure PTCDA islands were found to exhibit island borders completely decorated by CuPc molecules. The PTCDA molecules (Fig. B.3) assembled in the well-known herringbone structure with the typical two molecular unit cell and in addition, in a more complex arrangement with eight molecules in the unit cell. The initial growth of PTCDA on Cu(111) was studied before in the Möller group. Two phases observed in the first monolayer have already been described in detail for room-temperature STM experiments by the Wagner *et al.* in ref. [248]. However, the structure reported here does not match the characteristics of the cited work. The molecules appear in a closer packing and are found to be rotated in plane as compared to the herringbone structure. The new structure may be attributed to the low-temperature conditions (7K) assuming a phase-transition that occurs during the cooling of the sample. This was discussed in the

thesis by H. Karacuban (ref. [23]).

After an annealing step to about 400K and the subsequent deposition of CuPc, resulting in the stoichiometric ratio of 0.75ML PTCDA : 0.1ML CuPc a mixed structure is observed. The mixed islands resemble the ones reported by Bobisch *et al.* [168]. The islands exhibit high order and extend over more than one hundred nanometers. Pure PTCDA phases are still observed, too. In addition, groups of PTCDA molecules are now found in a disordered structure, entirely surrounded by CuPc molecules. One may interpret the disordered structure as an intermediate state in between phase separation and the intermixed phase. The most frequently observed clusters consist of 3 PTCDA molecules and 6 CuPc molecules (Fig. B.5a+b). The attractive intermolecular interaction between PTCDA and CuPc is stronger than the CuPc - CuPc repulsion. This is reflected by the observation of CuPc molecules in close contact to each other as soon as PTCDA is involved in the formation of the clusters.

The CuPc molecules appear in a two-fold symmetry not only when adsorbed individually on Cu(111), as reported in the main part of this work, but also when embedded in the heterogeneous system with PTCDA. The symmetry reduction from four-fold in the gas phase to two-fold on the substrate is not only maintained in the mixed phase, but even enhanced in STM contrast.

When the coverage of CuPc was further raised to about 0.17ML, larger parts of the surface are expected to be covered with the highly ordered mixed phase. Due to a lack of STM data on this system, LEED had to be used for a large-scale characterization. We combine the diffraction data with the FFT of STM data of the mixed phase for comparison (Fig.B.6). Indeed, the main features could be reproduced in this way. In contrast, comparing the LEED pattern with the FFT of STM images of pure PTCDA islands does not result in a considerable similarity (see the diploma thesis by Maren Cottin, ref. [116]) Thus, we conclude, that the highly ordered mixed phase now covers substantial parts of the surface.

Summarizing the CuPc coverage dependent study, we have learned how to transform highly ordered PTCDA islands into the highly ordered CuPc+PTCDA mixed phase. We used the inverse preparation sequence compared to the previous work [168]. The key preparation step is a moderate annealing to 400K. Thus, the preparation of the heterogeneous system

has become easier and the adjustment of different coverage on the sample has been found to be possible by the stepwise deposition of additional CuPc.

In the previous work, the additionally adsorbed PTCDA molecules could easily be used for the mixed structure growth due to the individually adsorbed and at room temperature highly diffusive CuPc molecules.

Here instead, the annealing to 400K is assumed to be the reason for the successful preparation starting from pure and stable PTCDA islands. The extra thermal energy may allow the highly diffusive CuPc to diffuse on top of the PTCDA islands (not only on the free Cu(111) terraces) and thus, to maximize the molecule - molecule interaction. This interaction is then energetically favored compared to the pure PTCDA assembly such that the PTCDA islands are cracked and PTCDA is dissolved from its dense islands. Also the in-plane penetration of CuPc molecules into the PTCDA island borders may be feasible. The cracking process results in mixed molecular clusters. The clusters are then complemented by additional molecules or by clusters that may diffuse (due to thermal energy at room-temperature or during the annealing step) and form the thermodynamically favored highly ordered mixed structure.

Alternatively, the cracking of the PTCDA islands might not be caused by intruding CuPc molecules but by a continued dissolution of PTCDA from the island borders due to the extra thermal energy upon annealing. In this scenario, the dissolved PTCDA molecules would quickly be surrounded by the highly mobile CuPc molecules. This picture would result in the same disordered cluster phase and - after annealing - lead to the highly ordered mixed structure as well.

As a matter of fact, no STM or LEED data exist, that can give final insight into the structural evolution during the annealing steps. Although the self-built STM allows to perform variable-temperature experiments, it is not possible to image CuPc at temperatures above 50K, since it is highly mobile. However, the mixed phase as well as the pure PTCDA phases might be observable in future experiments. The image quality cannot be expected to be as high as reported here, because the diffusing CuPc molecules under the tip of the STM will render stable imaging conditions impossible. In addition, it has to be expected, that organic material would stick to the STM tip resulting in worsened image quality. In order to avoid these technical problems, future studies might use a different approach. Temperature and coverage dependent LEED studies should help to gain further insight in

the initial growth of the PTCDA + CuPc binary system on Cu(111).

A different, complementary technique perfectly suited to study growth phenomena is the low-energy electron microscope (LEEM) [256] which is often used in the photoelectron emission microscopy (PEEM) mode to observe e.g. the growth of organic molecules on surfaces in real time [257].

In conclusion, this appendix has shown a new route to prepare a two-dimensional highly ordered self-assembled binary organic molecular system on the Cu(111) surface. In contrast to previous work, we were able to start from a pre-patterned sample and could control the characteristics of the binary system by the dosage of additional material.

Bibliography

[1] Wada, Y.: Prospects for single molecule information processing devices. In: *Proceedings of the IEEE* 89 (2001), aug, Nr. 8, S. 1147 –1173. http://dx.doi.org/10.1109/5.940278. – DOI 10.1109/5.940278. – ISSN 0018–9219

[2] Kim, Dae-Hyeong ; Lu, Nanshu ; Ma, Rui ; Kim, Yun-Soung ; Kim, Rak-Hwan ; Wang, Shuodao ; Wu, Jian ; Won, Sang M. ; Tao, Hu ; Islam, Ahmad ; Yu, Ki J. ; Kim, Tae-il ; Chowdhury, Raeed ; Ying, Ming ; Xu, Lizhi ; Li, Ming ; Chung, Hyun-Joong ; Keum, Hohyun ; McCormick, Martin ; Liu, Ping ; Zhang, Yong-Wei ; Omenetto, Fiorenzo G. ; Huang, Yonggang ; Coleman, Todd ; Rogers, John A.: Epidermal Electronics. In: *Science* 333 (2011), Nr. 6044, 838-843. http://dx.doi.org/10.1126/science.1206157. – DOI 10.1126/science.1206157

[3] Hwang, Suk-Won ; Tao, Hu ; Kim, Dae-Hyeong ; Cheng, Huanyu ; Song, Jun-Kyul ; Rill, Elliott ; Brenckle, Mark A. ; Panilaitis, Bruce ; Won, Sang M. ; Kim, Yun-Soung ; Song, Young M. ; Yu, Ki J. ; Ameen, Abid ; Li, Rui ; Su, Yewang ; Yang, Miaomiao ; Kaplan, David L. ; Zakin, Mitchell R. ; Slepian, Marvin J. ; Huang, Yonggang ; Omenetto, Fiorenzo G. ; Rogers, John A.: A Physically Transient Form of Silicon Electronics. In: *Science* 337 (2012), Nr. 6102, 1640-1644. http://dx.doi.org/10.1126/science.1226325. – DOI 10.1126/science.1226325

[4] Geffroy, Bernard ; Roy, Philippe le ; Prat, Christophe: Organic light-emitting diode (OLED) technology: materials, devices and display technologies. In: *Polymer International* 55 (2006), Nr. 6, 572–582. http://dx.doi.org/10.1002/pi.1974. – DOI 10.1002/pi.1974. – ISSN 1097–0126

[5] Görrn, P. ; Sander, M. ; Meyer, J. ; Kröger, M. ; Becker, E. ; Johannes, H.-H. ; Kowalsky, W. ; Riedl, T.: Towards See-Through Dis-

plays: Fully Transparent Thin-Film Transistors Driving Transparent Organic Light-Emitting Diodes. In: *Advanced Materials* 18 (2006), Nr. 6, 738–741. http://dx.doi.org/10.1002/adma.200501957. – DOI 10.1002/adma.200501957. – ISSN 1521–4095

[6] Mizukami, M. ; Hirohata, N. ; Iseki, T. ; Ohtawara, K. ; Tada, T. ; Yagyu, S. ; Abe, T. ; Suzuki, T. ; Fujisaki, Y. ; Inoue, Y. ; Tokito, S. ; Kurita, T.: Flexible AM OLED panel driven by bottom-contact OTFTs. In: *Electron Device Letters, IEEE* 27 (2006), Nr. 4, S. 249–251. http://dx.doi.org/10.1109/LED.2006.870413. – DOI 10.1109/LED.2006.870413. – ISSN 0741–3106

[7] Park, Jin-Seong ; Chae, Heeyeop ; Chung, Ho K. ; Lee, Sang I.: Thin film encapsulation for flexible AM-OLED: a review. In: *Semiconductor Science and Technology* 26 (2011), Nr. 3, 034001. http://stacks.iop.org/0268-1242/26/i=3/a=034001

[8] Mannini, M. ; Pineider, F. ; Sainctavit, P. ; Danieli, C. ; Otero, E. ; Sciancalepore, C. ; Talarico, A.M. ; Arrio, M.-A. ; Cornia, A. ; Gatteschi, D. ; Sessoli, R.: Magnetic memory of a single-molecule quantum magnet wired to a gold surface. In: *Nature Materials* 8 (2009), S. 194–197. http://dx.doi.org/10.1038/nmat2374. – DOI 10.1038/nmat2374

[9] Wang, Yongfeng ; Kröger, Jörg ; Berndt, Richard ; Hofer, Werner A.: Pushing and Pulling a Sn Ion through an Adsorbed Phthalocyanine Molecule. In: *Journal of the American Chemical Society* 131 (2009), Nr. 10, 3639-3643. http://dx.doi.org/10.1021/ja807876c. – DOI 10.1021/ja807876c. – PMID: 19243166

[10] So, Franky ; Kido, Junji ; Burrows, Paul: Organic Light-Emitting Devices for Solid-State Lighting. In: *MRS Bulletin* 33 (2008), 7, 663–669. http://dx.doi.org/10.1557/mrs2008.137. – DOI 10.1557/mrs2008.137. – ISSN 1938–1425

[11] Zhou, Y. ; Taima, T. ; Miyadera, T. ; Yamanari, T. ; Kitamura, M. ; Nakatsu, K. ; Yoshida, Y.: Phase separation of co-evaporated ZnPc:C60 blend film for highly efficient organic photovoltaics. In: *Applied Physics Letters* 100 (2012), S. 233302. http://dx.doi.org/10.1063/1.4726118. – DOI 10.1063/1.4726118

[12] Gimzewski, J. K. ; Joachim, C.: Nanoscale science of single molecules using local probes. In: *Science* 283 (1999), Nr. 5408, S. 1683–1688. http://dx.doi.org/10.1126/science.283.5408.1683. – DOI 10.1126/science.283.5408.1683

[13] Grill, Leonhard: Functionalized molecules studied by STM: motion, switching and reactivity. In: *Journal of Physics: Condensed Matter* 20 (2008), Nr. 5, S. 053001. http://dx.doi.org/10.1088/0953-8984/20/05/053001. – DOI 10.1088/0953–8984/20/05/053001

[14] Morgenstern, Karina ; Lorente, Nicolas ; Rieder, Karl-Heinz: Controlled manipulation of single atoms and small molecules using the scanning tunnelling microscope. In: *physica status solidi (b)* (2013), n/a–n/a. http://dx.doi.org/10.1002/pssb.201248392. – DOI 10.1002/pssb.201248392. – ISSN 1521–3951

[15] Uren, M. J. ; Day, D. J. ; Kirton, M. J.: 1/f and random telegraph noise in silicon metal-oxide-semiconductor field-effect transistors. In: *Applied Physics Letters* 47 (1985), Nr. 11, 1195-1197. http://dx.doi.org/10.1063/1.96325. – DOI 10.1063/1.96325

[16] Hung, K.K. ; Ko, P.K. ; Hu, C. ; Cheng, Y.C.: Random telegraph noise of deep-submicrometer MOSFETs. In: *Electron Device Letters, IEEE* 11 (1990), feb., Nr. 2, S. 90 –92. http://dx.doi.org/10.1109/55.46938. – DOI 10.1109/55.46938. – ISSN 0741–3106

[17] Fang, P. ; Hung, K.K. ; Ko, P.K. ; Hu, C.: Hot-electron-induced traps studied through the random telegraph noise. In: *Electron Device Letters, IEEE* 12 (1991), june, Nr. 6, S. 273 –275. http://dx.doi.org/10.1109/55.82058. – DOI 10.1109/55.82058. – ISSN 0741–3106

[18] Monzio Compagnoni, C. ; Gusmeroli, R. ; Spinelli, A.S. ; Lacaita, A.L. ; Bonanomi, M. ; Visconti, A.: Statistical Model for Random Telegraph Noise in Flash Memories. In: *Electron Devices, IEEE Transactions on* 55 (2008), jan., Nr. 1, S. 388 –395. http://dx.doi.org/10.1109/TED.2007.910605. – DOI 10.1109/TED.2007.910605. – ISSN 0018–9383

[19] Soni, R. ; Meuffels, P. ; Petraru, A. ; Weides, M. ; Kügeler, C. ; Waser, R. ; Kohlstedt, H.: Probing Cu doped Ge[sub 0.3]Se[sub 0.7] based resistance

switching memory devices with random telegraph noise. In: *Journal of Applied Physics* 107 (2010), Nr. 2, 024517. http://dx.doi.org/10.1063/1.3291132. – DOI 10.1063/1.3291132

[20] Wang, Xinyang ; Rao, P.R. ; Mierop, A. ; Theuwissen, A.J.P.: Random Telegraph Signal in CMOS Image Sensor Pixels. In: *Electron Devices Meeting, 2006. IEDM '06. International*, 2006, S. 1 –4

[21] Brederlow, R. ; Prakash, R. ; Paulus, C. ; Thewes, R.: A low-power true random number generator using random telegraph noise of single oxide-traps. In: *Solid-State Circuits Conference, 2006. ISSCC 2006. Digest of Technical Papers. IEEE International*, 2006. – ISSN 0193–6530, S. 1666 –1675

[22] Tokunaga, C. ; Blaauw, D. ; Mudge, T.: True Random Number Generator With a Metastability-Based Quality Control. In: *Solid-State Circuits, IEEE Journal of* 43 (2008), jan., Nr. 1, S. 78 –85. http://dx.doi.org/10.1109/JSSC.2007.910965. – DOI 10.1109/JSSC.2007.910965. – ISSN 0018–9200

[23] Karacuban, H.: *Grenzflächeneigenschaften organischer Moleküle auf Metalloberflächen*. Faculty of Physics, Surface Science Group Prof. Möller, Lotharstr. 1, 47048 Duisburg, Germany, University of Duisburg-Essen, Diss., 2010. http://d-nb.info/1001255755/34

[24] Karacuban, H. ; Lange, M. ; Schaffert, J. ; Weingart, O. ; Wagner, T. ; Möller, R.: Substrate-induced symmetry reduction of CuPc on Cu(111): An LT-STM study. In: *Surface Science* 603 (2009), Nr. 5, S. L39–L43. http://dx.doi.org/10.1016/j.susc.2009.01.029. – DOI 10.1016/j.susc.2009.01.029

[25] Durig, U. ; Pohl, D. W. ; Rohner, F.: Near-field optical-scanning microscopy. In: *Journal of Applied Physics* 59 (1986), Nr. 10, 3318-3327. http://dx.doi.org/10.1063/1.336848. – DOI 10.1063/1.336848

[26] Fowler, R.H. ; Nordheim, L.: Electron emission in intense electric fields. In: *Proc. R. Soc. Lond. A* 119 (1928), S. 173–181. http://dx.doi.org/10.1098/rspa.1928.0091. – DOI 10.1098/rspa.1928.0091

[27] *www.nobelprize.org*. www.nobelprize.org

[28] Bernhart, A.M.: *Mikroskopie mit ballistischen Elektronen und Löchern*. Faculty of Physics, Surface Science Group Prof. Möller, Lotharstr. 1, 47048 Duisburg, Germany, University of Duisburg-Essen, Diss., 2012

[29] Kaspers, M.: *Potentiometrie- und Elektromigrationsuntersuchungen an metallischen Oberflächen*. Faculty of Physics, Surface Science Group Prof. Möller, Lotharstr. 1, 47048 Duisburg, Germany, University of Duisburg-Essen, Diss., 2013

[30] Tersoff, J. ; Hamann, D. R.: Theory and Application for the Scanning Tunneling Microscope. In: *Physical Review Letters* 50 (1983), S. 1998–2001. http://dx.doi.org/10.1103/PhysRevLett.50.1998. – DOI 10.1103/PhysRevLett.50.1998

[31] Tersoff, J. ; Hamann, D. R.: Theory of the scanning tunneling microscope. In: *Phys. Rev. B* 31 (1985), Jan, 805–813. http://dx.doi.org/10.1103/PhysRevB.31.805. – DOI 10.1103/PhysRevB.31.805

[32] Bardeen, J.: Tunnelling from a Many-Particle Point of View. In: *Phys. Rev. Lett.* 6 (1961), Jan, 57–59. http://dx.doi.org/10.1103/PhysRevLett.6.57. – DOI 10.1103/PhysRevLett.6.57

[33] Chen, C. J.: Origin of atomic resolution on metal surfaces in scanning tunneling microscopy. In: *Phys. Rev. Lett.* 65 (1990), Jul, 448–451. http://dx.doi.org/10.1103/PhysRevLett.65.448. – DOI 10.1103/PhysRevLett.65.448

[34] Besenbacher, Flemming: Scanning tunnelling microscopy studies of metal surfaces. In: *Reports on Progress in Physics* 59 (1996), Nr. 12, S. 1737. http://dx.doi.org/10.1088/0034-4885/59/12/004. – DOI 10.1088/0034–4885/59/12/004

[35] Baró, A.M. ; Miranda, R. ; Alamán, J. ; García, N. ; Binnig, G. ; Rohrer, H. ; Gerber, Ch. ; Carrascosa, J.L.: Determination of surface topography of biological specimens at high resolution by scanning tunneling microscopy. In: *Nature* 315 (1985), S. 253–254. http://dx.doi.org/10.1038/315253a0. – DOI 10.1038/315253a0

[36] Gimzewski, J.K. ; Stoll, E. ; Schlittler, R.R.: Scanning tunneling microscopy of individual molecules of copper phthalocyanine adsorbed on polycrystalline silver surfaces. In: *Surface Science* 181 (1987), Nr. 1-2, 267-277. http://dx.doi.org/

10.1016/0039-6028(87)90167-1. – DOI 10.1016/0039–6028(87)90167–1. – ISSN 0039–6028

[37] Ohtani, H. ; Wilson, R. J. ; Chiang, S. ; Mate, C. M.: Scanning Tunneling Microscopy Observations of Benzene Molecules on the Rh(111)-(3 $\times$3) (C_6H_6 + 2CO) Surface. In: *Phys. Rev. Lett.* 60 (1988), Jun, 2398–2401. http://dx.doi.org/10.1103/PhysRevLett.60.2398. – DOI 10.1103/PhysRevLett.60.2398

[38] Lang, N. D.: Vacuum tunneling current from an adsorbed atom. In: *Phys. Rev. Lett.* 55 (1985), Jul, 230–233. http://dx.doi.org/10.1103/PhysRevLett.55.230. – DOI 10.1103/PhysRevLett.55.230

[39] Lang, N. D.: Theory of Single-Atom Imaging in the Scanning Tunneling Microscope. In: *Phys. Rev. Lett.* 56 (1986), Mar, 1164–1167. http://dx.doi.org/10.1103/PhysRevLett.56.1164. – DOI 10.1103/PhysRevLett.56.1164

[40] Lang, N. D.: Spectroscopy of single atoms in the scanning tunneling microscope. In: *Phys. Rev. B* 34 (1986), Oct, 5947–5950. http://dx.doi.org/10.1103/PhysRevB.34.5947. – DOI 10.1103/PhysRevB.34.5947

[41] Tsukada, Masaru ; Kobayashi, Katsuyoshi ; Isshiki, Nobuyuki ; Kageshima, Hiroyuki: First-principles theory of scanning tunneling microscopy. In: *Surface Science Reports* 13 (1991), Nr. 8, 267 - 304. http://dx.doi.org/10.1016/0167-5729(91)90006-J. – DOI 10.1016/0167–5729(91)90006–J. – ISSN 0167–5729

[42] Sautet, P. ; Joachim, C.: Electronic transmission coefficient for the single-impurity problem in the scattering-matrix approach. In: *Phys. Rev. B* 38 (1988), Dec, 12238–12247. http://dx.doi.org/10.1103/PhysRevB.38.12238. – DOI 10.1103/PhysRevB.38.12238

[43] Sautet, P. ; Joachim, C. ; L., Bocquet M. ; Sameron, M.: STM image calculation for adsorbate recognition. In: *Annales de Chimie France* 17 (1992), S. 217–227

[44] Sautet, P. ; Joachim, C.: Interpretation of STM images: copper-phthalocyanine on copper. In: *Surface Science* 271 (1992), Nr. 3, 387 - 394. http://dx.doi.

org/10.1016/0039-6028(92)90902-I. – DOI 10.1016/0039–6028(92)90902–I. – ISSN 0039–6028

[45] Feenstra, Randall M.: Scanning tunneling spectroscopy. In: *Surface Science* 299-300 (1994), Nr. 0, 965-979. http://dx.doi.org/10.1016/0039-6028(94)90710-2. – DOI 10.1016/0039–6028(94)90710–2. – ISSN 0039–6028

[46] Stroscio, Joseph A. ; Feenstra, R. M. ; Fein, A. P.: Electronic Structure of the Si(111)2x1 Surface by Scanning-Tunneling Microscopy. In: *Phys. Rev. Lett.* 57 (1986), Nov, 2579–2582. http://dx.doi.org/10.1103/PhysRevLett.57.2579. – DOI 10.1103/PhysRevLett.57.2579

[47] Feenstra, R.M. ; Stroscio, J.A. ; Fein, A.P.: Tunneling spectroscopy of the Si(111)2 times 1 surface. In: *Surface Science* 181 (1987), Nr. 1-2, 295-306. http://dx.doi.org/10.1016/0039-6028(87)90170-1. – DOI 10.1016/0039–6028(87)90170–1. – ISSN 0039–6028

[48] Binnig, G. ; Rohrer, H. ; Gerber, C. ; Weibel, E.: Surface Studies by Scanning Tunneling Microscopy. In: *Physical Review Letters* 49 (1982), S. 57–61. http://dx.doi.org/10.1103/PhysRevLett.49.57. – DOI 10.1103/PhysRevLett.49.57

[49] Hagedorn, T. ; El Ouali, M. ; Paul, W. ; Oliver, D. ; Miyahara, Y. ; Grütter, P.: Refined tip preparation by electrochemical etching and ultrahigh vacuum treatment to obtain atomically sharp tips for scanning tunneling microscope and atomic force microscope. In: *Review of Scientific Instruments* 82 (2011), S. 113903. http://dx.doi.org/10.1063/1.3660279. – DOI 10.1063/1.3660279

[50] Lucier, A.-S.: *Preparation and characterization of tungsten tips suitable for molecular electronics studies*, McGill University, Montréal, Canada, Thesis, 2004

[51] Ibe, J.P. ; Bey, P.P. ; Brandow, S.L. ; Brizzolara, R.A. ; Burnham, N.A. ; DiLella, D.P. ; Lee, K.P. ; Marrian, C.R.K. ; Colton, R.J.: On the electrochemical etching of tips for scanning tunneling microscopy. In: *J. Vac. Sci. Technol. A* 8 (1990), Nr. 4, S. 3570. http://dx.doi.org/10.1116/1.576509. – DOI 10.1116/1.576509

[52] Melmed, A.J.: The art and science and other aspects of making sharp tips. In: *J. Vac. Sci. Technol. B* 9 (1991), Nr. 2, S. 601. http://dx.doi.org/10.1116/1.585467. – DOI 10.1116/1.585467

[53] Matena, M.: *Mikroskopie mit ballistischen Elektronen*. Faculty of Physics, Lotharstr. 1, 47048 Duisburg, Germany, University of Duisburg-Essen, Duisburg, Germany, Diploma thesis, 2005

[54] Koslowski, B.: *Tunnelstromrauschen in der Raster-Tunnel-Mikroskopie*. Konstanzer Dissertationen, Band 395, Hartung-Gorre Verlag, Konstanz, Universität Konstanz, Diss., 1993. – ISSN 0930-8105 ISBN 3-89191-706-6

[55] Weissman, M. B.: $\frac{1}{f}$ noise and other slow, nonexponential kinetics in condensed matter. In: *Rev. Mod. Phys.* 60 (1988), Apr, 537–571. http://dx.doi.org/10.1103/RevModPhys.60.537. – DOI 10.1103/RevModPhys.60.537

[56] Stoll, E. ; Marti, O.: Restoration of scanning-tunneling-microscope data blurred by limited resolution, and hampered by 1f-like noise. In: *Surface Science* 181 (1987), Nr. 1-2, 222-229. http://dx.doi.org/10.1016/0039-6028(87)90162-2. – DOI 10.1016/0039–6028(87)90162–2. – ISSN 0039–6028

[57] Abraham, D.W. ; Williams, C.C. ; Wickramasinghe, H.K.: Noise reduction technique for scanning tunneling microscopy. In: *Appl. Phys. Lett.* 53 (1988), S. 1503. http://dx.doi.org/10.1063/1.99940. – DOI 10.1063/1.99940

[58] Moller, R. ; Esslinger, A. ; Koslowski, B.: Noise in vacuum tunneling: Application for a novel scanning microscope. In: *Applied Physics Letters* 55 (1989), nov, Nr. 22, S. 2360 –2362. http://dx.doi.org/10.1063/1.102018. – DOI 10.1063/1.102018. – ISSN 0003–6951

[59] Welland, M.E. ; Koch, R.H.: Spatial location of electron trapping defects on silicon by scanning tunneling microscopy. In: *Appl. Phys. Lett.* 48 (1986), S. 724. http://dx.doi.org/10.1063/1.96702. – DOI 10.1063/1.96702

[60] Eigler, D. M. ; Lutz, C. P. ; Rudge, W. E.: AN ATOMIC SWITCH REALIZED WITH THE SCANNING TUNNELING MICROSCOPE. In: *Nature* 352 (1991), Nr. 6336, S. 600–603. http://dx.doi.org/10.1038/352600a0. – DOI 10.1038/352600a0

[61] Lyo, I.-W. ; Avouris, P.: Field-Induced Nanometer- to Atomic-Scale Manipulation of Silicon Surfaces with the STM. In: *Science* 253 (1991), S. 173–176. http://dx.doi.org/DOI:10.1126/science.253.5016.173. – DOI DOI:10.1126/science.253.5016.173

[62] Stipe, B. C. ; Rezaei, M. A. ; Ho, W.: Inducing and viewing the rotational motion of a single molecule. In: *Science* 279 (1998), Nr. 5358, S. 1907–1909. http://dx.doi.org/10.1126/science.279.5358.1907. – DOI 10.1126/science.279.5358.1907

[63] Stroscio, Joseph A. ; Celotta, Robert J.: Controlling the Dynamics of a Single Atom in Lateral Atom Manipulation. In: *Science* 306 (2004), Nr. 5694, 242-247. http://dx.doi.org/10.1126/science.1102370. – DOI 10.1126/science.1102370

[64] Pennec, Y. ; Hoegen, M. Horn v. ; Zhu, Xiaobin ; Fortin, D. C. ; Freeman, M. R.: Dynamics of an Ising Chain under Local Excitation: A Scanning Tunneling Microscopy Study of Si(100) Dimer Rows at 5 K. In: *Phys. Rev. Lett.* 96 (2006), Jan, Nr. 2, S. 026102. http://dx.doi.org/10.1103/PhysRevLett.96.026102. – DOI 10.1103/PhysRevLett.96.026102

[65] Gaudioso, J. ; Lauhon, L. J. ; Ho, W.: Vibrationally mediated negative differential resistance in a single molecule. In: *Physical Review Letters* 85 (2000), Nr. 9, S. 1918–1921. http://dx.doi.org/10.1103/PhysRevLett.85.1918. – DOI 10.1103/PhysRevLett.85.1918

[66] Gaudioso, Jennifer ; Ho, Wilson: Steric Turnoff of Vibrationally Mediated Negative Differential Resistance in a Single Molecule. In: *Angewandte Chemie* 113 (2001), Nr. 21, 4204–4206. http://dx.doi.org/10.1002/1521-3757(20011105)113:21<4204::AID-ANGE4204>3.0.CO;2-0. – DOI 10.1002/1521–3757(20011105)113:21¡4204::AID–ANGE4204¿3.0.CO;2–0. – ISSN 1521–3757

[67] Pitters, Jason L. ; Wolkow, Robert A.: Detailed Studies of Molecular Conductance Using Atomic Resolution Scanning Tunneling Microscopy. In: *Nano Letters* 6 (2006), Nr. 3, 390-397. http://dx.doi.org/10.1021/nl0521569. – DOI 10.1021/nl0521569

[68] Iancu, Violeta ; Hla, Saw-Wai: Realization of a four-step molecular switch in scanning tunneling microscope manipulation of single chlorophyll-a molecules. In: *Proceedings of the National Academy of Sciences* 103 (2006), Nr. 37, 13718-13721. http://dx.doi.org/10.1073/pnas.0603643103. – DOI 10.1073/pnas.0603643103

[69] Liljeroth, P. ; Repp, J. ; Meyer, G.: Current-Induced Hydrogen Tautomerization and Conductance Switching of Naphthalocyanine Molecules. In: *Science* 317 (2007), S. 1203. http://dx.doi.org/10.1126/science.1144366. – DOI 10.1126/science.1144366

[70] Fu, Q. ; Yang, J. L. ; Luo, Y.: Mechanism for tautomerization induced conductance switching of naphthalocyanin molecule. In: *Applied Physics Letters* 95 (2009), Nr. 18, S. 3. http://dx.doi.org/10.1063/1.3224186. – DOI 10.1063/1.3224186

[71] Henningsen, N. ; Franke, K. J. ; Torrente, I. F. ; Schulze, G. ; Priewisch, B. ; Rück-Braun, K. ; Dokic, J. J. ; Klamroth, T. ; Saalfrank, P. ; Pascual, J. I.: Inducing the Rotation of a Single Phenyl Ring with Tunneling Electrons. In: *The Journal of Physical Chemistry C* 111 (2007), Nr. 40, 14843-14848. http://dx.doi.org/10.1021/jp0741861. – DOI 10.1021/jp0741861

[72] Gao, L. ; Liu, Q. ; Zhang, Y. Y. ; Jiang, N. ; Zhang, H. G. ; Cheng, Z. H. ; Qiu, W. F. ; Du, S. X. ; Liu, Y. Q. ; Hofer, W. A. ; Gao, H. J.: Constructing an Array of Anchored Single-Molecule Rotors on Gold Surfaces. In: *Physical Review Letters* 101 (2008), Nr. 19, S. 4. http://dx.doi.org/10.1103/PhysRevLett.101.197209. – DOI 10.1103/PhysRevLett.101.197209

[73] Liu, Q. ; Zhang, Y. Y. ; Jiang, N. ; Zhang, H. G. ; Gao, L. ; Du, S. X. ; Gao, H.-J.: Identifying Multiple Configurations of Complex Molecules in Dynamical Processes: Time Resolved Tunneling Spectroscopy and Density Functional Theory Calculation. In: *Phys. Rev. Lett.* 104 (2010), Apr, 166101. http://dx.doi.org/10.1103/PhysRevLett.104.166101. – DOI 10.1103/PhysRevLett.104.166101

[74] Nacci, Christophe ; Lagoute, Jérôme ; Liu, Xi ; Fölsch, Stefan: Conformational switching of single 1,5-cyclooctadiene molecules on Si(001) induced by inelastic electron tunneling. In: *Phys. Rev. B* 77 (2008), Mar, 121405. http://dx.doi.org/10.1103/PhysRevB.77.121405. – DOI 10.1103/PhysRevB.77.121405

[75] Nacci, Christophe ; Fölsch, Stefan ; Zenichowski, Karl ; Dokic, Jadranka ; Klamroth, Tillmann ; Saalfrank, Peter: Current versus Temperature-Induced Switching in a Single-Molecule Tunnel Junction: 1,5 Cyclooctadiene on Si(001). In: *Nano Letters* 9 (2009), Nr. 8, 2996-3000. http://dx.doi.org/10.1021/nl901419g. – DOI 10.1021/nl901419g. – PMID: 19583246

[76] Tierney, Heather L. ; Baber, Ashleigh E. ; Jewell, April D. ; Iski, Erin V. ; Boucher, Matthew B. ; Sykes, E. Charles H.: Mode-Selective Electrical Excitation of a Molecular Rotor. In: *Chemistry - A European Journal* 15 (2009), Nr. 38, 9678–9680. http://dx.doi.org/10.1002/chem.200902025. – DOI 10.1002/chem.200902025. – ISSN 1521–3765

[77] Parschau, Manfred ; Passerone, Daniele ; Rieder, Karl-Heinz ; Hug, Hans J. ; Ernst, Karl-Heinz: Switching the Chirality of Single Adsorbate Complexes. In: *Angewandte Chemie International Edition* 48 (2009), Nr. 22, 4065–4068. http://dx.doi.org/10.1002/anie.200805740. – DOI 10.1002/anie.200805740. – ISSN 1521–3773

[78] Simic-Milosevic, V. ; Meyer, J. ; Morgenstern, K.: Chirality Change of Chloronitrobenzene on Au(111) Induced by Inelastic Electron Tunneling. In: *Angewandte Chemie International Edition* 48 (2009), Nr. 22, 4061–4064. http://dx.doi.org/10.1002/anie.200805551. – DOI 10.1002/anie.200805551. – ISSN 1521–3773

[79] Wang, W. ; Shi, X. ; Jin, M. ; Minot, C. ; Van Hove, M.A. ; Collin, J.-P. ; Lin, N.: Electron Stimulation of Internal Torsion of a Surface-Mounted Molecular Rotor. In: *ACS Nano* 4 (2010), S. 4929–4935. http://dx.doi.org/10.1021/nn101330c. – DOI 10.1021/nn101330c

[80] Kühne, Dirk ; Klappenberger, Florian ; Krenner, Wolfgang ; Klyatskaya, Svetlana ; Ruben, Mario ; Barth, Johannes V.: Rotational and constitutional dynamics of caged supramolecules. In: *Proceedings of the National Academy of Sciences* 107 (2010), Nr. 50, 21332-21336. http://dx.doi.org/10.1073/pnas.1008991107. – DOI 10.1073/pnas.1008991107

[81] Jewell, April D. ; Tierney, Heather L. ; Baber, Ashleigh E. ; Iski, Erin V. ; Laha, Michael M. ; Sykes, E Charles H.: Time-resolved studies of individual

molecular rotors. In: *Journal of Physics: Condensed Matter* 22 (2010), Nr. 26, 264006. http://stacks.iop.org/0953-8984/22/i=26/a=264006

[82] Auwärter, W. ; Seufert, K. ; Bischoff, F. ; Ecija, D. ; Vijayaraghavan, S. ; Joshi, S. ; Klappenberger, F. ; Samudrala, N. ; Barth, J. V.: A surface-anchored molecular four-level conductance switch based on single proton transfer. In: *Nature Nanotechnology* 7 (2012), S. 41–46. http://dx.doi.org/10.1038/nnano.2011.211. – DOI 10.1038/nnano.2011.211

[83] Hahne, Susanne ; Ikonomov, Julian ; Sokolowski, Moritz ; Maass, Philipp: Determining molecule diffusion coefficients on surfaces from a locally fixed probe: Analysis of signal fluctuations. In: *Phys. Rev. B* 87 (2013), Feb, 085409. http://dx.doi.org/10.1103/PhysRevB.87.085409. – DOI 10.1103/PhysRevB.87.085409

[84] Sonntag, Andreas: *Rastertunnelmikroskopie und Dichtefunktionaltheorie zur Adsorption von organischen Molekuelen auf Metalloberflaechen*, University of Duisburg-Essen, Diploma Thesis, March 2010

[85] Martin, Richard: *Electronic Structure - Basic Theory and Practical Methods*. The Press Syndicate of the University of Cambridge, 2004. – ISBN 0 521 78285 6

[86] Payne, M. C. ; Teter, M. P. ; Allan, D. C. ; Arias, T. A. ; Joannopoulos, J. D.: Iterative minimization techniques for *ab initio* total-energy calculations: molecular dynamics and conjugate gradients. In: *Rev. Mod. Phys.* 64 (1992), Oct, 1045–1097. http://dx.doi.org/10.1103/RevModPhys.64.1045. – DOI 10.1103/RevModPhys.64.1045

[87] Capelle, K.: A bird's-eye view of density-functional theory. In: *Brazilian Journal of Physics* 36 (2006), 12, 1318 - 1343. http://www.scielo.br/scielo.php?script=sci_arttext&pid=S0103-97332006000700035&nrm=iso. – ISSN 0103–9733

[88] Kresse, Georg ; Furthmüller, Jürgen: *VASP the GUIDE*. http://cms.mpi.univie.ac.at/vasp/guide/vasp.html. Version: March 1999

[89] Hohenberg, P. ; Kohn, W.: Inhomogeneous Electron Gas. In: *Phys. Rev.* 136 (1964), Nov, S. B864–B871. http://dx.doi.org/10.1103/PhysRev.136.B864. – DOI 10.1103/PhysRev.136.B864

[90] Kohn: Walter Kohn - Nobel Lecture: Electronic Structure of Matter - Wave Functions and Density Functionals. In: *Nobel Lectures, Chemistry 1996-2000* (1998). http://www.nobelprize.org/nobel_prizes/chemistry/laureates/1998/kohn-lecture.html. – The Noble Foundation

[91] Born, M. ; Oppenheimer, R.: Zur Quantentheorie der Molekeln. In: *Annalen der Physik* 389 (1927), Nr. 20, S. 457–484. http://dx.doi.org/10.1002/andp.19273892002. – DOI 10.1002/andp.19273892002. – ISSN 1521–3889

[92] Kohn, W. ; Sham, L. J.: Self-Consistent Equations Including Exchange and Correlation Effects. In: *Phys. Rev.* 140 (1965), Nov, A1133–A1138. http://dx.doi.org/10.1103/PhysRev.140.A1133. – DOI 10.1103/PhysRev.140.A1133

[93] Perdew, J. P. ; Zunger, Alex: Self-interaction correction to density-functional approximations for many-electron systems. In: *Phys. Rev. B* 23 (1981), May, 5048–5079. http://dx.doi.org/10.1103/PhysRevB.23.5048. – DOI 10.1103/PhysRevB.23.5048

[94] Barth, U von ; Hedin, L: A local exchange-correlation potential for the spin polarized case. i. In: *Journal of Physics C: Solid State Physics* 5 (1972), Nr. 13, 1629. http://stacks.iop.org/0022-3719/5/i=13/a=012

[95] Gunnarsson, O. ; Lundqvist, B. I. ; Wilkins, J. W.: Contribution to the cohesive energy of simple metals: Spin-dependent effect. In: *Phys. Rev. B* 10 (1974), Aug, 1319–1327. http://dx.doi.org/10.1103/PhysRevB.10.1319. – DOI 10.1103/PhysRevB.10.1319

[96] Ceperley, D. M. ; Alder, B. J.: Ground State of the Electron Gas by a Stochastic Method. In: *Phys. Rev. Lett.* 45 (1980), Aug, 566–569. http://dx.doi.org/10.1103/PhysRevLett.45.566. – DOI 10.1103/PhysRevLett.45.566

[97] Mugarza, A. ; Robles, R. ; Krull, C. ; Korytár, R. ; Lorente, N. ; Gambardella, P.: Electronic and magnetic properties of molecule-metal interfaces: Transition-metal phthalocyanines adsorbed on Ag(100). In: *Phys. Rev. B* 85 (2012), Apr, S. 155437. http://dx.doi.org/10.1103/PhysRevB.85.155437. – DOI 10.1103/PhysRevB.85.155437

[98] Perdew, John P. ; Burke, Kieron ; Ernzerhof, Matthias: Generalized Gradient Approximation Made Simple. In: *Phys. Rev. Lett.* 77 (1996), Oct, 3865–3868. http://dx.doi.org/10.1103/PhysRevLett.77.3865. – DOI 10.1103/PhysRevLett.77.3865

[99] Perdew, John P. ; Burke, Kieron ; Ernzerhof, Matthias: Generalized Gradient Approximation Made Simple [Phys. Rev. Lett. 77, 3865 (1996)]. In: *Phys. Rev. Lett.* 78 (1997), Feb, 1396–1396. http://dx.doi.org/10.1103/PhysRevLett.78.1396. – DOI 10.1103/PhysRevLett.78.1396

[100] Perdew, John P. ; Chevary, J. A. ; Vosko, S. H. ; Jackson, Koblar A. ; Pederson, Mark R. ; Singh, D. J. ; Fiolhais, Carlos: Atoms, molecules, solids, and surfaces: Applications of the generalized gradient approximation for exchange and correlation. In: *Phys. Rev. B* 46 (1992), Sep, 6671–6687. http://dx.doi.org/10.1103/PhysRevB.46.6671. – DOI 10.1103/PhysRevB.46.6671

[101] Perdew, John P. ; Chevary, J. A. ; Vosko, S. H. ; Jackson, Koblar A. ; Pederson, Mark R. ; Singh, D. J. ; Fiolhais, Carlos: Erratum: Atoms, molecules, solids, and surfaces: Applications of the generalized gradient approximation for exchange and correlation. In: *Phys. Rev. B* 48 (1993), Aug, 4978–4978. http://dx.doi.org/10.1103/PhysRevB.48.4978.2. – DOI 10.1103/PhysRevB.48.4978.2

[102] Becke, A. D.: Density-functional exchange-energy approximation with correct asymptotic behavior. In: *Phys. Rev. A* 38 (1988), Sep, 3098–3100. http://dx.doi.org/10.1103/PhysRevA.38.3098. – DOI 10.1103/PhysRevA.38.3098

[103] Lee, Chengteh ; Yang, Weitao ; Parr, Robert G.: Development of the Colle-Salvetti correlation-energy formula into a functional of the electron density. In: *Phys. Rev. B* 37 (1988), Jan, 785–789. http://dx.doi.org/10.1103/PhysRevB.37.785. – DOI 10.1103/PhysRevB.37.785

[104] Grimme, Stefan: Semiempirical GGA-type density functional constructed with a long-range dispersion correction. In: *Journal of Computational Chemistry* 27 (2006), Nr. 15, 1787–1799. http://dx.doi.org/10.1002/jcc.20495. – DOI 10.1002/jcc.20495. – ISSN 1096–987X

[105] Bucko, Tomas ; Hafner, Jürgen ; Lebegue, Sebastien ; Angyan, Janos G.: Improved Description of the Structure of Molecular and Layered Crystals: Ab Initio

DFT Calculations with van der Waals Corrections. In: *The Journal of Physical Chemistry A* 114 (2010), Nr. 43, 11814-11824. http://dx.doi.org/10.1021/jp106469x. – DOI 10.1021/jp106469x

[106] Blöchl, P. E.: Projector augmented-wave method. In: *Phys. Rev. B* 50 (1994), Dec, Nr. 24, S. 17953–17979. http://dx.doi.org/10.1103/PhysRevB.50.17953. – DOI 10.1103/PhysRevB.50.17953

[107] Kresse, G. ; Joubert, D.: From ultrasoft pseudopotentials to the projector augmented-wave method. In: *Phys. Rev. B* 59 (1999), Jan, 1758–1775. http://dx.doi.org/10.1103/PhysRevB.59.1758. – DOI 10.1103/PhysRevB.59.1758

[108] Broyden, C. G.: A Class of Methods for Solving Nonlinear Simultaneous Equations. In: *Mathematics of Computation* 19 (1965), Nr. 92, pp. 577-593. http://www.jstor.org/stable/2003941. – ISSN 00255718

[109] Bendt, Paul ; Zunger, Alex: New approach for solving the density-functional self-consistent-field problem. In: *Phys. Rev. B* 26 (1982), Sep, 3114–3137. http://dx.doi.org/10.1103/PhysRevB.26.3114. – DOI 10.1103/PhysRevB.26.3114

[110] Srivastava, G P.: Broyden's method for self-consistent field convergence acceleration. In: *Journal of Physics A: Mathematical and General* 17 (1984), Nr. 6, L317. http://stacks.iop.org/0305-4470/17/i=6/a=002

[111] Feynman, R. P.: Forces in Molecules. In: *Phys. Rev.* 56 (1939), Aug, 340–343. http://dx.doi.org/10.1103/PhysRev.56.340. – DOI 10.1103/PhysRev.56.340

[112] *Kapitel* 1. In: Bocquet, Marie-Laure ; Lesnard, Hervé ; Monturet, Serge ; Lorente, Nicolás: *Theory of Elastic and Inelastic Electron Tunneling*. Wiley-VCH Verlag GmbH & Co. KGaA, 2009. – ISBN 9783527625482, 199–219

[113] Stipe, B. C. ; Rezaei, M. A. ; Ho, W.: A variable-temperature scanning tunneling microscope capable of single-molecule vibrational spectroscopy. In: *Rev. Sci. Instrum.* 70 (1999), Nr. 1, S. 137–143. http://dx.doi.org/10.1063/1.1149555. – DOI 10.1063/1.1149555

[114] Wintjes, N. ; Lange, M. ; Vörden, D. van ; Karacuban, H. ; Utzat, D. ; Möller, R.: Very compact design for a low-temperature tuning fork atomic force

microscope. In: *J. Vac. Sci. Technol. B* 28 (2010), May/Jun, Nr. 3, C4E21-C4E23. http://dx.doi.org/10.1116/1.3374720. – DOI 10.1116/1.3374720

[115] Weissler, G. L. ; Carlson, R. W. ; Marton, L. (Hrsg.) ; Marton, C. (Hrsg.): *Methods of Experimental Physics - Vacuum Physics and Technology*. Bd. 14. Academic Press, 1979

[116] Cottin, Maren C.: *Rastertunnelmikroskopie und -spektroskopie an organischen und anorganischen dünnen Schichten bei tiefen Temperaturen*, University of Duisburg-Essen, Diploma Thesis, March 2010

[117] Advanced Research Systems, Inc.: *Models LT-3-110 and LT-3B HELITRAN open cycle cryogenic refrigeration system*. -. 7476 Industrial Park Way, Macungie, PA 18062, USA: -, - -. http://www.arscryo.com/LT3B.html

[118] Lange, Manfred: *Frequenzmodulierte Rasterkraftmikroskopie: Aufbau eines Tieftemperatur-Gerätes*. Lotharstr. 1, D-47057 Duisburg, Germany, Faculty of Physics, University of Duisburg-Essen, Diploma Thesis, 2008

[119] Smith, D.P.E. ; Binnig, G.: Ultrasmall scanning tunneling microscope for use in a liquid-helium storage Dewar. In: *Rev. Sci. Instrum.* 57 (1986), 2630-2631. http://dx.doi.org/10.1063/1.1139072

[120] Fein, A. P. ; Kirtley, J. R. ; Feenstra, R. M.: Scanning tunneling microscope for low temperature, high magnetic field, and spatially resolved spectroscopy. In: *Review of Scientific Instruments* 58 (1987), Nr. 10, 1806-1810. http://dx.doi.org/10.1063/1.1139524. – DOI 10.1063/1.1139524

[121] Gaisch, R. ; Gimzewski, J.K. ; Reihl, B. ; Schlittler, R.R. ; Tschudy, M. ; Schneider, W.D.: Low-temperature ultra-high-vacuum scanning tunneling microscope. In: *Ultramicroscopy* 42-44, Part 2 (1992), Nr. 0, 1621 - 1626. http://dx.doi.org/10.1016/0304-3991(92)90495-6. – DOI 10.1016/0304–3991(92)90495–6. – ISSN 0304–3991

[122] Wolkow, R.A.: A variable temperature scanning tunneling microscope for use in ultrahigh vacuum. In: *Rev. Sci. Instrum.* 63 (1992), 4049-4052. http://dx.doi.org/10.1063/1.1143264

[123] Becker, T. ; Hövel, H. ; Tschudy, M. ; Reihl, B.: Applications with a new low-temperature UHV STM at 5 K. In: *Applied Physics A* 66 (1998), S27-S30. http://dx.doi.org/10.1007/s003390051093. – DOI 10.1007/s003390051093. – ISSN 0947–8396

[124] Schaffert, J. ; Cottin, M. C. ; Sonntag, A. ; Karacuban, H. ; Utzat, D. ; Bobisch, C. A. ; Möller, R.: Scanning noise microscopy. In: *Review of Scientific Instruments* 84 (2013), Nr. 4, 043702. http://dx.doi.org/10.1063/1.4801458. – DOI 10.1063/1.4801458

[125] Möller, R. ; Esslinger, A. ; Koslowski, B.: Thermal noise in vacuum scanning tunneling microscopy at zero bias voltage. In: *Journal of Vacuum Science & Technology A: Vacuum, Surfaces, and Films* 8 (1990), Nr. 1, 590-593. http://dx.doi.org/10.1116/1.576348. – DOI 10.1116/1.576348

[126] Möller, R. ; Baur, C. ; Esslinger, A. ; Kürz, P.: Scanning noise potentiometry. In: *Proceedings of the Fifth International Conference on Scanning Tunneling Microscopy/Spectroscopy* Bd. 9, AVS, 1991, 609-611

[127] Sung, Moon G. ; Lee, Hyungwoo ; Heo, Kwang ; Byun, Kyung-Eun ; Kim, Taekyeong ; Seo, David H. ; Seo, Sunae ; Hong, Seunghun: Scanning Noise Microscopy on Graphene Devices. In: *ACS Nano* 5 (2011), Nr. 11, 8620-8628. http://dx.doi.org/10.1021/nn202135g. – DOI 10.1021/nn202135g

[128] Hünlein, C. ; Klein, A.K.: *Präparation und Charakterisierung von Tunnelspitzen*. project thesis, Surface Science Group Prof. Möller, Faculty of Physics, University of Duisburg-Essen, Germany, 2010

[129] Ibach, H. H; L. H; Lüth ; Aufage, 6. (Hrsg.): *Festkörperphysik: Einführung in die Grundlagen*. Springer Verlag, 2002

[130] Straumanis, M.E. ; Yu, L.S.: Lattice Parameters, Densities, Expansion Coefficients and Perfection of Structure of Cu and of Cu-In α Phase. In: *Acta Cryst.* A25 (1969), S. 676–628

[131] Springer: *The Landolt-Börnstein Database*. www.springermaterials.com. Version: 2012

[132] Reinert, F. ; Nicolay, G. ; Schmidt, S. ; Ehm, D. ; Hüfner, S.: Direct measurement of the L-gap surface states on the (111) face of noble metals by photoelectron spectroscopy. In: *Phys. Rev. B* 63 (2001), S. 115415. http://dx.doi.org/10.1103/PhysRevB.63.115415. – DOI 10.1103/PhysRevB.63.115415

[133] Davis, L. C. ; Everson, M. P. ; Jaklevic, R. C. ; Shen, Weidian: Theory of the local density of surface states on a metal: Comparison with scanning tunneling spectroscopy of a Au(111) surface. In: *Phys. Rev. B* 43 (1991), Feb, 3821-3830. http://dx.doi.org/10.1103/PhysRevB.43.3821. – DOI 10.1103/PhysRevB.43.3821

[134] Hasegawa, Y. ; Avouris, Ph.: Direct observation of standing wave formation at surface steps using scanning tunneling spectroscopy. In: *Phys. Rev. Lett.* 71 (1993), Aug, 1071–1074. http://dx.doi.org/10.1103/PhysRevLett.71.1071. – DOI 10.1103/PhysRevLett.71.1071

[135] Crommie, M. F. ; Lutz, C. P. ; Eigler, D. M.: Imaging standing waves in a two-dimensional electron gas. In: *Nature* 363 (1993), S. 524–527. http://dx.doi.org/doi:10.1038/363524a0. – DOI doi:10.1038/363524a0

[136] Blochwitz, J. ; Pfeiffer, M. ; Fritz, T. ; Leo, K.: Low voltage organic light emitting diodes featuring doped phthalocyanine as hole transport material. In: *Appl. Phys. Lett.* 73 (1998), August, Nr. 6, S. 729–731. http://dx.doi.org/10.1063/1.121982. – DOI 10.1063/1.121982

[137] Peumans, P. ; Forrest, S. R.: Very-high-efficiency double-heterostructure copper phthalocyanine/C[sub 60] photovoltaic cells. In: *Applied Physics Letters* 79 (2001), Nr. 1, 126-128. http://dx.doi.org/10.1063/1.1384001. – DOI 10.1063/1.1384001

[138] Peumans, Peter ; Yakimov, Aharon ; Forrest, Stephen R.: Small molecular weight organic thin-film photodetectors and solar cells. In: *Journal of Applied Physics* 93 (2003), Nr. 7, 3693-3723. http://dx.doi.org/10.1063/1.1534621. – DOI 10.1063/1.1534621

[139] Hsiao, Yu-Sheng ; Whang, Wha-Tzong ; Suen, Shich-Chang ; Shiu, Jau-Ye ; Chen, Chih-Ping: Morphological control of CuPc and its application in organic solar

cells. In: *Nanotechnology* 19 (2008), Nr. 41, 415603. http://stacks.iop.org/0957-4484/19/i=41/a=415603

[140] Pandey, R. ; Holmes, R.J.: Organic Photovoltaic Cells Based on Continuously Graded Donor-Acceptor Heterojunctions. In: *IEEE Journal of Selected Topics in Quantum Electronics* 16 (2010), Nr. 6, S. 1537. http://dx.doi.org/10.1109/JSTQE.2010.2049256. – DOI 10.1109/JSTQE.2010.2049256

[141] Yamashita, Yoshiro: Organic semiconductors for organic field-effect transistors. In: *Science and Technology of Advanced Materials* 10 (2009), Nr. 2, 024313. http://stacks.iop.org/1468-6996/10/i=2/a=024313

[142] Lunt, R. R. ; Benziger, J. B. ; Forrest, S. R.: Growth of an ordered crystalline organic heterojunction. In: *Adv. Mat.* 19 (2007), Dezember, Nr. 23, S. 4229–4233. http://dx.doi.org/10.1002/adma.200701572. – DOI 10.1002/adma.200701572

[143] Schaffert, J. ; Cottin, M.C. ; Sonntag, A. ; Karacuban, H. ; Bobisch, C.A. ; Lorente, N. ; Gauyacq, J.-P. ; Möller, R.: Imaging the dynamics of individually adsorbed molecules. In: *Nature Materials* 12 (2013), 223-227. http://dx.doi.org/10.1038/nmat3527. – DOI 10.1038/nmat3527

[144] Semyannikov, P. P. ; Basova, T. V. ; Grankin, V. M. ; Igumenov, I. K.: Vapour pressure of some phthalocyanines. In: *Journal of Porphyrins and Phthalocyanines* 04 (2000), Nr. 03, 271-277. http://dx.doi.org/10.1002/(SICI)1099-1409(200004/05)4:3<271::AID-JPP205>3.0.CO;2-4. – DOI 10.1002/(SICI)1099–1409(200004/05)4:3¡271::AID–JPP205¿3.0.CO;2–4

[145] Aristov, V. Y. ; Molodtsova, O. V. ; Maslyuk, V. V. ; Vyalikh, D. V. ; Zhilin, V. M. ; Ossipyan, Yu. A. ; Bredow, T. ; Mertig, I. ; Knupfer, M.: Electronic structure of the organic semiconductor copper phthalocyanine: Experiment and theory. In: *The Journal of Chemical Physics* 128 (2008), Nr. 3, S. 034703. http://dx.doi.org/10.1063/1.2822170. – DOI 10.1063/1.2822170

[146] Hill, I.G. ; Kahn, A. ; Soos, Z.G. ; Pascal Jr., R.A.: Charge-separation energy in films of pi-conjugated organic molecules. In: *Chem. Phys. Lett.* 327 (2000), S. 181–188

[147] Kahn, A. ; Koch, N. ; Gao, W.: Electronic structure and electrical properties of interfaces between metals and π-conjugated molecular films. In: *Journal of Polymer Science Part B: Polymer Physics* 41 (2003), Nr. 21, 2529–2548. http://dx.doi.org/10.1002/polb.10642

[148] Schwieger, T. ; Peisert, H. ; Golden, M. S. ; Knupfer, M. ; Fink, J.: Electronic structure of the organic semiconductor copper phthalocyanine and K-CuPc studied using photoemission spectroscopy. In: *Phys. Rev. B* 66 (2002), Oct, 155207. http://dx.doi.org/10.1103/PhysRevB.66.155207. – DOI 10.1103/PhysRevB.66.155207

[149] Buchholz, J. C. ; Somorjai, G. A.: The surface structures of phthalocyanine monolayers and vapor-grown films: A low-energy electron diffration study. In: *Journal of Chemical Physics* 66 (1977), Januar, Nr. 2, S. 573–580. http://dx.doi.org/10.1063/1.433979. – DOI 10.1063/1.433979

[150] Lippel, P. H. ; Wilson, R. J. ; Miller, M. D. ; Wöll, Ch. ; Chiang, S.: High-Resolution Imaging of Copper-Phthalocyanine by Scanning-Tunneling Microscopy. In: *Phys. Rev. Lett.* 62 (1989), Jan, 171–174. http://dx.doi.org/10.1103/PhysRevLett.62.171. – DOI 10.1103/PhysRevLett.62.171

[151] Fritz, T. ; Hara, M. ; Knoll, W. ; Sasabe, H.: STM-investigations on heteroepitaxially grown overlayers of Cu-Phthalocyanine on Au(111) surfaces. In: *Mol. Crys. Liq. Crys. Sci. Techn. Sec. A- Mol. Crys. Liq. crys.* 252 (1994), S. 561–570

[152] Lu, X. ; Hipps, K.W. ; Wang, X.D. ; Mazur, U.: Scanning Tunneling Microscopy of Metal Phthalocyanines: d7 and d9 Cases. In: *J. Am. Chem. Soc.* 118 (1996), Nr. 30, S. 7197–7202

[153] Alvarado, S. F. ; Rossi, L. ; Muller, P. ; Riess, W.: Charge-carrier injection into CuPc thin films: a scanning tunneling microscopy study. In: *Synthetic Metals* 122 (2001), Nr. 1, S. 73–77. http://dx.doi.org/10.1016/S0379-6779(00)01372-2. – DOI 10.1016/S0379–6779(00)01372–2

[154] Grand, J.-Y. ; Kunstmann, T. ; Hoffmann, D. ; Haas, A. ; Dietsche, M. ; Seifritz, J. ; Möller, R.: Epitaxial growth of copper phthalocyanine monolayers on Ag(111). In: *Surface Science* 366 (1996), Nr. 3, 403 - 414. http://dx.doi.

org/10.1016/0039-6028(96)00838-2. – DOI 10.1016/0039–6028(96)00838–2. – ISSN 0039–6028

[155] Hipps, K.W. ; Lu, X. ; Wang, X.D. ; Mazur, U.: Metal d-Orbital Occupation-Dependent Images in the Scanning Tunneling Microscopy of Metal Phthalocyanines. In: *Journal of Physical Chemistry* 100 (1996), Nr. 27, 11207–11210. http://dx.doi.org/10.1021/jp960422o

[156] Manandhar, K. ; Ellis, T. ; Park, K. T. ; Cai, T. ; Song, Z. ; Hrbek, J.: A scanning tunneling microscopy study on the effect of post-deposition annealing of copper phthalocyanine thin films. In: *Surf. Sci.* 601 (2007), September, Nr. 17, S. 3623–3631. http://dx.doi.org/10.1016/j.susc.2007.07.007. – DOI 10.1016/j.susc.2007.07.007

[157] Böhringer, Matthias ; Berndt, Richard ; Schneider, Wolf-Dieter: Transition from three-dimensional to two-dimensional faceting of Ag(110) induced by Cu-phthalocyanine. In: *Phys. Rev. B* 55 (1997), Jan, 1384–1387. http://dx.doi.org/10.1103/PhysRevB.55.1384. – DOI 10.1103/PhysRevB.55.1384

[158] Song, Fei ; Huang, Han ; Dou, Weidong ; Zhang, Hanjie ; Hu, Yunwan ; Qian, Huiqin ; Li, Haiyang ; He, Pimo ; Bao, Shining ; Chen, Qiao ; Zhou, Wuzong: Electronic structures of CuPc on a Ag(110) surface. In: *Journal of Physics: Condensed Matter* 19 (2007), Nr. 13, 136002. http://stacks.iop.org/0953-8984/19/i=13/a=136002

[159] Oteyza, D. G. ; El-Sayed, A. ; Garcia-Lastra, J. M. ; Goiri, E. ; Krauss, T. N. ; Turak, A. ; Barrena, E. ; Dosch, H. ; Zegenhagen, J. ; Rubio, A. ; Wakayama, Y. ; Ortega, J. E.: Copper-phthalocyanine based metal–organic interfaces: The effect of fluorination, the substrate, and its symmetry. In: *The Journal of Chemical Physics* 133 (2010), Nr. 21, 214703. http://dx.doi.org/10.1063/1.3509394. – DOI 10.1063/1.3509394

[160] Saedi, Amirmehdi ; Berkelaar, Robin P. ; Kumar, Avijit ; Poelsema, Bene ; Zandvliet, Harold J. W.: Adsorption of Cu phthalocyanine on Pt modified Ge(001): A scanning tunneling microscopy study. In: *Phys. Rev. B* 82 (2010), Oct, 165306. http://dx.doi.org/10.1103/PhysRevB.82.165306. – DOI 10.1103/PhysRevB.82.165306

[161] Hersam, M C. ; Guisinger, N P. ; Lyding, J W.: Silicon-based molecular nanotechnology. In: *Nanotechnology* 11 (2000), Nr. 2, 70. http://stacks.iop.org/0957-4484/11/i=2/a=306

[162] Gorgoi, M ; Michaelis, W ; Kampen, T.U ; Schlettwein, D ; Zahn, D.R.T: Thickness dependence of the LUMO position for phthalocyanines on hydrogen passivated silicon (111). In: *Applied Surface Science* 234 (2004), Nr. 1-4, 138 - 143. http://dx.doi.org/10.1016/j.apsusc.2004.05.065. – DOI 10.1016/j.apsusc.2004.05.065. – ISSN 0169–4332

[163] Godlewski, Szymon ; Tekiel, Antoni ; Prauzner-Bechcicki, Jakub S. ; Budzioch, Janusz ; Szymonski, Marek: Controlled Reorientation of CuPc Molecules in Ordered Structures Assembled on the TiO2(011)-(2×1) Surface. In: *ChemPhysChem* 11 (2010), Nr. 9, S. 1863–1866. http://dx.doi.org/10.1002/cphc.201000165. – DOI 10.1002/cphc.201000165. – ISSN 1439–7641

[164] Qiu, X. H. ; Nazin, G. V. ; Ho, W.: Vibronic states in single molecule electron transport. In: *Phys. Rev. Lett.* 92 (2004), Mai, Nr. 20, S. 206102. http://dx.doi.org/10.1103/PhysRevLett.92.206102. – DOI 10.1103/PhysRevLett.92.206102

[165] Moore, A. M. ; Weiss, P. S.: Functional and Spectroscopic Measurements with Scanning Tunneling Microscopy. In: *Annual Review of Analytical Chemistry* 1 (2008), S. 857–882. http://dx.doi.org/10.1146/annurev.anchem.1.031207.112932. – DOI 10.1146/annurev.anchem.1.031207.112932

[166] Stöhr, M. ; Wagner, Th. ; Gabriel, M. ; Weyers, B. ; Möller, R.: Direct observation of hindered eccentric rotation of an individual molecule: Cu-phthalocyanine on C60. In: *Phys. Rev. B* 65 (2001), Dec, 033404. http://dx.doi.org/10.1103/PhysRevB.65.033404. – DOI 10.1103/PhysRevB.65.033404

[167] Chen, Wei ; Huang, Han ; Chen, Shi ; Gao, Xing Y. ; Wee, Andrew Thye S.: Low-Temperature Scanning Tunneling Microscopy and Near-Edge X-ray Absorption Fine Structure Investigations of Molecular Orientation of Copper(II) Phthalocyanine Thin Films at Organic Heterojunction Interfaces. In: *The Journal of Physical Chemistry C* 112 (2008), Nr. 13, 5036-5042. http://dx.doi.org/10.1021/jp710722s. – DOI 10.1021/jp710722s

[168] Bobisch, C. ; Wagner, Th. ; Bannani, A. ; Möller, R.: Ordered binary monolayer composed of two organic molecules: Copper-phthalocyanine and 3,4,9,10-perylene-tetra-carboxylic- dianhydride on Cu(111). In: *J. Chem. Phys.* 119 (2003), Nr. 18, S. 9804–9808. http://dx.doi.org/10.1063/1.1615492. – DOI 10.1063/1.1615492

[169] Cottin, M.C. ; Schaffert, J. ; Sonntag, A. ; Karacuban, H. ; Möller, R. ; Bobisch, C.A.: Supramolecular architecture of organic molecules: PTCDA and CuPc on a Cu(111) substrate. In: *Applied Surface Science* 258 (2012), Nr. 6, S. 2196 – 2200. http://dx.doi.org/10.1016/j.apsusc.2011.02.038. – DOI 10.1016/j.apsusc.2011.02.038. – ISSN 0169–4332

[170] Lu, Jun ; Lei, Sheng-bin ; Zeng, Qing-dao ; Kang, Shi-zhao ; Wang, Chen ; Wan, Li-jun ; Bai, Chun-li: Template-Induced Inclusion Structures with Copper(II) Phthalocyanine and Coronene as Guests in Two-Dimensional Hydrogen-Bonded Host Networks. In: *The Journal of Physical Chemistry B* 108 (2004), Nr. 17, 5161-5165. http://dx.doi.org/10.1021/jp037508j. – DOI 10.1021/jp037508j

[171] Krull, C. ; Robles, R. ; Mugarza, A. ; Gambardella, P.: Site- and orbital-dependent charge donation and spin manipulation in electron-doped metal phthalocyanines. In: *Nature Materials* (2013). http://dx.doi.org/doi:10.1038/nmat3547. – DOI doi:10.1038/nmat3547

[172] Uhlmann, C. ; Swart, I. ; Repp, J.: Controlling the Orbital Sequence in Individual Cu-Phthalocyanine Molecules. In: *Nano Letters* 13 (2013), Nr. 2, 777-780. http://dx.doi.org/10.1021/nl304483h. – DOI 10.1021/nl304483h

[173] Kresse, G ; Hafner, J: Norm-conserving and ultrasoft pseudopotentials for first-row and transition elements. In: *Journal of Physics: Condensed Matter* 6 (1994), Nr. 40, 8245. http://stacks.iop.org/0953-8984/6/i=40/a=015

[174] Kresse, G. ; Furthmüller, J.: Efficient iterative schemes for *ab initio* total-energy calculations using a plane-wave basis set. In: *Phys. Rev. B* 54 (1996), Oct, 11169–11186. http://dx.doi.org/10.1103/PhysRevB.54.11169. – DOI 10.1103/PhysRevB.54.11169

[175] Hafner, J. ; Kresse, G. ; Vogtenhuber, D. ; Marsman, Sensengasse 8/12 A-1090 Vienna A. M.; Computational Materials Physics P. M.; Computational Materials Physics: The VASP homepage. In: *online source* http://www.vasp.at

[176] Landolt ; Börnstein: Landolt-Börnstein-Tabellenwerk Zahlenwerte und Funktionen aus Physik, Chemie, Astronomie, Geophysik und Technik. In: *Springer Materials* (2012). http://www.springermaterials.com/navigation/index.html

[177] Shockley, William: On the Surface States Associated with a Periodic Potential. In: *Phys. Rev.* 56 (1939), Aug, S. 317–323. http://dx.doi.org/10.1103/PhysRev.56.317. – DOI 10.1103/PhysRev.56.317

[178] Lorente, Nicolás: *private communication*. CIN2: Centre d'Investigació en Nanociència i Nanotecnologia (CSIC-ICN), Campus de la Universitat Autònoma de Barcelona, 08193 Bellaterra, Spain, 2009-2013

[179] Cuadrado, Ramon ; Cerda, Jorge I. ; Wang, Yongfeng ; Xin, Ge ; Berndt, Richard ; Tang, Hao: CoPc adsorption on Cu(111): Origin of the C4 to C2 symmetry reduction. In: *The Journal of Chemical Physics* 133 (2010), Nr. 15, 154701. http://dx.doi.org/10.1063/1.3502682. – DOI 10.1063/1.3502682

[180] Baran, Jakub D. ; Larsson, J. A.: Structure and Energetics of Shuttlecock-Shaped Tin-Phthalocyanine on Ag(111): A Density Functional Study Employing Dispersion Correction. In: *The Journal of Physical Chemistry C* 116 (2012), Nr. 17, 9487-9497. http://dx.doi.org/10.1021/jp210771d. – DOI 10.1021/jp210771d

[181] Schaffert, J. ; Cottin, M. C. ; Sonntag, A. ; Bobisch, C. A. ; Möller, R. ; Gauyacq, J.-P. ; Lorente, N.: Tunneling electron induced rotation of a copper phthalocyanine molecule on Cu(111). In: *Phys. Rev. B* 88 (2013), Aug, 075410. http://dx.doi.org/10.1103/PhysRevB.88.075410. – DOI 10.1103/PhysRevB.88.075410

[182] Zahl, P. ; Bierkandt, M. ; Schröder, S. ; Klust, A.: The Flexible and Modern Open Source Scanning Probe Microscopy Software Package GXSM. In: *Review of Scientific Instruments* 74 (2003), S. 1222–1227. http://dx.doi.org/10.1063/1.1540718. – DOI 10.1063/1.1540718

[183] Zahl, P. ; Wagner, T. ; Moller, R. ; Klust, A.: Open source scanning probe microscopy control software package GXSM. In: *Journal of Vacuum Science & Technology B* 28 (2010), Nr. 3, S. 9. http://dx.doi.org/10.1116/1.3374719. – DOI 10.1116/1.3374719

[184] Horcas, I. ; Fernández, R. ; Gómez-Rodríguez, J. M. ; Colchero, J. ; Gómez-Herrero, J. ; Baro, A. M.: WSXM: a Software for Scanning Probe Microscopy and a Tool for Nanotechnology. In: *Review of Scientific Instruments* 78 (2007), Nr. 1, 013705. http://dx.doi.org/10.1063/1.2432410. – DOI 10.1063/1.2432410

[185] *Origin - Data Analysis and Graphing Software*. http://www.originlab.com/

[186] Schaffert, Johannes: *Rastertunnelmikroskopie an organischen Molekülen bei tiefen Temperaturen*. Lotharstr. 1, D-47057 Duisburg, Germany, Faculty of Physics, University of Duisburg-Essen, Diploma Thesis, 2009

[187] Savitzky, Abraham. ; Golay, M. J. E.: Smoothing and Differentiation of Data by Simplified Least Squares Procedures. In: *Analytical Chemistry* 36 (1964), Nr. 8, 1627-1639. http://dx.doi.org/10.1021/ac60214a047. – DOI 10.1021/ac60214a047

[188] Bader, R. F. W. ; Henneker, W. H. ; Cade, Paul E.: Molecular Charge Distributions and Chemical Binding. In: *The Journal of Chemical Physics* 46 (1967), Nr. 9, 3341-3363. http://dx.doi.org/10.1063/1.1841222. – DOI 10.1063/1.1841222

[189] Abram, R.A. ; Herzenberg, A.: Rotational excitation of H2 by slow electrons. In: *Chemical Physics Letters* 3 (1969), Nr. 4, 187 - 190. http://dx.doi.org/10.1016/0009-2614(69)80021-7. – DOI 10.1016/0009–2614(69)80021–7. – ISSN 0009–2614

[190] Li, Daocong ; Peng, Zhenghe ; Deng, Lizhi ; Shen, Yufang ; Zhou, Yunhong: Theoretical studies on molecular structure and vibrational spectra of copper phthalocyanine. In: *Vibrational Spectroscopy* 39 (2005), Nr. 2, 191 - 199. http://dx.doi.org/10.1016/j.vibspec.2005.03.004. – DOI 10.1016/j.vibspec.2005.03.004. – ISSN 0924–2031

[191] Heinrich, Benjamin W. ; Iacovita, Cristian ; Brumme, Thomas ; Choi, Deung-Jang ; Limot, Laurent ; Rastei, Mircea V. ; Hofer, Werner A. ; Ko-

RTUS, Jens ; BUCHER, Jean-Pierre: Direct Observation of the Tunneling Channels of a Chemisorbed Molecule. In: *The Journal of Physical Chemistry Letters* 1 (2010), Nr. 10, 1517-1523. http://dx.doi.org/10.1021/jz100346a. – DOI 10.1021/jz100346a

[192] CHANG, Shih-Hsin ; KUCK, Stefan ; BREDE, Jens ; LICHTENSTEIN, Leonid ; HOFFMANN, Germar ; WIESENDANGER, Roland: Symmetry reduction of metal phthalocyanines on metals. In: *Phys. Rev. B* 78 (2008), Dec, S. 233409. http://dx.doi.org/10.1103/PhysRevB.78.233409. – DOI 10.1103/PhysRevB.78.233409

[193] WANG, Yongfeng ; WU, Kai ; KROGER, Jorg ; BERNDT, Richard: Review Article: Structures of phthalocyanine molecules on surfaces studied by STM. In: *AIP Advances* 2 (2012), Nr. 4, 041402. http://dx.doi.org/10.1063/1.4773458. – DOI 10.1063/1.4773458

[194] SPERL, Alexander ; KRÖGER, Jörg ; BERNDT, Richard: Controlled Metalation of a Single Adsorbed Phthalocyanine. In: *Angewandte Chemie* 123 (2011), Nr. 23, 5406–5409. http://dx.doi.org/10.1002/ange.201100950. – DOI 10.1002/ange.201100950. – ISSN 1521–3757

[195] SHIBUTA, M. ; YAMAMOTO, K. ; MIYAKUBO, K. ; YAMADA, T. ; MUNAKATA, T.: Resonant effects on two-photon photoemission spectroscopy: Linewidths and intensities of occupied and unoccupied features for lead phthalocyanine films on graphite. In: *Phys. Rev. B* 81 (2010), Mar, 115426. http://dx.doi.org/10.1103/PhysRevB.81.115426. – DOI 10.1103/PhysRevB.81.115426

[196] EVANGELISTA, Fabrizio ; CARRAVETTA, Vincenzo ; STEFANI, Giovanni ; JANSIK, Branislav ; ALAGIA, Michele ; STRANGES, Stefano ; RUOCCO, Alessandro: Electronic structure of copper phthalocyanine: An experimental and theoretical study of occupied and unoccupied levels. In: *The Journal of Chemical Physics* 126 (2007), Nr. 12, S. 124709. http://dx.doi.org/10.1063/1.2712435. – DOI 10.1063/1.2712435

[197] RODRÍGUEZ, Roberto R.: *private communication*. CIN2: Centre d'Investigació en Nanociència i Nanotecnologia (CSIC-ICN), Campus de la Universitat Autònoma de Barcelona, 08193 Bellaterra, Spain, 2011-2013

[198] Mugarza, A. ; Lorente, N. ; Ordejón, P. ; Krull, C. ; Stepanow, S. ; Bocquet, M.-L. ; Fraxedas, J. ; Ceballos, G. ; Gambardella, P.: Orbital Specific Chirality and Homochiral Self-Assembly of Achiral Molecules Induced by Charge Transfer and Spontaneous Symmetry Breaking. In: *Phys. Rev. Lett.* 105 (2010), Sep, 115702. http://dx.doi.org/10.1103/PhysRevLett.105.115702. – DOI 10.1103/PhysRevLett.105.115702

[199] Gartland, P. O. ; Berge, S. ; Slagsvold, B. J.: Photoelectric Work Function of a Copper Single Crystal for the (100), (110), (111), and (112) Faces. In: *Phys. Rev. Lett.* 28 (1972), Mar, 738–739. http://dx.doi.org/10.1103/PhysRevLett.28.738. – DOI 10.1103/PhysRevLett.28.738

[200] Bendounan, Azzedine ; Forster, Frank ; Schöll, Achim ; Batchelor, David ; Ziroff, Johannes ; Umbach, Eberhard ; Reinert, Friedrich: Electronic structure of 1ML NTCDA/Ag(111) studied by photoemission spectroscopy. In: *Surface Science* 601 (2007), Nr. 18, 4013 - 4017. http://dx.doi.org/10.1016/j.susc.2007.04.054. – DOI 10.1016/j.susc.2007.04.054. – ISSN 0039–6028. – ¡ce:title¿ECOSS-24¡/ce:title¿ ¡xocs:full-name¿Proceedings of the 24th European Conference on Surface Science¡/xocs:full-name¿

[201] Kröger, Ingo ; Stadtmüller, Benjamin ; Stadler, Christoph ; Ziroff, Johannes ; Kochler, Mario ; Stahl, Andreas ; Pollinger, Florian ; Lee, Tien-Lin ; Zegenhagen, Jörg ; Reinert, Friedrich ; Kumpf, Christian: Submonolayer growth of copper-phthalocyanine on Ag(111). In: *New Journal of Physics* 12 (2010), Nr. 8, 083038. http://stacks.iop.org/1367-2630/12/i=8/a=083038

[202] Stadtmüller, Benjamin ; Kröger, Ingo ; Reinert, Friedrich ; Kumpf, Christian: Submonolayer growth of CuPc on noble metal surfaces. In: *Phys. Rev. B* 83 (2011), Feb, 085416. http://dx.doi.org/10.1103/PhysRevB.83.085416. – DOI 10.1103/PhysRevB.83.085416

[203] Erhardt, H. ; Linder, F.: Rotational Excitation of H2 by Slow Electrons in a Beam Experiment. In: *Physical Review Letters* 21 (1968), Nr. 7

[204] Teillet-Billy, D. ; Gauyacq, J. P. ; Persson, M.: Molecular rotation induced by inelastic electron tunneling. In: *Phys. Rev. B* 62 (2000), Nov, S.

R13306–R13309. http://dx.doi.org/10.1103/PhysRevB.62.R13306. – DOI 10.1103/PhysRevB.62.R13306

[205] Lorente, Nicolás ; Gauyacq, Jean-Pierre: Efficient Spin Transitions in Inelastic Electron Tunneling Spectroscopy. In: *Phys. Rev. Lett.* 103 (2009), Oct, 176601. http://dx.doi.org/10.1103/PhysRevLett.103.176601. – DOI 10.1103/PhysRevLett.103.176601

[206] Gauyacq, Jean-Pierre ; Novaes, Frederico D. ; Lorente, Nicolás: Magnetic transitions induced by tunneling electrons in individual adsorbed M-phthalocyanine molecules (M = Fe and Co). In: *Phys. Rev. B* 81 (2010), Apr, S. 165423. http://dx.doi.org/10.1103/PhysRevB.81.165423. – DOI 10.1103/PhysRevB.81.165423

[207] Gauyacq, Jean-Pierre ; Lorente, Nicolás ; Novaes, Frederico D.: Excitation of local magnetic moments by tunneling electrons. In: *Progress in Surface Science* 87 (2012), Nr. 5-8, S. 63–07. http://dx.doi.org/10.1016/j.progsurf.2012.05.003. – DOI 10.1016/j.progsurf.2012.05.003. – ISSN 0079–6816

[208] Ballmann, Stefan ; Hieringer, Wolfgang ; Secker, Daniel ; Zheng, Qinglin ; Gladysz, John A. ; Görling, Andreas ; Weber, Heiko B.: Molecular Wires in Single-Molecule Junctions: Charge Transport and Vibrational Excitations. In: *ChemPhysChem* 11 (2010), Nr. 10, S. 2256–2260. http://dx.doi.org/10.1002/cphc.200900974. – DOI 10.1002/cphc.200900974. – ISSN 1439–7641

[209] Djukic, D. ; Ruitenbeek, J. M.: Shot Noise Measurements on a Single Molecule. In: *Nano Letters* 6 (2006), Nr. 4, S. 789–793. http://dx.doi.org/10.1021/nl060116e. – DOI 10.1021/nl060116e

[210] Giessibl, Franz J.: High-speed force sensor for force microscopy and profilometry utilizing a quartz tuning fork. In: *Applied Physics Letters* 73 (1998), Nr. 26, 3956-3958. http://dx.doi.org/10.1063/1.122948. – DOI 10.1063/1.122948

[211] Giessibl, Franz J.: Atomic resolution on Si(111)-(7 x 7) by noncontact atomic force microscopy with a force sensor based on a quartz tuning fork. In: *Applied Physics Letters* 76 (2000), Nr. 11, 1470-1472. http://dx.doi.org/10.1063/1.126067. – DOI 10.1063/1.126067

[212] Fu, Ying-Shuang ; Schwöbel, Jörg ; Hla, Saw-Wai ; Dilullo, Andrew ; Hoffmann, Germar ; Klyatskaya, Svetlana ; Ruben, Mario ; Wiesendanger, Roland: Reversible Chiral Switching of Bis(phthalocyaninato) Terbium(III) on a Metal Surface. In: *Nano Letters* 12 (2012), Nr. 8, 3931-3935. http://dx.doi.org/10.1021/nl302166z. – DOI 10.1021/nl302166z

[213] Fendrich, M. ; Wagner, Th. ; Stöhr, M. ; Möller, R.: Hindered rotation of a copper phthalocyanine molecule on C60: Experiments and molecular mechanics calculations. In: *Phys. Rev. B* 73 (2006), Mar, S. 115433. http://dx.doi.org/10.1103/PhysRevB.73.115433. – DOI 10.1103/PhysRevB.73.115433

[214] Smakman, E.P. ; Verheyen, J. ; Helgers, P.L.J. ; Möller, R. ; Koenraad, P.M.: [no title]. In: *in preparation* - (2013), S. –

[215] Smakman, E. P. ; Bree, J. van ; Koenraad, P. M.: Laser and voltage manipulation of bistable Si dopants in the GaAs (110) surface. In: *Phys. Rev. B* 87 (2013), Feb, 085414. http://dx.doi.org/10.1103/PhysRevB.87.085414. – DOI 10.1103/PhysRevB.87.085414

[216] Buchner, F. ; Warnick, K.-G. ; Wölfle, T. ; Görling, A. A. G. A. Görling ; Steinrück, H.-P. ; Hieringer, W. ; Marbach, H.: Chemical Fingerprints of Large Organic Molecules in Scanning Tunneling Microscopy: Imaging Adsorbate-Substrate Coupling of Metalloporphyrins. In: *The Journal of Physical Chemistry C* 113 (2009), Nr. 37, S. 16450–16457. http://dx.doi.org/10.1021/jp904680c. – DOI 10.1021/jp904680c

[217] Wende, Heiko: Molecular magnets: How a nightmare turns into a vision. In: *Nature Materials* 8 (2009), 165-166. http://dx.doi.org/10.1038/nmat2391. – DOI 10.1038/nmat2391

[218] Bernien, M. ; Miguel, J. ; Weis, C. ; Ali, Md. E. ; Kurde, J. ; Krumme, B. ; Panchmatia, P. M. ; Sanyal, B. ; Piantek, M. ; Srivastava, P. ; Baberschke, K. ; Oppeneer, P. M. ; Eriksson, O. ; Kuch, W. ; Wende, H.: Tailoring the Nature of Magnetic Coupling of Fe-Porphyrin Molecules to Ferromagnetic Substrates. In: *Phys. Rev. Lett.* 102 (2009), Jan, S. 047202. http://dx.doi.org/10.1103/PhysRevLett.102.047202. – DOI 10.1103/PhysRevLett.102.047202

[219] Gambardella, P. ; Stepanow, S. ; Dmitriev, A. ; Honolka, J. ; Groot, F.M.F. de ; Lingenfelder, M. ; Gupta, S.S. ; Sarma, D.D. ; Bencok, P. ; Stanescu, S. ; Clair, S. ; Pons, S. ; Lin, N. ; Seitsonen, A.P. ; Brune, H. ; Barth, J.V. ; Kern, K.: Supramolecular control of themagnetic anisotropy in two-dimensional high-spin Fe arrays at a metal interface. In: *Nature Materials* 8 (2009), S. 189–193. http://dx.doi.org/10.1038/nmat2376. – DOI 10.1038/nmat2376

[220] Chylarecka, D. ; Wäckerlin, C. ; Kim, T. ; Müller, K. ; Nolting, F. ; Kleibert, A. ; Ballav, N. ; Jung, T.A.: Self-Assembly and Superexchange Coupling of Magnetic Molecules on Oxygen-Reconstructed Ferromagnetic Thin Film. In: *Journal of Physical Chemistry Letters* 1 (2010), S. 1408–1413. http://dx.doi.org/10.1021/jz100253c. – DOI 10.1021/jz100253c

[221] Chylarecka, D. ; Kim, T. K. ; Tarafder, K. ; Mueller, K. ; Goedel, K. ; Czekaj, I. ; Waeckerlin, C. ; Cinchetti, M. ; Ali, Md. E. ; Piamonteze, C. ; Schmitt, F. ; Wuestenberg, J.-P. ; Ziegler, C. ; Nolting, F. ; Aeschlimann, M. ; Oppeneer, P. M. ; Ballav, N. ; Jung, T. A.: Indirect Magnetic Coupling of Manganese Porphyrin to a Ferromagnetic Cobalt Substrate. In: *The Journal of Physical Chemistry C* 115 (2011), Nr. 4, S. 1295–1301. http://dx.doi.org/10.1021/jp106822s. – DOI 10.1021/jp106822s

[222] Herper, H. C. ; Bernien, M. ; Bhandary, S. ; Hermanns, C. F. ; Krüger, A. ; Miguel, J. ; Weis, C. ; Schmitz-Antoniak, C. ; Krumme, B. ; Bovenschen, D. ; Tieg, C. ; Sanyal, B. ; Weschke, E. ; Czekelius, C. ; Kuch, W. ; Wende, H. ; Eriksson, O.: Iron porphyrin molecules on Cu(001): Influence of adlayers and ligands on the magnetic properties. In: *Phys. Rev. B* 87 (2013), May, 174425. http://dx.doi.org/10.1103/PhysRevB.87.174425. – DOI 10.1103/PhysRevB.87.174425

[223] Wende, H. ; Bernien, M. ; Luo, J. ; Sorg, C. ; Ponpandian, N. ; Kurde, J. ; Miguel, J. ; Piantek, M. ; Xu, X. ; Eckhold, Ph. ; Kuch, W. ; Baberschke, K. ; Panchmatia, P.M. ; Sanyal, B. ; Oppeneer, P.M. ; Eriksson, O.: Substrate-induced magnetic ordering and switching of iron porphyrin molecules. In: *Nature Materials* 6 (2007), S. 516–520. http://dx.doi.org/10.1038/nmat1932. – DOI 10.1038/nmat1932

[224] Humphrey, William ; Dalke, Andrew ; Schulten, Klaus: VMD: Visual molecular dynamics. In: *Journal of Molecular Graphics* 14 (1996), Nr. 1, 33 - 38. http://dx.doi.org/10.1016/0263-7855(96)00018-5. – DOI 10.1016/0263–7855(96)00018–5. – ISSN 0263–7855

[225] Van Vörden, D. ; Lange, M. ; Schaffert, J. ; Cottin, M.C. ; Schmuck, M. ; Robles, R. ; Wende, H. ; Bobisch, C.A. ; Möller, R.: Surface-induced dechlorination of FeOEP-Cl on Cu(111). In: *ChemPhysChem* (accepted for publication). http://dx.doi.org/10.1002/cphc.201300497. – DOI 10.1002/cphc.201300497

[226] Van Vörden, D. ; Lange, M. ; Schmuck, M. ; Schaffert, J. ; Cottin, M.C. ; Bobisch, C.A. ; Möller, R.: Substrate induced dehydrogenation: Transformation of Octa-Ethyl-Porphyrin into Tetra-Benzo-Porphyrin. In: *The Journal of Chemical Physics* 138 (2013), 211102. http://dx.doi.org/10.1063/1.4810879. – DOI 10.1063/1.4810879

[227] Van Vörden, D. ; Lange, M. ; Schaffert, J. ; Cottin, M.C. ; Schmuck, M. ; Robles, R. ; Brendel, L. ; Bobisch, C.A. ; Möller, R.: working title: Surface kinetics and reactions of large organic molecules. In: *n/a* (in preparation)

[228] Tang, C.W.: Two-layer organic photovoltaic cell. In: *Appl. Phys. Lett.* 48 (1986), S. 183. http://dx.doi.org/10.1063/1.96937. – DOI 10.1063/1.96937

[229] Guo, Zhenyu ; Jenekhe, Samson A. ; Prezhdo, Oleg V.: Overcoming excitonic bottleneck in organic solar cells: electronic structure and spectra of novel semiconducting donor-acceptor block copolymers. In: *Phys. Chem. Chem. Phys.* 13 (2011), 7630-7636. http://dx.doi.org/10.1039/C0CP02180F. – DOI 10.1039/C0CP02180F

[230] Barrena, Esther ; Oteyza, Dimas G. ; Dosch, Helmut ; Wakayama, Yutaka: 2D Supramolecular Self-Assembly of Binary Organic Monolayers. In: *ChemPhysChem* 8 (2007), Nr. 13, S. 1915–1918. http://dx.doi.org/10.1002/cphc.200700494. – DOI 10.1002/cphc.200700494. – ISSN 1439–7641

[231] Oteyza, Dimas G. ; García-Lastra, Juan M. ; Corso, Martina ; Doyle, Bryan P. ; Floreano, Luca ; Morgante, Alberto ; Wakayama, Yutaka ; Rubio, Angel ; Ortega, J. E.: Customized Electronic Coupling in Self-Assembled

Donor-Acceptor Nanostructures. In: *Advanced Functional Materials* 19 (2009), Nr. 22, 3567–3573. http://dx.doi.org/10.1002/adfm.200901374. – DOI 10.1002/adfm.200901374. – ISSN 1616–3028

[232] Oteyza, Dimas G. ; Silanes, Iñaki ; Ruiz-Osés, Miguel ; Barrena, Esther ; Doyle, Bryan P. ; Arnau, Andrés ; Dosch, Helmut ; Wakayama, Yutaka ; Ortega, J. E.: Balancing Intermolecular and Molecule-Substrate Interactions in Supramolecular Assemblies. In: *Advanced Functional Materials* 19 (2009), Nr. 2, 259-264. http://dx.doi.org/10.1002/adfm.200801453. – DOI 10.1002/adfm.200801453. – ISSN 1616–3028

[233] Chen, Wei ; Li, Hui ; Huang, Han ; Fu, Yuanxi ; Zhang, Hong L. ; Ma, Jing ; Wee, Andrew Thye S.: Two-Dimensional Pentacene:3,4,9,10-Perylenetetracarboxylic Dianhydride Supramolecular Chiral Networks on Ag(111). In: *Journal of the American Chemical Society* 130 (2008), Nr. 37, S. 12285–12289. http://dx.doi.org/10.1021/ja801577z. – DOI 10.1021/ja801577z. – PMID: 18722423

[234] Yoshimoto, Soichiro ; Honda, Yosuke ; Ito, Osamu ; Itaya, Kingo: Supramolecular Pattern of Fullerene on 2D Bimolecular 'Chessboard' Consisting of Bottom-up Assembly of Porphyrin and Phthalocyanine Molecules. In: *Journal of the American Chemical Society* 130 (2008), Nr. 3, 1085-1092. http://dx.doi.org/10.1021/ja077407p. – DOI 10.1021/ja077407p

[235] Huang, Han ; Huang, Yuli ; Pflaum, Jens ; Wee, Andrew Thye S. ; Chen, Wei: Nanoscale phase separation of a binary molecular system of copper phthalocyanine and di-indenoperylene on Ag(111). In: *Applied Physics Letters* 95 (2009), Nr. 26, 263309. http://dx.doi.org/10.1063/1.3280858. – DOI 10.1063/1.3280858

[236] Tautz, F.S.: Structure and bonding of large aromatic molecules on noble metal surfaces: The example of {PTCDA}. In: *Progress in Surface Science* 82 (2007), Nr. 9-12, 479-520. http://dx.doi.org/http://dx.doi.org/10.1016/j.progsurf.2007.09.001. – DOI http://dx.doi.org/10.1016/j.progsurf.2007.09.001. – ISSN 0079–6816

[237] Gerlach, A. ; Sellner, S. ; Schreiber, F. ; Koch, N. ; Zegenhagen, J.: Substrate-dependent bonding distances of PTCDA: A comparative x-ray

standing-wave study on Cu(111) and Ag(111). In: *Phys. Rev. B* 75 (2007), Jan, 045401. http://dx.doi.org/10.1103/PhysRevB.75.045401. – DOI 10.1103/PhysRevB.75.045401

[238] Glöckler, K ; Seidel, C ; Soukopp, A ; Sokolowski, M ; Umbach, E ; Böhringer, M ; Berndt, R ; Schneider, W.-D: Highly ordered structures and submolecular scanning tunnelling microscopy contrast of {PTCDA} and DM-PBDCI monolayers on Ag(111) and Ag(110). In: *Surface Science* 405 (1998), Nr. 1, 1-20. http://dx.doi.org/http://dx.doi.org/10.1016/S0039-6028(97)00888-1. – DOI http://dx.doi.org/10.1016/S0039–6028(97)00888–1. – ISSN 0039–6028

[239] Duhm, S. ; Gerlach., A ; Salzmann., I. ; Bröcker, B. ; Johnson, R.L. ; Schreiber, F. ; Koch, N.: PTCDA on Au(111) and Ag(111) and Cu(111): Correlating bonding distance and interfacial charge transfer. In: *Organic Electronics* 9 (2008), 111. http://dx.doi.org/doi:10.1016/j.orgel.2007.10.004

[240] Fendrich, M.: *Frequenzmodulierte Rasterkraftmikroskopie an organischen Molekülen, phd thesis*, Universität Duisburg-Essen, Duisburg, Germany, Diss., 2008. http://duepublico.uni-duisburg-essen.de/servlets/DocumentServlet?id=18683

[241] Forrest, S. R. ; Burrows, P. E. ; Haskal, E. I. ; So, F. F.: Ultrahigh-vacuum quasiepitaxial growth of model van der Waals thin films. II. Experiment. In: *Phys. Rev. B* 49 (1994), Apr, 11309–11321. http://dx.doi.org/10.1103/PhysRevB.49.11309. – DOI 10.1103/PhysRevB.49.11309

[242] Kendrick, C. ; Kahn, A. ; Forrest, S.R.: {STM} study of the organic semiconductor {PTCDA} on highly-oriented pyrolytic graphite. In: *Applied Surface Science* 104-105 (1996), Nr. 0, 586 - 594. http://dx.doi.org/http://dx.doi.org/10.1016/S0169-4332(96)00207-3. – DOI http://dx.doi.org/10.1016/S0169–4332(96)00207–3. – ISSN 0169–4332. – ¡ce:title¿Proceedings of the Fifth International Conference on the Formation of Semiconductor Interfaces¡/ce:title¿

[243] Schmitz-Hübsch, T. ; Fritz, T. ; Sellam, F. ; Staub, R. ; Leo, K.: Epitaxial growth of 3,4,9,10-perylene-tetracarboxylic-dianhydride on Au(111): A STM and

RHEED study. In: *Phys. Rev. B* 55 (1997), Mar, 7972–7976. http://dx.doi.org/10.1103/PhysRevB.55.7972. – DOI 10.1103/PhysRevB.55.7972

[244] Seidel, C. ; Awater, C. ; Liu, X.D. ; Ellerbrake, R. ; Fuchs, H.: A combined STM, {LEED} and molecular modelling study of {PTCDA} grown on Ag(110). In: *Surface Science* 371 (1997), Nr. 1, 123 - 130. http://dx.doi.org/http://dx.doi.org/10.1016/S0039-6028(96)00981-8. – DOI http://dx.doi.org/10.1016/S0039–6028(96)00981–8. – ISSN 0039–6028

[245] Böhringer, M. ; Schneider, W.-D. ; Glöckler, K. ; Umbach, E. ; Berndt, R.: Adsorption site determination of {PTCDA} on Ag(110) by manipulation of adatoms. In: *Surface Science* 419 (1998), Nr. 1, L95 - L99. http://dx.doi.org/http://dx.doi.org/10.1016/S0039-6028(98)00733-X. – DOI http://dx.doi.org/10.1016/S0039–6028(98)00733–X. – ISSN 0039–6028

[246] Temirov, R. ; Soubatch, S. ; Luican, A. ; Tautz, F. S.: Free-electron-like dispersion in an organic monolayer film on a metal substrate. In: *Nature* 444 (2006), Nr. 7117, 350–353. http://dx.doi.org/10.1038/nature05270. – ISSN 0028–0836

[247] Rohlfing, Michael ; Temirov, Ruslan ; Tautz, Frank S.: Adsorption structure and scanning tunneling data of a prototype organic-inorganic interface: PTCDA on Ag(111). In: *Phys. Rev. B* 76 (2007), Sep, 115421. http://dx.doi.org/10.1103/PhysRevB.76.115421. – DOI 10.1103/PhysRevB.76.115421

[248] Wagner, Th ; Bannani, A ; Bobisch, C ; Karacuban, H ; Möller, R: The initial growth of PTCDA on Cu(111) studied by STM. In: *Journal of Physics: Condensed Matter* 19 (2007), Nr. 5, 056009. http://stacks.iop.org/0953-8984/19/i=5/a=056009

[249] Kendrick, C. ; Kahn, A.: Epitaxial growth and phase transition in multilayers of the organic semiconductor {PTCDA} on InAs(0 0 1). In: *Journal of Crystal Growth* 181 (1997), Nr. 3, 181 - 192. http://dx.doi.org/http://dx.doi.org/10.1016/S0022-0248(97)00285-6. – DOI http://dx.doi.org/10.1016/S0022–0248(97)00285–6. – ISSN 0022–0248

[250] Kunstmann, T. ; Schlarb, A. ; Fendrich, M. ; Wagner, Th. ; Möller, R. ; Hoffmann, R.: Dynamic force microscopy study of 3,4,9,10-perylenetetracarboxylic

dianhydride on KBr(001). In: *Phys. Rev. B* 71 (2005), Mar, 121403. http://dx.doi.org/10.1103/PhysRevB.71.121403. – DOI 10.1103/PhysRevB.71.121403

[251] Fendrich, M ; Kunstmann, T ; Paulkowski, D ; Möller, R: Molecular resolution in dynamic force microscopy: topography and dissipation for weakly interacting systems. In: *Nanotechnology* 18 (2007), Nr. 8, 084004. http://stacks.iop.org/0957-4484/18/i=8/a=084004

[252] Sheats, James R.: Stacked Organic Light-Emitting Diodes in Full Color. In: *Science* 277 (1997), Nr. 5323, 191-192. http://dx.doi.org/10.1126/science.277.5323.191. – DOI 10.1126/science.277.5323.191

[253] Shen, Zilan ; Burrows, Paul E. ; Bulovic, Vladimir ; Forrest, Stephen R. ; Thompson, Mark E.: Three-Color, Tunable, Organic Light-Emitting Devices. In: *Science* 276 (1997), Nr. 5321, 2009-2011. http://dx.doi.org/10.1126/science.276.5321.2009. – DOI 10.1126/science.276.5321.2009

[254] Forrest, Stephen R.: Ultrathin Organic Films Grown by Organic Molecular Beam Deposition and Related Techniques. In: *Chemical Reviews* 97 (1997), Nr. 6, 1793-1896. http://dx.doi.org/10.1021/cr941014o. – DOI 10.1021/cr941014o

[255] Stadler, Ch. ; Hansen, S. ; Kröger, I. ; Kumpf, Ch. ; Umbach, E.: Tuning intermolecular interaction in long-range-ordered submonolayer organic films. In: *Nature Physics* 5 (2009), January, S. 153–158. http://dx.doi.org/10.1038/nphys1176. – DOI 10.1038/nphys1176

[256] Bauer, E: Low energy electron microscopy. In: *Reports on Progress in Physics* 57 (1994), Nr. 9, 895. http://stacks.iop.org/0034-4885/57/i=9/a=002

[257] Heringdorf, Frank-J. Meyer z. ; Reuter, M. C. ; Tromp, R. M.: Growth dynamics of pentacene thin films. In: *Nature* 412 (2001), August, Nr. 6846, 517–520. http://dx.doi.org/10.1038/35087532. – ISSN 0028–0836

[258] Cottin, M. C. ; Bobisch, C. A. ; Schaffert, J. ; Jnawali, G. ; Sonntag, A. ; Bihlmayer, G. ; Moller, R.: Anisotropic scattering of surface state electrons at a point defect on Bi(111). In: *Applied Physics Letters* 98 (2011), Nr. 2, S. 022108–022108–3. http://dx.doi.org/10.1063/1.3536528. – DOI 10.1063/1.3536528. – ISSN 0003–6951

[259] Bobisch, C.A. ; Bernhart, A.M. ; Kaspers, M.R. ; Cottin, M.C. ; Schaffert, J. ; Möller, R.: Electronic Transport on the Nanoscale. Version: 2012. http://dx.doi.org/10.1007/978-3-642-28172-3_15. In: Joachim, Christian (Hrsg.): *Atomic Scale Interconnection Machines*. Springer Berlin Heidelberg, 2012 (Advances in Atom and Single Molecule Machines). – ISBN 978–3–642–28171–6, 197-214

[260] Cottin, Maren C. ; Bobisch, Christian A. ; Schaffert, Johannes ; Jnawali, Giriraj ; Bihlmayer, Gustav ; Möller, Rolf: Interplay between Forward and Backward Scattering of Spin-Orbit Split Surface States of Bi(111). In: *Nano Letters* 13 (2013), Nr. 6, 2717-2722. http://dx.doi.org/10.1021/nl400878r. – DOI 10.1021/nl400878r

List of Figures

List of Tables

List of Abbreviations

1 Å	1 Ångstrøm = 0.1 nm = $1 \cdot 10^{-10}$ m
AFM	atomic force microscope/microscopy
amu	atomic mass unit
app.	appendix
ch.	chapter
CuPc	copper-phthalocyanine
DFT	density functional theory
dI/dV	the derivative of the tunneling current with respect to the bias voltage
eq.	equation
ESQC	elastic scattering quantum chemistry
et al.	et alii (and others)
eV	electron volt
ext	external
fcc	face centered cubic
FeOEP-Cl	2,3,7,8,12,13,17,18-octaethylporphyrin Fe(III) chloride
FLUMO/F-LUMO	former lowest unoccupied molecular orbital
GGA	generalized gradient approximation
HK	Hohenberg-Kohn
hom	homogeneous
HOMO	highest occupied molecular orbital
HOMO-1	second highest occupied molecular orbital
IVC	current to voltage converter
KS	Kohn-Sham
LDA	local density approximation
LDOS	local density of states
LEED	low energy electron diffraction
LSDA	local spin density approximation

LT	low temperature
LT-STM	low-temperature scanning tunneling microscope/microscopy
LT-STS	low-temperature scanning tunneling spectroscopy
LUMO	lowest unoccupied molecular orbital
ML	monolayer
MPc	metal phthalocyanine
OLED	organic light emitting device
PDOS	projected density of states
PEEM	photoelectron emission microscopy
PES	potential energy surface
	or: photoelectron spectroscopy
PTCDA	3,4,9,10-perylene-tetracarboxylicacid-dianhydride
RDOS	rotational density of states
ref.	reference
RTN	random telegraph noise
sec.	section
SEM	scanning electron microscope/microscopy
SNM	scanning noise microscopy
SNS	scanning noise spectroscopy
SPM	scanning probe microscope/microscopy
STM	scanning tunneling microscope/microscopy
STS	scanning tunneling spectroscopy
TN	telegraph noise
UHV	ultra high vacuum
UPS	ultraviolet photoelectron spectroscopy
VASP	Vienna Ab Initio Simulation Package
vdW	van der Waals
XC	exchange and correlation
XPS	x-ray photoelectron spectroscopy

List of Publications

Articles

1. Karacuban, H.; Lange, M.; Schaffert, J.; Weingart, O.; Wagner, T.; Möller, R.: Substrate-induced symmetry reduction of CuPc on Cu(111): An LT-STM study. In: *Surface Science* **603**, L39-L43 (2009) → [24].

2. Schaffert, Johannes: Rastertunnelmikroskopie an organischen Molekülen bei tiefen Temperaturen. *Diploma Thesis*, University of Duisburg-Essen, Lotharstr. 1, D-47057 Duisburg, Germany, Faculty of Physics (2009).

3. Cottin, M. C.; Bobisch, C. A.; Schaffert, J.; Jnawali, G.; Sonntag, A.; Bihlmayer, G.; Möller, R.: Anisotropic scattering of surface state electrons at a point defect on Bi(111). In: *Applied Physics Letters* **98**, 022108-022108-3 (2011) → [258].

4. Cottin, M.C.; Schaffert, J.; Sonntag, A.; Karacuban, H.; Möller, R.; Bobisch, C.A., Supramolecular architecture of organic molecules: PTCDA and CuPc on a Cu(111) substrate. In: *Applied Surface Science* **258**, 2196 - 2200 (2012) → [169].

5. Bobisch, C.A.; Bernhart, A.M.; Kaspers, M.R.; Cottin, M.C.; Schaffert, J.; Möller, R.: Electronic Transport on the Nanoscale. In: *Atomic Scale Interconnection Machines*, 197-214, Series: Advances in Atom and Single Molecule Machines, Editor: Joachim, Christian; Springer Berlin Heidelberg (2012) → [259].

6. Schaffert, J.; Cottin, M.C.; Sonntag, A.; Karacuban, H.; Bobisch, C.A.; Lorente, N.; Gauyacq, J.-P.; Möller, R.: Imaging the dynamics of individually adsorbed molecules. In: *Nature Materials* **12**, 223-227 (2012) → [143].

7. Schaffert, J.; Cottin, M.C.; Sonntag, A.; Karacuban, H.; Utzat, D.; Bobisch, C.A.; Möller, R.: Scanning noise microscopy. In: *Review of Scientific Instruments* **84**, 043702 (2013) → [124].

8. Cottin, M.C.; Bobisch, C.A.; Schaffert, J.; Jnawali, G.; Bihlmayer, G.; Möller, R.: Interplay between Forward and Backward Scattering of Spin-Orbit Split Surface States of Bi(111). In: *Nano Letters* **13**, 2717-2722 (2013) → [260].

9. Van Vörden, D.; Lange, M.; Schmuck, M.; Schaffert, J.; Cottin, M.C.; Bobisch, C.A.; Möller, R.: Substrate induced dehydrogenation: Transformation of Octa-Ethyl-Porphyrin into Tetra-Benzo-Porphyrin. In: *The Journal of Chemical Physics* **138**, 211102 (2013) → [226].

10. Schaffert, J.; Cottin, M.C.; Sonntag, A.; Bobisch, C.A.; Möller, R.; Gauyacq, J. P.; Lorente, N.: *Tunneling electron induced rotation of a copper phthalocyanine molecule on Cu (111)*. In: *Physical Review B* **88**, 075410 (2013) → [181].

11. Van Vörden, D.; Lange, M.; Schaffert, J.; Cottin, M.C.; Schmuck, M.; Robles, R.; Wende, H.; Bobisch, C.A.; Möller, R.: Surface-induced dechlorination of FeOEP-Cl on Cu(111). In: *ChemPhysChem* (accepted for publication) → [225].

12. Cottin, M.C.; Lobo-Checa, J.; Schaffert, J.; Bobisch, C.A.; Möller, R.; Ortega, J.E.; Walter, A.L.: A chemically inert Rashba split interface: electronic structure of C_{60}, FeOEP and PTCDA on $BiAg_2$/Ag(111) substrates. In: *in review*.

13. Van Vörden, D.; Lange, M.; Schmuck, M.; Schaffert, J.; Cottin, M.C.; Robles, R.; Bobisch, C.A.; Möller, R.: Surface reactions and kinetics of large organic molecules (working title). In: *in preparation*.

14. Cottin, M.C.; Schaffert, J.; Bobisch, C.A.; Möller, R.: Low-temperature scanning tunneling spectroscopy study on Bi/Ag(111) (working title). In: *in preparation*

Conferences

Talks (selected)

1. Lange, M.*; Schaffert, J.*[3]; Wintjes, N.; Karacuban, H.; Möller, R.: Tieftemperatur-Rastertunnel- & -Rasterkraftmikroskopie. SFB616 Collaborators Workshop, Papenburg, Germany (2009).

[3] Asterisks indicate the presenting author(s).

2. Schaffert, J.*; Karacuban, H.; Cottin, M.C.; Sonntag, A.; Möller, R.: Spectroscopy of CuPc and PTCDA on Cu(111): The role of interface states. 26th European Conference on Surface Science (ECOSS26), Parma, Italy (2009).

3. Schaffert, J.*; Karacuban, H.; Cottin, M.C.; Sonntag, A.; Möller, R.: Spectroscopy of CuPc and PTCDA on Cu(111). SFB616 Summerschool, Essen, Germany (2009).

4. Schaffert, J.*; Cottin, M.C.; Sonntag, A.; Bobisch, C.A.; Lorente, N.; Möller, R.: Organische Elektronik - Beispiele für Grundlagenforschung mit dem Rastertunnelmikroskop. SFB616 Collaborators Workshop, Papenburg, Germany (2010).

5. Bobisch, C.A.*; Cottin, M.C.; Schaffert, J.; Sonntag, A.; Jnawali, G.; Horn-von Hoegen, M.; Bihlmayer, G.; Möller, R.: Electronic properties of thin Bi(111) films. 18th International Vacuum Congress and International Conference on Nanoscience + Technology (IVC18 + ICN+T2010), Beijing, China (2010).

6. Schaffert, J.; Cottin, M.C.; Sonntag, A.; Bobisch, C.A.; Karacuban, H.; Lorente, N.; Möller, R.*: Noise in tunneling current: Analysis of molecular switching. 18th International Vacuum Congress and International Conference on Nanoscience + Technology (IVC18 + ICN+T2010), Beijing, China (2010).

7. Bobisch, C.A.*; Kaspers, M.R.; Bernhart, A.M.; Cottin, M.C.; Schaffert, J.; Jnawali, G.; Sonntag, A.; Möller, R.: *Scattering of surface state electrons at defects*, International Workshop on Nanomaterials and Nanodevices, Beijing, China (2010).

8. Schaffert, J.*; Cottin, M.C.; Sonntag, A.; Karacuban, H.; Lorente, N.; Bobisch, C.A.; Möller, R.: Molecular switching analyzed with sub-molecular precision: CuPc on Cu(111). DPG Spring Meeting, Dresden, Germany (2011).

9. Cottin, M.C.*; Bobisch, C.A.; Schaffert, J.; Sonntag, A.; Jnawali, G.; Bihlmayer, G.; Möller, R.: Scattering of Bi(111) Surface State Electrons Visualized by Low Temperature Scanning Tunneling Microscopy. 28th European Conference on Surface Science (ECOSS28), Wroclaw, Poland (2011).

10. Bobisch, C.A.*; Schaffert, J.; Cottin, M.C.; Sonntag, A.; Karacuban, H.; Gauyacq, J.P.; Lorente, N.; Möller, R.: Revealing molecular dynamics through scanning noise microscopy and spectroscopy. 28th European Conference on Surface Science (ECOSS28), Wroclaw, Poland (2011).

11. Schaffert, J.*; Cottin, M.C.; Sonntag, A.; Karacuban, H.; Gauyacq, J.-P.; Lorente, N.; Bobisch, C.A.; Möller, R.: Revealing molecular switching by scanning noise microscopy and spectroscopy. *Best Poster Award Prize Talk*, SFB616 Summerschool, Waldbreitbach, Germany (2011).

12. Schaffert, J.*; Cottin, M.C.; Sonntag, A.; Karacuban, H.; Gauyacq, J.-P.; Lorente, N.; Bobisch, C.A.; Möller, R.: Revealing molecular switching by scanning noise microscopy and spectroscopy. Workshop of the SFB616, Remagen, Germany (2011).

13. Schaffert, J.*; Cottin, M.C.; Sonntag, A.; Karacuban, H.; Gauyacq, J.-P.; Lorente, N.; Bobisch, C.A.; Möller, R.: Revealing molecular dynamics through scanning noise microscopy and spectroscopy. Workshop of the SFB616, Langeoog, Germany (2012).

Poster Presentations (selected)

1. Karacuban, H.; Schaffert, J.*; Koch, S.; Wagner, T.; Möller, R.: LT-STM study of individual CuPc molecules on Cu(111). DPG Spring Meeting, Berlin, Germany (2008).

2. Schaffert, J.*; Cottin, M.C.; Sonntag, A.; Karacuban, H.; Lorente, N.; Bobisch, C.A.; Möller, R.: Visualization of molecular switching of CuPc on Cu(111). International Workshop of the SFB616, Kloster-Schöntal, Germany (2010).

3. Schaffert, J.*; Cottin, M.C.; Sonntag, A.; Karacuban, H.; Lorente, N.; Bobisch, C.A.; Möller, R.: Visualization of molecular switching of CuPc on Cu(111). 18th International Vacuum Congress and International Conference on Nanoscience + Technology (IVC18 + ICN+T2010), Beijing, China (2010).

4. Cottin, M.C.*; Schaffert, J.; Sonntag, A.; Karacuban, H.; Bobisch, C.A.; Möller, R.: Supramolecular architecture of organic molecules: PTCDA and CuPc on a Cu(111)-substrate. 18th International Vacuum Congress and International Conference on Nanoscience + Technology (IVC18 + ICN+T2010), Beijing, China (2010).

5. Schaffert, J.*; Cottin, M.C.; Sonntag, A.; Karacuban, H.; Utzat, D.; Gauyacq, J.-P.; Lorente, N.; Bobisch, C.A.; Möller, R.: Revealing molecular dynamics through scanning noise microscopy. SFB616 Summerschool, Waldbreitbach, Germany (2011).

6. Cottin, M.C.*; Schaffert, J.; Platz, W.; Möller, R.; Bobisch, C.A.: Implementing a Setup to Detect Ballistic and Inelastic Channels in an LT-STM Experiment. *Best Poster Award*, International Conference on Nanoscience + Technology (ICN+T2012), Paris, France (2012).

7. Cottin, M.C.*; Schaffert, J.; Lobo-Checa, J.; Ortega, J.E.; Walter, A.L.; Möller, R.; Bobisch, C.A.: Adsorption of Organic Layers on the BiAg Surface Alloy Exhibiting a Giant Spin Orbit Splitting. DPG Spring Meeting, Regensburg, Germany (2013).

8. van Vörden, D.; Lange, M.; Schaffert, J.; Schmuck, M.; Robles Rodríguez, R.; Bobisch, C.A.; Möller, R.: Adsorption of FeOEP-Cl on Cu(111). DPG Spring Meeting, Regensburg, Germany (2013).

9. Özen, E.*; Cottin, M.C.; Schaffert, J.; Platz, W.; Möller, R.; Bobisch, C.A.: The Detection of Light Emitted from the Tunneling Junction of a Low Temperature-STM. DPG Spring Meeting, Regensburg, Germany (2013).

10. Schaffert, J.*; Cottin, M.C.; Sonntag, A.; Karacuban, H.; Utzat, D.; Gauyacq, J.-P.; Lorente, N.; Bobisch, C.A.; Möller, R.: Imaging the dynamics of individually adsorbed molecules. International Workshop of the SFB616, Bad Honnef, Germany (2013).

Invited Talks

1. Schaffert, J.*; Lange, M.; Karacuban, H.; Möller, R.: Scanning tunneling microscopy and spectroscopy of organic molecules (CuPc and PTCDA) on Cu(111) at low temperatures. Seminar on Surface Science, University of Central Florida, Orlando, Florida, USA (2009).

2. Schaffert, J.*; Cottin, M.C.; Sonntag, A.; Karacuban, H.; Gauyacq, J.-P.; Lorente, N.; Bobisch, C.A.; Möller, R.: Revealing molecular dynamics through scanning noise microscopy and spectroscopy. Electron-driven processes at molecular level (EDPML), Prague, Czech Republic (2011).

3. Schaffert, J.*; Cottin, M.C.; Sonntag, A.; Karacuban, H.; Gauyacq, J.-P.; Lorente, N.; Bobisch, C.A.; Möller, R.: Analysis of the dynamics of an adsorbed organic molecule. Seminar of the Institute of Nanotechnology, Karlsruhe Institute of Technology (KIT), Karlsruhe, Germany (2013).

Awards

1. *Best Poster Award*, International Workshop of the SFB616, Kloster-Schöntal, Germany (2010).
2. *Best Poster Award*, SFB616 Summerschool, Waldbreitbach, Germany (2011).
3. *Best Poster Award*, International Workshop of the SFB616, Bad Honnef, Germany (2013).

Erklärung

Ich versichere an Eides statt durch meine Unterschrift, dass ich die vorstehende Arbeit selbstständig und ohne fremde Hilfe außer der angegebenen angefertigt habe. Die aus fremden Quellen direkt oder indirekt übernommenen Gedanken sind als solche kenntlich gemacht und ich habe mich keiner anderen als der angegebenen Literatur oder sonstiger Hilfsmittel bedient. Die Arbeit hat in dieser oder ähnlicher Form noch keiner anderen Prüfungsbehörde vorgelegen.

Die Arbeit wurde unter wissenschaftlicher Betreuung durch Herrn Prof. Dr. Rolf Möller am Institut für Experimentelle Physik der Universität Duisburg-Essen angefertigt.

Duisburg, 22. August 2013 _____

Johannes Schaffert

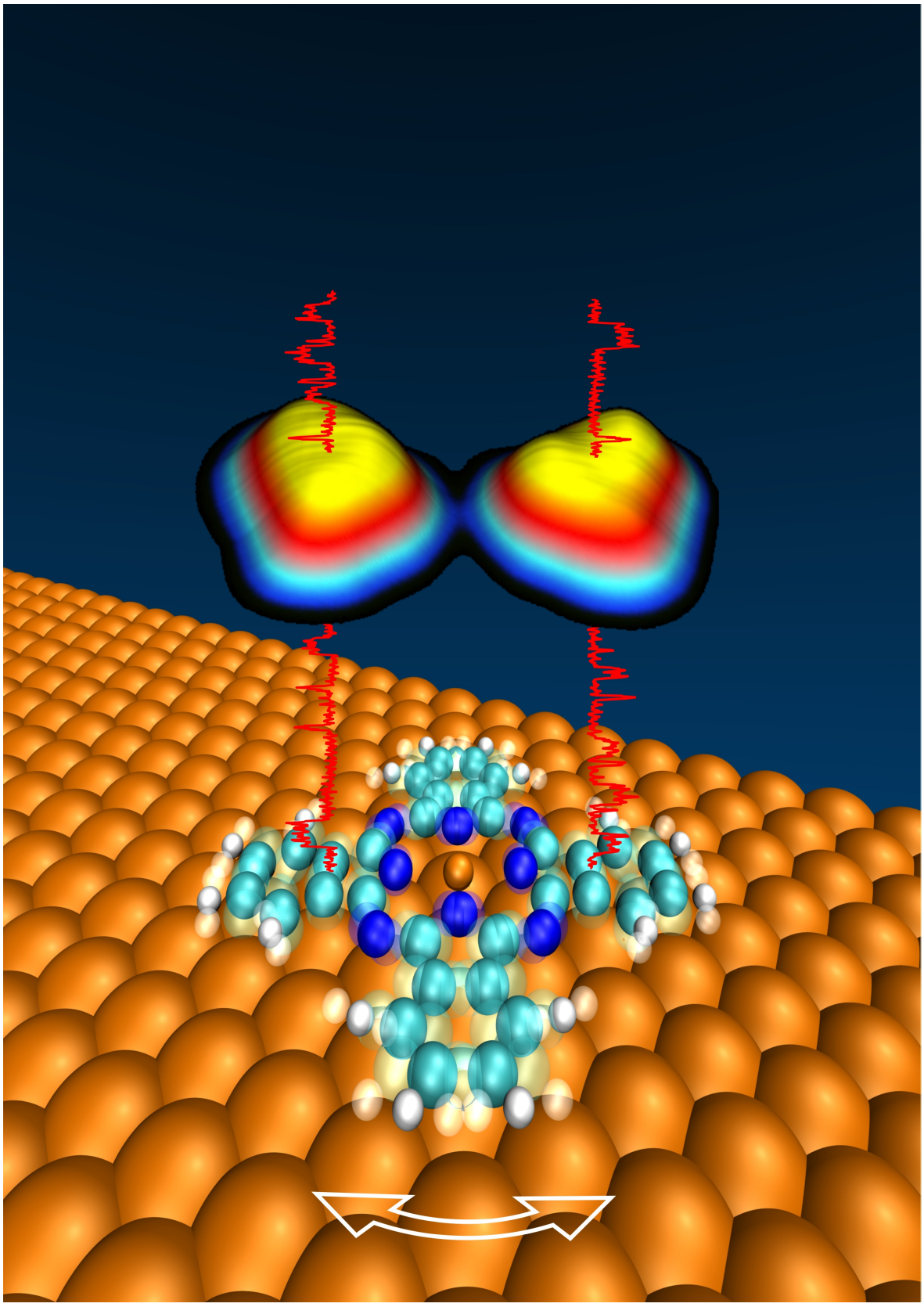

Acknowledgments

One of the most important things that I need to do after four wonderful years is to say thank you!

First, I want to thank Prof. Rolf Möller for giving me the opportunity to become part of his group for a few more years after my diploma thesis. The door of his office was always open and his shared experimental expertise cannot be appreciated highly enough. A very special atmosphere perfected the working conditions in his group.

I want to thank Dr. Christian Bobisch, who is the assistant of Prof. Möller and project leader in our SFB project, for his enormous helpfulness in each and every situation. Inside as well as outside the lab his constructive and very hands-on approach was a great help.

Dr. Nicolás Lorente is acknowledged for offering me to visit him at the campus of the Universitát Autonoma de Barcelona in 2009 and 2011. He invested a lot of time to teach an experimentalist how to unleash the powerful magic of density functional theory and how to make the machines work on the systems that I was interested in: organic molecules adsorbed on metal surfaces. Our productive collaboration continued after the research stays and profited a lot from his open and humorous style, explicit emails, and heavy workload.

Prof. Jean-Pierre Gauyacq joined our efforts on the molecular rotation excitation by electron scattering and shared his expertise without hesitation. Thank you, Jean-Pierre, for the fantastic cooperation and the many patient answers to my questions.

So much for the PIs :-) The everyday-life in the lab, however, the days and weeks and months of tries and errors, enthusiasm and desperation, and of course the long nights of measurements were shared primarily with Maren C. Cottin. Her initials MC^2 already say it all: Maren is an in-cre-di-bly energetic person and it was my pleasure to share a lab with her. Maren started in our lab as my diploma student together with Andreas Sonntag, who I thank for joining me on the first trip to theoretical physics in 2009, teaching me many linux commands and having a great time together. I want to thank Hatice Karacuban, who introduced me to both, our laboratory and the Möller group and supervised my diploma

thesis. Furthermore, it has always been a great pleasure to work and spend time with my colleagues and former colleagues Manfred Lange, Ben Wortmann, Alexander Bernhart, Mark Kaspers, David Krix, Hermann Nienhaus, Ulrich Hagemann, Dennis Van Vörden, Kornelia Huba, Markus Fendrich, Amin Bannani, Thorsten Wagner, Tobias Kunstmann, our cooperation partners Giriraj Jnawali, Gustav Bihlmayer, Heiko Wende, Bernhart Krumme, Roberto Robles, and our students Ebru Özen, Matthias Müller, Merlin Schmuck, Sebastian Bauer, Nico Schmidt, Martin Pfeiler, Achim Gerstenberg, Andrew Paolo Cadíz Bedini and Felix Becker. We shared an enthusiasm for music and visited concerts, played football in Duisburg-Meidrich and had hundreds of controversial and very entertaining discussions in the coffee breaks. Several friendships evolved from the last years which I wish to last.

Our laboratories would never develop their full potential without the expertise of our helpful technicians Doris Steeger, Willy Platz, Helmut Müntz, Tobias Roos, and Detlef Utzat. Detlef is especially acknowledged for the construction of the STM electronics and the SNM electronics.

Bureaucracy can be challenging at times. Luckily, Dagmar Thiele (Möller group) and Maria Dunke (SFB616) disburdened us at all times.

The Deutsche Forschungsgemeinschaft (DFG) is acknowledged for funding through the Sonderforschungsbereich 616 'Energy Dissipation at Surfaces'.

In Barcelona, I enjoyed to work with, learn from and spend time with Richard Korytar, Roberto Robles, Sandra García-Gil and Desanka Boskovic.

Furthermore, I want to thank my friends, who volunteered in proofreading: Thee Chanyaswad from the University of Oxford, Wallace Brown from the University of St. Andrews, the newlyweds Emily Wolak and Matthäus (Matt) Wolak from the Temple University, Philadelphia, Eric Jahn, as well as Nico Schmidt, Maren Cottin, Ben Wortmann, Ulrich Hagemann, Manfred Lange and Christian Bobisch from our group.

I want to thank my family Dorothee and Hellmuth Schaffert, Henrike Schaffert (who did her PhD faster than me ;-)), Kathrin Schaffert, Lena Schaffert, Christian Schaffert, Karin and Klaus Witt, and all the other members of our family and my friends for their support

and at times even interest in my work.

Most importantly, I want to thank Corinna, who always supported me and my project as my girlfriend, since 2009 as my wife, and since 2012 as the mother of our son Felix. Thank you for bearing all my stories from the lab, the good news and the bad news, and the overtime hours.

Can one thank someone in a PhD thesis who cannot even talk yet? I clearly think so, and therefore I finally want to thank Felix for giving me a great time and an extra load of motivation.

Figure B.7.: The LT-STM team. From left to right: Johannes Schaffert, Maren Cottin, Rolf Möller, and Christian Bobisch listening to noise.